



Cardiff
Catalysis Institute

Sefydliad Catalysis
Caerdydd

Linking Flow Reactor and Temporal Analysis of Product (TAP) Kinetic Studies

Thesis submitted in accordance with the requirements of
Cardiff University for the degree of Doctor of Philosophy by

Leticia Ruiz Castillo

School of Chemistry

Cardiff University

April 2020

Abstract

The study of chemical kinetics of various catalytic systems has been the focus of the work presented in this thesis, which was primarily supported on continuous flow approaches complemented with TAP reactor experimental analysis. Software development constituted an essential part in this research. On the one hand, the implementation of a software system made possible the automation of continuous flow reactions. On the other hand, a second piece of software allowed the extraction of kinetic information from experimental TAP data.

During the continuous flow investigation, inactivity of Au/TiO₂ toward the CO oxidation reaction was observed. Near atmosphere pressure (NAP)-XPS analyses revealed the presence of both Au¹⁺ and Au⁰ species on the surface of Au/CeO₂ while only Au⁰ was detected on Au/TiO₂. This suggested that the presence of both cationic and metallic gold species is important to kick start the CO oxidation reaction at low temperatures. Based on the different activities observed during temperature ramp up and ramp down stages when fresh and reused samples were tested, and also supported on the NAP-XPS analysis results, the transition from Au⁺¹ to Au⁰ starting at a temperature threshold of around 40-50 °C was proposed. Regarding activation energies, values around 40-45 kJ mol⁻¹ were calculated for both Au/CeO₂ and AuPd/CeO₂. Finally, orders of reaction with respect to CO at constant ratio between concentration of reactants (CO and O₂) with similar values of around 1 were obtained for both Au/CeO₂ and AuPd/CeO₂.

Flow reactor studies were complemented with TAP reactor experiments. Relevant parameters such as the number of molecules per pulse or the percentage of active surface oxygen were calculated. Finally, based on a series of qualitative assessments, a combination of both Eley-Rideal and Langmuir-Hinshelwood mechanisms was proposed to be taking place on the surface of Au/CeO₂.

STATEMENTS AND DECLARATIONS

STATEMENT 1

This thesis is being submitted in partial fulfilment of the requirements for the degree of *PhD*.

Signed:



Date: 13/04/2020

STATEMENT 2

This work has not been submitted in substance for any other degree or award at this or any other university or place of learning, nor is it being submitted concurrently for any other degree or award (outside of any formal collaboration agreement between the University and a partner organisation).

Signed:



Date: 13/04/2020

STATEMENT 3

I hereby give consent for my thesis, if accepted, to be available in the University's Open Access repository (or, where approved, to be available in the University's library and for inter-library loan), and for the title and summary to be made available to outside organisations, subject to the expiry of a University-approved bar on access if applicable.

Signed:

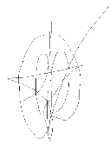


Date: 13/04/2020

DECLARATION

This thesis is the result of my own independent work, except where otherwise stated, and the views expressed are my own. Other sources are acknowledged by explicit references. The thesis has not been edited by a third party beyond what is permitted by Cardiff University's Use of Third Party Editors by Research Degree Students Procedure.

Signed:

A handwritten signature in black ink, appearing to be 'S. Jones', written over a faint circular stamp or watermark.

Date: 13/04/2020

WORD COUNT: 51106

(Excluding summary, acknowledgements, declarations, contents pages, appendices, tables, diagrams and figures, references, bibliography, footnotes and endnotes)

Acknowledgements

First, I would like to thank my supervisor Dr. David J. Willock, for his guidance over the course of my PhD program. His advice pushed me forward to search for alternatives, investigate new approaches and explore any possibility. He helped me to develop the necessary skills to excel at my research and ultimately to present this work. I would also like to acknowledge Professor Stan Golunski, who was a strong support from the very first day I started as a student at Cardiff University and who gave me useful feedback when he co-supervised the first period of my PhD studies.

I would also like to express my gratitude to Dr. Christian Reece, for helping me during my first PhD year, the toughest one. He also made possible my research at Harvard University, which was one of the best experiences during my PhD studies. Thanks for his advice and his TAP knowledge, even at the distance, I learned so much.

I would like to acknowledge Dr. Sankar Meenakshisundaram and his PhD student, Alexandra Barnes, for providing the catalytic samples tested in this study. Also, I wish to also acknowledge Dr. Alex Walton for all the help regarding the NAP-XPS analyses at Manchester University.

I would also like to thank the larger members of the Cardiff Catalysis Institute for their help throughout these last years. I would like to mention Dr. Greg Shaw and Dr. Michal Perdjon, for being there with anything I needed in the lab. Also, a big thanks to Professor Philip Davies, for his feedback as a member of my review panel and for the precious time he invested helping with his knowledge.

I wish to also acknowledge all my colleagues at the office, Keiko, Guillermo, Justyna, Ricardo, Russ, Luca, Giulia, Daniele and Max, those good moments really made the hard work a little bit easier.

I would like to thank EPSRC for funding my studies within the Centre for Doctoral Training in Catalysis.

Finally, I would also like to thank all of my friends and family for supporting me throughout the last few years. I also wish to mention two very special people. They have been beside me throughout every stage of my life, giving me strength when I felt I lacked it. Their knowledge about science is not much and yet, without them, none of this work would be possible. For this and for so much more, a huge thanks to them, to my parents.

Contents

	Page
1. Introduction	1
1.1 Gold-based catalytic materials for CO oxidation.....	2
1.1.1 The role of the Au particle size.....	4
1.1.2 The nature of the active Au species.....	6
1.1.3 The influence of the support material.....	8
1.1.4 The activation of oxygen and the active site for oxygen activation.....	16
1.1.5 Precursor and nature of the wash effect.....	20
1.2 Approaches adopted in this study.....	22
2. Methodology	31
2.1 Catalyst synthesis.....	31
2.2 Characterisation	32
2.2.1 XRD	32
2.2.2 BET.....	36

2.2.3 SEM/EDX and TEM.....	37
2.2.4 NAP-XPS.....	41
2.3 MATLAB programming environment.....	42
2.3.1 Creation of M-file functions in MATLAB.....	43
2.4 CO oxidation rig.....	45
2.4.1 Reactor setup.....	45
2.4.2 Calculations.....	47
2.4.3 Composition and flow of the inlet gases.....	50
2.4.4 GC calibration procedure.....	52
2.4.4.a Single point calibration method.....	52
2.4.4.b Multiple point calibration method.....	53
2.5 Temporal Analysis of Products (TAP).....	54
2.5.1 Basics of TAP experiments.....	55
2.5.2 Knudsen diffusion regime.....	57
2.5.3 Exit flow as Moments.....	60

3. Development and Application of the Flow Reactor Numerical Analysis Software.....	65
3.1 Development of Software responsible for the Automation of Reactions.....	65
3.1.1 Identifying and connecting physical devices within the rig.....	66
3.1.2 Creation of Matlab environment for upcoming Reaction.....	67
3.1.3 Interactive process between the physical devices within the rig and the software during the automated reaction.....	70
3.1.4 Automatic ‘modification on demand’ of water bath heating/cooling performance.....	78
3.2 Development of software responsible for the analysis and process of Raw Data.....	82
3.2.1 Importing user data.....	82
3.2.2 Reading and decoding GC data.....	83
3.2.2.1 Calculations performed with collected and decoded experimental data.....	88
3.3 Development of GUI.....	93

3.3.1 Phase 1 - Automated reaction.....	95
3.3.2 Phase 2 – Collection and analysis of raw data.....	96
3.3.3 Phase 3 – Generation of a data file.....	98
3.4 Summary.....	100
4. Development and Application of the TAP Reactor Numerical Analysis Software.....	102
4.1 Analysis of raw experimental responses.....	102
4.2 Baseline prediction.....	107
4.3 Height and area normalization.....	109
4.4 Rejection of bad quality signals.....	112
4.4.1 Rejection of high ratio noise/peak signals (Method 1).....	113
4.4.2 Rejection of high ratio negative/positive area signals (Method 2).....	114
4.4.3 Comparison between Method 1 and Method 2.....	117
4.5 Summary.....	124
5. Flow Reactor – Experimental.....	127
5.1 Selection of optimal experimental conditions.....	127

5.1.1 Catalyst dilution ratio.....	131
5.1.2 Effect of contact time and reusability.....	153
5.1.2.a Effect on contact time and reusability – – Fresh sample approach.....	155
5.1.2.b Effect on contact time – Reused sample Approach.....	167
5.1.3 Lambda.....	176
5.2 Activation energies.....	178
5.3 Order of reaction with respect to CO.....	182
5.4 Summary.....	212
6. TAP Reactor – Experimental.....	217
6.1 Number of molecules per pulse calculation Procedure.....	217
6.1.1 Non pulse experiments, calculation of V_I	219
6.1.1.a Calculation of $(V_L + V_I)$	219
6.1.1.b Calculation of V_I	221
6.1.2 Pulse experiments, calculation of the pulse size.....	222

6.2 Harvard Data - Qualitative reactive features based on experimental TAP responses.....	225
6.3 Cardiff Data.....	232
6.3.1 Troubleshooting.....	232
6.3.2 Empirical estimation to the number of active surface oxygen.....	248
6.4 Summary.....	251
7. General Conclusions.....	253
7.1 Future work.....	256

1 | Introduction

This work has been focused on the extraction of kinetic information for surface catalysed processes by means of continuous flow studies, which were complimented with transient kinetics measurements using the temporal analysis of products (TAP) method.

Software development constituted an essential part of this study. On the one hand, the automation of a flow reactor system was accomplished. The implementation of a software system that interfaces with the different instruments within a reactor rig and synchronises them to run reactions and compiles the resulting data in an automated way not only eased the acquisition of experimental data but also increased the robustness and precision of the method. On the other hand, the development of a second piece of software for the analysis of TAP reactor responses allowed the extraction of kinetic information from the experimental signals. Both pieces of software, when coupled with their respective reactor rig (i.e. flow reactor or TAP reactor), were designed to offer a high degree of versatility, meaning that they can be used to study a wide range of reactions. In order to get the most out of each of these systems and carry out 'in depth' studies, this work concentrated on the investigation of carbon monoxide (CO) oxidation reaction over different supported gold catalysts.

CO is one of the major pollutants emitted from vehicular exhausts, industrial off gases, solid fuel combustion and a variety of other sources. Heterogeneous catalysis is key to successful development of so-called "green chemistry" since it is widely used to reduce the amount of pollutants before gases are released to the atmosphere. For example, emission of CO from automobiles is substantially diminished by heterogeneous catalysts, such as oxide supported platinum-group materials used in the three-way catalysts¹. The discovery that supported gold catalysts are active for CO oxidation reactions at low temperatures² motivated a considerable amount of research on the activity of gold-based catalysts. The importance of new materials for low-temperature CO oxidation is underscored in fields such as automotive pollution control, where commercial catalysts are often

based on platinum-group metals which are not very active at low temperature. This leads to the “cold start-up” problem in which much of the CO produced by incomplete combustion is not oxidized at operation temperatures below 200°C^{3,4}. As will be widely discussed in Section 1.1, gold-based catalysts have been reported to oxidize CO at much lower temperature (even at room temperature or below), thus offering a low-temperature friendly alternative. A further possible application of gold-based catalysts could be in the removal of CO impurities from the hydrogen feedstock consumed by fuel cells (PROX). The removal of carbon monoxide from hydrogen feedstocks results in fuel cells exhibiting longer lifetimes and improved efficiency. The effectiveness of supported gold catalysts in this area has been demonstrated in studies like the one carried out by Kahlich’s group, where the higher activity of a Au/ α -Fe₂O₃ catalyst over the commercial Pt/ γ -Al₂O₃ was evidenced. Nieuwenhuys and co-workers⁵, in their study on nanoparticulate gold particles (5 nm) on mixed oxides, also showed the superior activity of gold based catalytic materials for CO oxidation at low temperatures. In addition to the relevance of the CO catalytic oxidation in the environmental field, this oxidation reaction happens to be a good test reaction for surface structure-activity studies^{6,7,8,9}, which is the main reason that this work focused on this particular reaction.

1.1 Gold-based catalytic materials for CO oxidation

In 1989, Haruta et al.² first reported that nanosize gold particles deposited on metal oxides catalyse CO oxidation reactions. Whereas, until that date, most studies on supported gold catalysts were focused on inactive ceramic oxides, such as SiO₂^{10,11,12}, Al₂O₃^{11,13}, MgO^{11,12,14} and TiO₂¹⁵, Haruta’s group prepared a series of gold catalysts where oxides of Group VIII 3d transition metals were used as the support. The new catalytic materials showed very good activities, catalysing the oxidation of CO at temperatures as low as -70°C². This report stimulated the development of extensive research in Au catalysis at low temperatures, which has not decayed since then. Oxide-supported Au nanoparticles typically show high activity for catalysing not only CO oxidation but a series of oxidation and reduction processes, with most prominent examples being water-gas shift reactions^{16,17,18,19}, selective and total

oxidation of hydrocarbons^{20,21}, in addition to the already highlighted and focus of this study CO oxidation^{22,23,24}. Despite already being three decades of intensive study in the area and publications on CO oxidation run into hundreds, gold-containing catalysts and the reaction in which they are involved are quite complex systems which are not fully understood yet. As a consequence, the debate about the physical origin of the high activity of this kind of catalysts and the underlying reaction mechanism keeps broadening as more results are generated. Open questions are for example (i) the role of the Au particle size^{25,26} or a high activity of under-coordinated Au atoms at corner and edges^{27,28,29,30,31,32}, (ii) the nature of the active Au species (metallic Au nanoparticles or ionic/partly charged Auⁿ⁺ or Au^{δ-} species)^{33,34,35,36}, (iii) the influence of the support material on the catalytic performance of the corresponding Au catalysts and its role in the reaction process^{36,37,38,39,40}, and in particular (iv) the activation of oxygen and the active site for oxygen activation^{40,41,42}. Each of these points will be considered in more detail in the following sections.

Containing comparatively small amounts of gold in the form of finely dispersed particles, gold catalysts are difficult to characterise by physicochemical methods. One method that can give averaged information on supported Au particles is X-ray photoelectron spectra (XPS), commonly used in discussions of metal oxidation states in material surfaces. However, the XPS parameters of supported gold catalysts, peak position and half-width, depend on the Au cluster size: as the cluster size decreases, the peak broadens and shifts to higher binding energies⁴³. The XPS spectra of oxidised gold nanoparticles changes under the action of X-rays⁴⁴. As an additional problem, it has been reported that the catalysts change their properties on prolonged storage^{45,46,47,48}.

Despite the difficulties to fully understand the way supported Au catalysts work within the particular reaction of interest, they clearly stand apart from other metal catalysts in both their unusual activity and selectivity, especially in reactions involving molecular oxygen. These are enough reasons to continue studying them in order to release their potential to help us in the optimisation of chemical

processes that constitute the key in our evolution to a more sustainable and efficient society.

In the following sections, issues (i) - (iv) previously commented are discussed within the confines of CO oxidation at low temperature. Also, the effect of the precursor and nature of the wash solution used during preparation methods would be accounted in section 1.1.5.

1.1.1 The role of the Au particle size

The strong dependency of the catalytic activity on the Au particle size is broadly accepted in the community^{25,26,27,28,29,30,31,32}. Lopez et al.²⁷ made a list of different effects that may contribute to the catalytic activity of nanosized gold particles and they ordered those into a hierarchy of contributions. They concluded that a property directly related to the size of the gold particles is the dominant effect in the exceptional catalytic performance of nanometer gold particles. They attributed such a dominant effect to the ability of low-coordinated gold atoms to bind adsorbates, which would ultimately lower the barrier for surface reactions. In another study, a steep indirect correlation between particle size and concentration of low-coordinated sites was found²⁹ (see Figure 1.1), which would explain the increased catalytic activity when decreasing Au particle diameter.

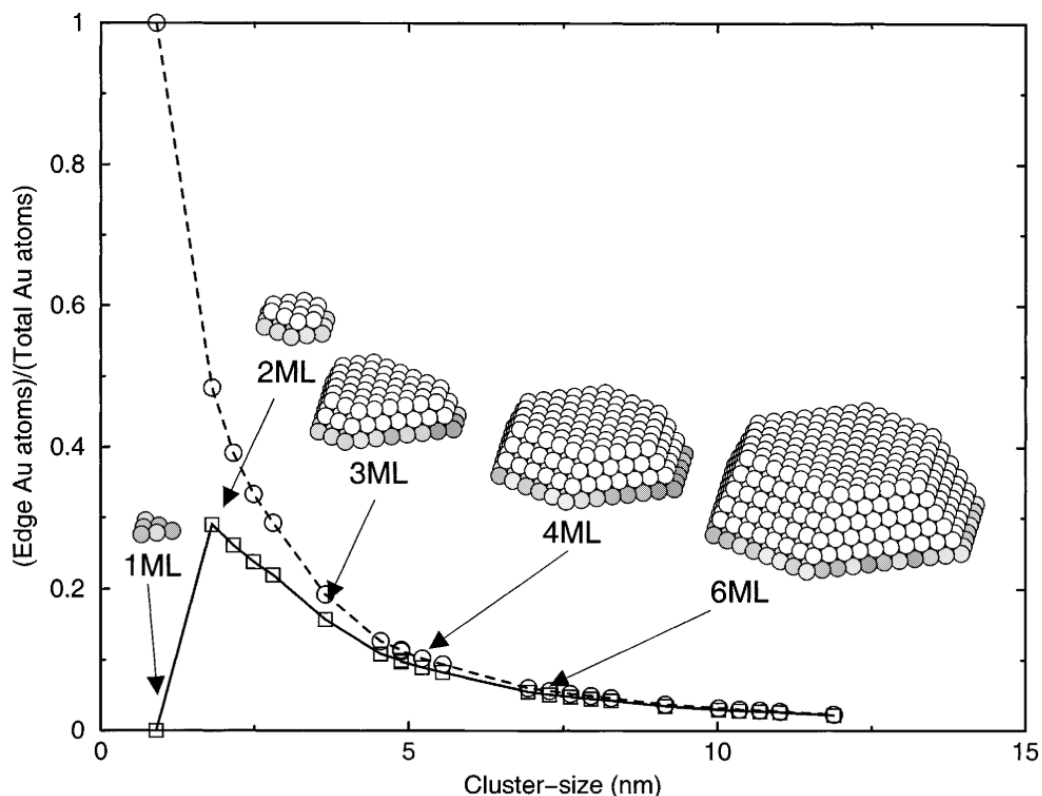


Figure 1.1. Calculated step density for Au particles on TiO_2 as a function of particle size. (o) corresponds to the total step sites on the Au particles. (□) corresponds to the step sites on the Au particles that are not in direct contact with the support. Insets illustrate the corresponding Wulff constructions⁴⁹ for selected particle sizes. Reproduced with permission from reference 29.

Regarding the factors that determine the particle size in a metal supported catalyst, although there is not complete agreement on this matter, there are a couple of factors commonly accepted by the community to directly affect this important characteristic of the catalytic material. These are catalyst synthesis temperature and Au loading. It has been experimentally observed that if a gold-containing catalyst is synthesized at rather low temperatures on a support with a large specific surface area, then, at a gold content of a few weight percent, the size of the resulting gold particles will be below 10 nm^{21,34,50,51,52,53,54,55,56,57,58}. Aside temperature and metal loading, interactions metal-support has also been suggested to influence the particle size. This is further discussed in Section 1.1.3.

1.1.2 The nature of the active Au species

There is great controversy related to the Au oxidation state of the active site^{59,60,61,62,63,64}. Although some authors hypothesize that cationic gold is essential for CO oxidation^{59,61,62,64} (see Figure 1.2), others defend that Au⁰ is indeed the active species³⁶, while there are some who report the need for a mixture of metallic and cationic gold species in order to get high catalytic activities^{63,60}. Since CO is a reducing agent, cationic gold initially present in the catalytic sample could turn into its metallic form provided that the treatment time is sufficient for its reduction⁶⁰. This might explain the origin for the confusion around this subject.

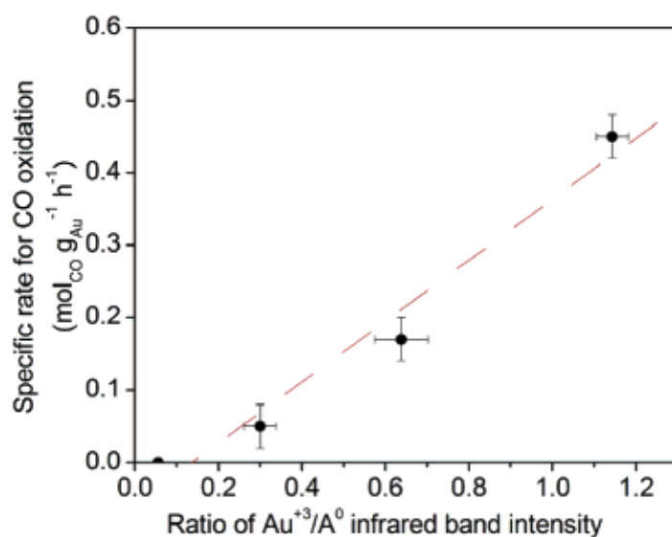


Figure 1.2. Correlation between Au³⁺ and Au⁰ species and specific rate for CO oxidation catalyzed by gold supported on nanocrystalline CeO₂. Infrared band frequency and intensity of CO adsorption on gold catalysts were used to identify Au³⁺ (band at 2148 cm⁻¹ representing Au³⁺-CO) and Au⁰ (band at 2104 cm⁻¹ representing Au⁰-CO). Reproduced with permission from reference 62.

Venezia et al.⁶⁵ studied a series of gold catalysts supported on cerium oxide, which were prepared by solvated metal atom dispersion (SMAD), by deposition-precipitation (DP), and by coprecipitation (CP) methods. They characterized them by X-ray diffraction (XRD), temperature programmed reduction (TPR) and X-ray photoelectron spectroscopy (XPS) and they tested their catalytic activity in the CO oxidation reaction. In that study they observed that the addition of gold improves substantially the CO oxidation activity of the pure support. However, such activity

was found to be strongly dependent on the preparation method, with the largest activity exhibited by the DP sample, which was just dried at 393 K without calcination. From their XRD analysis, metallic gold was not detected on the DP sample, while it was present in both SMAD and CP samples. In addition, the XPS spectrum showed that the Au 4f_{7/2} had two components located at 85.6 eV and 87.5 eV, designated to be Au⁺ and Au³⁺, respectively. The Au 4f_{7/2} peak shifted to 85.1 eV for the reaction tested catalyst and was assigned to the “almost unique presence of Au⁺” (see Figure 1.3). Binding energies typical of metallic gold were observed in the SMAD and CP samples XPS spectra (Table 1.1). Finally, Venezia and colleagues concluded that the presence of the metallic gold in the SMAD and the CP catalysts would weaken the C-O bond and therefore make easy the further insertion of oxygen with release of CO₂. In the case of the sample prepare following the DP method without high temperature calcinations, the presence of ionic species in intimate contact with the ceria would form a fluorite type structure of a mixed phase Au_xCe_{1-x}O_{2-δ} with a contracted lattice. This would weaken the Ce-O bond and increase oxygen mobility, eventually resulting in an extraordinarily active Au/ceria catalyst for the low temperature oxidation of CO.

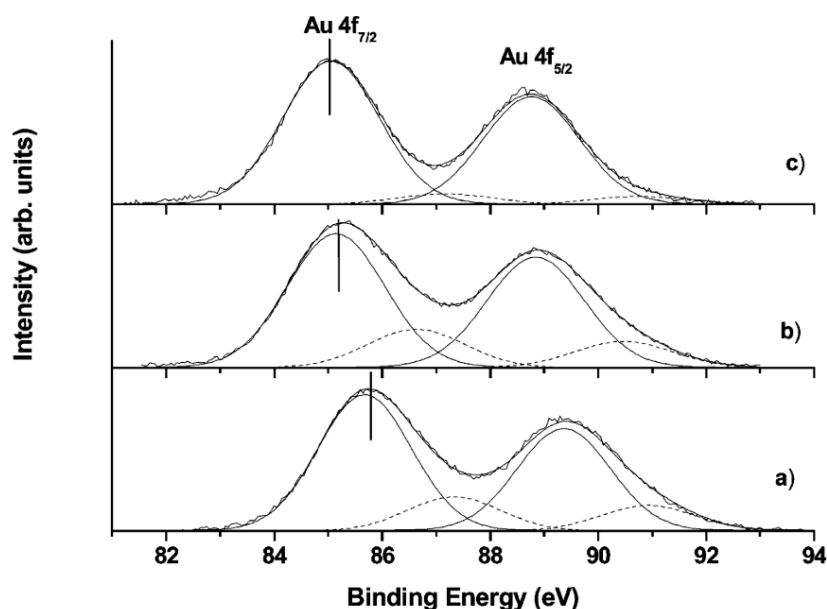


Figure 1.3. Experimental and fitted Au 4f peaks of the 3AuCe(DP): (a) as prepared, (b) after 1 month, and (c) after 40 h on stream. Reproduced with permission from reference 65.

Table 1.1. Au 4f_{7/2} binding energies of the various gold samples studied by Venezia's⁶⁵. Full width at half maximum (fwhm) are given in parentheses. Percentages of the chemical species are also given alongside. Reproduced with permission from reference 65.

sample	Au 4f _{7/2} (eV)
3.0AuCe(DP) (as prepared)	85.6 (2.2) 79% 87.5 (2.2) 21%
3.0AuCe(DP) (aged)	85.1 (2.1) 77% 87.3 (2.1) 23%
3.0AuCe(DP) ^a (used)	85.1 (2.1) 94% 87.2 (2.1) 6%
10AuCe(CP) calc. 393 K	85.4 (2.1) 81% 87.8 (2.1) 19%
10AuCe(CP) calc. 673 K	84.5 (2.0) 72% 85.8 (2.0) 28%
3AuCe(SMAD)	84.1 (1.9) 93% 86.1 (1.9) 7%

^a After 40 h of time on stream at room temperature.

According to the above discussion, it seems that preparation method and temperatures applied during calcinations are crucial factors which could ultimately change the oxidation state of gold to a broader or narrower range of species. However, whether Au⁰, Au⁺, Au³⁺ or a mix of them are the active species continues to be a topic of debate.

1.1.3 The influence of the support material

There have been conflicting reports on the dependence of CO oxidation activity on the nature of the support. The surface area and reducibility of the support are often regarded as possible important parameters in supported metal catalysts. It is reasoned that the metal particles are farther apart on the higher surface area support, such that they can maintain their small sizes better. However, as mentioned earlier, support surface area should not be a significant factor in most support Au catalysts since the metal loadings are usually just a few weight percent and the support areas generally high (> 50 m² g⁻¹). In fact, it has been reported that Au on a commercial lower surface area ceria (surface area 79 m² g⁻¹)⁶⁵ was three

times more active than the highly active Au on a higher surface area, nanocrystalline ceria ($180 \text{ m}^2 \text{ g}^{-1}$)⁶⁶.

Schubert et al.³⁷ distinguished between two major groups of support materials, reducible materials leading to “active” catalyst and non-reducible materials leading to “inactive” (or little active) catalysts. They based this classification on their results of a series of activity measurements on Au catalysts on different metal oxides. Such data is presented in Table 1.2, where TOFs for those catalysts with irreducible supports such as Al_2O_3 and MgO evidence significant lower activity than those catalysts which are supported on reducible transition metal oxides, such as Fe_2O_3 , NiO_x , CoO_x or TiO_2 . The difference was tentatively attributed to the different ability of these reducible materials to create oxygen vacancies on the support, close to the Au particles, which were proposed as active centres for oxygen during the CO oxidation reaction.

Table 1.2. Comparison of kinetic data for the CO oxidation over supported Au catalysts (Table published in Schubert’s report³⁷). All data was taken after 2 hours on a stream of simulated methanol at 80°C . Reproduced with permission from reference 37.

Catalyst	Prep. ^a	d_{Au} [nm]	$p(\text{CO})$ [kPa]	$p(\text{O}_2)$ [kPa]	$r (\times 10^4)$ [$\text{mol}_{\text{CO}}/\text{g}_{\text{Au}} \cdot \text{s}$]	TOF ^b [s^{-1}]
Au/ Fe_2O_3	DP	2.3–7	1	1	39 ^c	1.3–3.0
	CP	5.5–7	1	1	43 ^c	3.2–3.4
Au/ NiO_x	CP	3.2 ± 1.0	1	1	20	1.3
Au/ CoO_x	IMP	3.4 ± 1.4	1	1	22	1.8
Au/ TiO_x	IMP	2.4 ± 0.7	1	1	33 (51 ^d)	1.6 (2.5 ^d)
Au/ $\text{Mg}(\text{OH})_2$	CP	<4	1	1	13	0.5–0.9
Au/ MgO	CP	6.0	1	1	3.8	0.3
Au/ Al_2O_3	IMP	4.4	1	1	6.0	0.35

^a DP, deposition–precipitation; CP, coprecipitation; IMP, impregnation; CVD, chemical vapor deposition.

^b (Hemi-)spherical particles assumed.

^c Statistical average from all produced DP/CP catalysts.

^d After additional pre-treatment in H_2 (at 250°C during 30 min).

Additionally to directly participating in the reaction, the support may affect the reaction also indirectly, by influencing the shape and size of the Au nanoparticles during the catalyst preparation and activation procedure via metal–support interactions⁶⁷, by support-induced strain in the Au nanoparticles²⁹ or by charge

electron transfer to Au nanocluster⁶⁸. Reports on each of these points are further discussed in forthcoming lines.

In an attempt to discriminate among the above list of possible effects, Au catalysts with similar Au loading and particle sizes, synthesized by traditional routes, e.g., by DP techniques^{36,67}, or by depositing pre-formed Au nanoparticles of similar size on different support materials^{69,70,71}, have been studied in order to compare their activities. Janssens et al.⁶⁷ carried out transmission electron microscopy (TEM) studies where they compared Au catalyst supported on TiO₂, MgAl₂O₄, and Al₂O₃ with the same gold loading (4 wt%) and prepared following the same method (DP). In such study, they observed that the difference in activity between the Au/TiO₂ and Au/MgAl₂O₄ catalysts matched the difference of low-coordinated Au atoms located at the corners of the Au nanoparticles. The resulting turnover frequency per corner atom in these catalysts was 0.8 s⁻¹ for both of them. From those results they stated that the difference in catalytic activity of Au catalysts on a reducible and irreducible support can be entirely explained by a difference in Au particle geometry, regarding that only the low-coordinated Au corner atoms contribute to the activity. The different number of active sites was attributed to the different shape of the Au particles depending on the support used. Consequently, they suggested that a different interface energy when varying the support would result in different Au particle geometries, therefore different number of low-coordinated Au atoms, and ultimately in different activities. Nonetheless, Janssens and colleagues⁶⁷ could not arrive to a clear conclusion since the turnover frequency per corner gold atom in the case of Au/Al₂O₃ catalyst was about 4 times lower than those for the Au/TiO₂ and Au/MgAl₂O₄ cases. They concluded that other support-induced effects apart from the Au particle shape may play a role. In another study, Delannoy et al.³⁶ compared the CO oxidation activity of Au/TiO₂, Au/CeO₂ and Au/Al₂O₃ and the reduction behaviour of Au³⁺ species in those catalysts, which were prepared by DP and had the same gold loading (1 wt%).

They performed characterisation of the composition of those catalysts as a function of pre-treatment conditions (calcination, H₂ reduction, conditioning in CO/O₂ gas mixture) and their results indicated that the reduction of surface cationic gold to its metallic form translated to an increased catalytic activity. Delannoy's also observed

that, while an activation treatment was not essential to obtain highly active Au/TiO₂, gold supported on ceria and alumina was much less reducible under the same conditions (on stream under 1% CO/ 2% O₂/ He at 298 K). Nonetheless, after reduction in H₂ at 573 K, gold was metallic on all three catalysts (Au/TiO₂, Au/CeO₂ and Au/Al₂O₃), but catalytic activity was developed only on the reducible supports, TiO₂ and CeO₂. Therefore, they concluded that both catalytic activity and reducibility were strongly affected by the support, with the activity found to decrease in the order Au/TiO₂ ≈ Au/CeO₂ >> Au/Al₂O₃ (after reduction pre-treatment was applied). Comotti et al.⁷¹ prepared Au supported on TiO₂, Al₂O₃, ZnO and ZrO₂ by adsorption of Au colloids of a narrow size distribution onto the supports (see Figure 1.4). They observed that almost identical gold particle size distributions on different supports results in different activities for CO oxidation, evidencing the influence of metal-support interactions on the catalytic properties of the final materials. However, they also noted that this influence did not follow the reducibility of the support since they obtained higher activities from the supported alumina catalyst (non-reducible) than the ones obtained from the ZnO support case (reducible). Nonetheless, although gold particle sizes were not changed by deposition, the shape of the deposited particles did, being this study another example where the support affecting the number of defect sites was pointed as the most likely reason for the different activities obtained. Similar studies were performed also by Grunwaldt et al.⁷² and Arrii et al.⁷⁰, who also highlighted the strong dependency of the catalytic activity on the nature of the metal oxide used as support material.

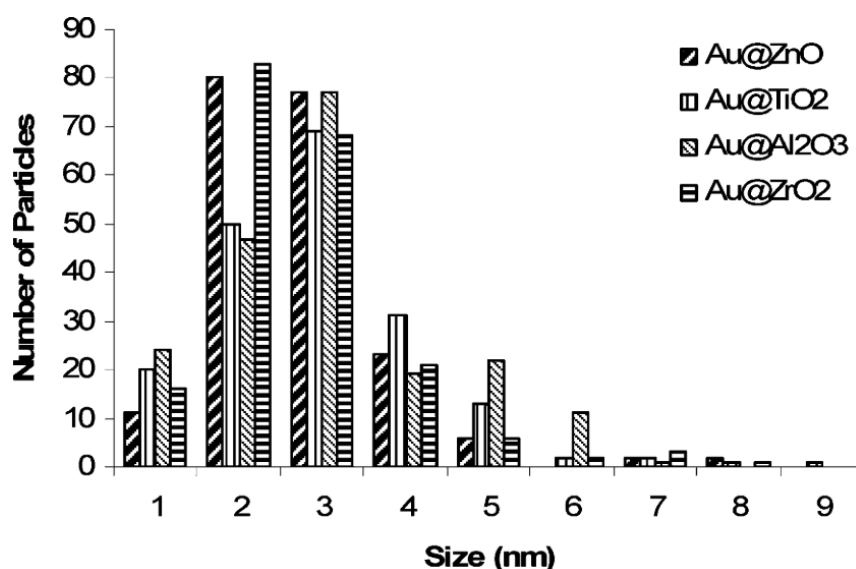


Figure 1.4. Size distribution histogram of gold clusters. Reproduced with permission from reference 71.

Temporal Analysis of Product (TAP) studies have also been carried out with the hope of lighting up the possible support material influence. Widmann et al.⁷³ applied TAP measurements to directly determine the oxygen storage capacity (OSC) and its correlation with the activity for the CO oxidation reaction and the reducibility of the support material. Au/TiO₂, Au/Al₂O₃, Au/ZnO and Au/ZrO₂ with similar Au loading and Au particle sizes (see Table 1.3) prepared by deposition of pre-formed Au colloids were studied.

Table 1.3. Physical properties of different supported gold catalysts after pre-treatment by calcination in 10% O₂/N₂ at 250 °C for 2 h. Reproduced with permission from reference 73.

	Au/TiO ₂	Au/ZrO ₂	Au/ZnO	Au/Al ₂ O ₃
Au loading (wt.%)	1.0	1.0	1.0	0.8
Au diameter (nm)	3.3 ± 1.0	2.4 ± 0.7	3.1 ± 0.9	3.5 ± 1.1
Surface area (m ² g _{cat} ⁻¹)	47	201	50	198
Dispersion (%)	30	42.	33	28

The OSC of all four catalysts (see Table 1.3) was measured at 120 °C reaction temperature in multi-pulse experiments, exposing the catalysts alternately to sequences of 200 CO/Ar pulses and 100 O₂/Ar pulses, starting with the CO/Ar

pulses. It was ensured that after these numbers of pulses there was no further uptake of CO or O₂, i.e., further reduction or oxidation of the corresponding catalysts was below the detection limit under those conditions. This reduction–oxidation cycle was repeated at least three times on each catalyst for determining the amount of active oxygen which is reversibly stored on the catalyst surface, i.e., which can be removed by reaction with CO during CO pulses and re-deposited by O₂ pulses. The corresponding mass spectrometric signals recorded over the different catalysts during those measurements are shown in Figure 1.5, which shows pulses of the reactants CO/Ar and O₂/Ar, respectively, and of the CO₂ signal obtained during the CO pulses.

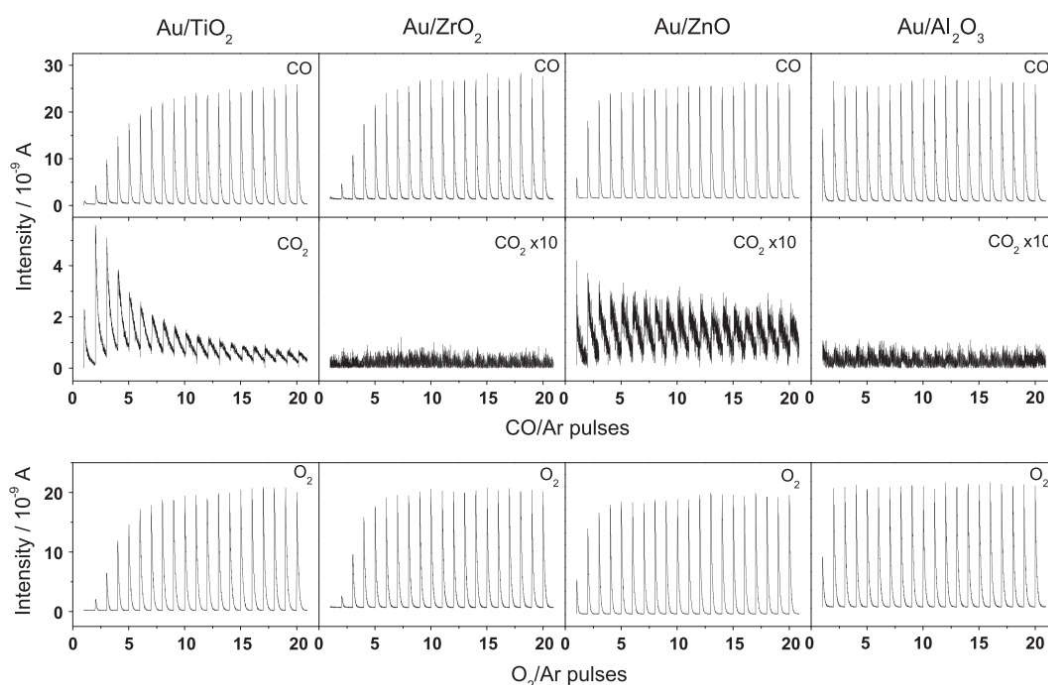


Figure 1.5. Pulse responses during the multi-pulse experiments at 120 °C on the four differently supported Au catalysts (Au/TiO₂, Au/ZrO₂, Au/ZnO, Au/Al₂O₃, see Table 1.3) for determination of the OSC. Since the biggest changes happened at the beginning of each sequence, only the first 20 pulses of each sequence were presented in this report. Reproduced with permission from reference 73.

The accumulated, absolute amounts of CO molecules converted or O₂ molecules adsorbed during those multi-pulse experiments (showed in Figure 1.5) over the four Au catalysts were also investigated in Widmann’s study (See Figure 1.6). For all catalysts, the overall uptake and conversion of CO was higher during the first

sequence of CO/Ar pulses, which was dosed on a freshly calcined catalyst, than in the following sequences. Hence, on all catalysts, thermal oxidation of the catalyst in a O₂/N₂ flow at 250 °C and atmospheric pressure results in a higher amount of active oxygen stored on the catalyst surface than can be obtained upon reoxidation by O₂ pulses. After the first sequence, the accumulated amounts of CO converted and O₂ adsorbed during the two following sequences equalled each other, reflecting reversible reduction and oxidation of the catalyst surface. This amount of oxygen, which is reversibly stored on the catalyst and which can be reversibly removed/replenished by sequences of CO pulses or O₂ pulses, respectively, was the given definition for the OSC⁷³. These results (Figures 1.5 and 1.6) showed that, measured under identical conditions, the OSC and the activity for CO oxidation differed significantly for those catalysts and were correlated with each other and with the reducibility of the respective support material following the order Au/TiO₂ > Au/ZrO₂ > Au/ZnO > Au/Al₂O₃. Therefore, Widmann and colleagues pointed to a distinct support effect with a direct participation of the support in the reaction mechanism (further discussed in Section 1.1.4).

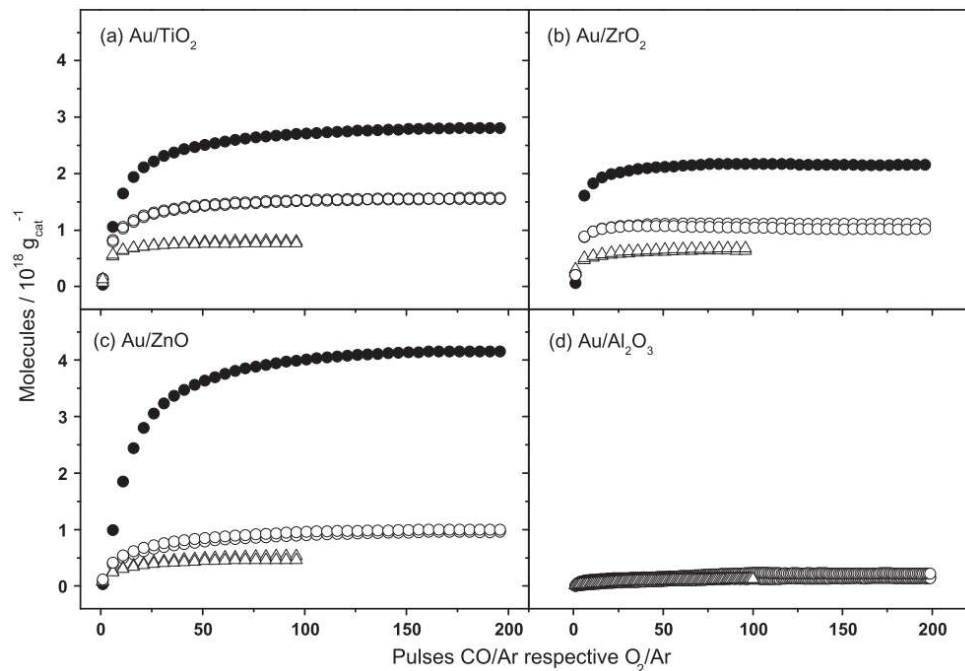


Figure 1.6. Total amounts of CO (first sequence: ●; following sequences: ○) and O₂ (Δ) consumed during the multi-pulse experiments (showed in Fig. 1.5) on the four differently supported Au catalysts (see Table 1.3). Reproduced with permission from reference 73.

Widmann et al.⁷³ also carried plug-flow reactor measurements under atmospheric pressure, turning out to follow a similar trend of the activity as the one obtained with TAP reactor measurements (see Figure 1.7), supporting the validity of the latter also under continuous reaction conditions. The direct correlation reducibility-CO oxidation activity found by Widmann's group⁷³ was supported by the H₂-TPR results obtained by Venezia et al.⁶⁵, where they also noted a linear relationship between the activity of a series of Au/CeO₂ catalysts and their oxygen surface reducibility.

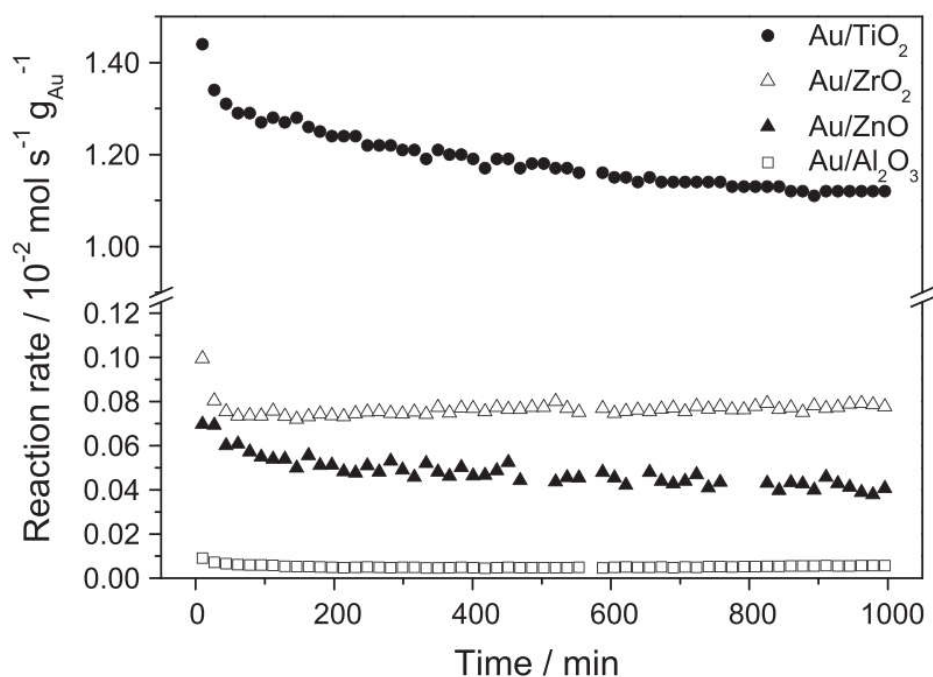


Figure 1.7. Au mass normalized reaction rates during the CO oxidation at 120 °C over the four differently supported Au catalysts after calcination (see Table 1.3 and Figures 1.5 and 1.6). Reactive gas mixture consisting of 1 kPa CO, 1 kPa O₂, and balance N₂. Reproduced with permission from reference 73.

In addition to the support effects already commented above, Mavrikakies et al.²⁹ studies led to a particle size distribution dependence on the oxide support being used. Specifically, through parameters such as the Au diffusion rate or the nucleation-site density on the oxide surface. Furthermore, they also discussed the possible strain-related effects on the catalytic properties of the gold particles, similarly to the case of other metals⁷⁴. As such, the tension at the surface of the Au particles and the tension at the Au-support interface could change the lattice

constant of Au and consequently, its reactivity²⁹. On the other hand, Sanchez et al.⁶⁸, investigated the combustion of CO (temperatures up to 800 K) on size-selected gold clusters supported on defect-poor and defect-rich MgO (100) films. They combined both experimental and computational methods that yielded results which revealed that charging of the cluster via partial electron transfer from the oxide support, as well as the presence of oxygen-vacancy defects in the substrate, play an essential role in the activation of nanosize gold model catalysts.

From the list of contributions mentioned in the above discussion, it is evidenced that, despite numerous studies already carried out on this matter, scientific consensus on how the nature of the support affects the catalytic activity towards the CO oxidation reaction has not been achieved yet.

1.1.4 The activation of oxygen and the active site for oxygen activation.

Another unresolved issue in the chemistry of gold-catalysed oxidation is the mechanism of oxygen activation and supply, including the nature and location of its adsorption. Various models have been postulated to account for the role of oxygen. According to some authors^{75,76}, oxygen adsorption proceeds directly on gold atoms, whereas others^{77,78} propose that oxygen adsorption also occurs on the support, in particular at oxygen vacancies^{41,79}, especially in the proximity of gold particles as a consequence of the Schottky junction⁸⁰.

The area related to activation processes and reaction pathways when using supported gold catalysts in CO oxidation reactions is not an exception apart from controversy. For that reason, in order to get a clearer idea of the scene we are facing in our research, it is essential to compare those results obtained from studies on materials with the same nature. From the information gathered in the previous sections, it seems elementary that if the support is having such a broad spectrum of influences on the catalytic properties and performances, there would be great chances of having it also influencing the way our reactants interact with the catalyst and the pathway the reaction turns out to follow. As such, and for the sake of the

purpose of the present study, this section will be focussed on a literature discussion based on nanoparticle gold supported on CeO_2 , Al_2O_3 and TiO_2 .

The focus of a study by Delannoy et al.³⁶ was on catalysts consisting of Au supported on the three supports commented above. Diffuse Reflectance Infrared Fourier Transform Spectroscopy (DRIFTS) and X-ray Adsorption near-edge structure (XANES) were used to follow the evolution of the oxidation state of gold in the three samples during CO oxidation in a $\text{CO}/\text{O}_2/\text{He}$ mixture. They observed that in the case of the non-reducible support (Al_2O_3), no activity was found at 298 K. Both the DRIFTS and XANES results showed that the reduction of the cationic gold species initially present was a slow and incomplete process, leading to the association of such inactivity to a low concentration of metallic gold in the sample. However, when the $\text{Au}/\text{Al}_2\text{O}_3$ sample was activated in air (773 K) or H_2 (573 K), Au was fully reduced, forming particles similar in size to those of the Au/TiO_2 catalyst (which showed high activity) and yet, the alumina sample remained catalytically inactive. This evidenced a decisive participation of the support in the activation mechanism. Furthermore, vibrational DRIFTS bands of CO adsorbed on metallic Au were noted, which is consistent with the mainstream view that CO is absorbed on metallic gold and that the support would play a role through providing sites for the activation of O_2 . From the observation of an influence of oxygen storage by ceria and the oxidation states of gold, Delannoy's group also pointed to an important difference between the two reducible supports CeO_2 and TiO_2 . They suggested that the high mobility of active oxygen on the former might facilitate a Mars-van Krevelen reaction mechanism, which would be in accordance with Venezia et al.⁶⁵. Also, in agreement with Guzman et al.⁸¹, Delannoy also considered the possibility of the formation of activated oxygen such as superoxide and peroxide-type species on the surface of CeO_2 . For gold supported on titania, in contrast, a mechanism with oxygen activation on the support or at the metal-support interface was suggested. This idea is supported by several studies as well^{30,79,82,83,84}.

When it comes to mechanistic studies, the TAP reactor method⁸⁵ can play a decisive role. With some examples already cited in previous sections, this method has been applied for numerous studies on the mechanism and dynamics of adsorption and

catalytic reaction processes on catalyst surfaces^{86,87,88}. Olea's group has intensely using TAP reactor studies in recent years^{89,90,91,92}, with CO oxidation reaction on Au/TiO₂ catalysts being one of its subjects⁹⁰. In that contribution⁹⁰, they performed single-pulse experiments using ¹⁸O₂ and ¹⁶O¹⁸O isotopes with results shown as in Figure 1.8. In this figure, the height normalized exit flows of the three oxygen isotopes (¹⁶O₂, ¹⁶O¹⁸O and ¹⁸O₂) at 400 K when a mixture of ¹⁸O₂, ¹⁶O¹⁸O and ¹⁶O₂ was pulsed on Au/TiO₂ were presented. The normalization of the experimental exit curves was made by dividing each response curve with the respective height of the peak. Since the height normalized response for the three species showed almost identical retention times (evidenced by the overlap of the curves) and they also observed that the ratio between the three isotopes at the exit of the reactor was almost the same as the initial composition in the isotope mixture, they concluded that no oxygen-isotope exchange with lattice oxygen occurred. They also carried out alternating pulse experiments using ¹⁸O₂ and C¹⁶O where almost only C¹⁶O¹⁸O isotopomer was observed. From those results, Olea's suggested that, on the Au/TiO₂ catalyst, molecular rather than lattice oxygen was involved in the production of CO₂ by the CO oxidation reaction⁹⁰.

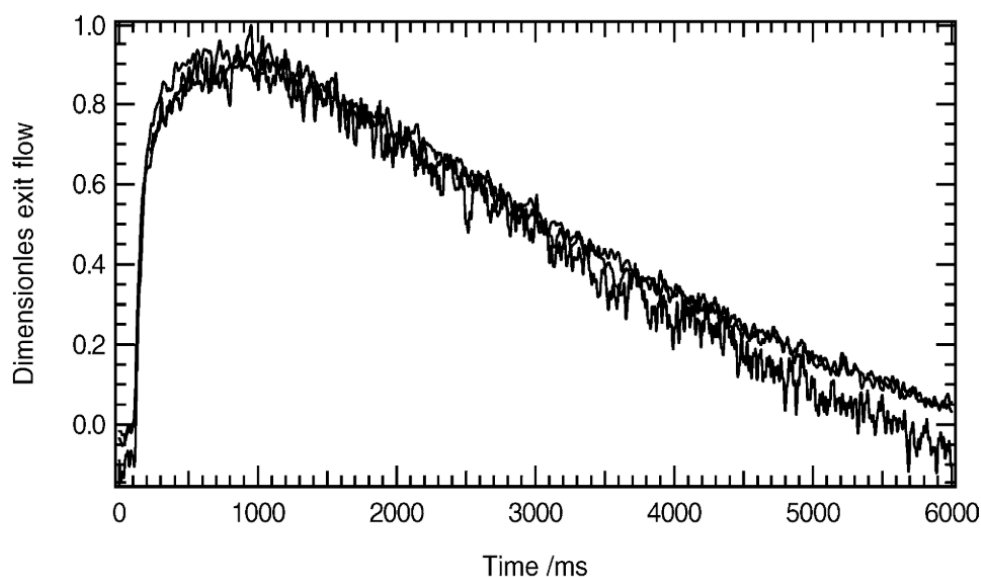


Figure 1.8. Dimensionless (height normalized) response of the oxygen isotopes ¹⁶O₂, ¹⁶O¹⁸O and ¹⁸O₂ when a mixture of ¹⁸O₂ (major), ¹⁶O¹⁸O and ¹⁶O₂ was pulsed on 0.03 g Au/TiO₂ at 400 K. Reproduced with permission from reference 90.

Kotobuki et al.⁴⁰ got to very different conclusions in their investigation on the OSC and activity of Au/TiO₂ during CO oxidation at relatively low temperature (80°C). The formation of CO₂ when pulsing CO over a previously O₂ dosed sample led to the conclusion that CO could react with stable oxygen that was reversibly stored on the catalyst surface. Hence, gas-phase oxygen would not be required for the CO oxidation reaction on Au/TiO₂. It was also noted that such a stable oxygen could be replenished by O₂ pulsing. The maximum number of stable surface oxygen species was stated to be constant for a given catalyst and it would increase linearly with increasing the number of Au perimeter sites, at the perimeter of the interface between the Au nanoparticles and the TiO₂ support. They also observed a linear correlation between CO conversion with the number of these Au perimeter sites, comparable to that between OSC and number of perimeter sites. Such a linear relation provided strong evidence for Kotobuki's group to assign those perimeter sites as active sites for the adsorption of stable, but nevertheless reactive oxygen, with the latter being the precursor for CO oxidation. Finally, CO₂ formation was not detected during an O₂ pulsing, thus pointing to CO being weakly adsorbed and rapidly desorbing. These findings were later supported by Widmann et al.⁷³ (some of their results presented in Section 1.1.3). In this contribution, they also studied Au/Al₂O₃ and very low oxygen storage capacity and CO oxidation activity were observed when tested similarly as the Au/TiO₂ catalyst. Consequently, they could not identify the direct participation of the support in the reaction mechanism for the non-reducible support case. Hence, a 'gold-only mechanism' was proposed as the dominant pathway for Au/Al₂O₃. In a previous contribution⁹³, Widmann also led a mechanistic study on CO oxidation using Au/CeO₂ as catalyst. These measurements not only revealed that CO clearly reacts with oxygen present on the catalyst, in the absence of a simultaneous O₂ pulse, but also revealed that the reactively removed oxygen can be reversibly 'refilled' by O₂ pulses, following the same trend as those found for Au/TiO₂^{40,73}. Widmann's group also noted that oxygen removal on the surface of Au/CeO₂ led to an activation of the catalyst for CO oxidation during simultaneous CO and O₂ pulses, contributing to the idea of the Mars-van Krevelen type reaction mechanism already suggested by Delannoy³⁶.

1.1.5 Precursor and nature of the wash effect.

From previous sections one can certainly realise that the co-existence of controversial reports is undeniable. There are multiple variables that could cause conflicting results, namely, different gold loading, different particle sizes, different reaction conditions and different preparation procedures as the most prominent candidates. However, there is one more possible factor that would definitively give origin to contradictory results even in the case of keeping the rest of commented variables exactly the same. This is catalytic poisoning. In particular, for the case of interest in the present study, supported Au catalysts are very susceptible to poisoning by chloride ions. Unfortunately, the chances of poisoning to occur during catalytic preparation are quite relevant since Au catalysts are often prepared using HAuCl_4 as precursor. It has been demonstrated that on $\text{Au}/\text{Al}_2\text{O}_3$ catalysts, residual Cl^- causes agglomeration of Au particles and suppresses the reducibility of Au cations^{45,94}. It was also shown that even after reducing the samples with H_2 under mild conditions, the catalytic activity remained poor⁴⁵. On the other hand, it was also noted that, in samples with agglomerated Au particles caused by Cl^- poisoning, significant activity improvement could be achieved by displacement of chloride at the active site by hydroxyl⁹⁴. This followed their postulate of the nature of the active site for CO oxidation, which was suggested to be an ensemble consisting of $\text{Au}^+\text{-OH}^-$ surrounded by Au atoms. Thus, Bare's group⁹⁴ proposed the formation of $\text{Au}^+\text{-Cl}^-$ as the cause for the catalytic poisoning by chloride. This idea was supported by Chen et al.⁹⁵, who defended the reduction of gold complex to metallic gold as a requirement for activating gold catalysts prepared by the DP method. Accordingly, the presence of chloride-contaminated gold hydroxides ($\text{AuCl}_y(\text{OH})_{3-y}$) would profoundly decrease the reducibility of the catalytic material, resulting in a lower activity. Both reports^{94,95} pointed at the isoelectric point (IEP) of the support as an important factor in the amount of adsorbed chloride. When a gold catalyst is prepared by DP with HAuCl_4 , the synthesis solution is typically adjusted to pH 7. Considering that the IEP of Al_2O_3 is 9.06 and the IEP of TiO_2 is 6.2, adjusting the pH of the synthesis solution to pH 7, which is below the IEP of alumina but higher than that of titania, implies that the alumina surface is positively charged due to

protonation of the surface hydroxyl groups, resulting in a greater tendency for it to retain Cl^- anions than titania, the surface of which is neutral or slightly negatively charged. Correspondingly, there is a much larger variation in the reported activities of $\text{Au}/\text{Al}_2\text{O}_3$ compared to Au/TiO_2 . Although other Au precursors have been attempted in order to circumvent the problem of chloride poisoning^{67,70,96}, it is not clear if better catalytic activities can be achieved by these alternative methods and thus HAuCl_4 still remains as the preferred precursor during preparation of supported Au catalysts.

In most of the cases, alkaline washes are used to remove Cl^- before the samples experience temperatures high enough for Cl^- - induced Au particle agglomeration. The nature of the wash solution is very important. While some authors reported active $\text{Au}/\text{Al}_2\text{O}_3$ catalysts prepared by washing with a pH 9 NaOH solution⁴⁵, others noted total inactivity when washing with NH_4OH solution⁹⁷. On the other hand, an active Au/TiO_2 was obtained with NH_4OH washing⁹⁷. $[\text{Au}(\text{NH}_3)_2(\text{H}_2\text{O})_{2-x}(\text{OH})_x]^{(3-x)+}$ was proposed to be present on both Au/TiO_2 and $\text{Au}/\text{Al}_2\text{O}_3$ after NH_4OH washing⁹⁷, but the thermal stability of this complex, the degree of retention of NH_4^+ by the support, and oxidation of nitrogen containing species to form nitrates may be support dependent. There are not yet studies on how or whether nitrates would negatively impact Au catalysis, but it is known that besides halides, anions like phosphates can also suppress the catalytic activity of $\text{Au}/\text{Al}_2\text{O}_3$, albeit to a much less extent⁹⁴. It should be noted that Cusumano⁹⁸ reported the danger of explosion associated with impregnation of gold salts and NH_4OH onto the support. Thus, attempting to prepare Au catalysts using this technique should not be the first alternative.

Although from previous sections it has been pointed how the catalytic activity is greatly influence by factors like support nature, gold loading and particle sizes, the influence of precursors and alkaline washes during the preparation method is not to be neglected either. All in all, the many possible variables taking play in the catalytic performance of supported gold catalysts could easily explain the unresolved controversy in the field of CO oxidation. Yet, these materials have already proved their potential to catalyse this kind of reactions. Therefore, rather

than abandon them, a further development of different approaches to get a better understanding of these systems would worth the means needed.

1.2 Approaches adopted in this study

As mentioned at the beginning of this chapter, this work has been focused on the investigation of catalytic systems by combination of both continuous flow and TAP reactor studies, with the CO oxidation reaction constituting the centre of such investigation. From the literature-based discussion developed in Section 1.1, a number of open questions seem to remain under debate. Thus, the experimental approaches adopted in this study have been aimed to answer some of those questions.

Firstly, the interplay of different factors was kept to a minimum. This means that experimental conditions were maintained almost constant throughout the different catalytic series of tests, changing only one variable at a time when required for the purpose of the particular series. Moreover, catalytic materials with a great similarity among them were tested. Specifically, only supported gold and gold-palladium catalysts were investigated, all of them prepared following the same deposition-precipitation method to yield a gold loading of 5 wt%. Thus, regarding those materials, the only variable was the metal oxide used for the supports, namely, CeO₂, TiO₂ and Al₂O₃. The ultimate goal of narrowing the number of variables coming into play during the course of the study was decreasing the chances of making erroneous attributions of a particular catalytic feature or behaviour to the effect of a certain factor.

Secondly, a structured sequence was followed for the continuous flow experiments. Hence, a series of initial tests were aimed to search for the optimal experimental conditions so that, once found, they were set as the 'base line' upon which, whenever required, minimal changes were made. At the same time, these tests looked into factors such as the influence of the support material (CeO₂, TiO₂ and Al₂O₃) and whether or not the gold particle size was playing a role on the different activities observed from the Au/TiO₂ and the Au/CeO₂ catalysts.

These initial tests also allowed the research to concentrate on a narrower list of materials, thus giving more time to the investigation to carry out a deeper study on the ceria supported catalytic materials, Au/CeO₂ and AuPd/CeO₂. Thereafter, a series of experimental approaches were developed to explore the catalytic dependence on two major factors, namely, the contact time and the ratio between reactants (i.e. O₂ and CO). Based on those experimental results, an answer to the question upon the nature of the active Au species was attempted, which was supported with data from NAP-XPS analyses. The final stages of the flow reactor study immersed into the estimation of the apparent activation energies and the order of reaction with respect to CO for both Au/CeO₂ and AuPd/CeO₂ catalysts.

TAP reactor studies at both Cardiff and Harvard Universities were carried out to further investigate the mechanistic perspective of the catalytic CO oxidation reaction, this way complementing results from the flow reactor study. While experiments at Cardiff were mainly aimed to estimate relevant parameters such as the number of molecules per pulse or the percentage of active surface oxygen, data from TAP experiments at Harvard supported a series of qualitative assessments regarding the mechanism taking place when Au/CeO₂ was used as the catalyst.

Finally, it is worth to note at this point that, due to the kinetic approach of this work, most of the characterisation analyses were carried out to get additional information that give a stronger support to our conclusions.

References

- 1 J. H. B. J. Hoebink, R. A. Van Gemert, J. A. A. Van Den Tillaart and G. B. Marin, *Chem. Eng. Sci.*, 2000, **55**, 1573–1581.
- 2 M. Haruta, N. Yamada, T. Kobayashi and S. Iijima, *J. Catal.*, 1989, **115**, 301–309.
- 3 C. T. Campbell, *Science*, 2004, **306**, 234–235.
- 4 C. W. Corti, R. J. Holliday and D. T. Thompson, *Appl. Catal. A Gen.*, 2005, **291**, 253–261.
- 5 R. Grisel, K. J. Weststrate, A. Gluhoi and B. E. Nieuwenhuys, *Gold Bull.*, 2002, **35**, 39–45.
- 6 P. Ciambelli, S. Cimino, G. Lasorella, L. Lisi, S. De Rossi, M. Faticanti, G. Minelli and P. Porta, *Appl. Catal. B Environ.*, 2002, **37**, 231–241.
- 7 C. J. Karwacki, P. Ganesh, P. R. C. Kent, W. O. Gordon, G. W. Peterson, J. J. Niu and Y. Gogotsi, *J. Mater. Chem. A*, 2013, **1**, 6051–6062.
- 8 M. S. Chen and D. W. Goodman, *Catal. Today*, 2006, **111**, 22–33.
- 9 A. Boubnov, S. Dahl, E. Johnson, A. P. Molina, S. B. Simonsen, F. M. Cano, S. Helveg, L. J. Lemus-Yegres and J. D. Grunwaldt, *Appl. Catal. B Environ.*, 2012, **126**, 315–325.
- 10 Y. L. Lam and M. Boudart, *J. Catal.*, 1977, **50**, 530–540.
- 11 S. Galvagno and G. Parravano, *J. Catal.*, 1978, **55**, 178–190.
- 12 J. Y. Lee and J. Schwank, *J. Catal.*, 1986, **102**, 207–215.
- 13 A. Buchanan and G. Webb, Chemistry Department, University of Glasgow, 1974, 134–144.
- 14 J. Schwank, G. Parravano and H. L. Gruber, *J. Catal.*, 1980, **61**, 19–28.
- 15 A. G. Shastri, A. K. Datye and J. Schwank, *J. Catal.*, 1984, **87**, 265–275.
- 16 Q. Fu, H. Saltsburg and M. Flytzani-Stephanopoulos, *Science*, 2003, **301**, 935–

- 938.
- 17 G. Jacobs, P. M. Patterson, L. Williams, D. Sparks and B. H. Davis, *Catal. Letters*, 2004, **96**, 97–105.
- 18 R. Burch, *Phys. Chem. Chem. Phys.*, 2006, **8**, 5483–5500.
- 19 W. Deng and M. Flytzani-Stephanopoulos, *Angew. Chemie - Int. Ed.*, 2006, **45**, 2285–2289.
- 20 T. Hayashi, K. Tanaka and M. Haruta, *J. Catal.*, 1998, **178**, 566–575.
- 21 R. J. H. Grisel and B. E. Nieuwenhuys, *J. Catal.*, 2001, **199**, 48–59.
- 22 M. Haruta, T. Kobayashi, H. Sano and N. Yamada, *Chem. Lett.*, 1987, 405–408.
- 23 G. J. Hutchings, *Gold Bull.*, 1996, **29**, 123–130.
- 24 G. C. BOND and D. T. THOMPSON, *Catal. Rev.*, 2002, **41**, 319–388.
- 25 H. Masatake, *Catal. Today*, 1997, **36**, 153–166.
- 26 M. C. Kung, R. J. Davis and H. H. Kung, *J. Phys. Chem. C*, 2007, **111**, 11767–11775.
- 27 N. Lopez, T. V. W. Janssens, B. S. Clausen, Y. Xu, M. Mavrikakis, T. Bligaard and J. K. Nørskov, *J. Catal.*, 2004, **223**, 232–235.
- 28 B. Schumacher, V. Plzak, M. Kinne, R.J. Behm, *Catal. Letters*, 2003, **89**, 109–114.
- 29 M. Mavrikakis, P. Stoltze, J.K. Nørskov, *Catal. Letters*, 2000, **64**, 101–106.
- 30 Z. P. Liu, P. Hu and A. Alavi, *J. Am. Chem. Soc.*, 2002, **124**, 14770–14779.
- 31 L. M. Molina and B. Hammer, *Phys. Rev. Lett.*, 2003, **90**, 1–4.
- 32 S. H. Overbury, V. Schwartz, D. R. Mullins, W. Yan and S. Dai, *J. Catal.*, 2006, **241**, 56–65.
- 33 E. Duck Park and J. Sung Lee, *J. Catal.*, 1999, **186**, 1–11.

- 34 J. Guzman and B. C. Gates, *J. Phys. Chem. B*, 2003, **107**, 2242–2248.
- 35 J. A. Van Bokhoven, C. Louis, J. T. Miller, M. Tromp, O. V. Safonova and P. Glatzel, *Angew. Chemie - Int. Ed.*, 2006, **45**, 4651–4654.
- 36 L. Delannoy, N. Weiher, N. Tsapatsaris, A. M. Beesley, L. Nchari, S. L. M. Schroeder and C. Louis, *Top. Catal.*, 2007, **44**, 263–273.
- 37 M. M. Schubert, S. Hackenberg, A. C. Van Veen, M. Muhler, V. Plzak and J. J. Behm, *J. Catal.*, 2001, **197**, 113–122.
- 38 Z. P. Liu, X. Q. Gong, J. Kohanoff, C. Sanchez and P. Hu, *Phys. Rev. Lett.*, 2003, **91**, 1–4.
- 39 L. M. Molina, M. D. Rasmussen and B. Hammer, *J. Chem. Phys.*, 2004, **120**, 7673–7680.
- 40 M. Kotobuki, R. Leppelt, D. A. Hansgen, D. Widmann and R. J. Behm, *J. Catal.*, 2009, **264**, 67–76.
- 41 H. Liu, A. I. Kozlov, A. P. Kozlova, T. Shido and Y. Iwasawa, *Phys. Chem. Chem. Phys.*, 1999, **1**, 2851–2860.
- 42 S. Carrettin, Y. Hao, V. Aguilar-Guerrero, B. C. Gates, S. Trasobares, J. J. Calvino and A. Corma, *Chem. - A Eur. J.*, 2007, **13**, 7771–7779.
- 43 S. Peters, S. Peredkov, M. Neeb, W. Eberhardt and M. Al-Hada, *Surf. Sci.*, 2013, **608**, 129–134.
- 44 P. Jiang, S. Porsgaard, F. Borondics, M. Kober, A. Caballero, H. Bluhm, F. Besenbacher and M. Salmero, *J. Am. Chem. Soc.*, 2010, **132**, 2858–2859.
- 45 J. H. Yang, J. D. Henao, C. Costello, M. C. Kung, H. H. Kung, J. T. Miller, A. J. Kropf, J. G. Kim, J. R. Regalbuto, M. T. Bore, H. N. Pham, A. K. Datye, J. D. Laeger and K. Kharas, *Appl. Catal. A Gen.*, 2005, **291**, 73–84.
- 46 M. Khoudiakov, M. C. Gupta and S. Deevi, *Appl. Catal. A Gen.*, 2005, **291**, 151–161.
- 47 M. Méndez-Cruz, J. Ramírez-Solís and R. Zanella, *Catal. Today*, 2011, **166**,

- 172–179.
- 48 N. F. P. Ribeiro, R. P. F. Bonfim, M. M. V. M. Souza and M. Schmal, *J. Power Sources*, 2010, **195**, 7386–7390.
- 49 N. Saliba, D. H. Parker and B. E. Koel, *Surf. Sci.*, 1998, **410**, 270–282.
- 50 P. A. Pyryaev, B. L. Moroz, D. A. Zyuzin, A. V. Nartova and V. I. Bukhtiyarov, *Kinet. Catal.*, 2010, **51**, 885–892.
- 51 Y. Liu, C. N. Jia, J. Yamasaki, O. Terasaki and F. Schüth, *Angew. Chemie - Int. Ed.*, 2010, **49**, 5771–5775.
- 52 E. Del Río, G. Blanco, S. Collins, M. L. Haro, X. Chen, J. J. Delgado, J. J. Calvino and S. Bernal, *Top. Catal.*, 2011, **54**, 931–940.
- 53 K. Qian, L. Luo, H. Bao, Q. Hua, Z. Jiang and W. Huang, *Catal. Sci. Technol.*, 2013, **3**, 679–687.
- 54 Q. Li, Y. Zhang, G. Chen, J. Fan, H. Lan and Y. Yang, *J. Catal.*, 2010, **273**, 167–176.
- 55 T. Tabakova, G. Avgouropoulos, J. Papavasiliou, M. Manzoli, F. Boccuzzi, K. Tenchev, F. Vindigni and T. Ioannides, *Appl. Catal. B Environ.*, 2011, **101**, 256–265.
- 56 T. Tabakova, M. Manzoli, D. Paneva, F. Boccuzzi, V. Idakiev and I. Mitov, *Appl. Catal. B Environ.*, 2011, **101**, 266–274.
- 57 K. Zhao, B. Qiao, J. Wang, Y. Zhang and T. Zhang, *Chem. Commun.*, 2011, **47**, 1779–1781.
- 58 A. Wolf and F. Schüth, *Appl. Catal. A Gen.*, 2002, **226**, 1–13.
- 59 J. C. Fierro-Gonzalez and B. C. Gates, *J. Phys. Chem. B*, 2004, **108**, 16999–17002.
- 60 J. Guzman and B. C. Gates, *J. Am. Chem. Soc.*, 2004, **126**, 2672–2673.
- 61 J. C. Fierro-Gonzalez, J. Guzman and B. C. Gates, *Top. Catal.*, 2007, **44**, 103–114.

- 62 J. Guzman, S. Carrettin and A. Corma, *J. Am. Chem. Soc.*, 2005, **127**, 3286–3287.
- 63 P. Concepción, S. Carrettin and A. Corma, *Appl. Catal. A Gen.*, 2006, **307**, 42–45.
- 64 M. P. Casaletto, A. Longo, A. M. Venezia, A. Martorana and A. Prestianni, *Appl. Catal. A Gen.*, 2006, **302**, 309–316.
- 65 A. M. Venezia, G. Pantaleo, A. Longo, G. Di Carlo, M. P. Casaletto, F. L. Liotta and G. Deganello, *J. Phys. Chem. B*, 2005, **109**, 2821–2827.
- 66 S. Carrettin, P. Concepción, A. Corma, J. M. López Nieto and V. F. Puentes, *Angew. Chemie - Int. Ed.*, 2004, **43**, 2538–2540.
- 67 T. V. W. Janssens, A. Carlsson, A. Puig-Molina and B. S. Clausen, *J. Catal.*, 2006, **240**, 108–113.
- 68 A. Sanchez, S. Abbet, U. Heiz, W. D. Schneider, H. Häkkinen, R. N. Barnett and U. Landman, *J. Phys. Chem. A*, 1999, **103**, 9573–9578.
- 69 J. D. Grunwaldt, C. Kiener, C. Wögerbauer and A. Baiker, *J. Catal.*, 1999, **181**, 223–232.
- 70 S. Arrii, F. Morfin, A. J. Renouprez and J. L. Rousset, *J. Am. Chem. Soc.*, 2004, **126**, 1199–1205.
- 71 M. Comotti, W. C. Li, B. Spliethoff and F. Schüth, *J. Am. Chem. Soc.*, 2006, **128**, 917–924.
- 72 J. Grunwaldt, M. Maciejewski, O. S. Becker, P. Fabrizioli and A. Baiker, 1999, **469**, 458–469.
- 73 D. Widmann, Y. Liu, F. Schüth and R. J. Behm, *J. Catal.*, 2010, **276**, 292–305.
- 74 M. Mavrikakis, B. Hammer, J. K. Nørskov, *Phys. Rev. Lett.*, 1998, **81**, 2819–2822.
- 75 M. Haruta, *ChemInform*, 2010, **30**, no-no.
- 76 J. Grandgirard, D. Poinso, L. Krespi, J. P. Nénon and A. M. Cortesero,

- Entomol. Exp. Appl.*, 2002, **103**, 239–248.
- 77 F. M. Ansia, M. G. Penedo, C. Mariño and A. Mosquera, *Pattern Recognit. Image Anal.*, 1999, **2**, 76–77.
- 78 A. Kozlov and A. Kozlova, *Phys. Chem. Chem. Phys.*, 1999, **264**, 252–264.
- 79 H. Liu, A. I. Kozlov, A. P. Kozlova, T. Shido, K. Asakura and Y. Iwasawa, *J. Catal.*, 1999, **185**, 252–264.
- 80 J. C. Frost, *Nature*, 1988, **334**, 577–580.
- 81 J. Guzman, S. Carrettin, J. C. Fierro-Gonzalez, Y. Hao, B. C. Gates and A. Corma, *Angew. Chemie - Int. Ed.*, 2005, **44**, 4778–4781.
- 82 T. V. Choudhary, C. Sivadinarayana, C. C. Chusuei, A. K. Datye, J. P. Fackler and D. W. Goodman, *J. Catal.*, 2002, **207**, 247–255.
- 83 H. Liu, A. I. Kozlov, A. P. Kozlova, T. Shido and Y. Iwasawa, *Phys. Chem. Chem. Phys.*, 1999, **1**, 2851–2860.
- 84 L. M. Molina and B. Hammer, *Appl. Catal. A Gen.*, 2005, **291**, 21–31.
- 85 J. T. Gleaves, G. S. Yablonskii, P. Phanawadee and Y. Schuurman, *Appl. Catal. A Gen.*, 1997, **160**, 55–88.
- 86 G. S. Yablonsky, M. Olea and G. B. Marin, *J. Catal.*, 2003, **216**, 120–134.
- 87 J. T. Gleaves, G. Yablonsky, X. Zheng, R. Fushimi and P. L. Mills, *J. Mol. Catal. A Chem.*, 2010, **315**, 108–134.
- 88 J. Pérez-Ramírez and E. V. Kondratenko, *Catal. Today*, 2007, **121**, 160–169.
- 89 *Phys. Chem. Chem. Phys.*, 2001, **3**, 627–631.
- 90 M. Olea and Y. Iwasawa, *Appl. Catal. A Gen.*, 2004, **275**, 35–42.
- 91 M. Olea, M. Tada and Y. Iwasawa, *J. Catal.*, 2007, **248**, 60–67.
- 92 M. Olea, M. Tada and Y. Iwasawa, *Top. Catal.*, 2007, **44**, 137–143.
- 93 D. Widmann, R. Leppelt and R. J. Behm, *J. Catal.*, 2007, **251**, 437–442.

- 94 S. R. Bare, M. C. Kung, H. S. Oh, J. H. Yang and C. K. Costello, *J. Catal.*, 2002, **210**, 375–386.
- 95 Y. J. Chen and C. T. Yeh, *J. Catal.*, 2001, **200**, 59–68.
- 96 M. Okumura, S. Tsubota, M. Iwamoto and M. Haruta, *Chem. Lett.*, 2003, **27**, 315–316.
- 97 L. Delannoy, N. El Hassan, A. Musi, N. N. Le To, J. M. Krafft and C. Louis, *J. Phys. Chem. B*, 2006, **110**, 22471–22478.
- 98 J. A. Cusumano, *Nature*, 1974, **247**, 456.

2 | Methodology

2.1 Catalyst synthesis

All catalysts studied in this work were prepared following the deposition precipitation method (DP). A maximum metal loading of 5 wt% (weight percent) was targeted in the preparation.

Details of such a method are given below:

Aqueous metal precursor solutions of HAuCl_4 (Au = 12.25 mg/mL) and PdCl_2 (15 mg/mL) were prepared. A beaker was equipped with a magnetic stirrer and distilled water. HAuCl_4 (5 wt% Au if complete deposition) was added and the solution was stirred. NaOH (0.2 M) was added dropwise until a steady pH 10 was reached. Titania P25 support was added over 15-20 minutes. NaOH (0.2 M) was added dropwise until the solution returned to a steady pH 10. The mixture was left stirring overnight at room temperature, then filtered using a Büchner funnel and the catalyst was washed thoroughly with distilled water to remove impurities. The catalyst was dried in an oven at 110 °C overnight. All catalysts were ground and sieved <100 μm .

For bimetallic AuPd catalysts, both HAuCl_4 and PdCl_2 (5 wt% AuPd, Au/Pd = 1 molar ratio) precursors were used following the above method. In the case of alumina and ceria supports, nanopowder of those were used instead of titania.

Note that, although HAuCl_4 and PdCl_2 were used as precursors, the synthesis solution was adjusted to pH 10. Such pH is higher than the isoelectric points (IEP) of TiO_2 (IEP = 6.2), Al_2O_3 (IEP = 9.06) and CeO_2 (IEP = 3.3) and, consequently, their surfaces were neutral or slightly negatively charged (see Section 1.1.5, Chapter 1). This approach was put in place to prevent catalytic Cl^- poisoning from being happening.

2.2 Characterisation

2.2.1 XRD

The X-ray diffraction technique is widely employed in material chemistry to identify and quantify different crystalline phases, when compared with a data bank database. Crystalline solid materials present characteristic structure in which their constituents, which can be atoms, molecules or ions, are spatially arranged in a highly ordered manner that is repeated in the three dimensions of the space. Crystals can act as a crystalline three-dimensional diffraction grating when there are irradiated with monochromatic X-rays. Therefore, X-rays can be used to study the spatial arrangement of components of the crystal by applying studying the diffracted radiation. When Bragg's law requirements are satisfied, at certain angles of diffraction constructive interference of the X-ray provide information about the crystalline lattice like the spacing between the planes (Equation 2.1).

$$n \cdot \lambda = d \cdot 2 \cdot \sin\theta; \quad d = \frac{n \cdot \lambda}{2 \cdot \sin\theta} \quad (2.1)$$

where n is an integer, λ is the wavelength of the X-ray radiation and θ is the angle between the diffracted beam and the sample. A schematic of the X-ray diffraction process is shown in Figure 2.1.

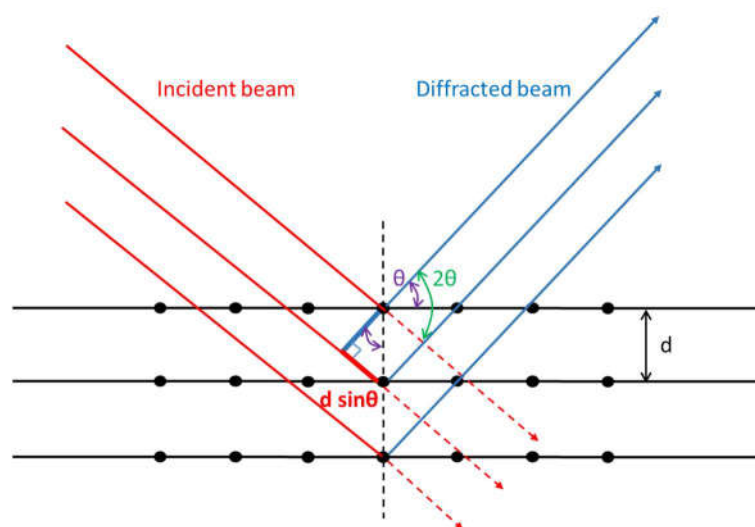


Figure 2.1. Scheme of diffraction phenomenon generated by the incidence of a monochromatic radiation into a crystalline structure according to the Bragg's law.

The incident radiation interacting with the different lattice planes, placed at distance d , will generate a diffracted radiation at θ .

Other than information of the d -spacing, it is also possible to calculate the crystalline size for small particles by using the Scherrer equation (Equation 2.2):

$$\tau = \frac{K \cdot \lambda}{\beta \cdot \cos \theta} \quad (2.2)$$

where K is a dimensionless shape factor (normally between 0.9-1), λ is the wavelength of the X-ray radiation, θ is the angle between the diffracted beam and the sample and β is the line broadening at Full Width Half Maximum intensity (FWHM).

The diffractometer is composed by three main components: the X-Ray generator, the sample holder and the detector (Figure 2.2).

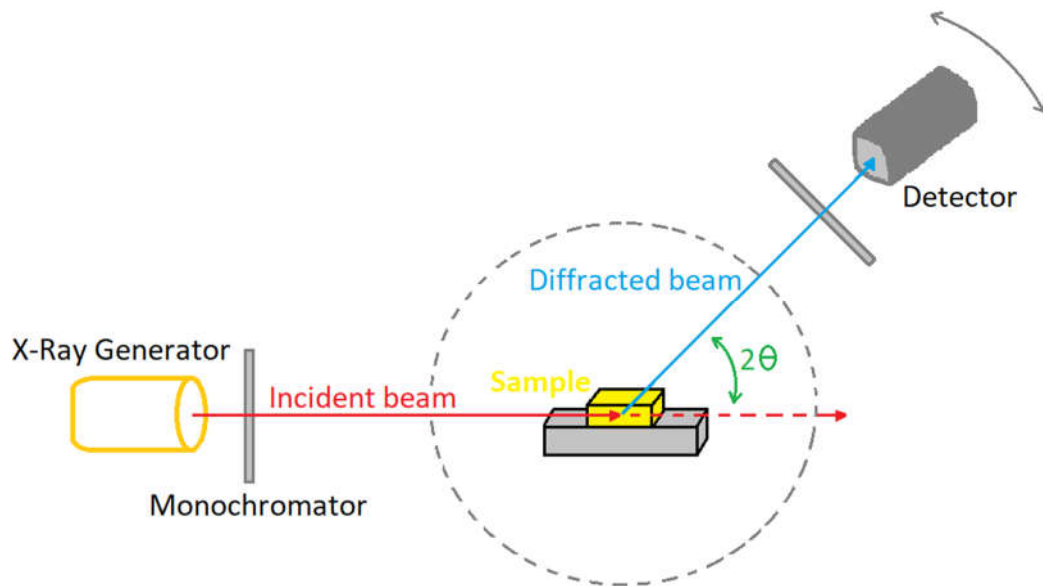


Figure 2.2. Schematic of a classical XRD machine. The monochromatic X-ray is generated by the generator and filter before hitting the sample. A mobile detector moves at different angles to record the intensity of the diffracted beam at 2θ angle respect to the incident radiation.

The X-ray radiation is generated by irradiating a foil of copper with a high-energy electron beam. An inner core electron of the copper atom will be expelled producing a vacancy that will be filled by one electron of the upper level, generating a cascade of electrons. This movement of electron will give rise to several X-ray photons that will pass through a monochromator to be filtered into a single monochromatic beam. Only a monochromatic X-ray, typically the $\text{CuK}\alpha$ radiation (1.5418 Å), will be selected and converged to the sample. The detector will move around an arc and will therefore collect the diffracted radiation at several angles, from ca. 5 to 80° 2θ . As a result from XRD analysis, a diffractogram is obtained and intensity of the diffracted beam are plotted against the diffraction angle 2θ .

In this work, a PANalytical X'Pert PRO X-ray diffractometer was employed for XRD analysis. A $\text{CuK}\alpha$ radiation source (40 kV and 40 mA) was utilised. Diffraction patterns were recorded between 6-80° 2θ (step size 0.0167°, total time = 1 h). Figures 2.3-2.5 show the XRD patterns for the series of catalysts tested during the different experiments performed (Chapter 5 and 6). As can be seen from Figure 2.3, all ceria-based supports clearly show the fluorite-type cubic structure^{1,2,3}. A broad XRD (1 1 1) peak at $2\theta \sim 38.18^\circ$ was noticed for AuPd/CeO_2 sample due to the face centered cubic structure of gold, indicating the presence of larger Au particles⁴. In contrast, no Au diffraction peak was found in the case of the Au/CeO_2 catalyst owing to the fact that the gold particle sizes are very small (<5 nm)⁵. The absence of Au diffraction peak also indicates the existence of highly dispersed gold particles on the catalytic surface that are too small to be detected by the XRD technique^{5,6}. Figure 2.4 shows the XRD patterns for the titania based catalysts, Au/TiO_2 and AuPd/TiO_2 . All the peaks on both patterns belong to the rutile and anatase phases of TiO_2 ⁷. The XRD patterns for the supported alumina catalysts, $\text{Au/Al}_2\text{O}_3$ and $\text{AuPd/Al}_2\text{O}_3$, are shown in Figure 2.5, which shows the existence of the gamma (γ) and delta (δ) phases⁸.

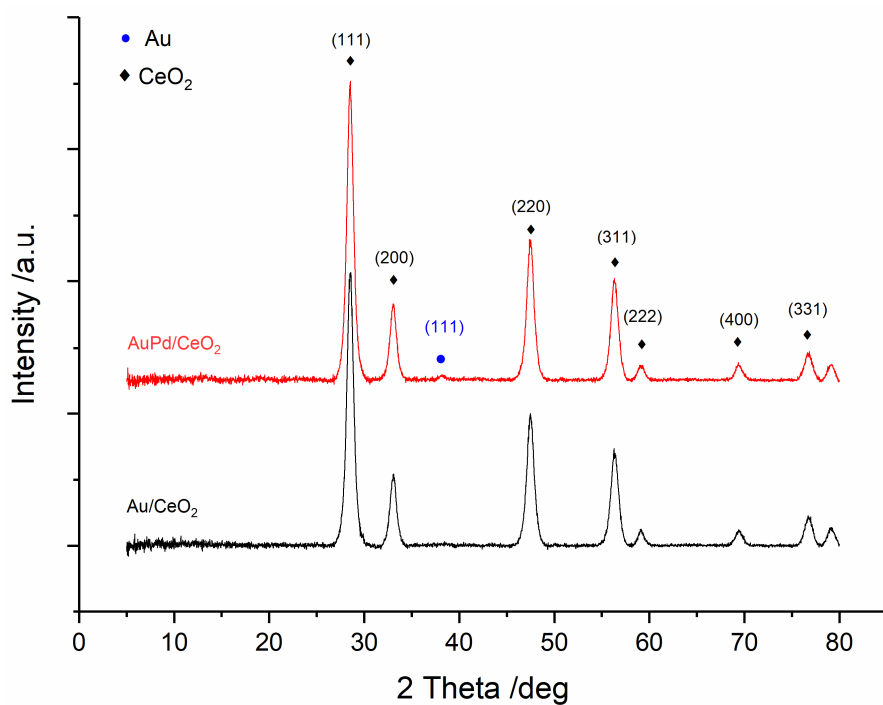


Figure 2.3. XRD pattern of Au/CeO₂ and AuPd/CeO₂ prepared according to the method described in Section 2.1.

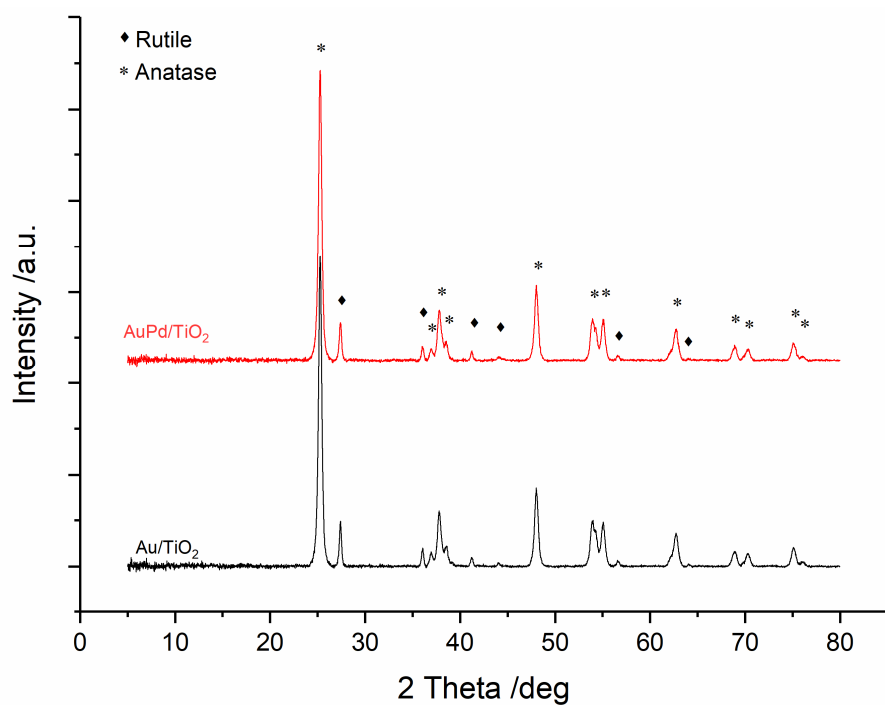


Figure 2.4. XRD pattern of Au/TiO₂ and AuPd/TiO₂ prepared according to the method described in Section 2.1.

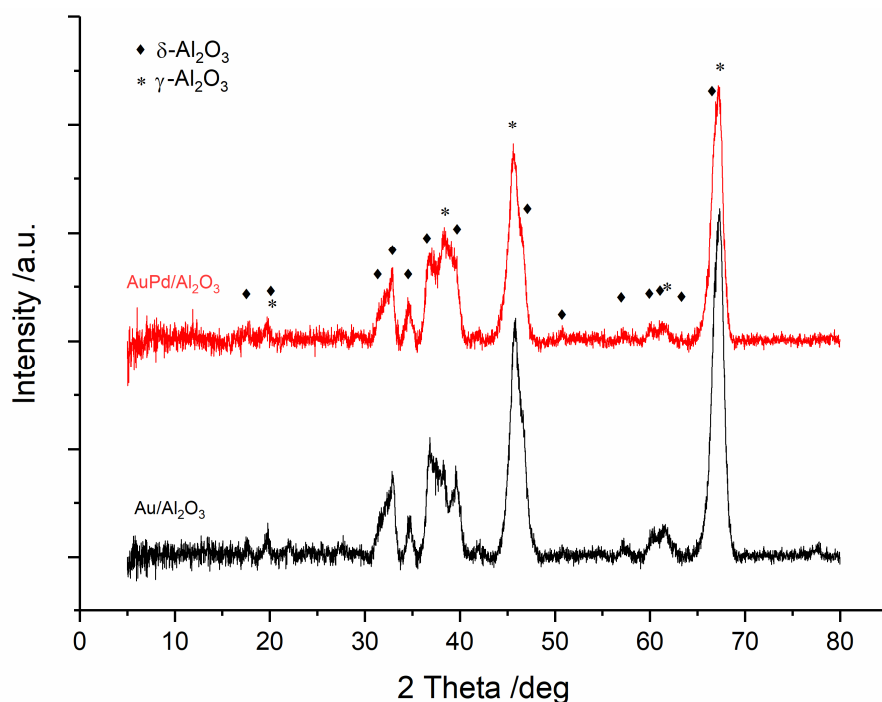


Figure 2.5. XRD pattern of Au/Al₂O₃ and AuPd/Al₂O₃ prepared according to the method described in Section 2.1.

2.2.2 BET

Surface areas were measured following the Brunauer-Emmett-Teller (BET) theory. The powdered catalytic samples were poured into 12 mm cells, which were previously empty weighted. Then, the samples were purged of adsorbed water by heating at 120 °C under a stream of helium for several hours, using a Micromeritics Flowprep 060. The purged samples were then evacuated, weighed and cooled using liquid nitrogen. Subsequently, a Gemini 2360 Surface Area analyser was used to carry out the sample surface area measurement. During this process, nitrogen gas is first admitted to the sample vial and an identical empty vial. A differential pressure transducer measures the imbalance in pressure between the sample and blank vials, caused by the adsorption of gas onto the sample surface. In the next steps, the physical adsorption of adsorbate is carried out at different pressures of nitrogen. The system uses this data to calculate the number of molecules of nitrogen required to form a monolayer on the sample surface according to Equation 2.3. And, since the molecular dimensions of nitrogen are known,

calculates the surface area of the sample in square meters per gram using Equation 2.4.

$$\frac{1}{v(P_0-P)} = \frac{1}{v_m C} + \frac{C-1}{v_m C} \left(\frac{P}{P_0} \right) \quad (2.3)$$

where P is the equilibrium pressure, P_0 is the saturation pressure, v is the volume of adsorbate injected into the vial, v_m is the volume required to cover the surface in a monolayer and C is a constant. P_0 was update prior the first run. This was done using an empty sample cell fitted to the measuring port as per a standard run.

Equation 2.3 is an adsorption isotherm and can be linearized by plotting $\frac{1}{v(P_0-P)}$ versus $\frac{P}{P_0}$, resulting in a straight line that intercepts at $\frac{1}{v_m C}$. Thus, the value of v_m can be obtained and Equation 2.4 applied to get the surface area of the sample ($Area_{surface}$).

$$Area_{surface} = \frac{v_m \cdot N_A \cdot A_{cs}}{M} \quad (2.4)$$

where N_A is the Avogadro's number (6.023×10^{23}), A_{cs} is the cross sectional area of the adsorbate molecules, i.e. N_2 (0.162 nm^2), and M is its molecular weight (28.0123 g).

Measured following the procedure above described, table 2.1 presents the surface areas for the most relevant samples used during this study.

Table 2.1. Surface areas measured following the Brunauer-Emmett-Teller (BET) method.

	Au/TiO ₂	AuPd/TiO ₂	Au/CeO ₂	AuPd/CeO ₂
<i>Area_{surface}</i> /m ² g ⁻¹	50	59	58	68

2.2.3 SEM/EDX and TEM

Energy Dispersive X-ray (EDX) techniques were used for the elemental analysis of both Au/CeO₂ and AuPd/CeO₂, the selected catalytic samples for their better performance above the rest. In particular, a Bruker XFlash detector and a Quantax

70 software coupled with a Hitachi TM3030Plus microscope were used. Hence, imaging of the analysed catalytic surface from the scanning electron microscope (SEM) were also obtained.

SEMs employ electron beams in order to get information from a sample at the nanoscale. The main type of signals that are detected are the backscattered (BSE) and secondary electrons (SE), which generate a grayscale image of the sample at very high magnifications. BSE come from deeper regions of the sample, while SE originate from surface regions (Figure 2.6). Therefore, BSE and SE carry different types of information. BSE produce images with contrast that carries information on the differences in atomic number while SE give topographic information.

The generation of the X-rays in a SEM is a two-step process. In the first step, the electron beam hits the sample and transfers part of its energy to the atoms of the sample. This energy can be used by the electrons of the atoms to jump to an energy shell with higher energy or be emitted from the atom. If such a transition occurs, the electron leaves behind a hole. Holes have a positive charge and, in the second step of the process, attract the negatively charged electrons from higher-energy shells. When an electron from such a higher-energy shell fills the hole of the lower-energy shell, the energy difference of this transition can be released in the form of an X-ray (Figure 2.7). This X-ray has energy which is characteristic of the energy difference between these two shells. It depends on the atomic number, which is a unique property of every element. In this way, X-rays are a fingerprint of each element and can be used to identify the type of elements that exist in a sample. An EDX detector can efficiently collect these X-rays and provide a quantitative or semi-quantitative measurement of the sample's composition.

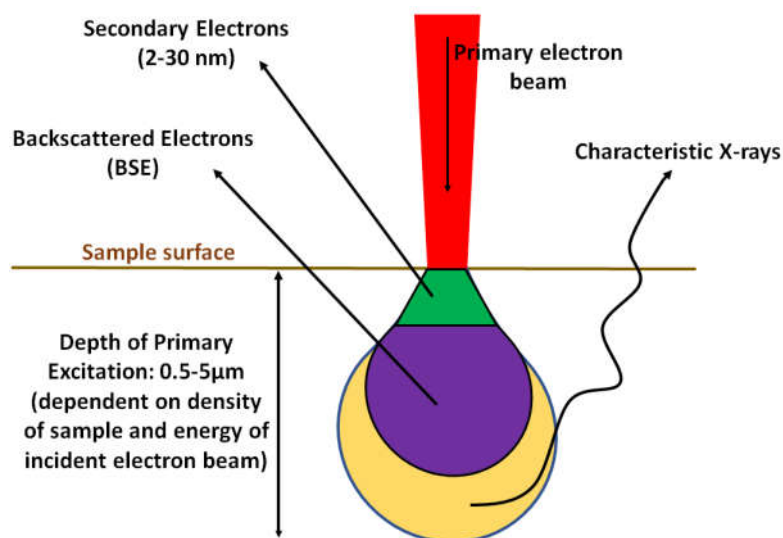


Figure 2.6. Schematic diagram of the backscattered electron, secondary electron and characteristic X-ray excitation volumes.

The spatial resolution and depth of analysis for EDX depends on two major factors: the accelerating voltage of the incident electron beam and the density of the material being analysed. In general, the higher the accelerating voltage, the deeper into the sample X-rays will be generated which will lead to more X-ray signal, but poorer spatial resolution. Low density materials such as carbon, oxygen and nitrogen will result in X-rays being generated much deeper into the surface compared to heavier elements such as gold or palladium. The highest spatial resolutions for EDX are therefore obtained at low accelerating voltages on higher density materials. However, low voltage is not always ideal as higher accelerating voltages are needed to excite X-ray peaks (especially for heavier elements). Therefore, there is not a perfect solution for resolution versus signal in EDX and rather a trial-based approach should be followed.

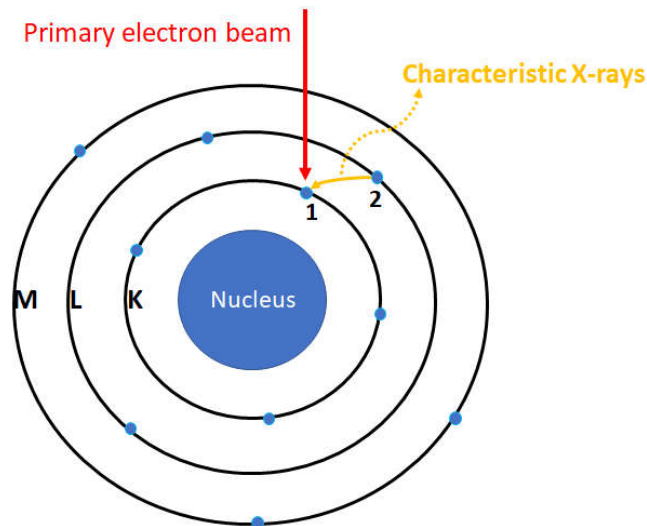


Figure 2.7. X-ray generation process. (1) The energy transferred to the atomic electron knocks it off leaving behind a hole. (2) Its position is filled by another electron from a higher energy shell and the characteristic X-ray is released.

Whenever high resolution images are needed, transmission electron microscopy (TEM) techniques can be used instead of SEM. This is due to the fact that TEM analyses are based on transmitted electrons whereas scattered electrons are the source of information in SEMs. This means that, while SEM creates an image by detecting reflected or emitted electrons, TEM uses electrons which are passing through the sample instead. The two electron microscope systems also differ in the way they are operated. SEMs usually use acceleration voltages up to 30 kV, while TEM users can set it in the range of 60 – 300 kV. The magnifications that TEMs offer are also much higher compared to SEMs: TEM users can magnify their samples by more than 50 million times, while for the SEM this is limited up to 1-2 million times. As a result, TEM offers invaluable information on the inner structure of the sample, such as crystal structure, morphology and stress state information, while SEM provides information on the sample's surface and its composition.

Despite the obvious advantages of using TEM techniques, SEM provides 3D images of the surface of the sample whereas TEM images are 2D projections, which in some cases makes the interpretation of the results more difficult. Also, due to the requirement for transmitted electrons, TEM samples must be very thin, generally below 150 nm, and in cases that high-resolution imaging is required, even below

30 nm, whereas for SEM imaging there is no such specific requirement. The complex preparation of the samples for TEM analysis is the reason why this technique is reserved to be followed by trained and experienced users.

2.2.4 NAP-XPS

X-ray photoelectron spectroscopy (XPS) has been employed for many years in fields such as catalysis, corrosion and electrochemistry to study the nature of material surfaces. In particular, XPS can measure the elemental composition, empirical formula, chemical state and electronic state of the elements within a material. During XPS analyses, a surface is irradiated with soft X-rays, which leads to the emission of photoelectrons. Since these photoelectrons have energies typically below 1500 eV and the depth of the sample is usually between 3 and 10 nm, only those electrons from the top atomic layers can escape and reach the detector.

Usual XPS systems require that both the sample and the detector are kept under high vacuum conditions during measurement, so that the photoelectrons are not absorbed by air molecules before reaching the detector. However, since the sample must be in high vacuum, one can only observe the state of the sample before and after a chemical reaction has occurred. Thus, it is not possible to look at the surface while the chemical reaction is taking place. This inconvenience is the reason behind the development of the near-ambient pressure (NAP) XPS. During NAP-XPS analyses, the sample is contained in a high pressure cell which is only open to the analyser via a small aperture. However, the sample is placed so close to the aperture that a fraction of the emitted photoelectrons can escape and reach the detector even when the area under analysis is in a high pressure of gas (see Figure 2.8). Then, after each aperture, a series of pumping stages quickly reduce the pressure back to high vacuum.

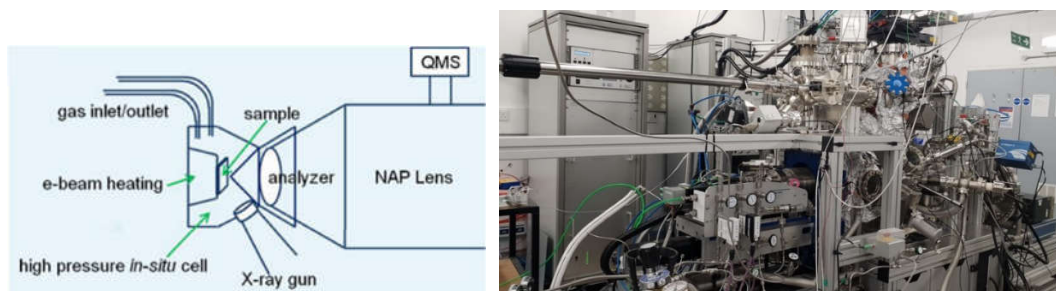


Figure 2.8. Gas cell attached to a horizontally oriented SPECS NAP analyser⁹ (left). NAP-XPS unit at Manchester University (right).

2.3 MATLAB programming environment

In order to develop software for data analysis, the first step is to decide which programming language to use. For this project, the multi-paradigm numerical computing environment MATLAB (*version 9.1.0.441655 (R2016b)*, *The MathWorks Inc., Natick, Massachusetts, United States*) was chosen. MATLAB is considered to be a high-level programming language, which means that there is a large degree of abstraction away from the internal computing code. This implies that the language is much more user friendly than other more common programming environments (*e.g.* Python, C, FORTRAN).

The MATLAB code is built around the MATLAB scripting language. It is highly interactive, meaning it is very easy to perform simple mathematics for example:

```
>> t = 5;  
>> t = t+1
```

would output:

```
t =  
6
```

Nonetheless, where MATLAB really excels is in its handling of vectors and matrices. Through simple commands it is easy to generate a matrix of elements and quickly perform any function on that matrix:

```
>> A = [1 2 3; 4 5 6; 7 8 0];  
>> inv(A)  
ans =  
   -1.7778    0.8889   -0.1111  
    1.5556   -0.7778    0.2222  
   -0.1111    0.2222   -0.1111
```

The generated data and defined variables are saved in the workspace accessed at the MATLAB command prompt, which is called the base workspace. This way they can be easily used on demand when needed. This is much facilitated when the use of M-file functions comes into play. These functions in conjunction with the creation of a graphical user interface (GUI) were the main pillars that supported the functionality of both the flow reactor and the TAP reactor software developed in this work (Chapters 3 and 4). A deeper insight of these systems is focused in the next subsection 2.3.1.

2.3.1 Creation of M-file functions in MATLAB

A function is a group of statements that together perform a task. In MATLAB, functions are defined in separate files. The name of the file and of the function should be the same. These functions operate on variables within their own workspace, which is also called the local workspace, separate from the base workspace. They can accept more than one input argument and may return more than one output argument. Listing 2.1 shows an example of a typical function syntax. This function `TC_ON_faster` is one of the secondary functions that assists the primary functions forming the flow reactor numerical analysis software (discussed in Chapter 3). In this case, the function `TC_ON_faster` takes two input arguments, namely 'types' and 'tcPath'. After running the script, the function returns one output argument, attributed to a variable called 'handle'. In line 7 of Listing 2.1, the function calls a major one, which has a larger and more complex body, called `TC_ON`. Then, in line 10, function 'mininterval' is also called. This is giving an example of how more than one function can be run within a single script. The way this kind of multiple function scripts works could be better understood by drawing upon Schematic 2.1. Accordingly, information gathered by the GUI directly from the User inputs, so-called 'Input A', constitute the feed to primary functions.

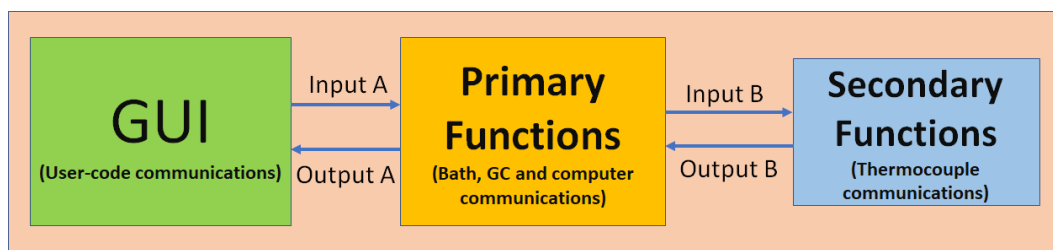
These primary functions, in turn, could be calling secondary functions. In that case, the input argument for those, 'Input B', had to be obtained from previous lines within the body of the primary function. After running those secondary functions, an output argument 'Output B' results. This is then used by the primary function in order to get the final 'Output A', which will be the final outcome/s that the user is going to see and use thereafter. As will be detailly discussed in Chapter 3, a GUI was developed in this work with the intention of making a more user-friendly software. The features of such a GUI will be displayed in subsection 3.3.

```

1 function handle = TC_ON_faster(types,tcPath)
2 % tcPath is the folder containing the DLLs. 'C:\Program Files (x86)\Pico Technology\SDK\lib'
3 % handle is the handle of the TC. types = Types of thermocouples connected.
4
5 tc_lib = 'usbtc08';
6
7 handle = TC_ON(types, tcPath)
8
9 % get the minimum interval time between samples. This is about 100 ms per channel
10 interval = mininterval(handle);
11
12 % set it to int64
13 interval64 = int64(interval);
14
15 % sends the instruction
16 interval_tc = calllib(tc_lib, 'usb_tc08_run', handle, interval64);
17
18 % See if tc started collecting temperatures
19 if ~interval_tc
20     error('Thermocouple did not start collecting temperatures.')
21 end

```

Listing 2.1. Script for the function 'TC_ON_faster', one of the secondary functions forming the flow reactor numerical analysis software.



Schematic 2.1. Communications within a system constituted of GUI, primary and secondary functions.

2.4 CO oxidation rig

In this study, catalytic information was extracted by the means of two different reactors, a continuous flow reactor and a TAP reactor. While the rigs used when performing TAP pulse experiments were already in place, meaning there was no need to design the components of those, for the case of the flow reactor studies, it was a 'starting from scratch' situation. This section is focused on describing the primary considerations and steps towards the design of the reactor rig used for the continuous flow reactions performed in this work.

2.4.1 Reactor setup

The design of the new reactor rig aimed to perform both CO oxidation alone (without H₂) and PROX reactions, thus a broader study on the catalytic performances regarding different types of CO oxidation could be implemented. Also, a high degree of automation was pursued when carrying out those reactions. Regarding the design of such a rig, some limitations came with the fact that three of its components were already set. In particular, reactor, gas chromatograph (GC), reactor heater/cooler and computer were bought before starting this work, hence type and model of those were already dictated. Also, a MATLAB environment was chosen as the most approachable to achieve the automative feature of the system previously commented. Accordingly, the characteristics of the rest of components had to be able to work as needed within that environment. In particular, suitable mass flow controllers (MFCs) and a digital thermocouple along with the gas mix cylinders to be used had to be chosen. Nevertheless, the search and comparison among the pros and cons of different brands, models or types is not the purpose of this thesis. Thus, the model of each physical component within our flow reactor rig is listed below:

1. Reactor: Quartz U-tube with 6 mm outer diameter, 1 mm wall thickness, 10.5 cm width and 11 cm height.
2. Reactor heater/cooler: Thermo Scientific VersaCool Refrigerated Circulating Bath, -20 °C to +150 °C.

3. GC: Agilent 490 Micro GC.

4. MFCs: Bronkhorst EL-FLOW *select* digital thermal mass flow controllers. Four units calibrated for four different gas mixtures (details in subsection 2.4.3).

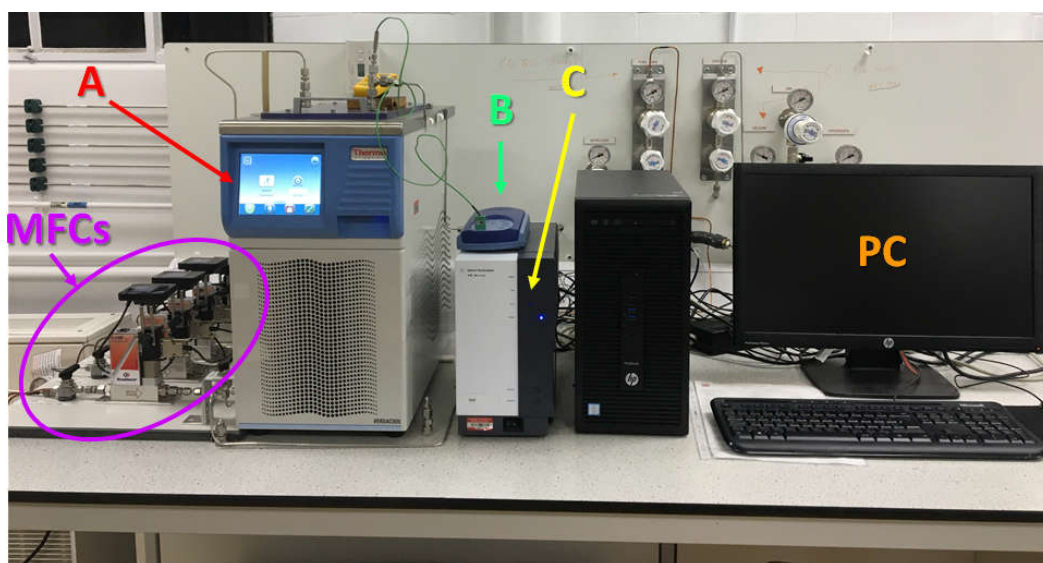
6. Thermocouple: Pico USB TC-08 Temperature Logger, coupled with a RS PRO Type K Thermocouple, +250 °C.

Catalytic tests were carried out under atmospheric pressure. Tubing and connections were made from stainless steel. The GC used for product analysis was equipped with two different columns:

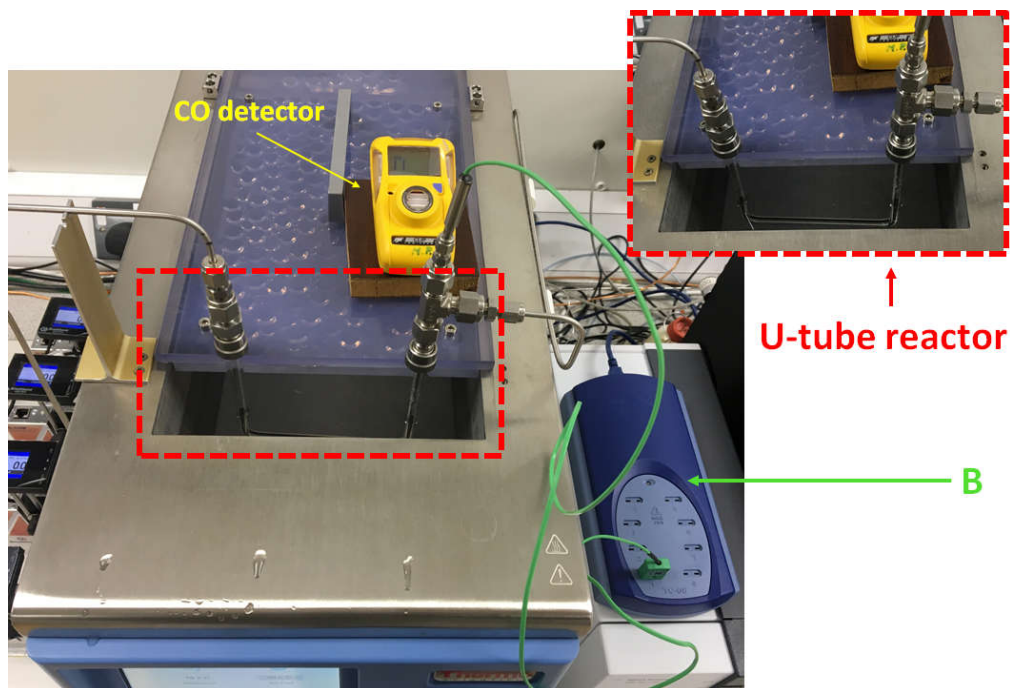
Column 1: A 5 Å molecular sieve filled column, for CO and O₂ separation.

Column 2: A polar column, Poropak Q, to separate CO₂ and H₂O from the other outlet gases.

Picture 2.1 shows the resulted reactor setup with the above listed components, while Picture 2.2 zooms on the reactor and thermocouple.



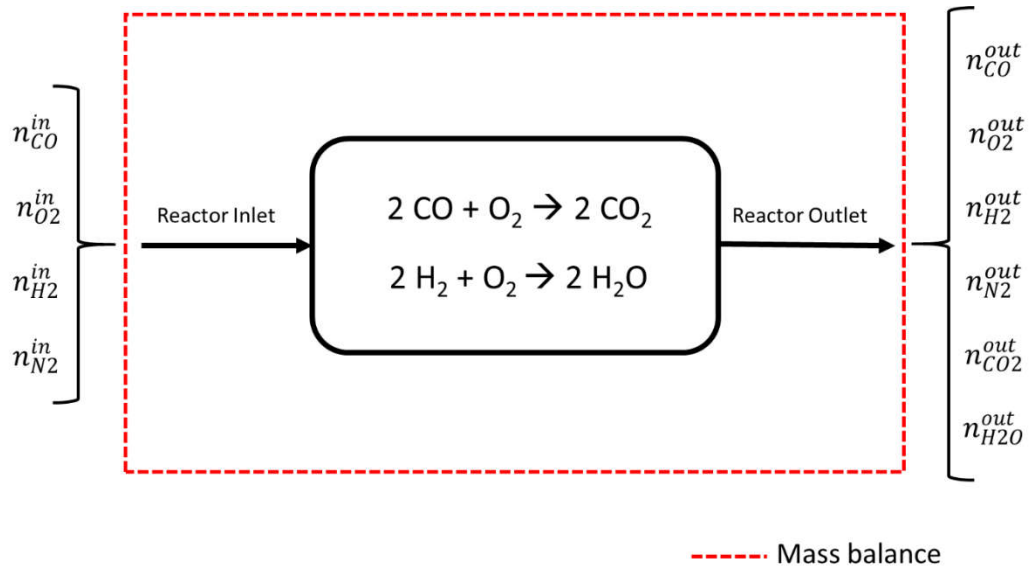
Picture 2.1. Flow reactor set up, where A points to bath, B to thermocouple data logger and C to GC. PC and MFCs are also highlighted.



Picture 2.2. Zoom on the reactor, thermocouple and its data logger (B).

2.4.2 Calculations

A series of basic calculations were applied when flow reactor experiments were performed. For those, the analysis of inlet and outlet flows is essential. When it comes to outlet flows, the GC used in this work places a relevant limitation. In this case, He is the carrier gas. Thermal conductivities of He and H₂ are too similar for the GC to distinguish these gases and so accurate estimation of H₂ concentrations is not possible. H₂O should not be measured in a direct way from GC analysis either. This is because gas mix cylinders come with some little amount of gaseous water as an impurity, and that, even being tiny, can disturb future calculations. These two reactants are key when it comes to PROX selectivity studies. Nevertheless, indirect measurement of both H₂ and H₂O outlet flows are possible. This is possible by performing a stoichiometric and mass balance between the inlet and the outlet of the reactor (red dashed area in Schematic 2.2).



Schematic 2.2. Continuous flow reactor diagram, where reactor inlet and outlet gases involved in CO oxidation and PROX reaction are signalled. Red dashed line specifies the area where mass balance equations (Eq. 2.5-2.8) apply.

According to Schematic 2.2, two competing reactions are taken into consideration: the CO oxidation and the hydrogen oxidation. The inlet amount of the different gasses is known: $n_{H_2}^{in}$, n_{CO}^{in} , $n_{CO_2}^{in}$, $n_{O_2}^{in}$, $n_{N_2}^{in}$. Thus, Equations 2.5-2.8 can be established from the stoichiometry and mass balances:

$$\text{H: } n_{H_2}^{in} = n_{H_2}^{out} + n_{H_2O}^{out} \quad (2.5)$$

$$\text{C: } n_{CO}^{in} = n_{CO}^{out} + n_{CO_2}^{out} \quad (2.6)$$

$$\text{O: } 2 n_{O_2}^{in} + n_{CO}^{in} = 2 n_{O_2}^{out} + 2 n_{CO_2}^{out} + n_{CO}^{out} + n_{H_2O}^{out} \quad (2.7)$$

$$\text{N: } n_{N_2}^{in} = n_{N_2}^{out} \quad (2.8)$$

There are 6 different outlet flows: n_{CO}^{out} , $n_{CO_2}^{out}$, $n_{O_2}^{out}$, $n_{H_2}^{out}$, $n_{H_2O}^{out}$ and $n_{N_2}^{out}$. Equations 2.5-2.7 are linearly independent, hence measurement of N_2 and 2 more outlet flows could define all the outlet parameters. In practice, CO and O_2 outlet amounts along with CO_2 (to check mass balance) were determined directly from GC analysis. Hydrogen and water concentrations can then be calculated from above equations.

The total conversion, X_{total} , is the same as the oxygen conversion, X_{O_2} , which can be obtained from the oxygen consumption:

$$X_{\text{total}} = X_{O_2} = \frac{n_{O_2}^{\text{in}} - n_{O_2}^{\text{out}}}{n_{O_2}^{\text{in}}} \cdot 100 \text{ (in \%)} \quad (2.9)$$

The selectivity, S , is defined as the ratio of the desired reaction (CO oxidation) to overall reactions, H_2 and CO consumption. This definition of the selectivity is also valid in the case of having methane formation:

$$S = \frac{n_{CO}^{\text{in}} - n_{CO}^{\text{out}}}{n_{CO}^{\text{in}} - n_{CO}^{\text{out}} + n_{H_2}^{\text{in}} - n_{H_2}^{\text{out}}} \cdot 100 \text{ (in \%)} \quad (2.10)$$

Selectivity is also given by the ratio of the oxygen transformed into CO_2 to the total oxygen consumed. When no methane is formed (as expected under the conditions used in our study) this is:

$$S = \frac{n_{CO_2}^{\text{out}}}{2(n_{O_2}^{\text{in}} - n_{O_2}^{\text{out}})} \cdot 100 \text{ (in \%)} \quad (2.11)$$

The CO conversion, X_{CO} , is defined as:

$$X_{CO} = \frac{n_{CO}^{\text{in}} - n_{CO}^{\text{out}}}{n_{CO}^{\text{in}}} \cdot 100 \text{ (in \%)} \quad (2.12)$$

And yield to CO_2 (Y_{CO_2}) as:

$$Y_{CO_2} = \frac{n_{CO_2}^{\text{out}}}{n_{CO}^{\text{in}}} \cdot 100 \text{ (in \%)} \quad (2.13)$$

Both X_{CO} and Y_{CO_2} should concur with each other since CO is expected to only convert into carbon dioxide in our case.

Lambda (λ) is the process parameter that characterizes the oxygen excess with respect to the amount of oxygen required for the oxidation of CO to CO_2 :

$$\lambda = \frac{2[O_2]}{[CO]} = \frac{2p_{O_2}}{p_{CO}} \quad (2.14)$$

where $[O_2]$ refers to concentration of oxygen, while $[CO]$ refers to concentration of carbon monoxide. p_{O_2} and p_{CO} are the oxygen and carbon monoxide partial pressures, respectively. A more detailed discussion on λ is included in Section 5.1.3.

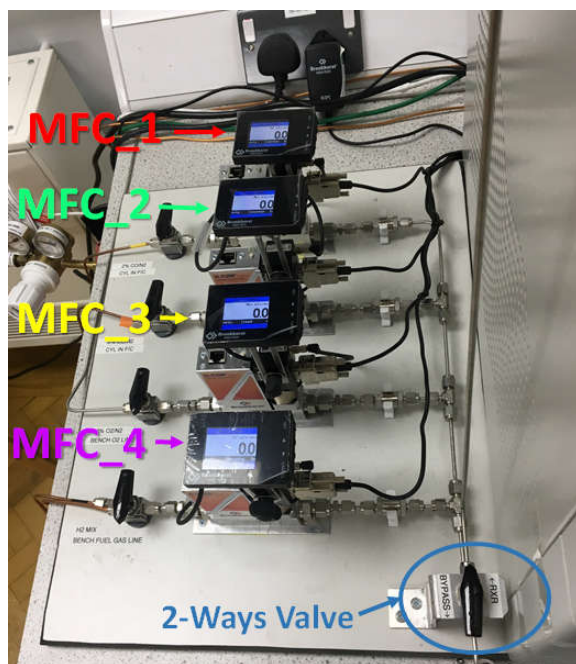
Above equations 2.9-2.14 configure the chemistry basics upon which the flow reactor data analysis software developed in this work, Chapter 3, operates. Although the resulting code is the same for both CO oxidation alone and PROX, the necessary mathematical calculations for both kind of oxidations differ from each other, since the presence or lack of hydrogen in the reactor inlet should not be ignored. Therefore, the way the code is used changes depending on which oxidation case is being dealt with. As mentioned above, a graphical user interface (GUI) was developed alongside the code. This GUI is the key part that transfers the reaction conditions of the present experiment to the running code, making sure the reaction is performed as desired and that correct calculations are implemented after reaction is finished. Chapter 3 is dedicated to exploring the features and applications of that software.

2.4.3 Composition and flow of the inlet gases

As previously mentioned, a system capable of performing different types of oxidations, specifically CO oxidation and PROX, was intended in the design of the reactor rig. Prime criterion for PROX is minimization of hydrogen oxidation at complete CO oxidation. For this reason, limited λ values should be tested¹⁰. The low λ criterion is also applicable to CO oxidation alone, since higher λ values imply higher CO conversion and with this, overheating within the catalytic bed. CO oxidation is a quite exothermic reaction and kinetic studies require a precise temperature measurement, this is why a temperature gradient along catalyst bed must be avoided. This is further discussed in Section 5.1.3.

The desired composition of the total flow is reached by four mass flow controllers (MFCs), shown in Picture 2.3, namely MFC_1, MFC_2, MFC_3 and MFC_4. Each of these were calibrated for the following flow ranges:

- MFC_1: 200 – 4 ml min⁻¹
- MFC_2: 100 – 2 ml min⁻¹
- MFC_3: 200 – 4 ml min⁻¹
- MFC_4: 100 – 2 ml min⁻¹



Picture 2.3. Mass flow controllers within the CO oxidation rig.

Above flow ranges are a limitation when looking for the optimal composition of the gases to be used. Furthermore, percentage of each gas in the total flow entering the reactor should be designed in a way that safe work outside explosive limits is carried out¹¹. In order to respect this safety paradigm, the following gaseous mixes were chosen for the reactor feed:

- MFC_1: 2% CO/H₂
- MFC_2: 10% O₂/N₂
- MFC_3: 2% CO/N₂
- MFC_4: 80% H₂/N₂ or 100% N₂

The use of the above mixes with four different MFCs would allow the performance of a wide range of oxidation reactions, namely PROX, CO alone, CO oxidation, H₂ alone and H₂ oxidation, where CO alone and H₂ alone refer to experiments when no oxygen is entering the reactor. In those cases, any CO or H₂ oxidation taking place would involve the uptake of catalytic surface oxygen as a reactant. Since conversion factors for both N₂ and H₂ were the same for the MFCs used in this work, MFC_4 could control the flows of both 80% H₂/N₂ and 100% N₂ gases. This also gave

chance to carry out the study on the order of reaction with respect to CO (disclosed in Section 5.3) without the necessity of an extra MFC for the inert (N₂).

Although PROX reactions could not be performed experimentally due to time limitations during this work, the designed rig with the above composition of gases and flows was intended to keep the percentage of H₂ around 80%-82% in the total mixture. As an example, if 25 ml min⁻¹ were set for the 2% CO/H₂ mixture and 5 ml min⁻¹ for the 10% O₂/N₂ one, this would give a total gas stream with the composition: 1.67% CO, 1.67% O₂, 81.67% H₂, 15% N₂.

Related to the CO oxidation experiments included in this work, a typical flow reactor experiment would involve catalyst masses of around 25 mg, total flows of 30 ml min⁻¹ and a λ -value of 2. Percentages of around 2% carbon monoxide in the total mixture were kept during all experimental tests.

Conclusively, the above discussed reactor setup and composition of gases offer the possibility of performing a wide variety of catalytic oxidation reactions while respecting the safety in terms of explosive limits¹¹.

2.4.4 GC calibration procedure

2.4.4.a Single point calibration method

This method involves repeating a series of GC runs while injecting a gaseous mix with a constant known composition. For the case of the continuous flow CO oxidation reactions carried out in this work, a constant flow of both the 2% CO/N₂ and the 10% O₂/N₂ gaseous mixes were fed into the reactor towards the GC when calibrating its response to CO. When calibrating to CO₂, a similar procedure was followed with the only difference of using a 2% CO₂/N₂ mix instead of the CO containing one. In the case of O₂, since the mix O₂/N₂ was introduced into the feed line in both calibration cases previously mentioned, GC calibration to oxygen could be obtained from either one of those. Nevertheless, since O₂ is always detected in Column 1 (see above Section 2.4.1), the same results should be found regardless the choice.

No catalyst was packed into the reactor and a series of GC runs were then executed. Since nitrogen acts as an inert for the CO oxidation reaction, this was used as the internal standard. A response factor (R_f) was calculated from data obtained after each GC run according to Equation 2.15:

$$R_f = \frac{A_x \cdot C_{IS}}{A_{IS} \cdot C_x} \quad (2.15)$$

where A_x is the GC measured area for the gas being calibrated (CO, CO₂ or O₂) and A_{IS} the area for the internal standard (N₂). C_{IS} refers to the concentration of N₂ in the total gaseous flow injected into the GC while C_x do the same but for the concentration of CO, CO₂ or O₂. Units for areas and concentrations are mV·s and %, respectively.

For each calibration, ten GC runs were carried out, which yielded ten values for the response factor. Those were then averaged into a unique R_f . The procedure followed during this method implies that the obtained value of the response factor can only be used when the same gas composition is used during catalytic reactions. Thus, if a ratio CO/O₂ corresponding to a λ -value of 2 was present in the gaseous mix used for calibrations, such a R_f could only be applied when calculating A_x in experiments where $\lambda = 2$ was kept constant. This carried obvious limitations onto the research study, reason why a switch to a multiple point calibration method took place.

2.4.4.b Multiple point calibration method

For this method, experimental procedure described above for the case of the single point calibration was also followed. However, in this case, such procedure was repeated for a series of λ -values. In particular, $\lambda = 0.8, 1, 1.5, 2$ and 2.5 were investigated. For each of those λ -values, the obtained value of A_x (average of ten GC runs) was plotted against C_x . Figure 2.9 gives example of the typical outcome of applying the multiple point calibration method.

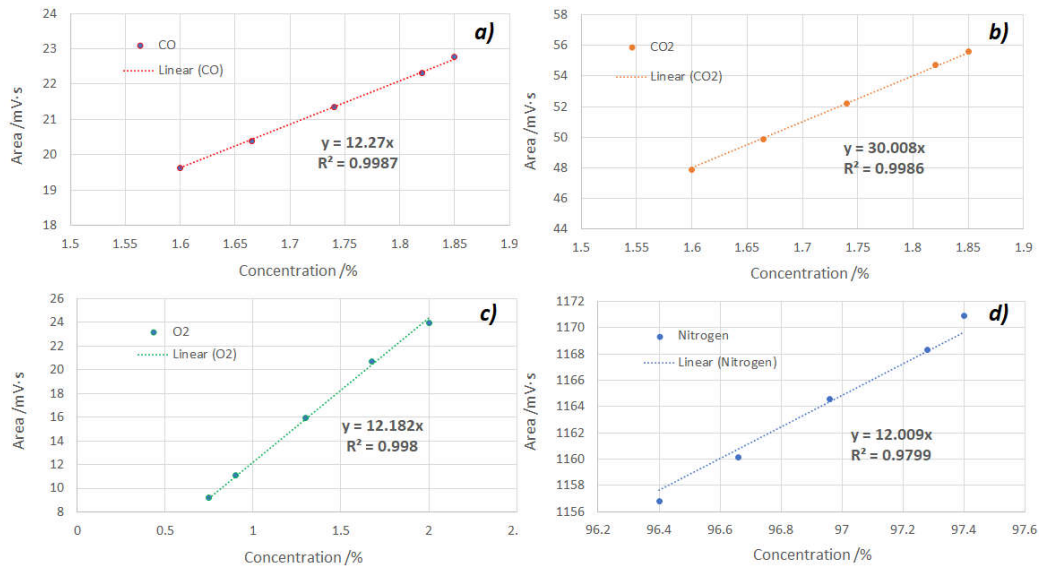


Figure 2.9. GC calibration following the multiple point method for the gases: a) CO, b) CO₂, c) O₂ and d) N₂.

As seen in above figure 2.9, a quite good linear regression is obtained from the A_x versus C_x plots, which gives a slope that is then used as a conversion factor CV_f , which relates A_x and C_x as in Equation 2.16:

$$CV_f = \frac{A_x}{C_x} \quad (2.16)$$

Therefore, CV_f is used instead of R_f (Eq. 2.15) to convert the GC measured areas to its conversion equivalent. This way, since CV_f can be applied to studies at different λ -values, the previously mentioned limitations associated with the single point calibration method are sorted out.

2.5 Temporal Analysis of Products (TAP)

TAP reactor studies were also carried out during the course of this study. The present section is dedicated to set the basics of this kind of systems in a way to introduce that presented and discussed in Chapter 4 and 6. TAP experiments are designed around the idea of using the standard diffusion through a packed bed reactor, comparing the exit flow responses for the reactants and products, and

using the differences to calculate different kinetic parameters. The basic theory behind TAP is outlined in the 1997 paper by John Gleaves¹².

2.5.1 Basics of TAP experiments

The temporal analysis of products technique was first developed by John Gleaves in 1988¹³ as an advance on molecular beam scattering (MBS) experiments (see Figure 2.10). A molecular beam is defined as a beam of particles (atoms, free radicals, molecules or ions) moving at approximately equal velocities, with few collisions occurring between them. During both MBS and TAP experiments, molecular beams are produced by allowing a gas at higher pressure to expand through a small orifice into a container at lower pressure (10^{-7} – 10^{-9} Pa). However, whereas in molecular beam experiments a pulse (or beam) of gas is sent at a single crystal target and the scattering recorded by a mass spectrometer, the TAP experiment consists of sending a pulse (or beam) of gas through a catalyst sample and the flow of gas out the end of the reactor is detected instead.

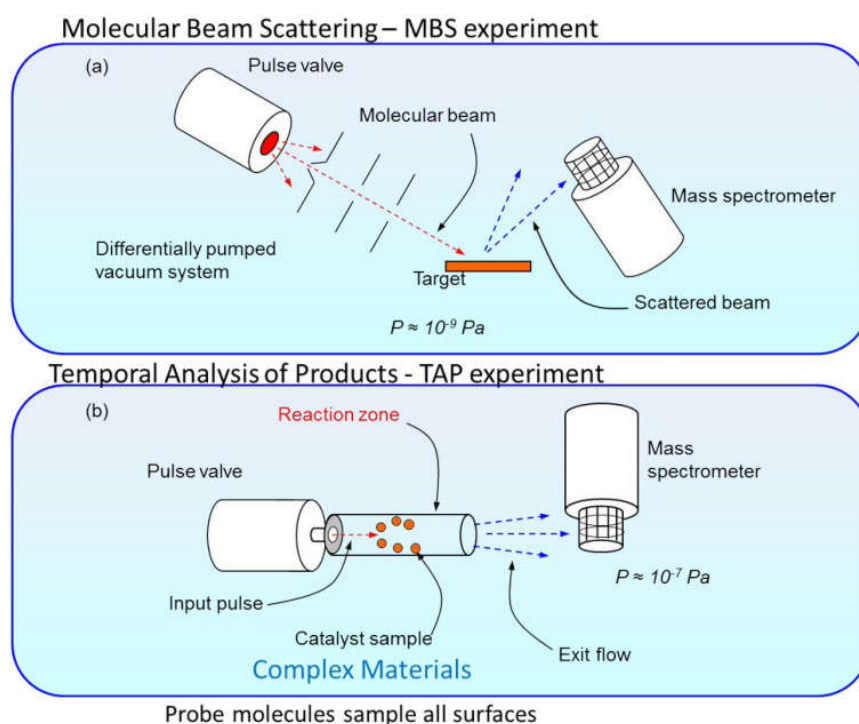
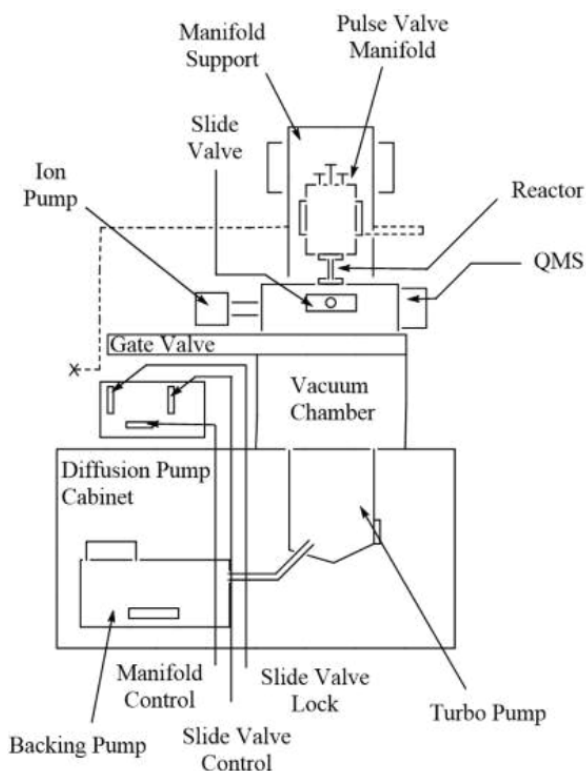


Figure 2.10. Comparison between MBS and TAP experiments¹⁴.

The TAP reactor itself is a highly complicated piece of machinery (Schematic 2.3) which contains multiple moving parts. Nonetheless, the system can be broken down into four main components.



Schematic 2.3. Schematic of a TAP reactor system.

First is the ultra-high vacuum chamber. This is backed out using high throughput vacuum pump such as a turbo molecular pump, or an oil diffusion based pump down to approximately 10^{-7} mbar. The second component is the quadrupole mass spectrometer (QMS), which is housed inside the vacuum chamber and is used to detect the exit flow of the gas out of the reactor. On top of the vacuum chamber, just above the QMS, is the reactor. The reactor is approximately 4 cm in length and it is where the catalyst is packed. The final component is the pulse valve manifold. Inside the manifold the pulse valves are located. These valves control the amount of gas entering and exiting the system. The manifold is the only part of the main system that is not under ultra-high vacuum conditions. As can be seen in Figure 2.11, the reactor is packed with an inert (usually SiC) and in the centre there is a thin layer of the catalyst.

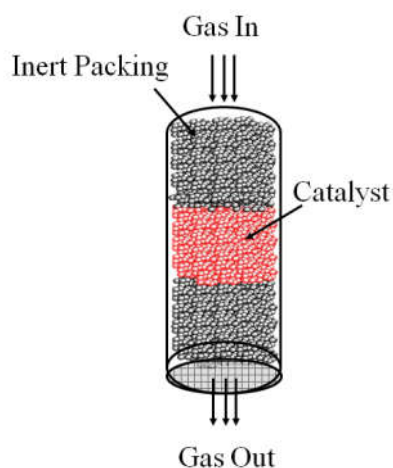


Figure 2.11. Distribution of catalyst and inert zones inside the TAP reactor.

When performing TAP experiments, a voltage is sent to one of the pulse valves causing it to retract. Then, due to the pressure differential between the gas in the pulse valve and the vacuum chamber, the gas flows from the pulse valve through the catalyst packed reactor and into the vacuum chamber, finally getting collected by the QMS. Subsequently, the current is turned off and the pulse valve closes so that the reactor is brought back to ultra-high vacuum conditions. The time the valve is open is very small (approximately 300 μs), which means that the size of the pulse is also very small (around 10^{-15} molecules). These features of the TAP pulses can be seen in Chapter 6, where TAP experimental results are presented.

2.5.2 Knudsen diffusion regime

Due to the small size of TAP pulses, it can be assumed that each individual pulse does not significantly change the structure of the catalyst. Consequently, each pulse brings information of the catalyst at that particular state. This means that TAP techniques allow studying catalytic structures far from the equilibrium, which can be useful when cross interpretation between TAP and flow reactor experiments comes into play. Considering that one of the goals of this research was to see how reliable such cross interpretation can be for the case of CO oxidation, this attribute of the TAP reactor offers a great bonus. In addition to non-equilibrium studies, by following the principle of Chemical Calculus¹⁵, changes can be induced in the catalyst to eventually reaching its steady state conditions.

The theory behind the *Chemical Calculus* is that, even though an individual pulse will not change the state of the catalyst significantly, a long train of sequential pulses can indeed induce such a change. Therefore, by performing sequential pulsing, one can get the catalyst from its initial state to its equilibrium one. But more importantly, since each pulse brings information of the state of the catalyst at that particular moment, every single point during this catalytic state evolution can be viewed.

Due to the small pulse size and the throughput vacuum, the diffusion through the TAP is classified as Knudsen Diffusion. This special case of diffusion occurs when the dimensions of the voids between the catalyst particles are much smaller than the mean free path of the gas molecules involved. The input pulse in a TAP experiment typically contains only 10 nmol of reactant, and the local pressure in the reaction zone may reach around 10^{-3} torr during a pulse. In a packed reactor, the mean free path is around $4000 \mu\text{m}^{16}$, which is significantly larger than the space between particles. As a result, in a packed-bed reactor, molecules collide with particles, but seldom with one another, hence gas-gas interactions can be neglected. Equation 2.17 represents the calculation of the of Knudsen Diffusivity coefficient (D)¹⁷.

$$D = \frac{\epsilon}{t_r} \frac{d_i}{3} \sqrt{\frac{8RT}{\pi M_w}} \quad d_i = \frac{2\epsilon}{3(1-\epsilon)} d_p \quad (2.17)$$

where ϵ is the fractional voidage of the reactor bed, d_p the particle diameter, M_w the molecular weight of the gas and t_r the bed tortuosity.

When a system is governed by Knudsen diffusion, the gas transport throughout the system is defined by the interaction between the gas and the porous medium rather than the molecule-molecule collision frequency. From Figure 2.12 it can be seen that the exit flow purely defined from Knudsen transport is different to the exit flow where adsorption/desorption also exists. In the latter case, the transport of the species through the reactor is still governed by Knudsen diffusion but it is also affected by the interaction between the gas and the surface of the particles in the reactor. As long as the reactor is packed with an inert and the catalyst, it can be said that by removing the well defined Knudsen diffusion, the exit flow can be used to study the interaction between the gas and the catalyst. This principle constitutes

the base that allowed the development of the kinetic theory supporting TAP reactor experiments.

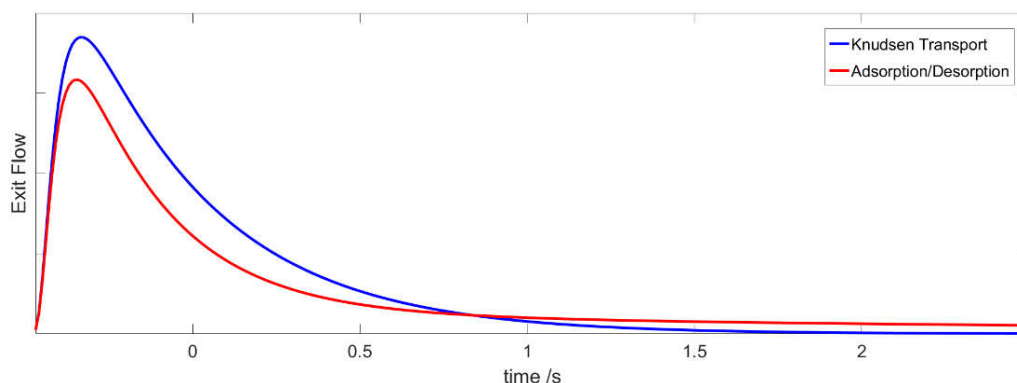


Figure 2.12. Comparison between an exit flow where only Knudsen diffusion occurred and a flow where adsorption/desorption along with diffusion took place.

Regarding the TAP experiments carried out in this study, a similar procedure to that followed by Shekhtman et al.¹⁸ was applied. Accordingly, after the reactor was packed and before performing any pulse experiment, the reactor was pumped out until pressures were equal or below 10^{-6} torr in order to reach Knudsen diffusion conditions.

Along with the Knudsen diffusion, there are a series of assumptions that need to be made:

- Uniformity along both the catalytic zone and the inert zones within the reactor bed.
- Absence of radial concentration gradient in the catalyst bed.
- The temperature in the catalytic bed is completely uniform.

In order to meet the above list of conditions with ease, a Thin Zone TAP Reactor (TZTR)¹⁹ setup was established in the experiments performed for this thesis. The idea behind the TZTR setup is that the thickness of the catalyst zone is considered to be very small when compared to the total length of the reactor (and subsequent inert zones). In fact, in this model the catalyst zone is considered as a boundary between two inert zones rather than its own individual zone. This means that any

deviation in the mean concentration of gas along the axial coordinate of the bed is considered to be very small.

2.5.3 Exit flow as Moments

Another way of viewing the TAP exit flow is as a probability density:

$$\rho = \frac{F_A}{N_{pA}} \quad (2.18)$$

where ρ is the temporal probability density, F_A is the exit flow of gas A measured at the outlet of the reactor, and N_{pA} is the total number of moles of A released from the flow valve. By differentiating ρ with respect to time, the probability of finding a molecule at the reactor exit for a specific time interval can be expressed as:

$$P_t = \int_0^t \rho dt \quad (2.19)$$

where P_t is the probability of finding a molecule between the interval $0 \rightarrow t$. If t is set as ∞ , then P_t at this most basic level can give some information on the reaction mechanism. If $P_\infty = 1$, then all of the gas that entered the reactor is recorded at the exit, which indicates that either no reaction occurred (diffusion only) or a reversible adsorption type of reaction happened. If $P_\infty < 1$, then it can be assumed that some of the gas reacted or irreversibly adsorbed to the catalytic surface. In this case, conversion can be defined as:

$$X = 1 - P_\infty \quad (2.20)$$

The definition of P_∞ introduces the concept of moments, which are very useful in TAP analysis and come defined by Equation 2.21:

$$M_n = \int_0^\infty t^n F(t) dt \quad (2.21)$$

where n is the moment number and $F(t)$ is the exit flow.

The physicochemical interpretation of the TAP moments can be gleaned from their dimensions. For the case of the zeroth moment (M_0), its dimension is *moles*. Thus,

M_0 determines the total number of gas molecules that passes through a given reactor cross-section. Normalised to the number of injected moles, the zeroth moment is equivalent to P_{∞} , hence Equation 2.20 may also take the expression below:

$$X = 1 - M_0 \quad (2.22)$$

The first moment (M_1) has the dimension *moles* · *s* and is the number of molecules multiplied by the time. This means that M_1 can be used to determine the residence time

(t_{res}) of the gas in the reactor at a given point by normalising it to the zeroth moment:

$$t_{res} = \frac{M_1}{M_0} \quad (2.23)$$

t_{res} can be defined as the average delay in the pulse as it travels through the reactor.

The final moment that is commonly used is the second moment (M_2) which is the exit flow multiplied by time squared and has the dimension *moles* · *s*². The actual physical meaning of the second moment is slightly more complex as it relates to the relative amount of time the gas spends in the reactor when compared to the residence time and it is correlated to processes such as desorption.

According to the moment definition (Eq. 2.21), M_0 corresponds to the area underneath the curve $F(t)$, while M_1 and M_2 are the integrands of the curves $F(t) \cdot s$ and $F(t) \cdot s^2$, respectively. This is illustrated in Figure 2.13, which clearly shows how these integrands are shifted to longer times while increasing the moment number. Consequently, the higher the degree of the moment, the greater the contribution from slow processes that show up in the curve tail or the slow portion of the curve.

For the purpose of the TAP studies presented in this thesis, the parameter of interest is the zeroth moment, M_0 .

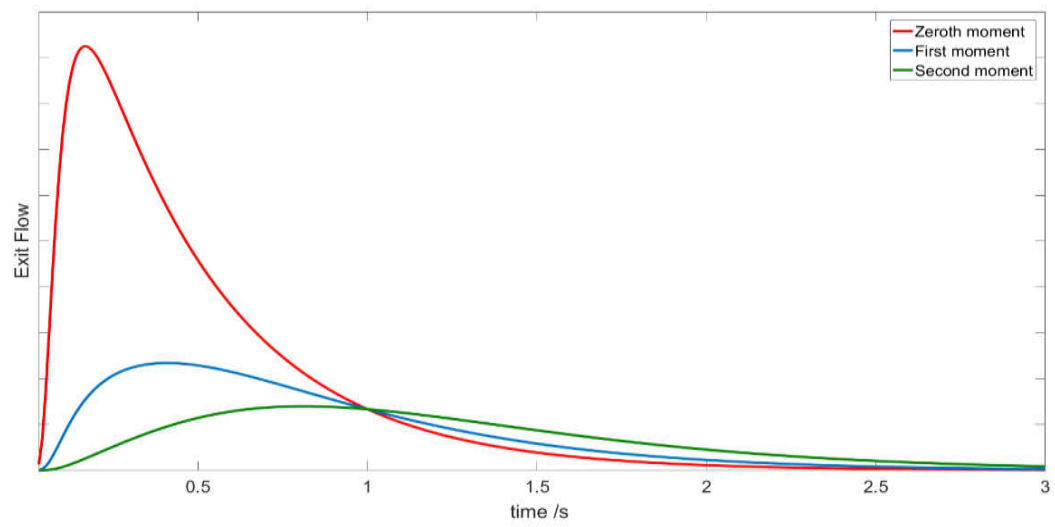


Figure 2.13. Integrands of the zeroth, first and second moments for a simulated Knudsen exit flow.

References

- 1 B. M. Reddy, G. Thrimurthulu, L. Katta, Y. Yamada and S. E. Park, *J. Phys. Chem. C*, 2009, **113**, 15882–15890.
- 2 L. Katta, P. Sudarsanam, B. Mallesham and B. M. Reddy, *Catal. Sci. Technol.*, 2012, **2**, 995–1004.
- 3 P. Sudarsanam, B. Mallesham, P. S. Reddy, D. Großmann, W. Grünert and B. M. Reddy, *Appl. Catal. B*, 2014, **144**, 900–908.
- 4 A. M. Venezia, G. Pantaleo, A. Longo, G. Di Carlo, M. P. Casaletto, F. L. Liotta and G. Deganello, *J. Phys. Chem. B*, 2005, **109**, 2821–2827.
- 5 W. Yan, B. Chen, S. M. Mahurin, V. Schwartz, D. R. Mullins, A. R. Lupini, S. J. Pennycook, S. Dai and S. H. Overbury, *J. Phys. Chem. B*, 2005, **109**, 10676–10685.
- 6 L. F. Liotta, G. Di Carlo, G. Pantaleo and A. M. Venezia, *Catal. Today*, 2010, **158**, 56–62.
- 7 M. N. Khan and J. Bashir, *J. Mod. Phys.*, 2011, **02**, 962–965.
- 8 C. Karunakaran, P. Anilkumar and P. Gomathisankar, *Chem. Cent. J.*, 2011, **5**, 31.
- 9 C. Arble, M. Jia and J. T. Newberg, *Surf. Sci. Rep.*, 2018, **73**, 37–57.
- 10 T. Davran-candan, S. T. Tezcanlı and R. Yildırım, *Catcom*, 2011, **12**, 1149–1152.
- 11 U.S Department of the Interior, Bureau of Mines, 2001, **443**, 22.
- 12 J. T. Gleaves, G. S. Yablonskii, P. Phanawadee and Y. Schuurman, *Appl. Catal. A Gen.*, 1997, **160**, 55–88.
- 13 J. T. Gleaves, J. R. Ebner and T. C. Kuechler, *Catal. Rev. Sci. Eng.*, 1988, **30**, 49-116.
- 14 J. T. Gleaves, G. Yablonsky, X. Zheng, R. Fushimi and P. L. Mills, *J. Mol. Catal.*

- A Chem.*, 2010, **315**, 108–134.
- 15 G. Marin and G. S. Yablonsky, *Kinetics of chemical reactions*, John Wiley & Sons, 2011.
- 16 Z. I. Önsan and A. K. Avci, *Multiphase Catalytic Reactors*, John Wiley & Sons, Inc., Hoboken, NJ, USA, 2016.
- 17 J. R. Welty, C. E. Wicks, G. Rorrer and R. E. Wilson, *Fundamentals of momentum, heat, and mass transfer*, John Wiley & Sons, 2009.
- 18 S. O. Shekhtman, A. Goguet, R. Burch, C. Hardacre and N. Maguire, *J. Catal.*, 2008, **253**, 303–311.
- 19 S. O. Shekhtman, G. S. Yablonsky, S. Chen and J. T. Gleaves, *Chem. Eng. Sci.*, 1999, **54**, 4371–4378.

3 | Development and Application of the Flow Reactor Numerical Analysis Software

This chapter aims to provide detail of the process followed until the final version of our flow reactor numerical analysis software was fully operating. In the next sections, such process has been broken up so the different conforming parts of this software are disclosed in a clearer way.

Three main code scripts form our flow reactor software, described and discussed below in Sections 3.1, 3.2 and 3.3. These, respectively, correspond to the code responsible for the actual automation of the CO oxidation reaction, the code responsible for the analysis and process of raw data and the graphical user interface (GUI) that make easier the interaction user-code.

3.1 Development of Software responsible for the Automation of Reactions

The first step towards the software design was the identification and definition of both physical and chemical components within our CO oxidation rig. Understanding those as the ones necessary to run the CO oxidation reaction and that could be implemented within our software. Starting with the physical components, these are the instruments that are going to be synced for the automation of the reaction to take place. Considering the whole list of components playing a role in the designed CO oxidation rig (see Chapter 2, Section 2.4.1), there are four instruments to interface: water bath, thermocouple, GC and computer. Among them, the computer is the one which controls and sync the entire system, role performed by a code written in a Matlab environment. Therefore, such a code must firstly detect, connect and provide the necessary means to sync each of the four devices. This is the starting point from which the rest of actions can be implemented. The next subsections follow the flow of steps given towards the design of this part of the software.

3.1.1 Identifying and connecting physical devices within the rig

As mentioned above, first action in this software is the identification of the devices that are going to sync with each other and that will actively participate during the course of the reaction experimental tests. Nonetheless, the GC used in our rig did not provide the necessary means for its remote control. Thus, a different approach was implemented to include it within the synced system (subsection 3.1.3). This implied that, when it comes to software coding, GC was not considered yet. Therefore, as it is shown in Listing 3.1, communications with thermocouple and water bath were firstly set.

The water bath comes with a series of executing files which are loaded using the `loadlibrary` function. The instructions inside these files must be converted into a code that Matlab can read. For that, a C/C++ compiler (MinGW-w64) is run. Right after this, the function `TC_ON_faster` is called (Listing 3.1, line 11). This function was coded to use the instructions previously gathered from the executing files so that, every time it is called, temperature measured by the thermocouple is read and gets stored in the function output, called 'handle' (see Section 2.3.1, where Listing 2.1 was discussed).

Communications with the water bath are set differently. No executables have to be installed in the computer or compiled. Instead, the code has to identify the port the bath is connected to and define its type. This is done by making use of the function `instrfind` (line 15, Listing 3.1). Finally, our port object (water bath) is named as 'obj1' and a carriage return followed by a line feed terminator is set.

```

7  %% Communication with thermocouple
8  - setenv('MW_MINGW64_LOC', 'C:\TDM-GCC-64')
9  - mex -setup
10 - loadlibrary('C:\Program Files (x86)\Pico Technology\SDK\lib\usbtc08.dll', 'C:\Program Files (x86)\Pico Technology\SDK\lib\usbtc08.h');
11 - handle = TC_ON_faster('K', 'C:\Program Files (x86)\Pico Technology\SDK\lib');
12
13 %% Communication with the water bath
14 % Finds a serial port object.
15 - obj1 = instrfind('Type', 'serial', 'Port', 'COM4', 'Tag', '');
16 % Creates the serial port object if it does not exist
17 % Otherwise use the object that was found.
18 - if isempty(obj1)
19 -     obj1 = serial('COM4');
20 - else
21 -     fclose(obj1);
22 -     obj1 = obj1(1);
23 - end
24 % Connects to instrument object, obj1.
25 - fopen(obj1);
26 % Configures instrument object, obj1.
27 - set(obj1, 'Terminator', 'CR/LF');

```

Listing 3.1. Snippet of script used to identify thermocouple and water bath along with executing files.

3.1.2 Creation of Matlab environment for upcoming reaction

After device identification, experimental conditions under which the user want the reaction to be run must be set. The transfer of commands from user to Matlab code is facilitated by the GUI. As it will be discussed in detail in subsection 3.3, the information collected by the GUI code can be grabbed when demanded by a function. The code that is object of the present discussion, the one responsible for the automation of the reaction, is contained in a function called `Tcontrol`. Firstly, this function grabs the set of experimental conditions collected by the GUI. In particular, such conditions relate to initial and final temperatures that define the range being studied, the temperature ramp and the time each tested temperature is kept constant (see Figure 3.1). Also, after a series of experiments, the need of introducing an initial period of time, during which the reactant gaseous mixture was flowed over the catalytic sample before starting the catalytic test, was evidenced. This is exemplified in Figures 3.2 and 3.3, where a significant initial deactivation, normally over the first 1-2 hours from the time a catalyst was put on-steam (0.5% CO/air mixture), is observed. In order to represent steady-state conditions, starting to test the performance of a catalyst in a non-equilibrium CO coverage must be avoided¹. Otherwise, results where a change in temperature does not seem to correlate with a change in conversion, as those shown in Figure 3.2, could be obtained. Thus, the software allows the user to set a period of time while the

catalytic sample is kept on-stream before starting the test (ramping up in temperature, etc). Figure 3.3 shows a typical example of the data obtained when that CO coverage time was introduced in the code.

The set of experimental conditions referred to above are grabbed from the GUI and defined within the `TCONTROL` function in lines 34-42 of the script snippet shown in Listing 3.2. Along with that, in the following lines of the same listing, empty arrays are created. This way, once the experiment starts, collected parameters are stored in the respective array. Then, the code is interrupted for 25 seconds. This is related to the already commented impossibility to directly communicate with the GC via Matlab. Hence, a series of concatenated runs have to be pre-set manually before starting the automated reaction. The GC takes several seconds to begin with such a series. On the other hand, the code is extremely quick to run. Therefore, to avoid errors due to the information from the GC not being ready yet and to make the syncing process feasible, a minimal interruption was coded. The interactive process carried out during a standard automated reaction is fully described in the subsection below.

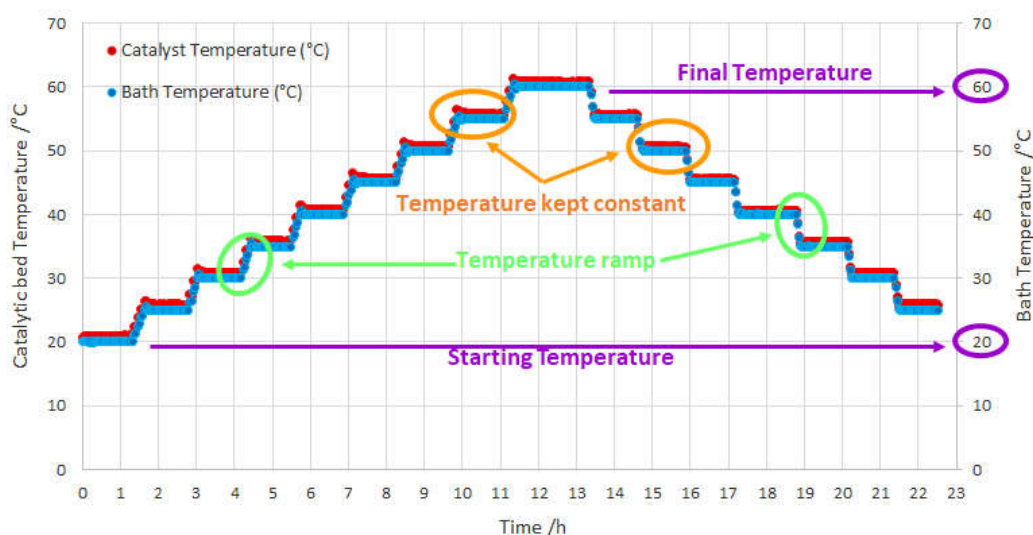


Figure 3.1. Set of experimental conditions that define the reaction to be run automatically.

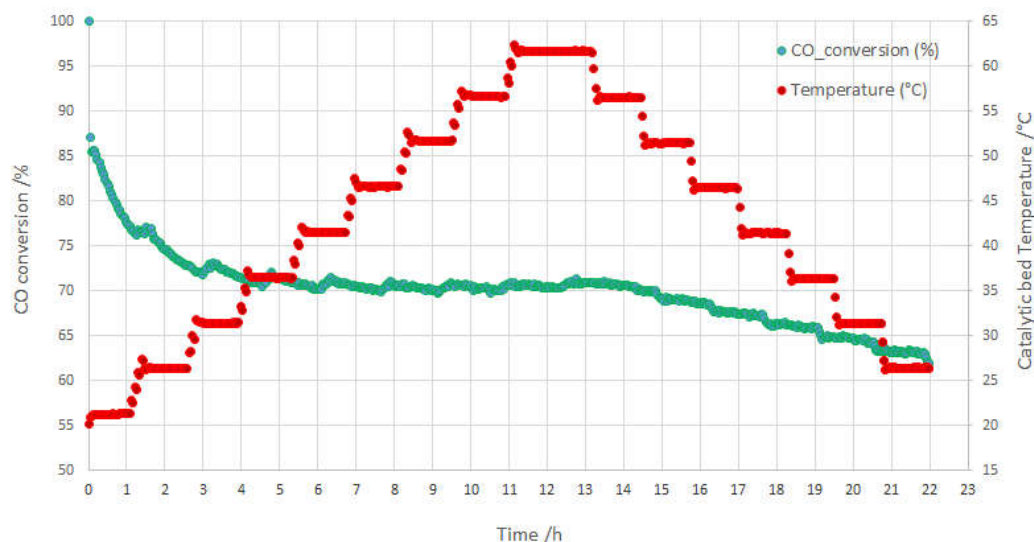


Figure 3.2. Experimentally obtained CO conversion temperature dependence over time when flowing 0.5% CO in air over a sample consisting of 25 mg of 2.5% Au/CeO₂. The temperature test was started straight away, i.e. reactants were flowed over the sample for an initial period of time at room temperature.

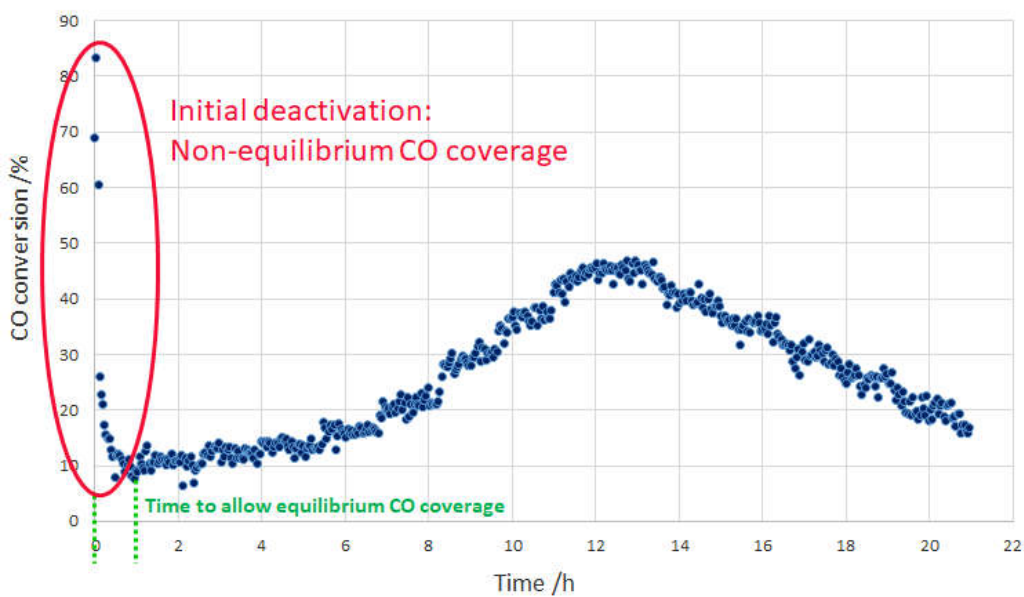


Figure 3.3. Initial catalytic deactivation observed during the CO coverage of the catalytic surface. 0.5% CO in air was flowed over 25 mg of 1% Au/CeO₂ for 1 hour at room temperature to assure an equilibrium of the surface ahead to the conversion temperature dependence test. After that 1 h period, a ramp up/down of 5 °C was performed.

```

29 -   clc;      % Clear the command window.
30 -   workspace; % Make sure the workspace panel is showing.
31 -   format longg;
32 -   format compact;
33 -   %% Sets the time
34 -   run_time = str_Runtime*60;
35 -   COcovering_time = str_COcoveringtime*60;
36 -   %% Sets up temperature range
37 -   Starting_Temp = Starting_temp;
38 -   Final_Temp = Final_temp;
39 -   Interval = Interval_Temp;
40 -   Temp_Array = Starting_Temp:Interval:Final_Temp;
41 -   interval_Time = str_Time*60;
42 -   intervalo = interval_Time;
43 -   A = 2;
44 -   C = length(Temp_Array);
45 -   B = 0;
46 -   d = 0;
47 -   m = 2;
48 -   %% Approximates the number of files
49 -   q = interval_Time/run_time + 5;
50 -   num_files = 2*(C*q+200); % 200 is the extra for the unknown points to get desired Temperature
51 -   num_files_ini = num_files/2;
52 -   %% Sets up a number of data array's (variables)
53 -   Time = zeros(num_files,1);
54 -   Temp = zeros(num_files,1);
55 -   Temp_A = zeros(num_files,1);
56 -   Set_Temp = zeros(num_files,1);
57 -   BedTemp = zeros(num_files,1);
58 -   Time_ini = zeros(num_files_ini,1);
59 -   Temp_ini = zeros(num_files_ini,1);
60 -   Set_Temp_ini = zeros(num_files_ini,1);
61 -   BedTemp_ini = zeros(num_files_ini,1);
62 -
63 -   %% Giving time for the GC to start and create folder in computer
64 -   wait1 = 25;
65 -   pause(wait1)

```

Listing 3.2. Script used to grab experimental conditions set by user in GUI and create arrays where measured parameters are going to be stored during the course of the reaction.

3.1.3 Interactive process between the physical devices within the rig and the software during the automated reaction

As already mentioned, the GC used in our CO oxidation rig did not allow command-response communications, thus a direct remote control of the instrument via Matlab coding was not an available option. Therefore, a different strategy needed to be implemented. At a first step, a series of GC runs were timed and averaged. This method implied considering the time taken during the entire process from injection to completed analysis of the reactor outlet gases as a constant. Specifically, this averaged time gave a value of 2 minutes. Hence, such a time was included in the code in a way such that temperature readings were taken and new instructions were sent to the water bath every 2 minutes. Unfortunately, the results

of this first attempt did not outcome with a good sync temperature-GC data, as it can be observed in Figure 3.4. Consequently, another syncing method was thought.

Listing 3.3 below shows the key part of the code responsible for including the GC within the synced triangle 'bath-thermocouple-GC'. Once the GC starts to run, a folder is created in which subfolders will be created every time a new run begins. During each run, different files are created and saved inside these subfolders. Finally, once each run finishes, the information gathered from the analysis of the reactor outlet gases is saved in a file. This is read afterwards by the part of the code described in Section 3.2.

The function `uigetdir` opens a dialog box asking the user to select the folder where the above mentioned subfolders will be saved (line 70, Listing 3.3). Such a folder is named as 'topLevelFolder'. However, as seen in Listing 3.3, `uigetdir` is not used once but twice. The second time, line 75 in the same listing, the directory of a recovery folder is asked for and it is named as 'recoveryFolder'. This 'recoveryFolder' is manually created inside our 'topLevelFolder' and its purpose is the recovery of all data stored in Matlab in case the GC stops functioning correctly during the reaction (this is a not uncommon occurrence). If this happens, the user just needs to create an empty folder inside 'recoveryFolder'. The code will then notice the new folder and it will securely save all data, make it visual and recoverable in the Matlab workplace and therefore allowing its future analysis. It is important to point out here that, in case a run is suddenly stopped, all data will be lost unless an approach like this, where it is transferred to the workplace, is developed. Along with the start of the GC, the creation of the 'recoveryFolder' is the only manual action required for the entire reaction process to run automatically.

The last lines of Listing 3.3 show how the functions `dir` and `numel` (lines 80 and 83) are used to count the number of files and folders inside 'topLevelFolder'. This is the essential part that will make the running code, our `Tcontrol` function, know when the GC finishes a run and starts the next one (new subfolder created inside 'topLevelFolder'). As it will be discussed further below, this triggers the initialization of another automated controlled temperature-time loop. Scheme 3.1 exemplifies

in a more visual way how the syncing method described above works, while Figure 3.5 shows the final result of implementing such a method.

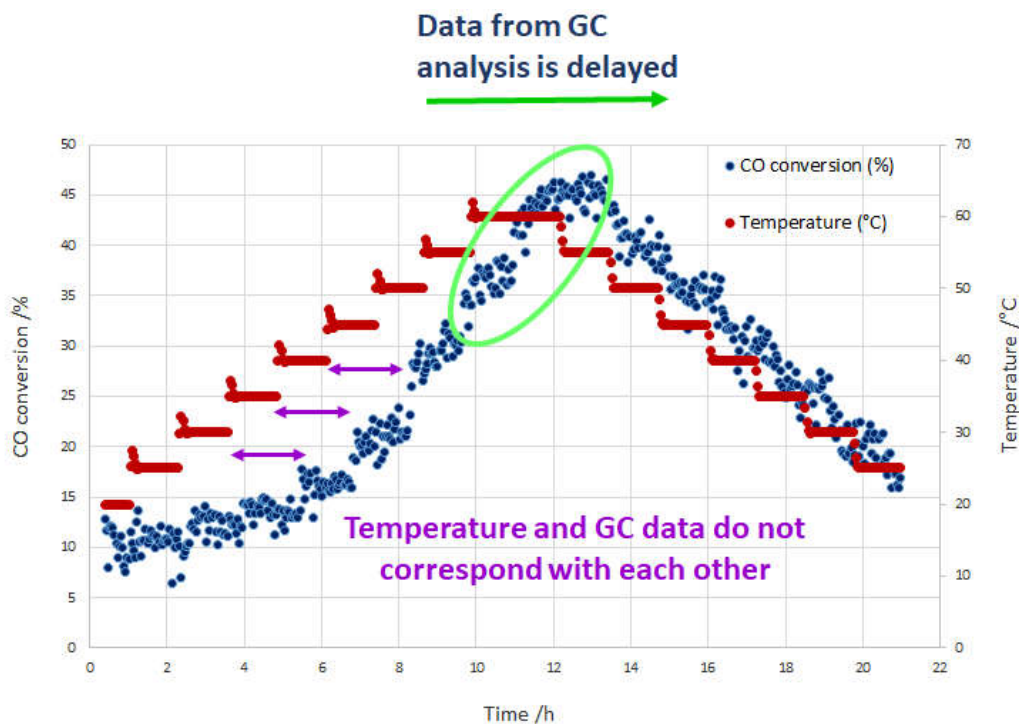


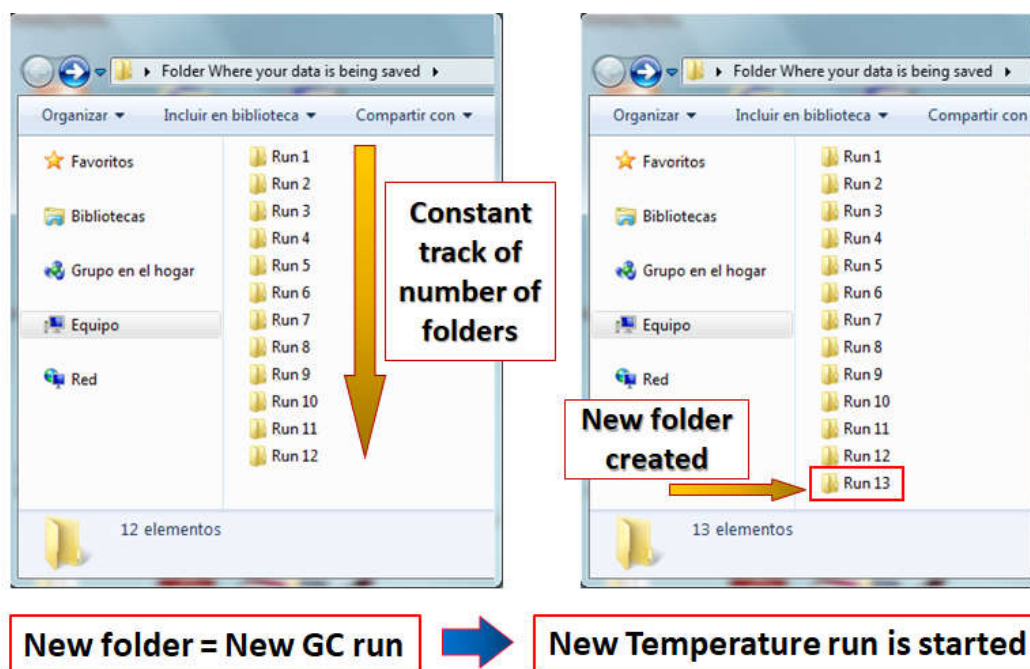
Figure 3.4. Example of the experimental outcome obtained before the implementation of the syncing method showed in Listing 3.3.

```

67 | %% Defines a starting folder.
68 | start_path = fullfile('C:\');
69 | %% Asks user to confirm or change.
70 | topLevelFolder = uigetdir(start_path, 'Select the folder where your GC data is stored');
71 | if topLevelFolder == 0
72 |     return;
73 | end
74 | %% Defines SOS recovery folder.
75 | recoveryFolder = uigetdir(topLevelFolder, 'Select the empty folder for the SOS recovery');
76 | if topLevelFolder == 0
77 |     return;
78 | end
79 | %% Gets list of all immediate subfolders
80 | directory = dir(topLevelFolder);
81 | all_files = directory;
82 | all_dir = all_files([all_files(:).isdir]);
83 | num_dir = numel(all_dir)-2; % all_dir be a structure. First two will give . and .. So minus 2

```

Listing 3.3. Part of the `Tcontrol` function code responsible for including the GC within the synced system.



Scheme 3.1. Exemplification scheme of the syncing method implemented by the part of the code showed in Listing 3.3.

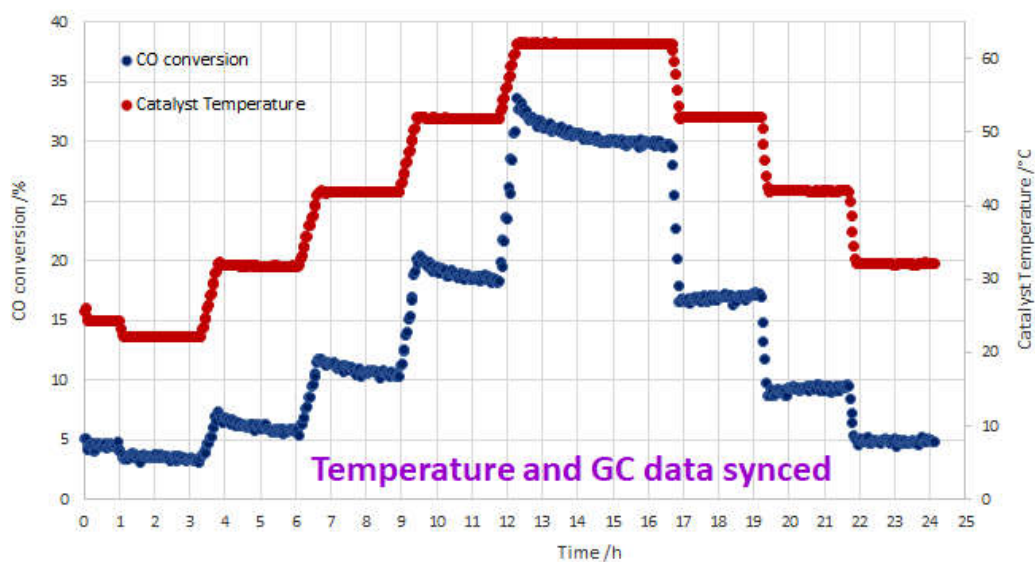


Figure 3.5. Example of the experimental outcome obtained once the syncing method showed in Listing 3.3 was implemented in the code.

Once the set of experimental conditions has been grabbed from the GUI and defined within the code, as the means for the GC getting included in the syncing process established, the active command-response series of actions that keeps the reaction going under such a set of conditions can be initiated. Communications with the water bath constitute the core of this process. Every new series of actions gets triggered by the start of a new GC run and every reading of the water bath temperature is coupled with a thermocouple reading of the catalytic bed. The Matlab command `query` is used when sending instructions to the bath. Those instructions have different nature, namely, switching on/off the instrument (i/ii), reading the temperature of the water where the reactor is immersed (iii) or setting the next temperature this water must be heated up/cooled down to (iv). Accordingly, the arguments `'SO 1'` (i), `'SO 0'` (ii), `'RT'` (iii) and `'RS'` (iv) are used along the code script. Then, `sscanf` and the specifier `'%f'` are used to convert the read temperature data to floating-point number format. Finally, the command `fprintf` leaves track of the instruction being given to the bath at different stages during the run of the code. This way, short information messages are displayed in the Matlab command window so that the user gets some feedback. These three commands, `query`, `sscanf` and `fprintf`, are the essential Matlab commands that are being used during the course of the automated reaction, strategically played along the code, as they can be spotted out in Listings 3.4-3.9.

Listing 3.4 shows the basic foundations of the command-response mechanism with the water bath. In particular, this snippet of the script corresponds to the first steps made after turning on the bath. Hence, this is the code responsible of all actions performed during the initial surface CO coverage period of time mentioned earlier. These actions are based on comparisons between the water bath temperature and the set temperature coupled with precise timing. Thus, according to Listing 3.4, the bath is turned on and it is asked what the temperature of the water contained in it is. Time zero, i.e. time at the start, is taken. From this point, a loop is opened. Such a loop is not going to be closed until a series of conditions are fulfilled. These conditions must be followed in a certain order, which has also been coded. Accordingly, the actions instructed by the code follow the flow showed below:

1. Time: while time is less than that the user set for the equilibrium surface CO coverage to be reached, the bath will not heat or cool the water, therefore it stays at room temperature.

2. If time indicated in '1' is completed, there are 2 possibilities:

a) Set temperature, i.e. initial temperature set in the GUI by the user, is higher than that of the water bath by more than 1°C: in this case orders are sent to the bath to heat the water to increase its temperature in 1°C. The code will wait until the current GC run is finished before checking and comparing temperatures again.

b) Set and water bath temperatures differ with each other in less than 1°C: in this case, orders are sent to the bath in order to keep that temperature, i.e. not heating or cooling. Necessary conditions set for this stage of the automated reaction have been fulfilled, therefore the loop is closed and the next lines in the code can be run now.

Comparisons performed in a) and b) belong to the strategy developed to avoid temperature overshoots experienced when normally using our bath. This overshoot issue is exemplified in the experimental data plotted in Figure 3.6. As observed in this figure, every time the water bath was set to increase the temperature, a systematic overheating followed by a cooling down was happening. This phenomenon is usual when heating instruments are involved and it is simply due to the heater overestimation of the power needed to reach a certain temperature. The implementation of temperature comparisons and derived actions in a) and b), where the code forces the bath into a lower heating power, were included in several parts of the `Tcontrol` function. Accordingly, not only the CO coverage phase discussed above (Listing 3.4) but the ramp up and ramp down stages include it, as it will be seen in subsection 3.1.4. Figure 3.7 presents the result of implementing this strategy in the code.

```

85  %% Sets up starting temperature on the water bath
86  Temperature = ['ss', ' ', num2str(Starting_Temp)];
87  data1 = query(obj1, 'RT');
88  temp_ini = sscanf(data1, '%f');
89  temp_ini = ['ss', ' ', num2str(temp_ini)];
90  data2 = query(obj1, temp_ini);
91  data1 = query(obj1, 'SO 1');
92  d_ini = 1;
93  n_ini=1;
94  time_start = now;
95  while d_ini > 0
96  time_now = (now-time_start)*(24*60*60)
97  data1 = query(obj1, 'RT');
98  temp_ini = sscanf(data1, '%f');
99  fprintf('Temperature: %f\n', temp_ini);
100 Temp_ini(n_ini) = temp_ini;
101 Time_ini(n_ini) = time_now;
102 if Time_ini(n_ini) <= COcovering_time
103     Set_Temp_ini(n_ini)= temp_ini;
104 else
105     if Starting_Temp > (temp_ini + 1)
106         temp_ini = temp_ini +1;
107         temp_ini = ['ss', ' ', num2str(temp_ini)];
108         data2 = query(obj1, temp_ini);
109     else
110         data2 = query(obj1, Temperature);
111         d_ini = 0;
112         d = 1;
113     end
114     data3 = query(obj1, 'RS');
115     fprintf('set point set to %s\n', data3)
116     Set_Temp_ini(n_ini)= sscanf(data3, '%f');
117 end

```

Listing 3.4. Part of the code responsible of the automated actions carried out during the initial surface CO coverage.

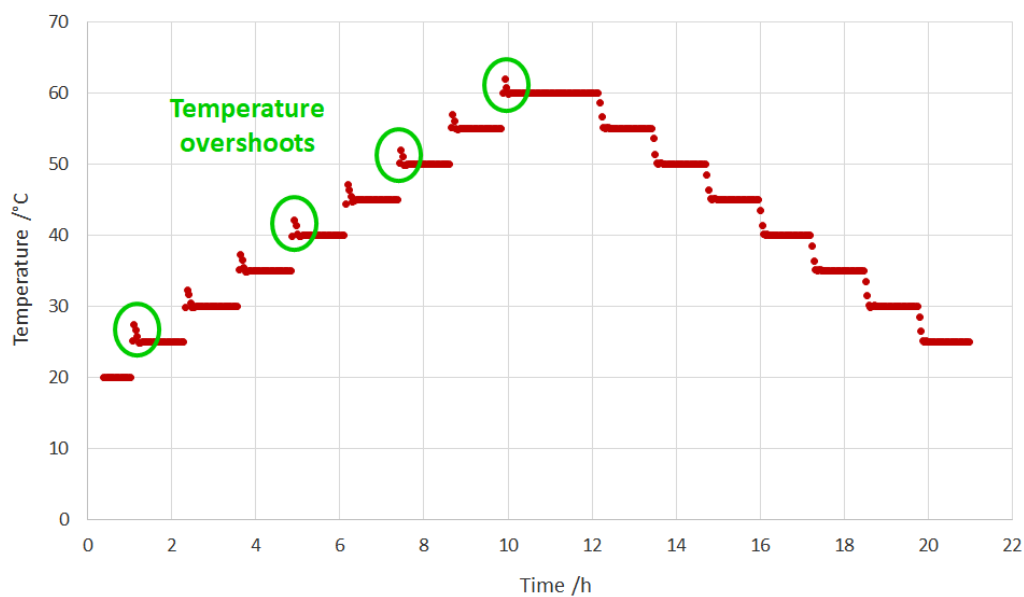


Figure 3.6. Example of the water bath temperature overshoot experienced before the implementation of the code showed in Listing 3.4.



Figure 3.7. Experimental example of the water bath temperature after the implementation of the code showed in Listing 3.4.

After a temperature loop is closed, i.e. after the water bath temperature satisfy the conditions set in that loop, the function `TC_query` is called. This function picks up the temperature measured in the catalytic bed by the thermocouple at that time. This is done by reading the value stored in the output of the `TC_ON_faster` function (called 'handle', see subsection 3.1.1), and making necessary conversions in the value format so that it agrees with the ones used in our `Tcontrol` function. Therefore, every time a loop is closed, a water bath temperature is stored in the respective array created for this purpose (discussed in subsection 3.1.2) and so it is done for case of the catalytic bed. Consequently, temperatures measured in both places can be coupled and matched along with their specific timing.

The last step to puzzle out a perfect synced system comes with the introduction of the GC. At this point, the part of code previously discussed for Listing 3.3 is used again and every time temperatures are collected. As explained before, running those code lines lets the `Tcontrol` function know when the GC finishes a run and starts the next one. Thus, the code starts another temperature loop and the process is repeated again. Ultimately, when the reaction is ended, temperatures and times collected in their respective Matlab arrays will match with the correct GC file, thus with the analysis of the reactor outlet gases at the respective time for those temperatures.

The part of the code responsible for the above process of collecting thermocouple measured temperatures and syncing with the GC run are showed in Listing 3.5 below.

```

118 - %% For each bath temperature saved, picking up respective temperature of the catalytic bed
119 - TC_Temp = TC_query(handle);
120 - BedTemp_ini(n_ini) = TC_Temp(1,1);
121 -
122 - %% Syncing bath with GC, starting next temperature loop when GC starts next run
123 - syncing = 1; % If equals 1, GC has not finished with the current run yet
124 - wait2 = 4;
125 - while syncing > 0
126 - clear directory
127 - directory = dir(topLevelFolder);
128 - all_files = directory;
129 - all_dir = all_files([all_files(:).isdir]);
130 - num_dir2 = numel(all_dir)-2; % all_dir be a structure. First two will give '.' and '..'. Thus, minus 2
131 - % In case the GC gets stuck
132 - GC_stuck_directory = dir(recoveryFolder);
133 - stuck_files = GC_stuck_directory;
134 - stuck_dir = stuck_files([stuck_files(:).isdir]);
135 - stuck_num_dir2 = numel(stuck_dir)-2;
136 -
137 - if stuck_num_dir2 == 0 % GC is running fine
138 - if num_dir2 > num_dir
139 - num_dir = num_dir2;
140 - syncing = 0;
141 - else
142 - pause(wait2); % GC has not finished with the current run yet
143 - end
144 - else % GC got stuck, shutting down process and recovery of data stored till that moment
145 - syncing = 0;
146 - d_ini = 0;
147 - d = 0;
148 - end
149 - end
150 - n_ini = n_ini + 1;
151 - end

```

Listing 3.5. Snippet of the code responsible for syncing thermocouple measured temperatures and GC analysis files with water bath temperatures.

3.1.4 Automatic ‘modification on demand’ of water bath heating/cooling performance

This subsection is focused on detailing the interaction Matlab code-water bath that defines the automative run of a reaction. As done during the CO surface coverage stage, previously discussed when Listing 3.4 was referred, temperature is read from bath and instructions are sent to it when such a temperature must be changed. Also, as mentioned before when discussing Listing 3.5, thermocouple temperature is collected and GC data is synced after each loop is closed. However, there are specific circumstances across the course of a reaction that have to be considered in the code in order to keep the reaction under the experimental conditions set by the user. Also, since the performance of both a temperature ramp up and ramp down were required, additional lines need to be included in our code.

Firstly, once the time set for the initial CO coverage of the surface is completed, bath temperatures and time are read. The definition of a so-called 'Time_elapsed' is made. As seen in Listing 3.6, this 'Time_elapsed' is defined as the extraction of a 'Time_Start' from a 'time_now'. 'time_now' is the time just before an order is sent to the water bath. 'Time_Start' is the last time stored in our time array, i.e. the time when a set temperature was reached and stabilised in the water bath. Therefore, ('time_now' - 'Time_Start') gives the span of time such set temperature was kept constant for. This is an important key of the code, since it will determine if an increase/decrease is required in the reaction temperature at any time during our experiment. According to that stated before, for a temperature to be considered as kept constant for a period of time, it should have been previously stabilised. Thus, part to the code must reflect such stabilisation. This is presented in Listing 3.7, where the `Tcontrol` function makes some checks to verify if fluctuations in the water bath temperature are still happening. These checks consist of a series of comparisons. In particular, when a new temperature is set in the bath by the code, this code will allow the GC to do five consecutive runs and respective temperatures will be stored before carrying out any further action. After these five runs, the five collected temperatures as compared with each other. If they are all the same, stabilisation has already been achieved and lines with new instructions are going to be read and performed. Otherwise, if those five temperatures are not the same, 'Time_elapsed' is reset and the process is repeated until the condition for temperature stabilisation is fulfilled.

```

152 | %% Starts reaction temperature-time test
153 | n = 1;
154 | nointerval = 0;
155 | while d > 0 % If complete temperature ramp up and ramp down processes are not finished yet
156 |     if nointerval == 1
157 |         interval_Time = run_time;
158 |         fprintf('checked file')
159 |         time_now = (now-time_start)*(24*60*60)
160 |         % Communicating with instrument object, obj1.
161 |         fprintf ('reading Temperature');
162 |         datal =query(obj1, 'RT');
163 |         templ = sscanf(datal, '%f');
164 |         fprintf('Temperature bath: %f\n',templ);
165 |         Temp(n) = templ;
166 |         Time(n) = time_now;
167 |         % Checks temperature and compares
168 |         Time_Start = Time(n - B);
169 |         Time_elapsed = (time_now - Time_Start); % Time_elapsed gives the time spent at a constant temperature
170 |         datal =query(obj1, 'RT');
171 |         templ = sscanf(datal, '%f');
172 |         Temp_A(n)=templ;

```

Listing 3.6. Code lines within the temperature loop where times elapsed are defined.

```

214 %Checks temp and compares
215 - if n == 1 || n == 2 || n == 3 || n == 4 || n == 5
216 -     fprintf('first five runs')
217 - else
218 -     if strcmp(num2str(Temp(n)), num2str(temp1)) && strcmp(num2str(Temp(n-1)), num2str(temp1)) && strcmp(num2str(Temp(n-2)), ...
219 -         (num2str(temp1)) && strcmp(num2str(Temp(n-3)), num2str(temp1)) && strcmp(num2str(Temp(n-4)), num2str(temp1))
220
221 -         Time_Start = Time(n - B);
222 -         Time_elapsed = (time_now - Time_Start);
223 -         data1 = query(obj1, 'RT');
224 -         temp1 = sscanf(data1, '%f');
225 -         Temp A(n)=temp1;

```

Listing 3.7. Snippet of the script where temperature stabilisation is checked.

Once bath temperature has been stabilised at the set point, different orders will be sent to the bath depending on what the current temperature of the water at that moment is. A series of conditions are coded in a way that, depending of which condition such temperature ticks, different actions are going to be carried out. These conditions, which correspond to the code presented in Listing 3.8, are:

1. If set temperature has been kept constant for the required time: if the set temperature was kept constant for the period of time set by the user in the GUI, two main pathways are differenced:

- a) Temperature ramp up: if the higher temperature, which was set in the GUI by the user, has not still been reached and tested, the experiment is still in the ramp up stage. Therefore, orders are sent to the bath to heat the water in 1°C (overshoot strategy discussed in subsection 3.1.3).

- b) Temperature ramp down: if the higher temperature set in the GUI has already been reached and tested, the experiment is in the ramp down stage. Hence, the bath is instructed to cool down the water to the next set temperature. To do so, the code goes backwards within the array where set temperatures are stored, picking up a lower temperature that, at the same time, is the closest to the one established at that moment.

2. If set temperature has not been kept constant for the required time: if the set temperature was not kept constant for the period of time set by the user in the GUI, timing continues using the already mentioned 'Time_elapsed' variable.

```

226 -         if Time_elapsed > (interval_Time)
227 -             if A == length(Temp_Array) + 1 % Ramp down
228 -                 nointerval = 0;
229 -                 m = C;
230 -                 Temperature = ['ss', ' ', num2str(Temp_Array(m))];
231 -                 data2 = query(obj1, Temperature);
232 -                 fprintf('Changed')
233 -                 C = C - 1; % Going backwards, lower temperature is next
234 -                 B=0;
235 -                 data3= query (obj1, 'RS');
236 -                 fprintf('set point set to %s\n',data3)
237 -             else
238 -                 m = A; % Ramp up
239 -                 Temp_true = Temp_Array(m);
240 -                 data1 = query(obj1, 'RT');
241 -                 Temp_false = sscanf(data1, '%f');
242 -                 if Temp_false < (Temp_true - 1) % If bath temperature differs more than 1 degree from set temperature:
243 -                     nointerval = 1;
244 -                     Temp_false = Temp_false +1; % Avoids temperature overshoot
245 -                     Temperature = ['ss', ' ', num2str(Temp_false)];
246 -                     data2 = query(obj1, Temperature);
247 -                     fprintf('Changed')
248 -                     B=0;
249 -                     data3= query (obj1, 'RS');
250 -                     fprintf('set point set to %s\n',data3)
251 -                 else % If bath temperature is close enough (less the 1 degree) to set temperature:
252 -                     nointerval = 0;
253 -                     Temperature = ['ss', ' ', num2str(Temp_true)];
254 -                     data2 = query(obj1, Temperature);
255 -                     fprintf('Changed')
256 -                     A = A+1; % Continue heating to the next set temperature
257 -                     B=0;
258 -                     data3= query (obj1, 'RS');
259 -                     fprintf('set point set to %s\n',data3)
260 -                 end
261 -             end

```

Listing 3.8. Script that performs temperature ramp up and ramp down.

Finally, once ramp up and down are completed, the automated reaction process is shut down (see Listing 3.9). First thing is the storage of all time and temperature data collected during the entire experiment in two different kind of arrays. On the one hand, there are the arrays where data measured during the initial CO coverage stage will be accessible. On the other hand, there are the arrays which contains data collected during the ramp up and down stages. Therefore, differentiation are established between end of room temperature reactive processes and beginning of temperature controlled ones. Thermocouple data logger and water bath are then turned off, leaving everything ready for running the function responsible for the analysis of the raw data just obtained. This is discussed in the next Section 3.2.

```
324 - %% Saving temperature and time stored in arrays
325 - Temp_ini = Temp_ini(Temp_ini~=0);
326 - Tl = length(Temp_ini);
327 - Time_ini = Time_ini(1:Tl,1);
328 - Set_Temp_ini = Set_Temp_ini(1:Tl,1);
329 - BedTemp_ini = BedTemp_ini(1:Tl,1);
330 -
331 - Temp = Temp(Temp~=0);
332 - Tl = length(Temp);
333 - Time = Time(1:Tl,1);
334 - Temp_A = Temp_A(1:Tl,1);
335 - Set_Temp = Set_Temp(1:Tl,1);
336 - BedTemp = BedTemp(1:Tl,1);
337 -
338 - Time_ini_min = Time_ini./60;
339 - Time_ini_h = Time_ini_min./60;
340 - Time_min = Time./60;
341 - Time_h = Time_min./60;
342 -
343 - fprintf('finished')
344 - data3=query(obj1, 'SO 0'); % Turns off water bath
345 - TC_OFF(handle)%disconnect thermocouple
346 - % Disconnect from instrument object, obj1.
347 - fclose(obj1);
348 - end
```

Listing 3.9. Shutting down of experimental automated reaction test.

3.2 Development of software responsible for the analysis and process of Raw Data

After the reaction finished, time and temperature having been collected and devices involved turned off, a series of actions needs to be carried out. These were implemented in a code and the resulting function was called Data_analysis, name that clearly reveals the purpose of it.

3.2.1 Importing user data

Firstly, some information is required before attempting to analyse and treat the GC data. This information is grabbed from the GUI, where a series of fields are available for the user to fill out. In particular, response factors for each reactant (calibration procedure, Section 2.4.4), flows for each of the gas mixtures used in the reaction and composition of those, along with the mass of noble metal present in the catalytic sample, are requested. Listing 3.10 shows the part of the software where this is done.

```
8 %% Grabbing gases composition, flows and catalyst mass from GUI
9 % Response factors
10 Rf_CO2 = str_RfCO2;
11 Rf_CO = str_RfCO;
12 Rf_H2 = str_RfH2;
13 Rf_O2 = str_RfO2;
14 % Flows
15 flow = str_flow;
16 flowO2 = str_O2flow;
17 flowCO_H2 = str_CO_H2flow;
18 flowH2 = str_H2flow;
19 flowN2pure = str_N2pureflow;
20 % Gases compositions
21 compflow = str_compflow;
22 compO2flow = str_compO2flow;
23 compCO_H2flow = str_compCO_H2flow;
24 compH2flow = str_compH2flow;
25 % Noble metal mass present in catalytic sample
26 catmass = str_catmass;
```

Listing 3.10. Part of script where experimental conditions are grabbed from the GUI.

3.2.2 Reading and decoding GC data

Once experimental conditions have been properly stored within our Matlab environment, such information is going to be used differently across the code. First thing is the definition of the type of oxidation reaction being studied in each particular case. Although CO oxidation was the focus of the flow reactor experiments carried out during the present work (see Chapter 5), the software was designed to deal with a broader spectrum. According to the snippet of script presented in Listing 3.11, five possibilities are considered, namely: PROX, CO alone, CO oxidation, H₂ alone and H₂ oxidation. Code uses the information previously grabbed from the GUI and apply it through a flow of conditions, resulting in the identification of the kind of reacting being faced at. Bearing always in mind that four different gaseous mixtures are available for their use in our flow reactor rig, CO/N₂, O₂/N₂, H₂/N₂ and CO/H₂ (discussed in Section 2.4), such conditions flow as detailed below:

1. Are both CO/N₂ and H₂/N₂ flows null? If these gaseous mixtures were not used in the reaction, preferential CO oxidation (PROX) is being studied.
2. If condition 1 is not true, are H₂/N₂, CO/H₂ and O₂/N₂ flows null? If so, this is a CO alone reaction case. This refers to the study of CO oxidation during which the oxygen involved in the reaction is coming exclusively from the catalytic surface, i.e. there is not any source of gaseous O₂ in the reactor feed.

3. If neither condition 1 nor condition 2 are true, are both H₂/N₂ and CO/H₂ flows inexistent? If affirmative, a normal CO oxidation reaction (without H₂) constitutes the focus of the study.
4. In the case that none of the previous conditions were fulfilled, if CO/N₂, CO/H₂ and O₂/N₂ mixtures were not used in the reaction, a H₂ alone case must be considered. This is when the possible hydrogen oxidation in the absence of gaseous oxygen, i.e. only lattice oxygen is present, is being investigated.
5. Finally, if any of the possibilities listed above where affirmatively answered, are both CO/N₂ and CO/H₂ flows null? In that case, H₂ oxidation is the reaction of interest, since this would imply that H₂/N₂ and O₂/N₂ gaseous mixtures are the ones used in the feed line.

```

28  %% Defining which kind of reaction is being faced
29  PROX = 0;
30  COalone = 0;
31  H2alone = 0;
32  COoxidation = 0;
33  H2oxidation = 0;
34  if isnan(flow) && isnan(flowH2)
35      disp('PROX reaction')
36      PROX = 1;
37      totalflow = flowO2 + flowCO_H2;
38  else
39      if isnan(flowH2) && isnan(flowCO_H2) && isnan(flowO2)
40          disp('CO alone')
41          COalone = 1;
42          totalflow = flow;
43      else
44          if isnan(flowH2) && isnan(flowCO_H2)
45              disp('CO oxidation reaction')
46              COoxidation = 1;
47              totalflow = flow + flowO2 + flowN2pure;
48          else
49              if isnan(flow) && isnan(flowCO_H2) && isnan(flowO2)
50                  disp('H2 alone')
51                  H2alone = 1;
52                  totalflow = flowH2;
53              else
54                  if isnan(flow) && isnan(flowCO_H2)
55                      disp('H2 oxidation reaction')
56                      H2oxidation = 1;
57                      totalflow = flowO2 + flowH2;
58                  end
59              end
60          end
61      end
62  end

```

Listing 3.11. Series of conditions coded to identify the type of oxidation reaction being studied.

At this point, when experimental conditions and reaction type were already defined, the process of grabbing, reading, analysing and treating GC data files starts.

Different files are created during each GC run. Specifically, the results of the outlet gas stream analysis are saved in two types of documents, PDF and text files. The text type are the ones that allow the machine to read and interpret the lines printed on them. Therefore, the code uses the function `uigetdir` to ask the user to select the folder where those GC files are located in the computer. Then, `dir` is used to pick up only those with a '.TXT' extension, storing their names in an array called 'Namestamp', as shown in Listing 3.12. In the following lines, a one-by-one process begins. Accordingly, the series of actions detailed below are repeated for each of the mentioned text files and a new loop of actions is not started until the previous one is finished.

```
64      %% Grabbing GC analysis files
65 -    Folder = uigetdir;
66 -    pathstr = Folder;
67 -    txtfile = dir ([pathstr '\*.TXT']);
68 -    Timestamp = {txtfile.date};
69 -    Namestamp = {txtfile.name};
70 -    Namestamp = Namestamp';
```

Listing 3.12. Selection of folder where GC analysis files are located, grabbing text files and storing their names.

Firstly, the code goes through each to the file names stored in 'Namestamp' following a prior to later file creation order. Then, the file with the same name stored in our folder 'pathstr' is opened. `fscanf` is used to read and interpret the information in it. However, Matlab cannot be used to decode Unicode characters, format each of these text GC files are coded to. Thus, prior to any attempt to decode the necessary information, conversion to a suitable format must be carried out. In particular, ASCII code is targeted. After conversion has successfully performed, each printed line is split into separate columns. Every time the code finds a space in a line, it jumps to another column where the next characters are saved. `Textscan` is used for this, all columns of characters saved in a cell array called 'textdata'. The first array of this cell array contains all the information. Desired data from that information is grabbed and stored apart. Such desired data

relates to two parameters: retention times and measured peak areas for each of the detected gases. Listing 3.13 shows the snippet of the script where responsible part is coded.

```

126 %% Reading each individual text file
127 for k = 1:length(Namestamp)
128     filename = char(Namestamp(k));
129     fid = fopen([pathstr '\ ' filename]);
130     endfile = 0;
131     fprintf('Reading File: %s\n',filename);
132     %reads the file and splits into separate array's by collums in the document
133     while endfile ~= 1
134         txt = fscanf(fid,'%c');
135         txtANSI = unicode2native(txt,'ISO-8859-1'); % Files are in ASCII CODE now
136         txtANSI = txtANSI(txtANSI~=0); % Deleting all null characters
137         txtANSI = char(txtANSI); % Converting to char version, so that textscan can be used in the next step
138         textdata = textscan(txtANSI,'%s %s %s');
139         primero = [textdata(1,:)];
140         data = [textdata(1,2) textdata(1,5) textdata(1,6)];
141         endfile = feof(fid);
142     end
143     fclose(fid);
144     fprintf('Finished reading file: %s\n',filename)
145     %combines the peak area and counts with the retention time
146     peak = [str2double(data(20:end,1)),str2double(data(20:end,2)),str2double(data(20:end,3))];

```

Listing 3.13. Part of the code that opens each individual GC text file, converts it to ASCII and picks up retention times and peak areas for all gases analysed.

The most important piece of code within our `Data_analysis` function is contained in the lines presented in Listing 3.14. This reads through lines of the already selected columns of characters, searching for values that fall within some of the retention time ranges previously input in the GUI and that, at this point, are being grabbed by the code. As it will be discussed in more detail in Section 3.3, an upper and a lower value are set in the GUI for each of the gases that exits our reactor. Those values define the boundaries of the range within which the retention time for each individual gas should be located. Retention times may vary from one GC run to another, however, for a given gas, very similar values are obtained. The design of the GUI considers these variations. Thus, instead of looking for a single value, the code search for a range of them. Similarly to that done in other parts of the code, each read character is subject of a series of interrogations. Accordingly, if the character is an integer and such an integer belongs to the range set for some the gases of interest, i.e CO, CO₂, O₂, H₂O or N₂, it will be stored in the respective array created for that specific gas. Scheme 3.2 shows the format of a typical text file generated at the end of a GC analysis and the data the part of the code

presented in Listing 3.14 picks up. Once required information has been collected, this is used to perform a series of calculations. This is discussed below.

```

145 %combines the peak area and counts with the retention time
146 peak = [str2double(data(20:end,1)),str2double(data(20:end,2)),str2double(data(20:end,3))];
147 %scans through the retention time and determines if CO, CO2, O2, H2O and N2 are present.
148 %If so, takes their respective peak areas.
149 for i = 1:length(peak)
150     if (peak(i,1)<=str_CO2Max) && (peak(i,1)>=str_CO2Min) && (peak(i,3)<900)
151         peak_data(k) = peak(i,3)';
152     end
153     if isnan(peak_data(k)) == 1
154         CO2_peak = 0;
155         peak_data(k) = CO2_peak;
156     end
157     if (peak(i,1)<=str_COMax) && (peak(i,1)>=str_COMin)
158         peak_dataCO(k) = peak(i,3)';
159     end
160     if isnan(peak_dataCO(k)) == 1
161         CO_peak = NaN;
162         peak_dataCO(k) = CO_peak;
163     end
164
165     if (peak(i,1)<=str_O2Max) && (peak(i,1)>=str_O2Min)
166         peak_dataO2(k) = peak(i,2)';
167     end
168     if (peak(i,1)<=str_H2OMax) && (peak(i,1)>=str_H2OMin)
169         peak_dataH2O(k) = peak(i,2)';
170     end
171     if (peak(i,1)<=str_N2chan1Max) && (peak(i,1)>=str_N2chan1Min) && (peak(i,3)>=900)%Internal standard for Column 1
172         peak_dataN2_chan1(k) = peak(i,3)';
173     end
174     if (peak(i,1)<=str_N2chan2Max) && (peak(i,1)>=str_N2chan2Min)%Internal standard for Column 2
175         peak_dataN2_chan2(k) = peak(i,3)';
176     end
177 end
178 -end

```

Listing 3.14. Script that reads through lines looking for the retention time measured for each gas.

```

Data File C:\Chem32\2\Data\Leticia 2019-01-16 14-05-14\F-001-NV-Au-CeO2.D
Sample Name: Au-CeO2
490 Micro GC 1 1/16/2019 2:07:41 PM User
=====
Acq. Operator   : User                               Seq. Line :    1
Acq. Instrument : 490 Micro GC 1                     Location  :    - (F)
Injection Date  : 1/16/2019 2:06:08 PM              Inj       :    1
                                                    Inj Volume: No inj
Sequence File   : C:\Chem32\2\Data\Leticia 2019-01-16 14-05-14\Leticia.s
Method          : C:\Chem32\2\Data\Leticia 2019-01-16 14-05-14\Leticia_GC_23102018.M (
                Sequence Method)
Last changed    : 1/16/2019 2:05:14 PM by User
Data Store Operator: User
Data Store Target Path: /Data/490 Micro GC 1
=====

```

Area Percent Report

```

=====
Sorted By      :      Signal
Multiplier    :      1.0000
Dilution      :      1.0000
Do not use Multiplier & Dilution Factor with ISTDs

```

Signal 1: GC1 A, Channel 1, 10m MS5A Heated Injector, Backflush

Peak #	RetTime [min]	Type	Width [min]	Area [mV*s]	Height [mV]	Area %	
1	0.436	BV	7.29e-3	13.56647	32.35749	1.13818	→ O ₂
2	0.471	VB S	0.0315	1155.70715	611.34692	96.95969	→ N ₂
3	0.730	BB	0.0321	22.67243	10.98946	1.90214	→ CO
Totals :				1191.94605	654.69387		

Column 1

Signal 2: GC1 B, Channel 2, 10m PPQ Heated Injector

Peak #	RetTime [min]	Type	Width [min]	Area [mV*s]	Height [mV]	Area %	
1	0.392	BB S	9.98e-3	2854.33130	4172.92822	99.62471	→ N ₂
2	0.461	BB T	0.0113	4.12079e-1	6.22765e-1	0.01438	→ CO ₂
3	0.666	BB	0.0138	10.34031	10.92826	0.36091	→ H ₂ O
Totals :				2865.08369	4184.47925		

Column 2

*** End of Report ***

Scheme 3.2. Typical text file generated at the end of a GC analysis. Squared in green are the retention times the code looks for when reading through lines. Squared in red are the peak areas that the code grabs. The specific gas that corresponds to each retention time and area, along with columns responsible for the analysis of such gases, are also indicated.

3.2.2.1 Calculations performed with collected and decoded experimental data

Listing 3.15 shows the part of the script where individual flows and percentages for each of the gases entering the reactor are calculated. The number and nature of those gases, according to the reaction classification discussed previously for Listing 3.11, will depend on the type of reaction being studied at that moment. Nonetheless, in all cases, the basis for such calculations are the same. Thus, when the flow of one of the reactor inlet gases is considered, Equation 3.1 is applied. Note that data used in this equation was previously grabbed from the GUI, as it was

shown in Listing 3.10. Relating to the percentage each individual gas type is present in the total gaseous stream flowing over the catalytic sample, Equation 3.2 is used. As seen in this equation, data for percentage calculations is almost the same than that in Equation 3.1, with the only addition of the total reactor inlet flow, which was also previously calculated after identification of the reaction type (see Listing 3.11). Both Equation 3.1 and 3.2 are used in the code and the respective snippet of the script is showed in Listing 3.15. Note that the terminology used in equations resembles the one in the listing. This practice has been continued in forthcoming equations regarding the code they refers to.

$$flow_{gas_type} = \frac{comp_flow \cdot flow_{gas_mix}}{100} \text{ in } [ml \cdot min^{-1}] \quad (3.1)$$

where $flow_{gas_type}$ is the gas type flow entering the reactor. $comp_flow$ is the composition of the gaseous mixture where the targeted chemical is present. $flow_{gas_mix}$ is the flow of such gaseous mixture.

$$percent_{gas_type} = \frac{comp_flow \cdot flow_{gas_mix}}{totalflow} \text{ in } [\%] \quad (3.2)$$

where $percent_{gas_type}$ is the percentage each gas type is present in the total gaseous stream flowing over the catalytic sample. $totalflow$ refers to the flow of such total stream.

```

221 -     if PROX == 1
222 -         flowCOin = compCO_H2flow*flowCO_H2/100;
223 -         flowH2in = flowCO_H2-(compCO_H2flow*flowCO_H2)/100;
224 -         flowO2in = compO2flow*flowO2/100;
225 -         flowN2in = flowO2-(compO2flow*flowO2)/100;
226 -         percentCO = compCO_H2flow*flowCO_H2/totalflow;
227 -         percentH2 = ((flowCO_H2-(compCO_H2flow*flowCO_H2)/100)/totalflow)*100;
228 -         percentO2 = compO2flow*flowO2/totalflow;
229 -         percentN2 = ((flowO2-(compO2flow*flowO2)/100)/totalflow)*100;
230 -     else
231 -         if COalone == 1
232 -             flowCOin = compflow*flow/100;
233 -             flowN2in = flow-(compflow*flow)/100;
234 -             percentCO = compflow*flow/totalflow;
235 -             percentN2 = ((flow-(compflow*flow)/100)/totalflow)*100;
236 -         else
237 -             if H2alone == 1
238 -                 flowH2in = compH2flow*flowH2/100;
239 -                 flowN2in = flowH2-(compH2flow*flowH2)/100;
240 -                 percentH2 = compH2flow*flowH2/totalflow;
241 -                 percentN2 = ((flowH2-(compH2flow*flowH2)/100)/totalflow)*100;
242 -             else
243 -                 if COoxidation == 1
244 -                     flowCOin = compflow*flow/100;
245 -                     flowO2in = compO2flow*flowO2/100;
246 -                     flowN2in = flow-(compflow*flow)/100 + flowO2-(compO2flow*flowO2)/100 + flowN2pure;
247 -                     percentCO = compflow*flow/totalflow;
248 -                     percentO2 = compO2flow*flowO2/totalflow;
249 -                     percentN2 = ((flow-(compflow*flow)/100)/totalflow)*100 + ...
250 -                                 ((flowO2-(compO2flow*flowO2)/100)/totalflow)*100 + (flowN2pure/totalflow)*100;
251 -                 else
252 -                     if H2oxidation == 1
253 -                         flowH2in = compH2flow*flowH2/100;
254 -                         flowO2in = compO2flow*flowO2/100;
255 -                         flowN2in = flowH2-(compH2flow*flowH2)/100 + flowO2-(compO2flow*flowO2)/100;
256 -                         percentH2 = compH2flow*flowH2/totalflow;
257 -                         percentO2 = compO2flow*flowO2/totalflow;
258 -                         percentN2 = ((flowH2-(compH2flow*flowH2)/100)/totalflow)*100 + ...
259 -                                     ((flowO2-(compO2flow*flowO2)/100)/totalflow)*100;
260 -                     end

```

Listing 3.15. Snippet of the script where Equations 3.1 and 3.2 are used. Differences are based on the type of oxidation reaction being studied.

Equations 2.9-2.14 discussed in Section 2.4.2, were coded in our `Data_analysis` function, so that O_2 and CO conversions, yield to CO_2 and selectivity are also machine calculated. The part of the code responsible for this is presented in Listings 3.16 and 3.17. Examples of how the single point calibration was applied before swapping to the multiple point method have been left for information purposes, as seen in Listing 3.16. Note that the calibration method followed in this work was discussed in detail in Section 2.4.4. The identification of the type of oxidation reaction carried out in the previous code lines makes the script in Listing 3.17 know when selectivity calculation is applicable, i.e. PROX reaction, and when O_2 conversion is also pursued, i.e. every case where O_2 is entering the reactor.

```

269 %% O2 concentration
270 pO2 = peak_dataO2(:,1);
271 O2_conc = pO2/Rf_O2;
272 %%% Old method calibration(only one point)%%
273 % N = peak_dataN2_chan1(:,1);
274 % O2_conc = (pO2./N).*(79.6/Rf_O2);
275
276 %% CO concentration
277 pp = peak_dataCO(:,1);
278 CO_conc = pp/Rf_CO;
279 rr = percentCO-CO_conc;
280 CO_conc = pp/Rf_CO;
281 rr = percentCO-CO_conc;
282 %%% Old method calibration(only one point)%%
283 % CO_conc = (pp./N).*(79.6/Rf_CO);
284
285 %% CO2 concentration
286 p = peak_data(:,1);
287 CO2_conc = p/Rf_CO2;
288
289 %% Mass balance for H2O concentration and H2 concentration:
290 % H: n_H2in = n_H2out + n_H2Oout
291 % C: n_COin = n_COout + n_CO2out
292 % O: 2*n_O2in + n_COin = 2*n_O2out + 2*n_CO2out + n_COout + n_H2Oout
293 % N2: n_N2in = n_N2out
294 % So, using this for H2O & H2
295 n_O2out = O2_conc(:,1);
296 n_CO2out = CO2_conc(:,1);
297 n_COout = CO_conc(:,1);
298 H2O_conc = 2*percentO2 + percentCO - 2*n_O2out - 2*n_CO2out - n_COout;
299 n_H2Oout = H2O_conc(:,1);
300 H2_conc = percentH2-n_H2Oout;
301 n_H2out = H2_conc(:,1);

```

Listing 3.16. Part of the code where O₂ and CO are calculated applying the calibration method discussed in Section 2.4.4 to the raw data previously collected. H₂O and H₂ are calculated by means of the mass balance equations discussed in Section 2.4.2 (Equations 2.5-2.8).

```

299 %% Conversions, yield and selectivity
300 CO_conversion = NaN(v,1);
301 yield_CO2 = NaN(v,1);
302 lambda = NaN;
303 O2_conversion = NaN(v,1);
304 selectivity = NaN(v,1);
305 selectivity_allcases = NaN(v,1);
306 if percentCO ~=0
307     CO_conversion = (rr/percentCO).*100;
308     yield_CO2 = (CO2_conc/percentCO).*100;
309     lambda = 2*percentO2/percentCO;
310 end
311 if percentO2 ~=0
312     O2_conversion = ((percentO2-O2_conc)/percentO2).*100;
313     if percentCO && percentH2 ~=0
314         %selectivity even when methane formation
315         selectivity_allcases = (percentCO-n_COout)./(percentCO - n_COout + percentH2 - n_H2out).*100;
316         selectivity = [0.5*CO2_conc/(percentO2-O2_conc).*100]'; %selectivity when no methane formation
317     end
318 end

```

Listing 3.17. Code lines where CO and O₂ conversion, along with yield to CO₂ and selectivity are calculated from their individual concentrations.

Approximation to molar flows are also carried out within the `Data_analysis` function code. For those approximation, the total gas flow entering the reactor ($totalflow$) and the individual gas percentages ($percent_{gas_type}$) previously calculated are used. Then, the assumption of ideal gas in standard condition was taken. Thus, 1 mol of each gas being occupying 22.4 litres under standard conditions. Applying Equation 3.3 to each of gases flowing over the catalytic sample would yield a good estimation of their respective molar flows ($Molar_flow_{gas_type}$). Absolute reaction rates calculation ($r_{CO_{mass}}$) was also coded. For this, Equation 3.4, where CO conversions previously calculated (see Listing 3.17) and CO molar flows ($Molar_flow_{CO}$) are needed, is applied. A snippet of the script where these calculations were coded is presented in Listing 3.18. Finally, CO and O₂ partial pressures are also obtained when running the software. Code lines showed in Listing 3.19 are responsible for such calculation, which agrees with Equation 3.5 below.

$$Molar_flow_{gas_type} = \frac{totalflow \cdot percent_{gas_type}}{100 \cdot 22400} \text{ in } [mol \cdot min^{-1}] \quad (3.3)$$

$$r_{CO_{mass}} = \frac{CO \text{ conversion} \cdot Molar_flow_{CO} \cdot (60 \text{ min}/1 \text{ h})}{m_{metal}} \text{ in } [mol_{CO} \cdot gr_{metal}^{-1} \cdot h^{-1}] \quad (3.4)$$

where m_{metal} is the mass of noble metal in the reactor bed.

$$p_{gas_type} = \frac{Molar_flow_{gas_type} \cdot R \cdot T}{totalflow} \text{ in } [atm] \quad (3.5)$$

where p_{gas_type} is the partial pressure of a particular gas entering the reactor. R is the ideal gas constant and T the temperature in Kelvin.

```

320     %% Approximation to molar flows: mol/min & mol/h
321
322     molesCOin_min = totalflow*percentCO/(100*22400);
323     molesH2in_min = totalflow*percentH2/(100*22400);
324     molesO2in_min = totalflow*percentO2/(100*22400);
325     molesN2in_min = totalflow*percentN2/(100*22400);
326     totalmolesin_min = molesCOin_min + molesH2in_min + molesO2in_min + molesN2in_min;
327
328     molesCOin_h = molesCOin_min*60;
329     molesH2in_h = molesH2in_min*60;
330     molesO2in_h = molesO2in_min*60;
331     molesN2in_h = molesN2in_min*60;
332
333     %% Reaction rates: molCO/(h*mg)
334     rate = CO_conversion.*molesCOin_h;
335     ratepermass = CO_conversion.*molesCOin_h/catmass;

```

Listing 3.18. Snippet of the script where molar flow and absolute reaction rates calculation are coded.

```

352     %% CO and O2 partial pressures
353     for i=1:Tl_ini
354         Temp_ini_kelvin(i) = Temp_ini(i)+275.15;
355     end
356     idealgasconstant = 82; % ml*atm/(k*mol)
357     partialpressure_CO_ini = (molesCOin_min*idealgasconstant/totalflow)*Temp_ini_kelvin';
358     partialpressure_O2_ini = (molesO2in_min*idealgasconstant/totalflow)*Temp_ini_kelvin';

```

Listing 3.19. Code lines where CO and O₂ pressures are calculated.

3.3 Development of GUI

With the intention of creating a more user-friendly software, the development of a Graphical User Interface (GUI) was included as part of the design. By making use of a GUI, the mathematics and code specifics responsible for the processes carried out during phases 1 and 2 of the automated process, Section 3.1 and 3.2 respectively, are hidden away from the user. This means that, as long as the reactor rig is set up correctly, anyone could pick up the software and get their kinetic analysis, regardless their level of knowledge. The MATLAB Graphical user Interface Development Environment (GUIDE) was used as a tool to design the particular GUI that suits the requirements for our study case. The resulting GUI becomes then the heart of the software. This is where required information for the successful running of the `T_control` and the `Data_analysis` functions previously discussed (Section 3.1 and 3.2 respectively) is collected and used as demanded for these. In

order to get the user to communicate with the hidden scripts, a series of control objects, mainly push-buttons, are included in the interface. These control objects are functions that are activated when clicking on them. Such activation triggers the code, the particular object is linked to, to be run. The data also needs to be presented to the user. The GUI used in our flow reactor studies was designed to do so in two different ways, a graphical plot and the generation of an excel file with all raw and processed data obtained through the automated reaction process. Figure 3.8 shows the final design of this GUI. In such figure, the applications involved in each of the phases are differentiated.

The actual generation of an user-interface is not the subject of this thesis. Rather, the mathematics and programming outlined in previous sections are the most interest relating to the present work. Nonetheless, in order to give a broad idea of how this part of the software is linked to functions earlier discussed, the different parts conforming the GUI are detailed in the subsections below.

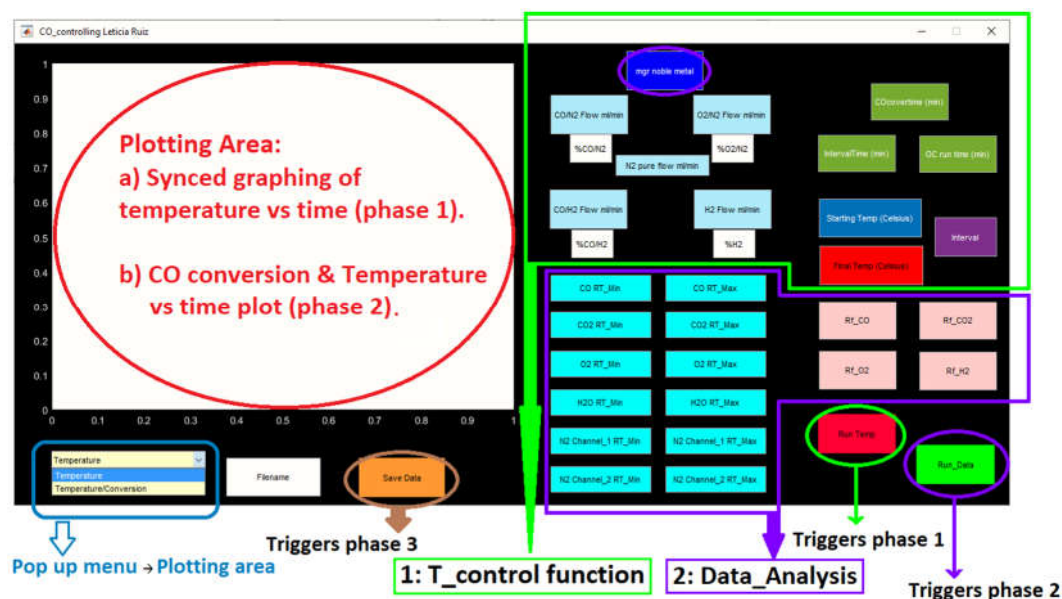


Figure 3.8. Design of graphical User Interface (GUI) used in flow reactor studies. Applications involved in phase 1, i.e. T_control function (Section 3.1), are squared in green. Those for phase 2, i.e. Data_Analysis function (Section 3.2), squared in purple. Plotting area and its related menu highlighted in red and blue respectively. Trigger push-button for phase 3, i.e. generation of data file, squared in brown.

3.3.1 Phase 1 - Automated reaction

Phase 1 refers to the mechanism and functions involved in the automation of an experimental reaction, discussed in Section 3.1. Figure 3.9 extracts the part of the GUI responsible for triggering that part of the code and for the collection of the required information regarding experimental conditions. The different buttons in this figure are numbered. According to such numeration, their particular purposes are as detailed:

1. Period of time when reactants are flowing over the catalytic sample at room temperature.
2. Period of time each tested temperature is kept constant for.
3. Average of time taken during each GC run (used when pausing `T_control` function).
4. Lower temperature to be tested.
5. Higher temperature to be tested.
6. Temperature ramp.
- 7a. Flow of CO/N₂ mixture used in the feed line.
- 7b. Composition of the CO/N₂ mixture.
- 8a. Flow of O₂/N₂ mixture used in the feed line.
- 8b. Composition of the O₂/N₂ mixture.
- 9a. Flow of CO/H₂ mixture used in the feed line.
- 9b. Composition of the CO/H₂ mixture.
- 10a. Flow of H₂/N₂ mixture used in the feed line
- 10b. Composition of the H₂/N₂ mixture.
11. Flow of pure N₂ used in the feed line.

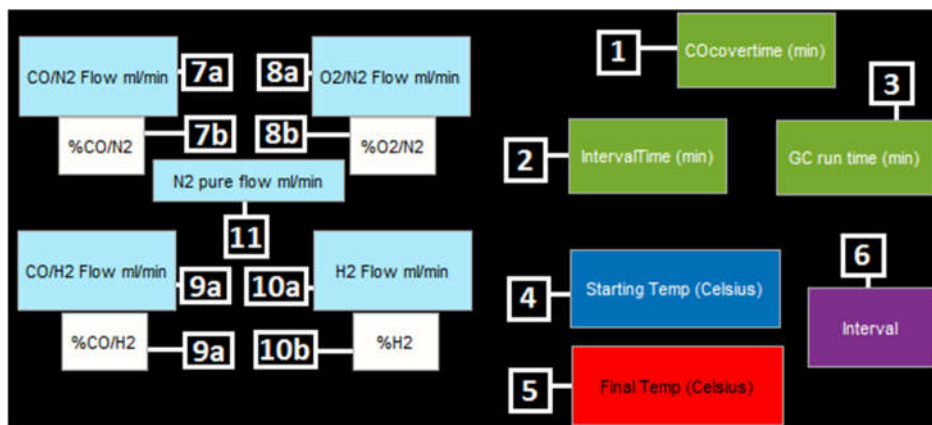


Figure 3.9. Part of the GUI related to the reaction automation, i.e. phase 1 (Section 3.1).

Figure 3.10 shows an example of the kind of plot that is visualised within the GUI during phase 1. As it was highlighted in Figure 3.8, the plot of temperature versus time is synchronized with our `T_control` function. This means that the user gets instant feedback of the temperature measured at both water bath and catalytic bed.

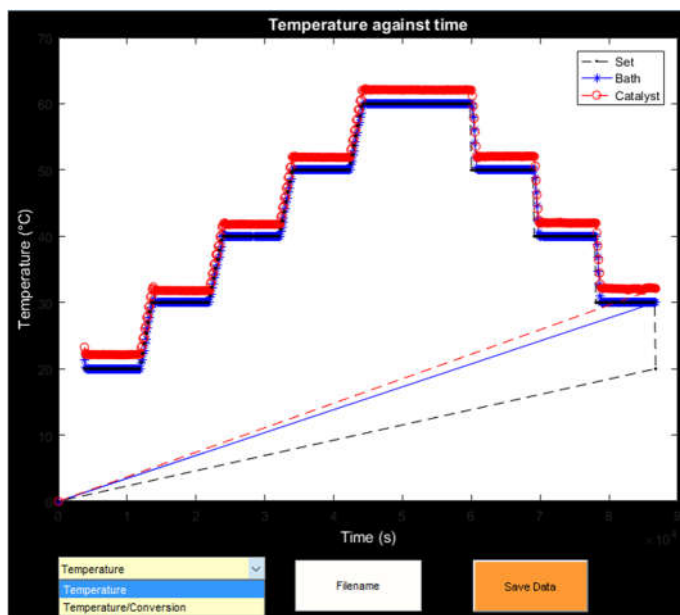


Figure 3.10. Temperature versus time graph visualised within the GUI.

3.3.2 Phase 2 – Collection and analysis of raw data

The process carried out during the run of our `Data_analysis` function (see Section 3.2) has been referred as phase 2. Figure 3.11 extracts the part of the GUI

liked to such a phase. Similarly to that in subsection 3.3.1, the different buttons in this figure have been numbered and their specific purposes noted below:

1. CO response factor.
2. CO₂ response factor.
3. O₂ response factor.
4. H₂ response factor.
5. Mass of noble metal in the catalytic sample.
6. Upper and lower boundaries expected for the CO retention time.
7. Upper and lower boundaries expected for the CO₂ retention time.
8. Upper and lower boundaries expected for the O₂ retention time.
9. Upper and lower boundaries expected for the H₂O retention time.
10. Upper and lower boundaries expected for the N₂ retention time in Column 1.
11. Upper and lower boundaries expected for the N₂ retention time in Column 2.

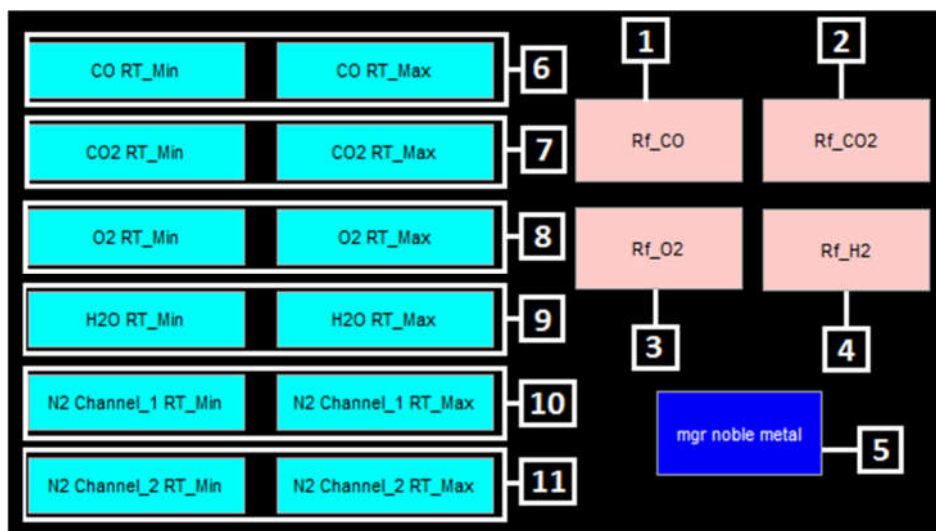


Figure 3.11. Part of the GUI involved in the collection and analysis of data, i.e. phase 2 (Section 3.2).

Figure 3.12 shows the type of plot that can be visualised within the GUI after phase 2 have been performed. In this graph, CO conversion versus time is added to the previously obtained data in phase 1, i.e. temperature versus time.

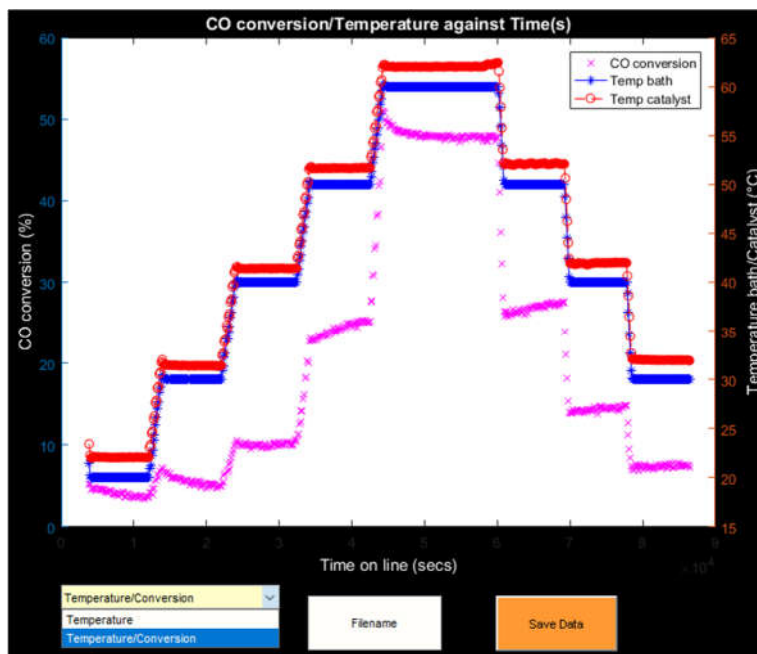


Figure 3.12. CO conversion and temperature versus time graph visualised within the GUI.

3.3.3 Phase 3 – Generation of a data file

A push-button is responsible of triggering a series of Matlab objects and functions that result in the generation of an excel file where both raw and processed data are collected, making it accessible to the user for any further analysis. Figures 3.13 and 3.14 show a typical example of the kind of information these files contain. Such information agrees with that noted previously in Sections 3.1 and 3.2 and that allows experimental results to be presented as in Chapter 5 of this thesis.

	A	B	C	D	E	F	G	H	I
1	Rf_CO	12.27							
2	Rf_CO2	30.008			lambda	1.517241379			
3	Rf_O2	12.182							
4	Rf_H2								
5			Pre-ramping						
6	Area O2	Area CO	Area CO2	Area H2O	Area N2_channel_1	Area N2_channel_2	Time(s)	Time(min)	Time(h)
7	13.05851	0.207992	0.429141	0	1164.44836	2865.81641	1120.497	18.67495	0.311249
8	13.03356	17.24934	0.432807	0	1164.75061	2865.60156	1254.789	20.91315	0.348552
9	13.10699	17.30908	0.417141	0	1164.04919	2864.97876	1385.071	23.08452	0.384742
10	13.02951	17.30724	0.412999	0	1164.00195	2865.08862	1519.364	25.32273	0.422046
11	13.02859	17.30215	0.410995	0	1164.2489	2863.71387	1649.646	27.4941	0.458235
12	13.02568	17.36003	0.43213	0	1163.6416	2866.67212	1787.947	29.79912	0.496652
13	13.01941	17.28256	0.422119	0	1163.66943	2865.448	1922.239	32.03732	0.533955
14	13.03256	17.28126	0.417919	0	1163.73792	2863.97778	2056.531	34.27552	0.571259
15	13.02186	17.25643	0.408989	0	1163.52222	2865.01855	2186.814	36.4469	0.607448
16	13.00847	17.2694	0.41728	0	1163.81201	2864.60059	2321.12	38.68533	0.644756
17	13.01955	17.28252	0.412332	0	1163.44141	2864.46216	2451.402	40.8567	0.680945
18	13.01186	17.24157	0.402319	0	1163.09705	2863.27124	2589.702	43.1617	0.719362
19	13.03008	17.28576	0.413106	0	1163.18127	2861.83008	2723.995	45.39992	0.756665
20	13.00649	17.308	0.59425	0	1163.33752	2860.75171	2854.276	47.57127	0.792854
21	13.00268	17.32479	0.399622	0	1163.2616	2861.18164	2992.577	49.87628	0.831271
22	13.02789	17.2731	0.404165	0	1162.84998	2860.7627	3126.876	52.1146	0.868577
23	13.00991	17.25574	0.395639	0	1162.86255	2860.94702	3261.181	54.35302	0.905884
24	13.01469	17.26206	0.411318	0	1162.84277	2861.15186	3391.463	56.52438	0.942073
25	12.99118	17.23413	0.398562	0	1163.55432	2860.81421	3525.754	58.76257	0.979376
26	13.00587	17.29037	0.387511	0	1163.15637	2860.80762	3656.051	60.93418	1.01557
27			Ramping						
28	Area O2	Area CO	Area CO2	Area H2O	Area N2_channel_1	Area N2_channel_2	Time(s)	Time(min)	Time(h)
29	13.03244	17.24841	0.358292	0	1163.11108	2861.94116	3794.327	63.23878	1.05398
30	13.04775	17.28473	0.30839	0	1163.5531	2861.81836	3926.797	65.44662	1.090777
31	13.04945	17.32255	0.269777	0	1162.82507	2861.54883	4059.161	67.65268	1.127545
32	13.05847	17.37226	0.2313	0	1162.99377	2859.80005	4191.525	69.85875	1.164313
33	13.04235	17.34826	0.212564	0	1162.63135	2860.73047	4323.874	72.06457	1.201076
34	13.0492	17.33659	0.210091	0	1162.89722	2860.552	4456.254	74.2709	1.237848
35	13.03747	17.41494	0.215774	0	1162.63892	2860.94922	4586.617	76.47695	1.274616
36	13.05279	17.31502	0.226445	0	1163.27893	2861.18091	4720.981	78.68302	1.311384
37	13.03963	17.32611	0.209719	0	1162.57471	2861.29126	4853.329	80.88882	1.348147

Figure 3.13. Raw data collected in the software generated excel file. This regards to GC measured areas and reaction times.

	A	B	C	D	E	F	G	H	I	J	K	L
5						Pre-ramping						
6	CO_conc(%)	CO_conversion(%)	O2_conc(%)	O2_conversion(%)	CO2_conc(%)	yield_CO2(%)	Rate(molCO/h)	Rate(molCO/(h*mgr))	Temp_Bath(°C)	Temp_Cat.pCO	pO2	
7	0.016951263	98.83094736	1.07195124	2.549887315	0.014300886	0.98626803	0.076770468	0.051180312	28.8	30.93806	0.016134	0.012239
8	1.405814181	3.047297867	1.069903136	2.736078566	0.014423054	0.994693369	0.002367097	0.01578065	28.8	30.91306	0.016134	0.012239
9	1.410682967	2.711519546	1.075930882	2.18810167	0.013900993	0.958689177	0.00210627	0.0140041798	28.8	30.90011	0.016134	0.012239
10	1.410533007	2.721861563	1.069570678	2.766301995	0.013762963	0.949169877	0.002114303	0.014095355	28.8	30.87906	0.016134	0.012239
11	1.410118174	2.75047073	1.069495157	2.773167565	0.013696181	0.944564208	0.002136526	0.014243509	28.8	30.8747	0.016134	0.012239
12	1.414835371	2.42514684	1.06925628	2.794883658	0.014400493	0.993137462	0.001883819	0.012558796	28.8	30.87951	0.016134	0.012239
13	1.408521597	2.86057949	1.068741596	2.841674005	0.014066882	0.970129804	0.002222057	0.014813715	28.8	30.90289	0.016134	0.012239
14	1.408415648	2.86788635	1.069821047	2.743541141	0.013928919	0.960477206	0.002227733	0.014851554	28.8	30.89198	0.016134	0.012239
15	1.406392013	3.007447377	1.068942702	2.823390696	0.013629332	0.939953943	0.002336142	0.015574281	28.8	30.90533	0.016134	0.012239
16	1.407449063	2.934547396	1.06784354	2.923314577	0.013905625	0.959008632	0.002279514	0.015196763	28.8	30.91002	0.016134	0.012239
17	1.408518337	2.860804317	1.068753078	2.840629244	0.013740736	0.947636952	0.00222232	0.014814879	28.8	30.91441	0.016134	0.012239
18	1.405180929	3.090970407	1.068121819	2.898016448	0.013407058	0.924624698	0.002401022	0.016006811	28.8	30.90433	0.016134	0.012239
19	1.408782396	2.842593373	1.069617468	2.762048328	0.013766529	0.949415788	0.002208086	0.014720573	28.8	30.91181	0.016134	0.012239
20	1.410594947	2.71758986	1.067681005	2.938090476	0.019803053	1.36572776	0.002110985	0.014073233	28.8	30.92249	0.016134	0.012239
21	1.411963325	2.623218953	1.067368248	2.966522888	0.013317182	0.918426351	0.002037679	0.013584527	28.8	30.91882	0.016134	0.012239
22	1.407750611	2.913750948	1.069437695	2.778391367	0.013468575	0.928867245	0.00226336	0.015089067	28.8	30.92076	0.016134	0.012239
23	1.406335778	3.011325633	1.067961747	2.912568469	0.013184451	0.90927247	0.002339155	0.015594365	28.8	30.92214	0.016134	0.012239
24	1.406850856	2.975803052	1.068354129	2.87689736	0.013706945	0.945306539	0.002311561	0.015410409	28.8	30.91672	0.016134	0.012239
25	1.404574572	3.132788129	1.066424232	3.052342502	0.013281858	0.915990219	0.002433505	0.016223367	28.8	30.93388	0.016134	0.012239
26	1.409168109	2.816682123	1.06763011	2.942717273	0.01291359	0.890592394	0.002187958	0.01458639	28.8	30.88598	0.016134	0.012239
27			Ramping									
28	CO_conc(%)	CO_conversion(%)	O2_conc(%)	O2_conversion(%)	CO2_conc(%)	yield_CO2(%)	Rate(molCO/h)	Rate(molCO/(h*mgr))	Temp_Bath(°C)	Temp_Cat.pCO	pO2	
29	1.405738386	3.052525082	1.069811197	2.74443665	0.011939883	0.823440186	0.002371158	0.015807719	27.6	29.47094	0.01607	0.012191
30	1.408698452	2.848382655	1.071067969	2.630184624	0.010276926	0.708753528	0.002212583	0.014750553	25.8	27.76142	0.015975	0.012119
31	1.411780766	2.635809235	1.071207519	2.617498246	0.008990169	0.620011675	0.002047459	0.013649726	24.1	26.14016	0.015884	0.01205
32	1.415832111	2.356406149	1.071947956	2.550185818	0.007707945	0.531582383	0.001830423	0.012202818	22.5	24.58719	0.015799	0.011986
33	1.413876121	2.491302026	1.070624692	2.67048253	0.007083578	0.488522601	0.001935208	0.012901385	21	23.24802	0.01572	0.011925
34	1.41292502	2.556895147	1.071186997	2.61936389	0.007001166	0.482839059	0.00198616	0.013241064	20.2	22.57171	0.015677	0.011893
35	1.419310513	2.116516314	1.070224101	2.706899897	0.007190549	0.495899944	0.00164408	0.010960531	20	22.47285	0.015667	0.011885
36	1.411167074	2.678132816	1.071481694	2.592573245	0.007546154	0.520424439	0.002080335	0.013868902	20	22.47854	0.015667	0.011885
37	1.412070905	2.61579968	1.07041783	2.68928822	0.00698877	0.481984115	0.002031916	0.013546105	20	22.48173	0.015667	0.011885

Figure 3.14. Processed data collected in the software generated excel file. This regards to gases concentrations, conversions, yields, reaction rates and partial pressures.

3.4 Summary

In this Chapter, the development of software capable of automating chemical reactions, tailoring them under the desired experimental conditions, constituted the focus of discussion. Three main scripts play the principal roles. In Section 3.1, the code responsible for the actual automation of the reaction, the so-called `T_control` function, was minutely described. Important implementations, such as the inclusion of an initial period of time to allow an in-equilibrium CO surface coverage, ensured the reliability of steady state studies. Furthermore, modifications in the code successfully controls the heating power utilised by the water bath, thus avoiding the usual temperature overshoot experienced before and impeding the reactor to light off. Ultimately, an inventive approach made it possible to include the GC in the synced system. In Section 3.2, the function that reads through all GC files and picks up the information of interest was detailed. This function, called `Data_Analysis`, also performs an analysis of the collected raw data, performing a series of chemistry based mathematical operations. Finally, Section 3.3 focuses on the design of a Graphical User Interface (GUI) that transforms the software into a more user-friendly tool. Simple push-buttons trigger each piece of software to be run at the correct moment in the right way. At the end of the process, an excel file, which contains all raw and treated data obtained through the entire process, is generated.

Although this software contains specific features for the oxidation processes of interest for our experimental study, it offers a high versatility for being applied in other reactive processes with ease.

References

- 1 M. J. Kahlich, H. A. Gasteiger and R. J. Behm, *J. Catal.*, 1997, **171**, 93-105.

4 | Development and Application of the TAP Reactor Numerical Analysis Software

The necessity of reading and treating the raw data obtained after carrying out TAP experiments, making it accessible for extracting kinetic information, pushed forward the development of a TAP numerical analysis software. This chapter will explain the most relevant parts of the code that gives function to such software.

4.1 Analysis of raw experimental responses

The first action is also the most basic. This is related to the selection of the experimental text file/s that need to be analysed. Matlab commands such as `uigetfile`, `fopen`, `textscan` and `textdata` are used with this purpose, as shown in code lines presented in Listing 4.1. Once the whole document has been loaded, the software searches for a specific marker that tells it the line where the actual experimental data starts to be listed. This is due to the fact that these text files may contain not only the intensity values obtained during each pulse experiment but also the set of conditions for that particular experiment. In particular, such a marker is the symbol `'*'`. Thus, in order to ensure that only the intensity values are studied, extra information, if any, is deleted from the stored arrays. Such a process is carried out by lines presented in Listing 4.2. Schemes 4.1 and 4.2 gives a more visual way of how the part of the code showed in Listing 4.1 works and how that information is used afterward by the codes in Listing 4.2 and Listing 4.3.

```

1  %% Reads in experimental data
2  % Opens file explorer window - try/catch is used to save the filepath.
3  try
4  [fileName,filePath] = uigetfile({'*.','*'},'Please select Ar TAP pulse',handles.path);
5  catch
6  [fileName,filePath] = uigetfile({'*.','*'},'Please select Ar TAP pulse');
7  end
8  % Open the file and set endFile to 0
9  fid = fopen([filePath fileName]);
10 endfile = 0;
11 % Saves the path to handles structure to keep for later
12 handles.path = filePath;
13 % Reads through each line of the data
14 fprintf('Reading in File\n');
15 while endfile ~= 1
16     % Grabs each line and saves it as a string
17     textdata = textscan(fid,'%s');
18     data = textdata{1,1};
19     % When end of file is reached sets endFile to 1
20     endfile = feof(fid);
21 end
22 fprintf('Finished reading file with %d lines\n',length(data))

```

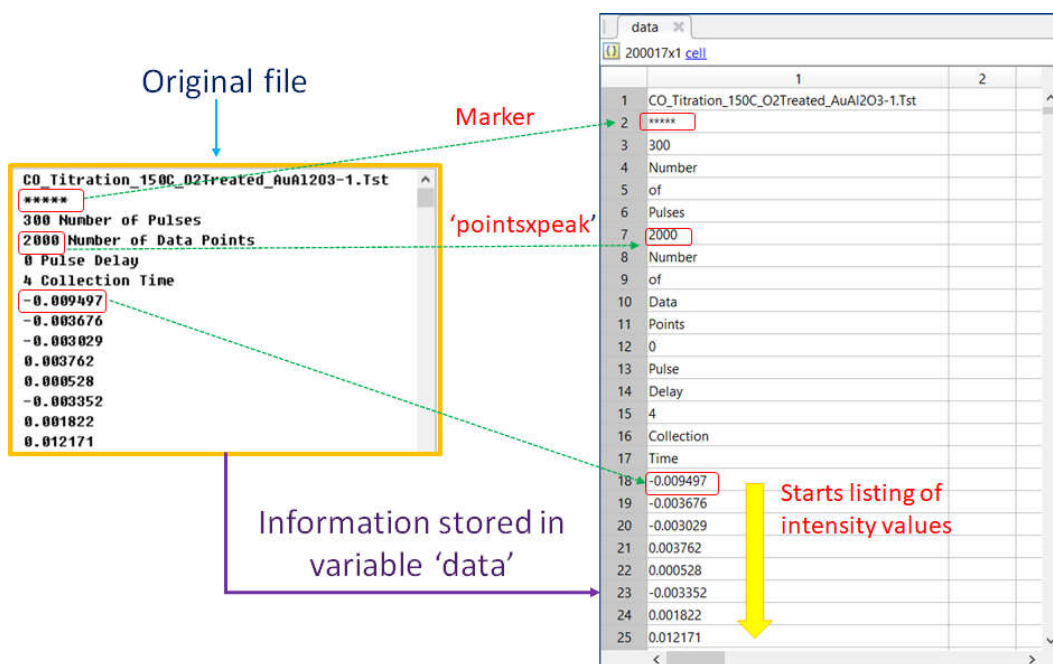
Listing 4.1. Snippet of script used to read in raw experimental data.

The diagram illustrates the file paths and contents for two TAP reactor rigs: Cardiff and Harvard.

Cardiff File: The file path is `C:\Users\lr89\Documents\TAP\Cardiff` and the file name is `500 pulses 5.4 V 20percent O2_Ar_160C 1`. The file content consists of a list of intensity values: 7792.02, 8623.01, 9976.07, 7696.17, 9480.01, 7699.41, 9515.67, 5762.51, 7435.90, 6223.07, 8733.96, 5782.26, and 7201.51. A note indicates: "Only intensity values from start to end of file".

Harvard File: The file path is `C:\Users\lr89\Documents\TAP\Harvard` and the file name is `CO_Titration_150C_O2Treated_AuAl2O3-1.Tst`. The file content includes a header section with experimental conditions: "CO Titration_150C_O2Treated_AuAl2O3-1.Tst", "*****", "300 Number of Pulses", "2000 Number of Data Points", "0 Pulse Delay", "4 Collection Time", "-0.009497", "-0.003676", "-0.003029", "0.003762", "0.000528", "-0.003352", "0.001822", and "0.012171". A red arrow points to the "*****" line, labeled "Marker". A note indicates: "Filename and experimental conditions before listing the intensity values".

Scheme 4.1. Scheme exemplifying what 'filePath' and 'fileName' (see Listing 4.1) refer to and a typical example of a file generated in the TAP reactor rig at Cardiff University and at Harvard University.



Scheme 4.2. Scheme showing how data in an original file (raw data) generated at Harvard University is stored in the variable 'data' after implementing the part of the code showed in Listing 4.1. The presence and location of the marker '*' is used afterward by code showed in Listing 4.2. 'pointsexpeak' refers to the variable with the same name defined in Listing 4.3.

```

26     %% Chooses which data to load
27     str = strsplit(data{1},',');
28     strL = length(str);
29     inldata = 1;
30     %% Looks for '*'
31
32     for i = 1:10
33         if ~isempty(findstr('*',data{i,1}))
34             inldata = isempty(findstr('*',data{i,1}));
35             iloc = i;
36         else
37             continue
38         end
39     end
40
41     try
42         data(2:iloc-1,:) = []; %% Deletes from 'data' all file content other than data points.
43     end

```

Listing 4.2. Script used to discard unnecessary information in experimental file.

As commented above, the code looks for the marker '*'. The presence or absence of this marker not only serves as a tool for discarding unnecessary data but also gives information about the TAP reactor rig that was used when the particular experimental file was obtained. For the case of the work developed in this thesis,

TAP experiments were carried out in two different facilities, the one located at Cardiff University and the one at Harvard University. Identification of the file provenance is crucial since information and its line location will differ depending on that. Accordingly, if our marker '*' is found, the text file was originated at Harvard University, otherwise the data was generated in Cardiff.

Once file source has been identified, as shown in Listing 4.3, the set of conditions such as the number of sample points per gas fire and the time each fire takes are required for further data analysis. These two are called as 'pointsexpeak' and 'timexpeak', respectively (see Listing 4.3). In the case of Harvard text files, such information is also recorded and it is always located in the same lines. Thus, the code goes to those lines and pick them up. For the case of Cardiff text files, they only contain the intensity values for each fire, hence such experimental conditions must be entered manually in the code before running it. Nonetheless, these are often the same for most of the experiments carried out during this work. Therefore, rare manual modification was required.

```

43 - if inldata == 0           % If pointer '*' was found, data is from Harvard.
44 -     fprintf('Data is from Harvard...');
45 -     pointsexpeak = str2double(data{7,1}); % data{7,1} is where the number of pulses per peak is located.
46 -     peakno = (length(data)-17)/pointsexpeak;
47 -     handles.datatype = 2;
48 -     delay = str2double(data{12,1});
49 -     timexfire = str2double(data{15,1});
50 -     str = strjoin(data(18:length(data)));
51 -     d = sscanf(str,'%f');
52 -     data = d;
53 - else                   % If pointer '*' wasn't found, data is from Cardiff.
54 -     fid = fopen([filePath fileName]);
55 -     endfile = 0;
56 -     fprintf('Data is from Cardiff... loading into arrays\n');
57 -     %Reads in Cardiff Data: number of pulses per peak is not located in
58 -     %Cardiff files. It is deduced from the number of pulses and the
59 -     %total number of data point in the whole file.
60 -     pointsexpeak = 1100; % Important!! In this experiment it is 1100 points.
61 -     timexfire = 2; % Important!! In this experiment.
62 -     str = strjoin(data);
63 -     d = sscanf(str,'%f');
64 -     data = d;
65 - end

```

Listing 4.3. Part of the code that identifies which TAP reactor rig was used when the particular data being read was obtained.

From that collected and stored at this point, raw data can be treated in order to extract the desired information. The first step into this data treatment begins with a series of basic mathematical operations that, based on the number of pulses,

chop down the one-column data series in the original file format. The number of pulses is calculated according to Equation 4.1 below:

$$\text{num_of_peaks} = \frac{\text{total_data}}{\text{pointsxpeak}} \quad (4.1)$$

where *total_data* is the total number of intensity data points listed in the original text file. In order to make it easier for the reader to follow up the information, terminology used in Equation 4.1 resembles the one in the code (see Listing 4.4). This practice has been continued whenever it is possible in forthcoming equations regarding the code they refer to.

A relevant feature of the TAP experimental files generated at both Harvard and Cardiff must be pointed out. This is related to the last peak they record, which corresponds to the sum of all the pulses performed throughout the experimental series for a given chemical species (see Figure 4.1). Thus, since it does not carry true kinetic information for a single pulse, it must be removed before any further analysis.

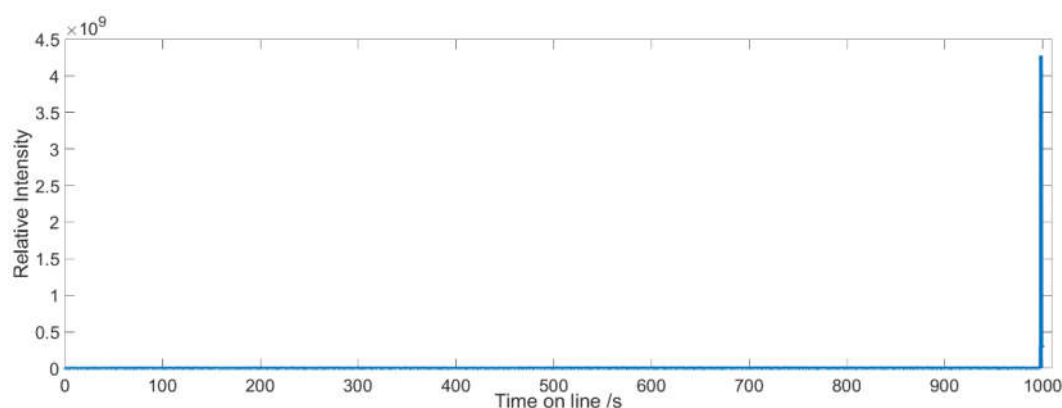


Figure 4.1. Result of plotting all intensity data points versus time.

The removal of the last peak above commented is done in lines 75-77 of Listing 4.4, that results in the effective number of peaks, the so-called 'num_of_peaks_notfinal'. Subsequently, an array for the total time the experiment took can be deduced, as well as the period of time each individual pulse lasts. This is shown in lines 79-80 of Listing 4.4, which applies Equation 4.2 and the Matlab command `linspace`. Figure 4.2 shows the result of plotting intensity versus time after running those code lines.

$$\text{totaltime} = \text{timexfire} \cdot \text{num_of_peaks_notfinal} \quad (4.2)$$

```

71  %% Number of peaks and time array
72  total_data = length(data);
73  num_of_peaks = total_data/pointsxpeak; % Total number of peaks
74
75  nonfinalpeakdata = pointsxpeak * (num_of_peaks - 1); % Discarded the final peak (sum of all peaks)
76  datapeak = data(1:nonfinalpeakdata);
77  num_of_peaks_notfinal = length(datapeak)/pointsxpeak; % Effective number of peaks
78
79  totaltime = timexfire*num_of_peaks_notfinal;
80  t=linspace(0,totaltime,length(datapeak)); % Time array: time for each intensity data point.

```

Listing 4.4. Snippet of the script responsible of calculating the total number of peaks from each pulse response and the respective experimental time.

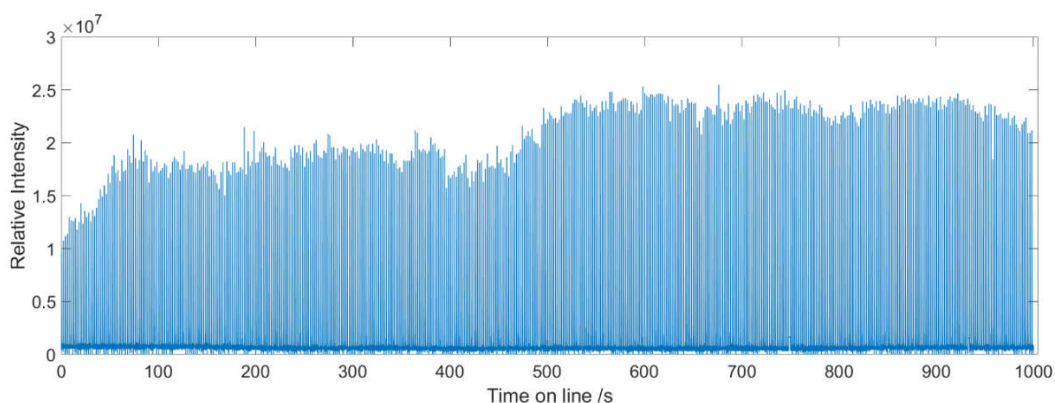


Figure 4.2. Relative intensity versus time showed in Figure 4.1 after removal of data points belonging to the last peak.

4.2 Baseline prediction

Once data has been loaded as described in the previous section, some corrections on the experimentally obtained pulse responses are carried out. The first phase of those corrections is related to the prediction of the baseline for each peak. As shown in Figure 4.3, where a single peak has been isolated from data presented in Figure 4.2, the baseline of experimentally obtained data does not lay along the x-axis at zero ordinate. Thus, corrections on such a baseline must be performed. Although different approaches have been proposed for baseline correction in analytical chemistry^{1,2,3,4,5,6,7}, TAP pulse responses feature long-time tail decays that are difficult to be differentiated from the baseline. This makes it likely that those type of approaches, where an automated algorithm is implemented, would not work for TAP experimental signals. This is the reason why, in this work, an

alternative approach that fits better to the particular characteristics of TAP pulse responses has been implemented.

Listing 4.5 contains the lines of the code responsible of performing such baseline correction. It has been empirically proven, at least at the set of conditions applied in our TAP studies, that peaks obtained as the response for a given species always happen during the first half of the entire time each individual pulse takes. Based on that, line 83 of Listing 4.5 below set a variable called 'base_start'. Therefore, for a particular pulse, which is conformed of a series of data points, 'base_start' will correspond to the position number of the data point located in the middle of such a series. Right after, the variable 'base_end' is also defined, which is used to discard the last ten points of the given pulse. Since usually the last points of the signals tend to be quite noisy and they do not really provide any extra information to the study, it is better to delete those. From line 88 to line 100 of the same Listing 4.5, a loop is set. Thanks to such a loop, the software is going throughout the entire data series, thus through every peak that conform the experimentally obtained pulse response for the particular chemical species being studied. According to those lines, the variable 'base_av' is defined as the average of all the data points located between 'base_start' and 'base_end' previously mentioned. This way, 'base_av' serves as a good estimation of the deviation from the baseline each experimental signal experiences. Once such a deviation is calculated, the corrected peak is created by extracting that from the raw signal. The result after performing this baseline correction is exemplified in Figure 4.3. Regarding the last code lines presented in Listing 4.5, zeroth moments (M_0) are calculated for each peak. According to the moment definition given by Equation 2.21, back to Section 2.4, the area underneath the curve obtained when representing exit flow versus time is calculated, which is equivalent to M_0 . The Matlab function trapz is used for the integration of such an area, which performs numerical integration via the trapezoidal method⁸. Finally, at the end of the loop, zeroth moments, exit flow intensities and respective times are accordingly stored in three different arrays.

```

82  %% Baseline correction and underneath peak area (moment) calculation
83  base_start = pointxpeak/2;           % Peak has already happened from 'base_start'
84  base_end = pointxpeak-10;           % Last data points tend to be very noisy. Discarded last 10.
85  m0_array=[];
86  peaks_array = [];
87  peakttime_array = [];
88  for i=0:num_of_peaks-2
89      start=i*pointxpeak+1;
90      peak=data(start:start+pointxpeak-10); % Last 10 intensity points are discarded
91      peakttime = t(start:start+pointxpeak-10); % Last 10 time points are discarded
92      base_av=mean(peak(base_start:base_end)); % Baseline obtained by averaging values from 'base_start' to 'base_end'
93      peak=peak-base_av;
94
95      m0=trapz(peakttime,peak); % Storage of zero moment calculated for the peak currently being read
96      m0_array=[m0_array,m0]; % Each column of this array contains data for each peak
97
98      peaks_array = [peaks_array,peak]; % Storage of data for the peak currently being read
99      peakttime_array = [peakttime_array,peakttime']; % Each column of this array contains data for each peak
100  end

```

Listing 4.5. Part of the script where baseline correction and zeroth moments calculation are performed, along with the generation of arrays to store collected and generated data.

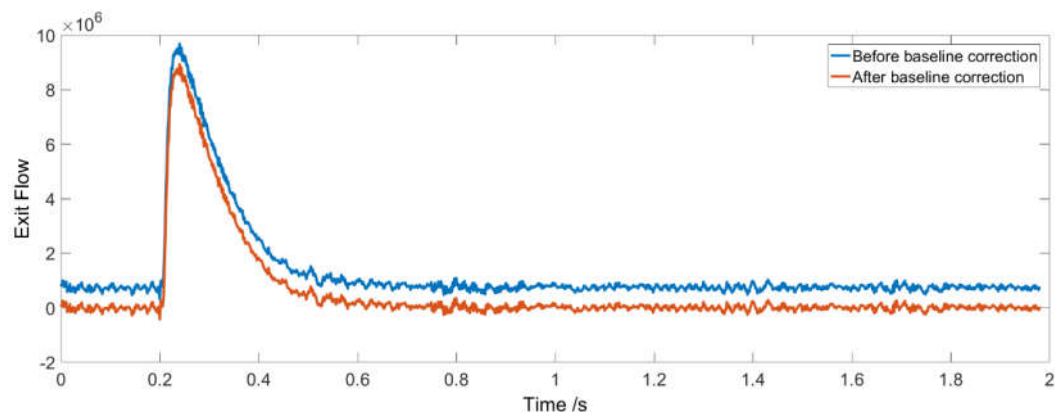


Figure 4.3. Isolated peak from data presented in Figure 4.2, both in its raw form and after applying the baseline correction performed by the part of the code presented in Listing 4.5.

4.3 Height and area normalization

The process described in previous Sections 4.1 and 4.2 is repeated for each one of the species being monitored. Thus, if CO oxidation is the case of the study, where both CO and O₂ along with the internal standard (Ar) are pulsed into the reactor, then, code lines explained in those sections are repeated four times, i.e. Ar, CO, O₂, and CO₂. Thereafter, using the internal standard (Ar), normalization of the obtained peaks should be carried out for a proper comparison among them. Two types of normalization are performed within our software code lines, one based on the peak heights and the other one based on the area underneath those peaks. The height

normalization has qualitative assessment purposes while the area normalization gives the right values for any further quantitative analysis.

According to that commented above, when qualitative assessment of the pulse response is pursued, getting all peaks to have the same height becomes quite useful. As it will be presented and discussed in Chapter 6, Section 6.2, comparative studies of residence and peak times found in the diffusion only curve (Argon) and the rest of species could give a good glimpse into the reaction mechanism taking place. Code lines responsible of performing such a normalization are presented in Listing 4.6. For that, average of all peaks obtained for each of the species is calculated. Then, the maxima of those peaks is taken and used for their normalization according to Equation 4.3.

$$peak_{height_norm} = \frac{mean\ peak}{peak_{max}} \quad (4.3)$$

where $peak_{height_norm}$ is the normalized peak (referred as arrays in lines 1128-1131, Listing 4.6) and $mean\ peak$ (lines 1118-1121) is the average of the entire pulse response for a given species, with $peak_{max}$ ('max' in lines 1123-1126) being its maxima.

According to the comments lined through the code, above process can be followed in Listing 4.6 below.

```

1117 %% Height normalization
1118 - mean_peaks_array_Ar_norm = mean(peaks_array_Ar,2); %Average of all Argon peaks
1119 - mean_peaks_array_CO_norm = mean(peaks_array_CO,2); %Average of all CO peaks
1120 - mean_peaks_array_O2_norm = mean(peaks_array_O2,2); %Average of all O2 peaks
1121 - mean_peaks_array_CO2_norm = mean(peaks_array_CO2,2); %Average of all CO2 peaks
1122 % Picking up the maximum value of the average peaks:
1123 - max_Ar = max(mean_peaks_array_Ar_norm);
1124 - max_CO = max(mean_peaks_array_CO_norm);
1125 - max_O2 = max(mean_peaks_array_O2_norm);
1126 - max_CO2 = max(mean_peaks_array_CO2_norm);
1127 % Height normalised peaks:
1128 - peaks_array_Ar_height_norm = mean_peaks_array_Ar_norm/max_Ar;
1129 - peaks_array_CO_height_norm = mean_peaks_array_CO_norm/max_CO;
1130 - peaks_array_O2_height_norm = mean_peaks_array_O2_norm/max_O2;
1131 - peaks_array_CO2_height_norm = mean_peaks_array_CO2_norm/max_CO2;
1132 % Plotting height normalised peaks
1133 - figure
1134 - plot(peaktime_array_Ar(:,1),peaks_array_Ar_height_norm);
1135 - hold on
1136 - plot(peaktime_array_O2(:,1),peaks_array_O2_height_norm);
1137 - plot(peaktime_array_CO(:,1),peaks_array_CO_height_norm);
1138 - plot(peaktime_array_CO2(:,1),peaks_array_CO2_height_norm);
1139 - xlabel('Time/s')
1140 - ylabel('Height Normalised Exit Flow')
1141 - legend('Argon','O2','CO','CO2')

```

Listing 4.6. Height normalization of the obtained pulse response.

Regarding the area normalization, this is the one that should always be done prior to any quantitative analysis. Experimental results presented in Chapter 6, Section 6.3, are all in line with this kind of normalization. Knowing the gas composition of the gaseous mix being pulsed into the reactor is essential since the ratio reactant/inert ($ratio_{mix}$) will be used along the course of the calculations. For the case of the example showed in Listing 4.7, which correspond to an experiment where 20 % CO/Ar was fired into the TAP reactor, this can be checked in line 3. Then, in lines 4-9, a loop is taking place. This allows calculation of conversions along with reactant and inert area normalized peaks for the entire experimental pulse series. Equations 4.4-4.7 are applied in those lines.

$$r^{t=0}_{(i)} = M_{0_inert(i)} \cdot ratio_{mix} \quad (4.4)$$

where $r^{t=0}$ is proportional to the number of reactant molecules entering the reactor and M_{0_inert} is the zeroth moment calculated for the internal standard (inert), both related to their pulse response number i . Since our instrument can only monitor one mass at a time, the inert pulse measurement used as a reference for normalisation is just the most recent pulse of inert and not the same pulse as used for the measurement of a reactant/product zeroth moment. Results showed at the end of Section 4.4.3 validates this approach.

$$X_i = \frac{M_{0_inert(i)} \cdot ratio_{mix} - M_{0_r(i)}}{M_{0_inert(i)} \cdot ratio_{mix}} \quad (4.5)$$

where X is the conversion and M_{0_r} the zeroth moment calculated for the reactant.

$$Rp_{aN(i)} = \left(\frac{Rp(i)}{M_{0_r(i)}} \right) \cdot (1 - X_{(i)}) \quad (4.6)$$

where Rp_{aN} is the area normalized version of Rp , both referring to the pulse response of a reactive species.

$$Ip_{aN(i)} = \left(\frac{Ip(i)}{M_{0_inert(i)}} \right) \quad (4.7)$$

Ip_{aN} refers to the area normalized version of Ip , both referring to the pulse response of the internal standard being used.

Similarly, product pulse response should also be area normalized with reference to the inert. For the specific case of this study, a single product, CO₂, is produced. Thus, Equation 4.8 is applied.

$$Pp_{aN(i)} = \left(Pp^{(i)} / M_{0,p(i)} \right) \cdot X_{(i)} \quad (4.8)$$

where Pp_{aN} is the area normalized version of Pp , both referring to the pulse response of the single product yielded in the reaction. $M_{0,p}$ is the product zeroth moment.

```

1  %% Area normalised peaks
2  % Reactants:
3  ratiomixCO_Ar = 20/80; %Percentages of gases must be checked before running. In this case 20% CO/Ar
4  for i = 1:length(m0_array_Ar)
5      %Conversion = (pulsesize - measured)/pulsesize;
6      X(i) = (m0_array_Ar(i)*(ratiomixCO_Ar) - m0_array_CO(i))/(m0_array_Ar(i)*(ratiomixCO_Ar));
7      peaks_array_CO_norm(:,i) = peaks_array_CO(:,i)/m0_array_CO(i)*(1-X(i)); % (1-X) = CO unconverted
8      peaks_array_Ar_norm(:,i) = peaks_array_Ar(:,i)/m0_array_Ar(i);
9  end
10 % Products:
11 for i = 1:length(m0_array_ArtoCO2)
12     peaks_array_CO2_norm(:,i) = peaks_array_CO2(:,i)/m0_array_CO2(i)*(X(i));
13 end

```

Listing 4.7. Area normalization of the obtained pulse response.

4.4 Rejection of bad quality signals

The different parts of the code described and discussed in above Sections 4.1-4.3 constitute an essential that allow the analysis of experimental TAP reactor results. The outcome of applying such a code would contain every pulse response of the experimental series. Thus, no discrimination is made. Nonetheless, this could become an issue when it comes to the calculation of moments. Since this implies the integration of the area underneath the curve responses and such an integration is performed by the software in an automatic way, it could happen that the final result of such an integration is not representative of the actual experiment. This is mainly due to the fact that, occasionally, the instrument misfires and produces an unusually small pulse which cannot be spotted out from the noise the signal carries. However, some experimentally observed phenomena which involves random peaks with a strong negative area contribution is also a source of inaccuracy. In essence, experimentally obtained TAP reactor pulse responses not always come with good enough quality. Thus, a nice ratio peak/noise with a constant stable baseline, as

that showed in Figure 4.4, is not always the case. Subsections 4.4.1 and 4.4.2 focus on the discussion of that implemented in an attempt to sort out these issues.

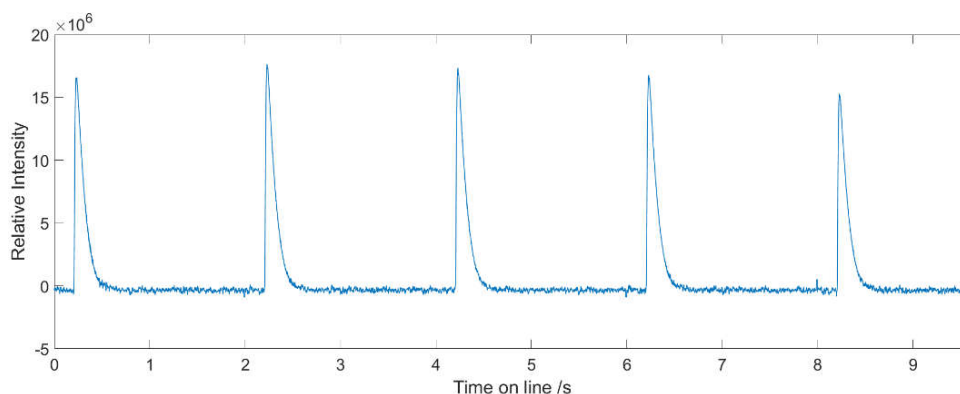


Figure 4.4. Fragment of an experimentally obtained pulse response which represents an example of a good quality signal.

4.4.1 Rejection of high ratio noise/peak signals (Method 1)

There are times when the degree of noise is so high and the detected signal for the particular species is so weak, that it is impossible to differentiate one from another. This is exemplified in Figure 4.5, where one of the peaks was isolated from a 500 pulses experimental series. The higher the degree of noise in a signal, the lower the accuracy of the calculation. In theory, if no signal is detected for a given chemical species, a null value of the moment should be obtained. However, in practice, if the signal carries significant noise with it, such a moment could greatly differ from that zero value. Rejection of this kind of responses should be carried out prior to the calculation of moments. Listing 4.8 shows the code lines that were implemented with that purpose. As previously commented in Section 4.3, peaks obtained as the response for a given species always happen during the first half of the entire time each individual pulse takes. Thus, the maxima found within that first section would correspond to the peak maxima. Then, doing the same for the second section would give information of the maximum intensities the noise reach. Calculating the ratio of the maximas obtained in that way could therefore serve as an indicative of the possibility or not of distinguishing peak from noise for that particular pulse response. Accordingly, line 141 (Listing 4.8) uses such a ratio and compares it to a

threshold. This way, if ratio peak/noise is smaller than 1.1, that pulse response is rejected. The threshold value of 1.1 was chosen based on the empirical observation that any ratio below it meant not observable distinction between the actual peak and the noise.

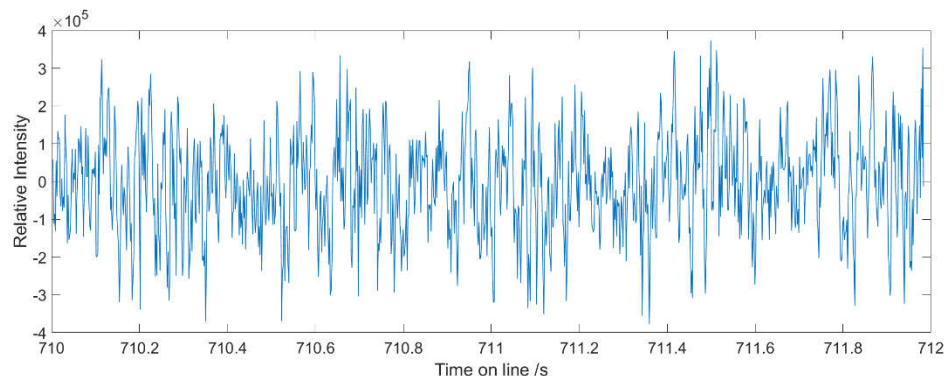


Figure 4.5. Pulse response number 356, isolated from a 500 Argon pulses experimental series.

```

135  %% Discarding too small peaks (ratio peak/noise <= 1.1)
136  peak_section = 500; % Each pulse has around 1000 points, peak should located in the first haft
137  max_peak = max(peak(1:peak_section)); % Finds the maxima in the first half, i.e. peak maxima
138  max_noise = max(peak(peak_section:end)); % Finds the maxima in the second haft, i.e. maxima within noise signal
139  ratio_peak_to_noise = max_peak/max_noise;
140  % if ratio (peak maxima/noise maxima) is smaller than 1.1:
141  if ratio_peak_to_noise < 1.1
142      for i = 1:length(peak)
143          peak(i) = 0; % whole pulse = 0, so it is still in peaks_array, but m0 will be 0
144      end
145  end

```

Listing 4.8. Snippet of the code containing the lines responsible of rejecting signals with very high degree of noise.

4.4.2 Rejection of high ratio negative/positive area signals (Method 2)

Despite some improvement in the accuracy of the zeroth moment calculation achieved after the implementation of the code discussed in above subsection (examples in Section 4.4.3), further progress was required in order to discriminate signals such as those exemplified in Figures 4.6 and 4.7. As observed in the former, the first peak baseline is below the horizontal axis at zero ordinate. Integration of

the area underneath such a curve would yield a negative value of M_0 , which would have no physical meaning. In the case of Figure 4.7, a very noisy signal is observed. Although peaks can still be spotted from that noise, integration of the area underneath the first of those peaks would also give a negative value of M_0 . Thus, in order to deal with these cases, another addition was made to our TAP software code, presented in Listing 4.9. Similar to that done previously, the maxima within the first half of the signal is searched. This is then coupled with the index where that maxima occurs, which is called 'lpeak'. Subsequently, the software sweeps the signal from lpeak towards its end looking for the first data point with an intensity value lower or equal to zero. When it is found, that is set as the endpoint of the peak and its tail. Lines 148-156 in Listing 4.9 performs such a process. Subsequently, trapz is used here again to calculate the area underneath the peak section and the one obtained from integrating the second section. Notice here that any value different from zero obtained from that second section area integration will be due the noise itself. Accordingly, the area integration from first and second sections were called 'areaonlypeak' and 'areaonlynoise', respectively. In a similar way as that explained in previous subsection, ratios were calculated to give an indicative of the degree of noise in the signal and how it compares with the intensity of the peak. In this case, though, areas instead of maximas are considered. Thus, in Line 164, the ratio 'areaonlynoise'/'areaonlypeak' is calculated. The absolute value of such a ratio is also applied as it will be used as 'threshold' in the next lines. Finally, a loop is opened and it will only be closed once the entire experimental data has been analysed. In particular, in order to keep or discard a particular curve, two conditions are set:

- Condition 1. 'areaonlynoise' < 0 and 'threshold' \geq 0.5:

If the curve features these conditions, it is discarded. This is because such a pulse response not only presents a negative area contribution from the second part of the signal (or a negative 'areaonlynoise') but, also, the area underneath the peak is not significantly bigger than that coming from the noise.

- Condition 2. Ratio 'areaonlynoise'/'areaonlypeak' \geq 1/1.1:

If the area underneath the peak section is smaller or equal to 1.1 times the area coming from the noise section of the signal, the pulse response is discarded.

Examples of the results from application of this approach (corresponding to Listing 4.9) are presented and discussed in Section 4.4.3.

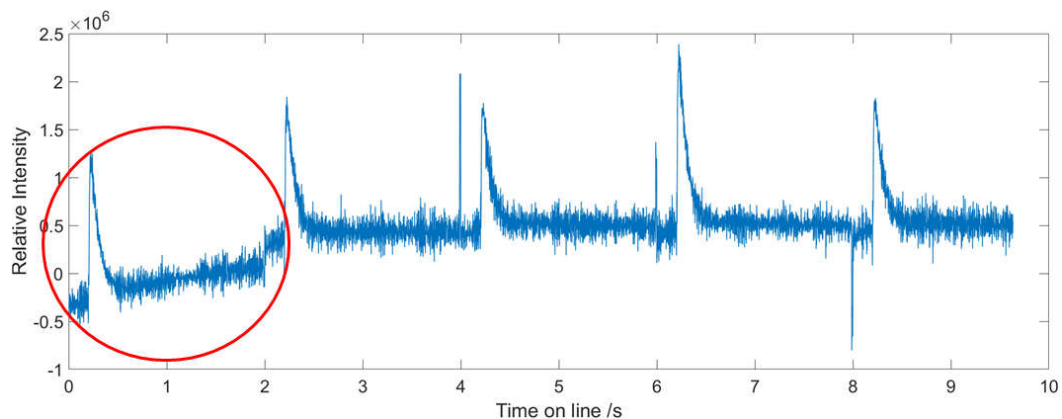


Figure 4.6. Fragment of an experimentally obtained pulse response. Surrounded in red is the first of the peaks which baseline is, for its most part, below the horizontal axis at $y = 0$.

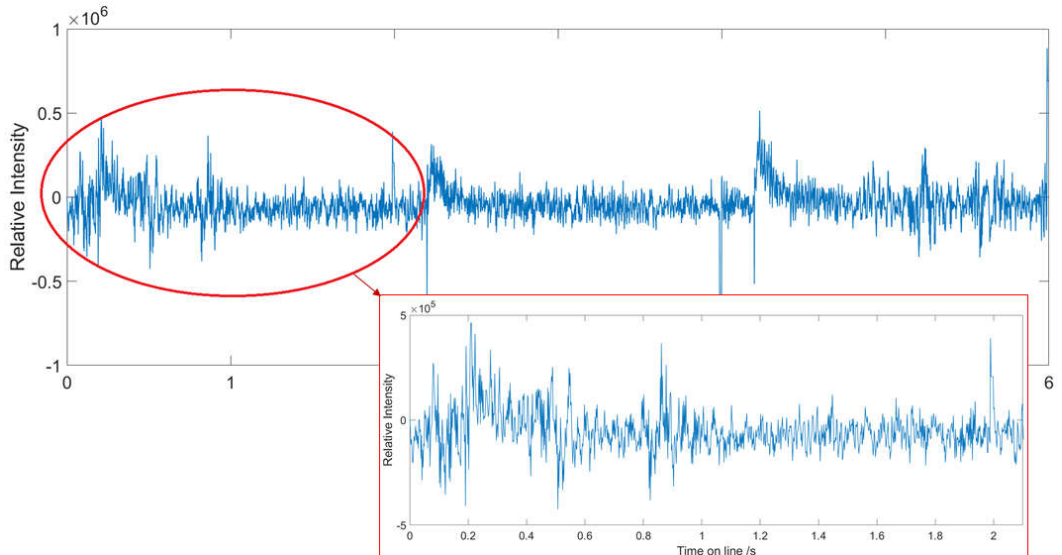


Figure 4.7. Fragment of an experimentally obtained pulse response which show three of the peaks. Noise is quite relevant in the three cases with the most acute case being the first one (zoomed and surrounded in red). The calculation of M_0 from this first pulse response would yield a negative value.

```

147 % Discarding peaks with too big contribution from negative areas
148 [Mpeak, Ipeak] = max(peak(1:peak_section)); % Finds not only the maximum value in first 500 points but the index for that value (Ipeak)
149 for i=Ipeak:length(peak)
150     if peak(i) <= 0
151         calculateareafromhere=i; % First y<=0 after peak maxima is considered the end point for m0 calculation, rest must be noise
152         break
153     else
154         continue
155     end
156 end
157
158 onlypeak = peak(1:calculateareafromhere); % Taking part of the pulse from i=1 to i=calculateareafromhere
159 onlypeaktme = peaktime(1:calculateareafromhere); % Taking time frame from i=1 to i=calculateareafromhere
160 onlynnoise = peak(calculateareafromhere:end); % Taking part of the pulse from i=calculateareafromhere to i=end
161 onlynnoisetme = peaktime(calculateareafromhere:end); % Taking time frame from i=calculateareafromhere to i=end
162 areaoonlypeak=trapz(onlypeaktme,onlypeak); % Area underneath peak
163 areaoonlynoise=trapz(onlynoisetme,onlynoise); % Noise contribution to area
164 ratio_noise_to_peak = areaoonlynoise/areaoonlypeak; % Opposite to ratio_peak_to_noise, but comparing areas underneath instead of maximas
165 threshold = abs(areaoonlynoise)/areaoonlypeak; % Same as ratio_noise_to_peak but taking the absolute value of areaoonlynoise
166 % Rejection of peaks with too big negative contribution or too small peaks:
167 if areaoonlynoise < 0 && threshold >= 1/2 || ratio_noise_to_peak >= 1/1.1
168     for i = 1:length(peak)
169         peak(i) = 0; % whole pulse = 0, so it is still in peaks_array, but m0 will be 0
170     end
171 end

```

Listing 4.9. Part of the script responsible of discarding pulse responses with a very high degree of noise or with a significant negative area contribution coming from it.

4.4.3 Comparison between Method 1 and Method 2

A visual comparison of both rejection methods, Method 1 and Method 2 (discussed in subsections 4.4.1 and 4.4.2, respectively) could give more light into the field of action of those methods and their effectiveness. For that comparison, Argon and CO zeroth moments (M_{0_Ar} and M_{0_CO} , respectively) have been calculated from a TAP experiment where 500 pulses of a gaseous mix consisting of 20 % CO/Ar were pulsed over an inert packed reactor (SiC). The obtained values of these moments for each pulse are represented in Figures 4.8 and 4.9, where an obvious decay is appreciable. This is due to an instrumental problem of the Cardiff TAP reactor unit related to the decrease in the intensity of the pulse over time. This issue derives in a very high degree of dispersion, which translates in the large standard deviations (σ) presented in Table 4.1. Figures 4.8 and 4.9 give example of the effect the application of Method 1 and Method 2 over untreated experimental data has. As seen in those figures, negative values of both M_{0_Ar} and M_{0_CO} are partially eliminated after applying Method 1 and completely eliminated after applying Method 2. Nonetheless, rejection of those negative values is not the only sign to verify the good performance of these methods. As it was discussed in previous sections, these approaches are based on refusing those pulses with a low peak-to-

noise ratio and those with a high negative area contribution (discussed in Section 4.4.1 and 4.4.2). This means that even positive values of M_{0_Ar} and M_{0_CO} could present those features and therefore being eliminated when applying one of these methods. Thus, in order to get a better idea of the related improvement, average values and respective σ have also been calculated for each rejection method and for the combination of both (Table 4.1). Looking at those values, it seems that Method 2 performs better than Method 1, although it is the combination of both which gives the greater reduction in the standard deviation relative to the average value.

The M_{0_ratio} for each of the 500 pulses has also been calculated according to Equation 4.9.

$$M_{0_ratio(i)} = \frac{M_{0_Ar(i)}}{M_{0_CO(i)}} \quad (4.9)$$

where M_{0_Ar} is the zeroth moment calculated from the argon signal and M_{0_CO} the zeroth moment calculated from the CO signal, both related to its respective pulse response number i .

Figures 4.10-4.13 show values from application of Equation 4.9 to data presented in Figures 4.8 and 4.9. Average M_{0_ratio} and respective standard deviation have also been included in Table 4.1. Although the σ of the M_{0_ratio} from application of Method 2 does not seem to be improved, the resulted value of $M_{0_ratio} = 3.2$ was the closest to the expected value of 4 (20 % CO/Ar). Nonetheless, the error was the smallest when both rejection methods (Method 1 and Method 2) were combined, which gave an average M_{0_ratio} of 2.8.

It is important to remind here that both methods can only act on the cases where noise plays a noticeable role. Since most part of data dispersion is due to the pulse valve getting trouble at firing a consistent volume of gas, the inclusion of these rejection methods in the code can only diminish such dispersion in a small degree.

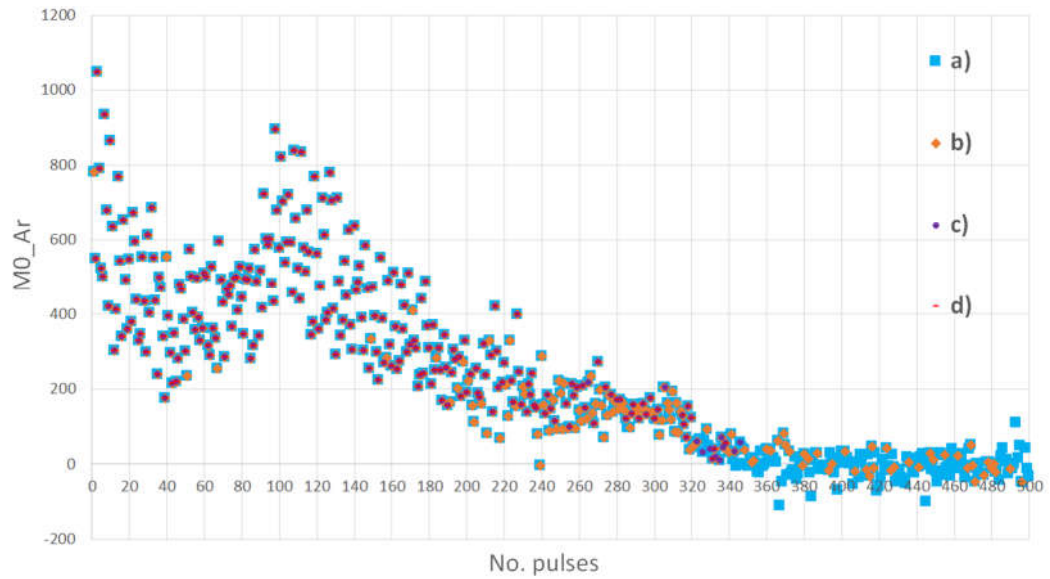


Figure 4.8. M_{0_Ar} versus number of pulses from an experimental series where 500 pulses of 20 % CO/Ar were fired into an inert packed reactor with a voltage of 5.1 V: a) without applying any rejection method, b) after application of Method 1, c) after application of Method 2 and d) after applying both Method 1 and Method 2 combined.

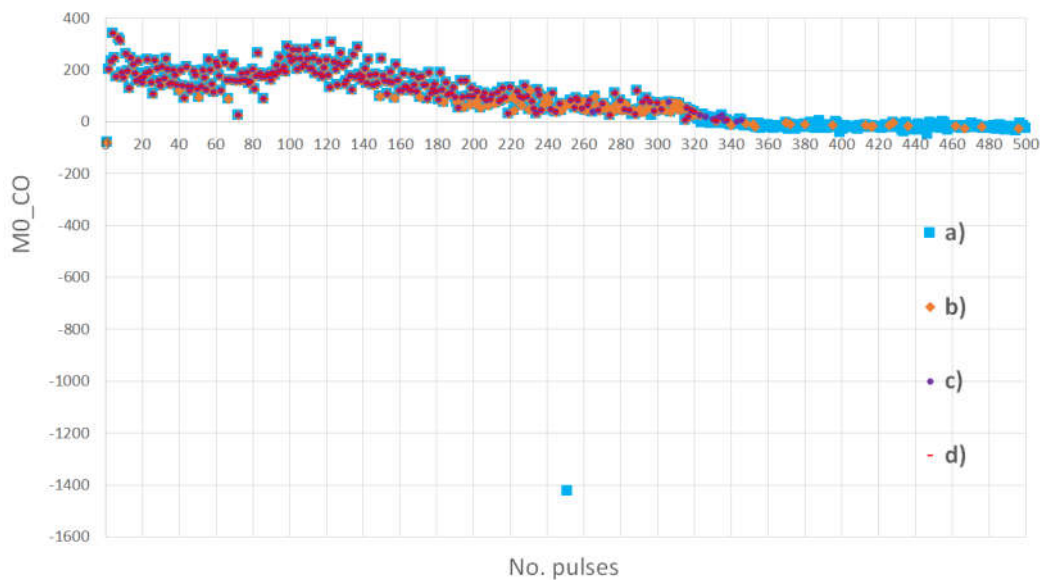


Figure 4.9. M_{0_CO} versus number of pulses from an experimental series where 500 pulses of 20 % CO/Ar were fired into an inert packed reactor with a voltage of 5.1 V: a) without applying any rejection method, b) after application of Method 1, c) after application of Method 2 and d) after applying both Method 1 and Method 2 combined.

after application of Method 2 and d) after applying both Method 1 and Method 2 combined.

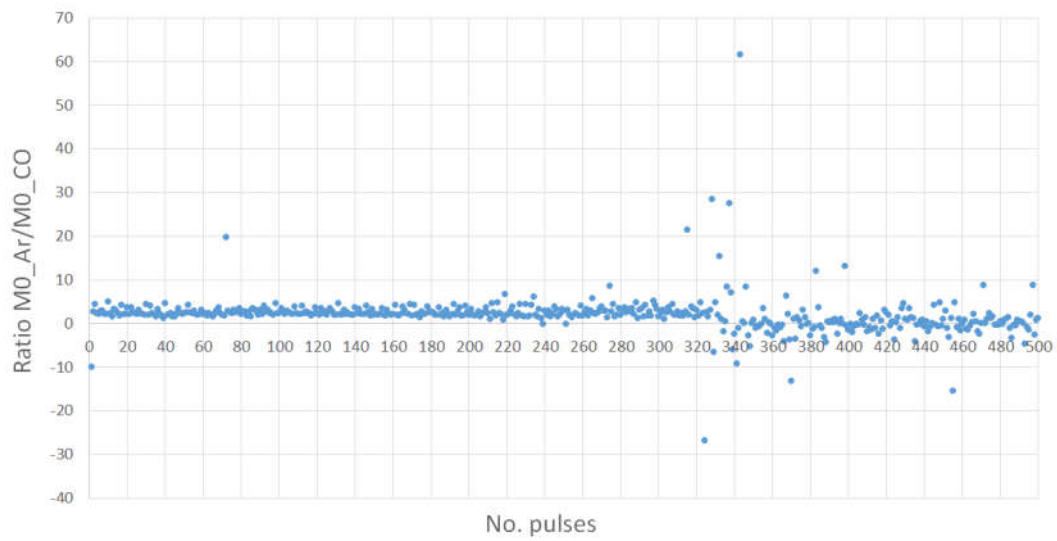


Figure 4.10. M_{0_ratio} versus number of pulses from data presented in Figures 4.8a and 4.9a, i.e. no filtering has been applied (raw data).

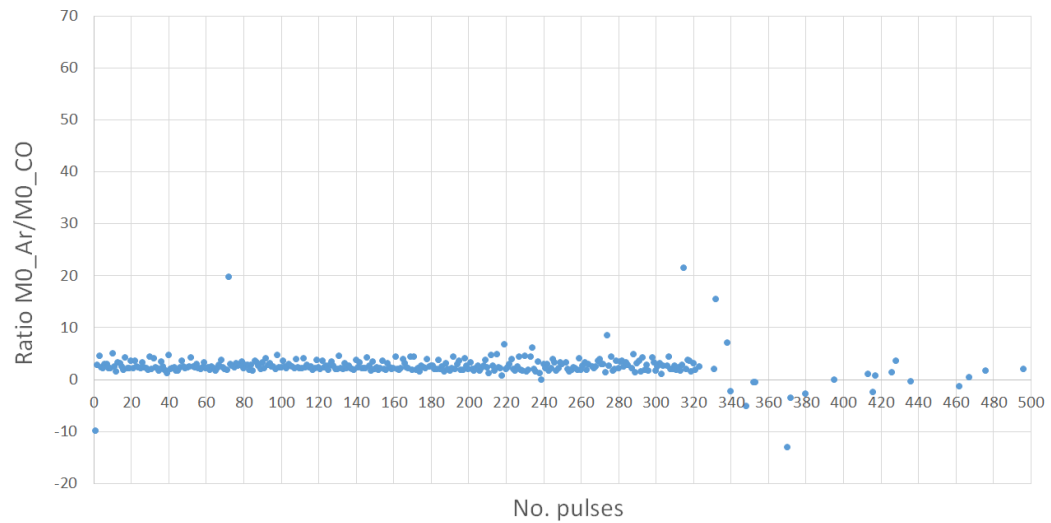


Figure 4.11. M_{0_ratio} versus number of pulses from data presented in Figures 4.8b and 4.9b, i.e. after applying Rejection Method 1.

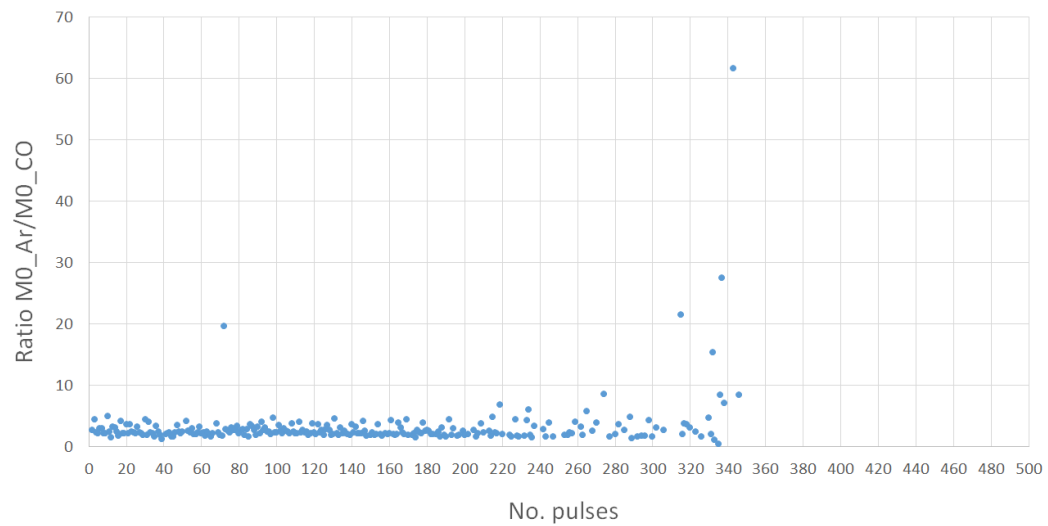


Figure 4.12. M_{0_ratio} versus number of pulses from data presented in Figures 4.8c and 4.9c, i.e. after applying Rejection Method 2.

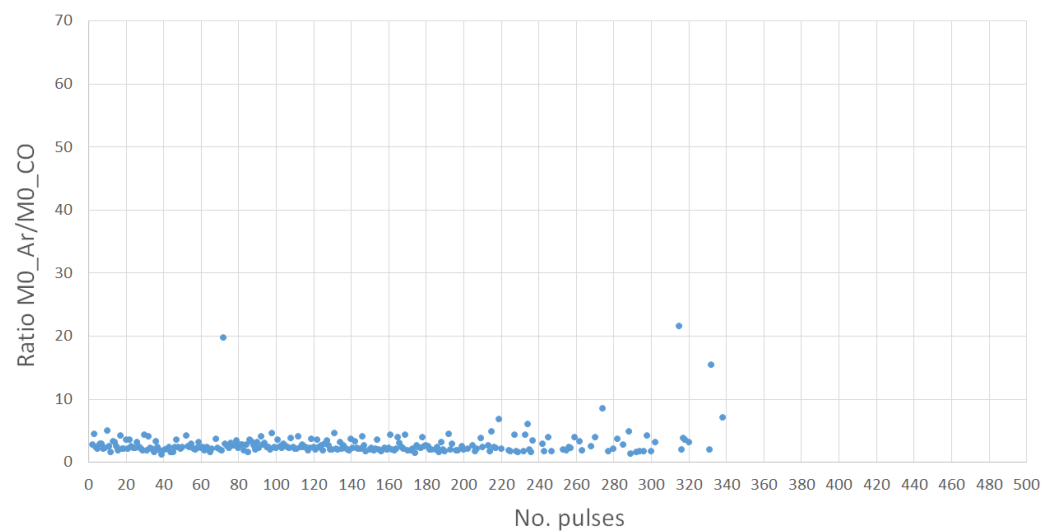


Figure 4.13. M_{0_ratio} versus number of pulses from data presented in Figures 4.8d and 4.9d, i.e. after applying both Method 1 and Method 2 combined.

Table 4.1. Average values and standard deviations (σ) calculated from data presented in Figures 4.8-4.13. N refers to the respective number of data points considered for those calculations.

	Raw	Method 1	Method 2	Combination
M_{0_Ar}	219.7 ($\sigma = 224.7$) (N = 500)	295.6 ($\sigma = 212.1$) (N = 372)	376.3 ($\sigma = 196.6$) (N = 258)	389.8 ($\sigma = 189.3$) (N = 247)
M_{0_CO}	77.3 ($\sigma = 113.8$) (N = 500)	104.8 ($\sigma = 87.1$) (N = 398)	148.8 ($\sigma = 71.5$) (N = 258)	154.5 ($\sigma = 67.4$) (N = 274)
M_{0_ratio}	2.0 ($\sigma = 4.4$) (N = 500)	2.6 ($\sigma = 2.2$) (N = 338)	3.2 ($\sigma = 4.5$) (N = 258)	2.8 ($\sigma = 2.1$) (N = 247)

Figures 4.14 and 4.15 are presented as examples of the above mentioned limited area of action of these rejection methods. Data presented in these two figures corresponds to a TAP pulse experiment where the voltage applied was slightly increased. It is expected that the higher the voltage the bigger the signal detected by the mass spectrometer, thus the higher the intensity of the peak and the less relevant the noise is. Looking at Figures 4.14 and 4.15 and comparing them with those previously discussed for a lower voltage (Figures 4.8 and 4.9), it is obvious that the increase in voltage translates in an absence of negative M_0 -values and an, overall, in a better ratio peak-to-noise. Consequently, average values presented in Table 4.2 are essentially the same for raw and treated data. Although large standard deviations for both M_{0_Ar} and M_{0_CO} were obtained in this case too (see Table 4.2), M_{0_ratio} values showed a much lower dispersion (see Figure 4.16), with average values of 3 in all cases and σ of 0.4 (Table 4.2). This is in accordance with above results obtained by application of Method 2 alone and when combined with Method 1 (see Table 4.1), where M_{0_ratio} values of 3.2 and 2.8 were calculated, respectively. The fact the 20 % CO/Ar was the gaseous mix used and a ratio around 3 instead of 4 was repeatedly obtained suggests that instrumental problems were playing an important role in the measurements. Nonetheless, these results also serve as evidence that, as long as the voltage is high enough to avoid very low peak-to-noise ratios, a consistent M_{0_ratio} is obtained, thus validating the use of the most

recent pulse of inert as a reference for normalisation purposes (discussed in Section 4.3).



Figure 4.14. M_{0_Ar} versus number of pulses from an experimental series where 500 pulses of 20 % CO/Ar were fired into an inert packed reactor with a voltage of 5.3 V: a) without applying any rejection method, b) after application of Method 1, c) after application of Method 2.

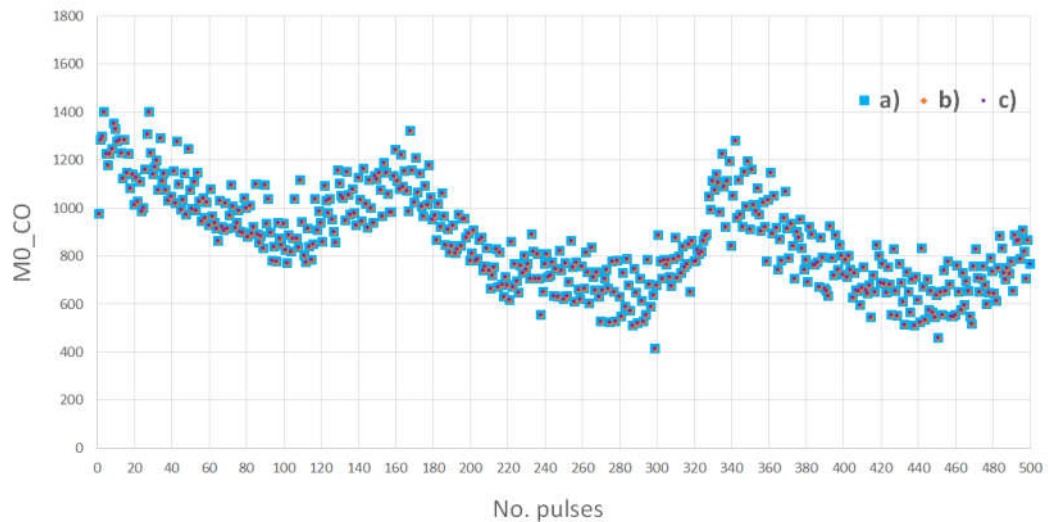


Figure 4.15. M_{0_CO} versus number of pulses from an experimental series where 500 pulses of 20 % CO/Ar were fired into an inert packed reactor with a voltage of 5.3 V: a) without applying any rejection method, b) after application of Method 1, c) after application of Method 2.

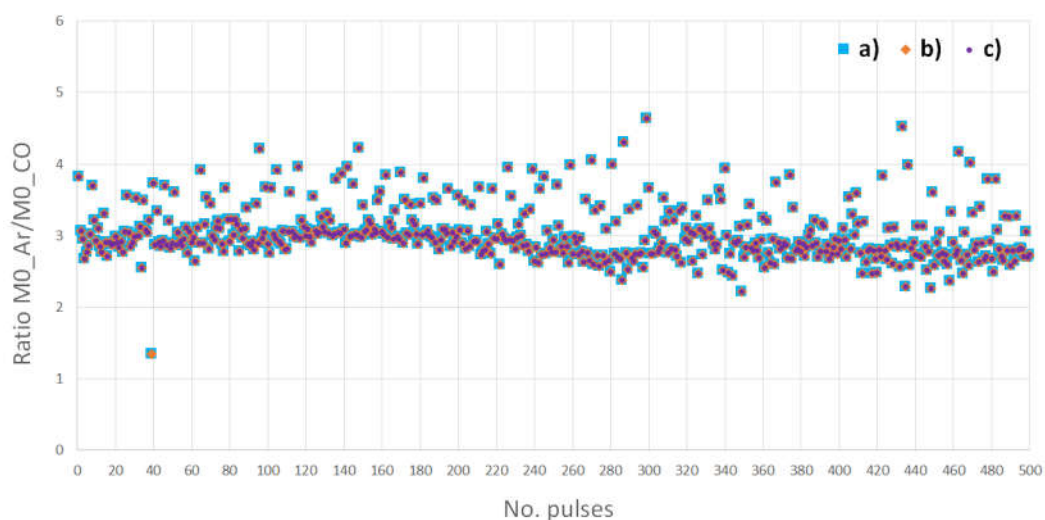


Figure 4.16. M_{0_ratio} versus number of pulses from data presented in Figures 4.14 and 4.5: a) without applying any rejection method, b) after application of Method 1, c) after application of Method 2.

Table 4.2. Average values and standard deviations (σ) calculated from data presented in Figures 4.14 -4.16. N refers to the respective number of data points considered for those calculations.

	Raw	Method 1	Method 2
M_{0_Ar}	2612.2 ($\sigma = 642.8$) (N = 500)	2612.2 ($\sigma = 644.1$) (N = 500)	2610.4 ($\sigma = 643.5$) (N = 499)
M_{0_CO}	867.6 ($\sigma = 209.2$) (N = 500)	867.6 ($\sigma = 209.0$) (N = 500)	864.2 ($\sigma = 194.3$) (N = 499)
M_{0_ratio}	3.0 ($\sigma = 0.4$) (N = 500)	3.0 ($\sigma = 0.4$) (N = 500)	3.0 ($\sigma = 0.4$) (N = 499)

4.5 Summary

This chapter has been dedicated to describe and discuss the different functionalities of the software developed as part of our kinetic study using the TAP reactor approach. The way the code loads and reads raw data as well as the necessary file format modifications carried out for the forthcoming calculations

were the focus of Section 4.1. Then, in Section 4.2, the importance of performing a baseline correction and the way this is implemented within the software code was pointed out. Once signals have been accordingly treated, normalization of those constitute an essential part to properly develop comparative kinetic studies among the different chemical species on focus. Section 4.3 was dedicated to explain the two different versions of normalization applied in our studies and the practical applications of both of them. Finally, since plenty of data is obtained in a single TAP pulse series, discarding bad quality signals become affordable and it works towards a higher degree of accuracy when it comes to the calculation of moments. Two different methods were implemented in this TAP reactor analysis software, each of them discussed and compared in Section 4.4. Data presented in the same section also highlighted that the instrument parameters, in particular the pulse valve voltage, are key to obtaining reliable data. If voltage is too low over long times, the signal height drops so that pulses become indistinguishable from the electrical noise.

References

- 1 Z. M. Zhang, S. Chen and Y. Z. Liang, *Analyst*, 2010, **135**, 1138–1146.
- 2 Z. M. Zhang, S. Chen, Y. Z. Liang, Z. X. Liu, Q. M. Zhang, L. X. Ding, F. Ye and H. Zhou, *J. Raman Spectrosc.*, 2010, **41**, 659–669.
- 3 J. Carlos Cobas, M. A. Bernstein, M. Martín-Pastor and P. G. Tahoces, *J. Magn. Reson.*, 2006, **183**, 145–151.
- 4 A. F. Ruckstuhl, M. P. Jacobson, R. W. Field and J. A. Dodd, *J. Quant. Spectrosc. Radiat. Transf.*, 2001, **68**, 179–193.
- 5 Y. Z. Liang, A. K. M. Leung and F. T. Chau, *J. Chemom.*, 1999, **13**, 511–524.
- 6 H. F. M. Boelens, R. J. Dijkstra, P. H. C. Eilers, F. Fitzpatrick and J. A. Westerhuis, *J. Chromatogr. A*, 2004, **1057**, 21–30.
- 7 V. Mazet, C. Carteret, D. Brie, J. Idier and B. Humbert, *Chemom. Intell. Lab. Syst.*, 2005, **76**, 121–133.
- 8 Trapezoidal numerical integration - MATLAB trapz - MathWorks United Kingdom, <https://uk.mathworks.com/help/matlab/ref/trapz.html#bua4lsr>.

5 | Flow Reactor

5.1 Selection of optimal experimental conditions

Before heading to run reactions, it is necessary to specify those experimental conditions that keep our reactions within the desired path, which would be different depending on reaction type and purpose of the study. Therefore, in the case of this study, the desired path is described by the following considerations:

a. Chemical reaction of interest.

Reaction 5.1 shows the thermodynamic form of the reaction we focus on, where CO_2 from the oxidation of CO is produced.



Reaction 5.1. CO oxidation reaction.

b. General thermodynamic characteristic of the reaction.

As shown in Reaction 5.1, the reaction is exothermic and so heat is released (ΔH is negative) in conjunction with products. Since our system runs at constant pressure, this heat is equal to the change in the enthalpy of the system (ΔH). It can be stated that the reaction is thermodynamically favourable as long as the temperature times the change in the entropy of the system ($T\Delta S$) is a positive value or a negative value smaller than ΔH . This is given by Equation 5.1, which defines the Gibbs free energy (ΔG) of a system that occurs during a reaction run at constant pressure and temperature.

$$\Delta G = \Delta H - T\Delta S \tag{5.1}$$

Notice here that the reaction of interest in our study (Reaction 5.1), is going from 3 mols of reactants to 2 mols of products, both in a gaseous state. Thus, our system undergoes a higher to lower disorder transition or, in other words, a change from

a higher to lower entropy. Therefore, the term ΔS in equation 5.1 would be negative. On the other hand, the CO oxidation reaction is known to be highly exothermic, which implies a highly negative ΔH (see Figure 5.1). All in all, for the reaction to be spontaneous, a negative Gibbs free energy (ΔG) is required. Consequently, in order to satisfy such spontaneity, the system must be kept at low enough temperatures so that, as mentioned above, the value of the term $T\Delta S$ is maintained below that of ΔH . Nonetheless, according to the data presented in Figure 5.1, which evidences enthalpies of reaction around -280 kJ mol^{-1} for a wide temperature range, the temperature of the system can actually be increased to quite high temperatures while preserving the spontaneity of the reaction. This is because $\Delta H - T\Delta S < 0$, and hence $\Delta G < 0$. Therefore, for the case of this present work, where maximum tested temperatures were below 100°C , the transition to a positive Gibbs free energy (ΔG) is not a matter of concern. Nonetheless, how the released heat affects the reaction profile must be considered. This is discussed below.

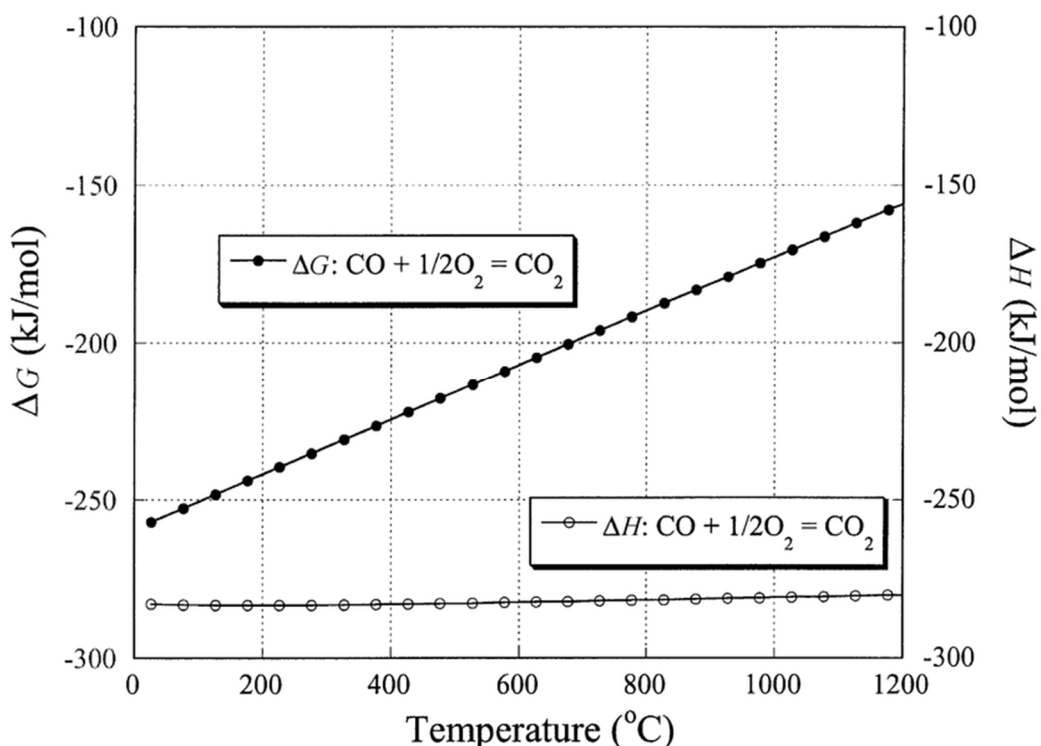


Figure 5.1. The temperature dependence of H (enthalpy) and G (Gibbs free energy) for the $\text{CO} + 1/2 \text{O}_2 = \text{CO}_2$ reaction¹.

One of the main problems when exothermic reactions are the subject of study is the non-uniformity of the temperature across the catalytic bed. This means that, despite keeping our reactor immersed in a bath at constant temperature, the temperature of the catalyst is higher than that set in our bath. Moreover, the temperature at different spots within the catalytic bed may differ, leading to a non-uniform temperature profile and even to a shift from kinetic control to external diffusion control^{2,3,4}.

External diffusion control regime is linked to strongly exothermic reactions. In this regime, the activity of the catalyst is determined by conversions rather than heater temperature. The higher the conversion the bigger the amount of heat released, leading to an increase in the temperature of the catalytic bed. If this temperature reaches a critical point at which the increase in exothermic heat flux from the reaction exceeds the increase in heat loss flux, the reaction will switch from kinetic to external regime. This critical point is known as the ignition temperature and reaching it and beyond leads to a self-acceleration of the reaction rate⁵. This catalytic ignition is thus a heat balance and kinetics problem that should be avoided. CO oxidation is one of the reactions typically proceeding in external diffusion regime⁶. Therefore, the following strategies were taken.

- Water bath temperature kept low.

The use of water instead of oil in our bath was already strongly limiting the possible temperatures to be tested. Since water evaporates at 100 °C, testing below this point should work fine. However, and despite having a lid to cover the bath with the reactor already immersed, water was lost at temperatures close to this maximum, leaving our reactor partially exposed to air. 80 °C was experimentally tested to be the maximum workable temperature without appreciable loss of water in our bath. However, 60 °C was decided to be the maximum to be tested for all our catalytic samples. This decision was taken after evaluating two different aspects. One being the fact that the intention of this study was the comparison in catalytic performance of different materials at the same experimental conditions. Since Au/CeO₂ showed very high conversions even at temperatures below 50 °C,

while no significant differences were observed in the rest of catalysts at temperature between 60 °C - 80 °C, it seemed to be a good temperature upper boundary that would, simultaneously, work against the exothermic effect of the reaction discussed above.

- Dilution of catalytic bed.

Dilution of the catalyst sample with inert material is a recurrent strategy to get catalytic material sparsely distributed across the bed and avoid light off, i.e. the exotherm dominates the catalyst temperature. Different dilution ratios were tested before the optimal one was chosen. This is discussed in Section 5.1.1.

- Thermocouple to measure catalytic bed temperature.

Last measure considered to get exothermic effects under control was the implementation of a thermocouple that would read the catalytic bed temperature. This serves as an ultimate check of the effectiveness of the two previous actions already taken, i.e. low temperature tests and dilution of catalytic bed, by providing a comparison between the bath temperature and the actual temperature of the catalyst.

c. Gases compositions and mass flows being used.

How the optimal gases composition of the inlet gases was chosen has been described in Section 2.4.3. Which mass flows were tested and the effect of their related contact time will be discussed in Section 5.1.2. Both composition and mass flows of inlet gasses determine the value of lambda ($\lambda = \frac{2[O_2]}{[CO]}$), which selection and effect are the focus of Section 5.1.3. In advance of those sections and in order to point out the contribution of this last consideration to the path the reaction follows, it is important to keep in mind that the outlet flow composition will be dependent on the inlet flow composition and the contact time with the catalyst.

The next three sections contain detailed discussion on the last points exposed above.

5.1.1 Catalyst dilution ratio

The dilution ratio, R_{dil} , specifies the ratio of catalyst mass to the mass of the diluted mixture (1:1 meaning undiluted). Three different dilutions were tested and then an optimal dilution selected for all further experiments based on the factors discussed below:

a. The conversions obtained throughout the temperature range to be used were not too high for valid kinetic interpretation.

As discussed in the previous section, the reaction is exothermic, so that at high conversions significant heat is generated and there is a greater chance of getting in a situation where the temperature is not controlled by the external source (bath) and even to a shift to external diffusion control regime.

b. The chosen ratios must show appreciable activity.

The chosen dilution ratio must still contain enough catalytic material to allow measurable conversions.

c. Requirements 'a' and 'b' must be true for all the catalytic samples tested at that R_{dil} .

Comparison between different catalysts is key in this study. If results from testing some of them have not been obtained in a temperature controlled situation or if conversions are too low to allow good quality analysis, then the comparison would be impossible or inaccurate.

Regarding the diluting material, it is essential that it is an inert for the reaction under the experimental conditions being tested. Also, it should mix well with the catalyst and have a similar particle size in order to avoid any possible change in diffusion mechanisms. In the case of this study, we have a series of metal supported catalysts for which the support is CeO_2 , TiO_2 or Al_2O_3 . Diluting with the same

support the catalyst is made of would constitute then the best alternative, since it would be the material with closest physical properties and chemical composition to the actual catalyst. This is only true if those supports act as inerts when tested in CO oxidation experiments. Due to an initial unavailability of the Au/Al₂O₃ catalytic material and the alumina used for its preparation, only the ceria and titania were tested at first, holding up the Al₂O₃ inactivity test for later. However, when it was realised that the activity of the Au/Al₂O₃ material was very low compared to the Au/CeO₂ this catalyst was not tested further and so the blank was not required.

In the cases of ceria and titania, 25 mg of the respective metal oxide was packed in the reactor as it would be done for our supported gold catalysts. Then it was put on-stream (CO/O₂/N₂ mixture) at room temperature before starting the temperature monitored test of the reaction. As discussed in Chapter 3, an initial deactivation is usually observed over the first 1-2 hours from the time a catalyst is put on-stream. This deactivation is due to the catalytic surface initially being in a non-equilibrium CO coverage⁷. To avoid starting to test the performance of the material in such non-equilibrium stage, a period of time of at least 60 minutes was always used at the start of the experiment to establish equilibrium before the activity was recorded. Nevertheless, this conditioning time is recorded as well, so that the change of catalyst activity and selectivity can be monitored and equilibrium behaviour confirmed. For the case being discussed at this point, and despite the expectations of observing any catalytic property from either ceria or titania alone were almost null, these supports were also left on-stream for 1 hour before testing them. Regarding temperatures, 20 °C - 60 °C, with both a ramp up and a ramp down of 20 °C, were studied. Figures 5.2 and 5.3 respectively evidence the inactivity of CeO₂ and TiO₂ under the CO oxidation conditions commented above. Such inactivity is in agreement with reported studies^{8,9}. Furthermore, it can be observed that the conversion versus time is a horizontal line which is not located across the abscissa axis (time) at a constant conversion value of zero. Although it could be tentative to attribute it to a certain degree of activity, this is discarded for two reasons. Firstly, the conversion keeps a constant value with time, independent of the catalytic bed temperature. Secondly, such a constant value of the conversion is practically the

same for both ceria and titania, specifically, 0.465 ± 0.007 % for CeO_2 and 0.459 ± 0.002 % for TiO_2 . These two features lead to the conclusion that we are facing baselines which carry the error that comes with the instrument (GC). Therefore, averaging both values, an instrumental error of 0.462 ± 0.009 % is calculated. Consequently, the inactivity of both supports can be reaffirmed.

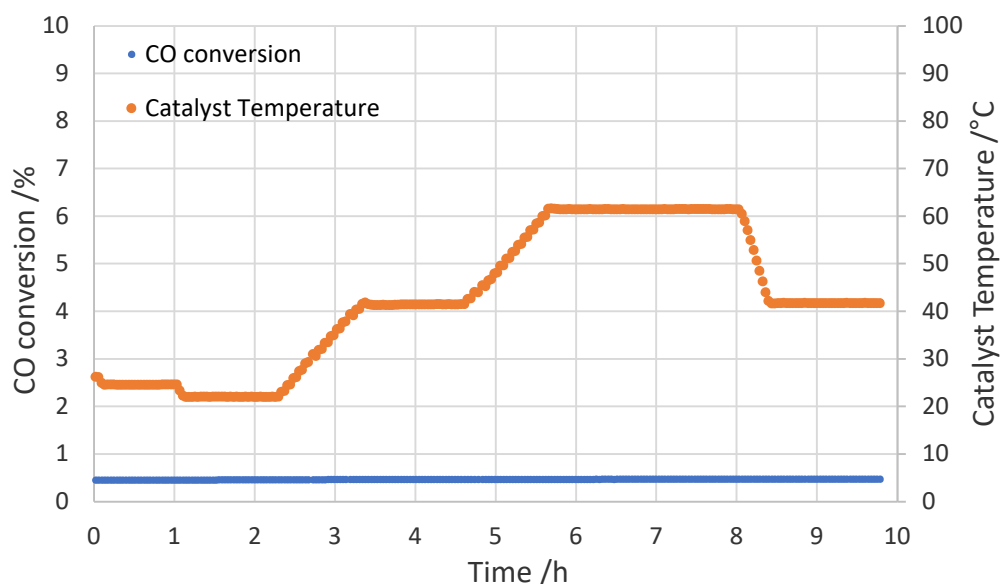


Figure 5.2. CO conversion and temperature of catalytic bed versus time when flowing 25 ml min^{-1} of 2% CO/N_2 and 5 ml min^{-1} of 10% O_2/N_2 (corresponding to $\lambda = 2$) over 25 mg CeO_2 .

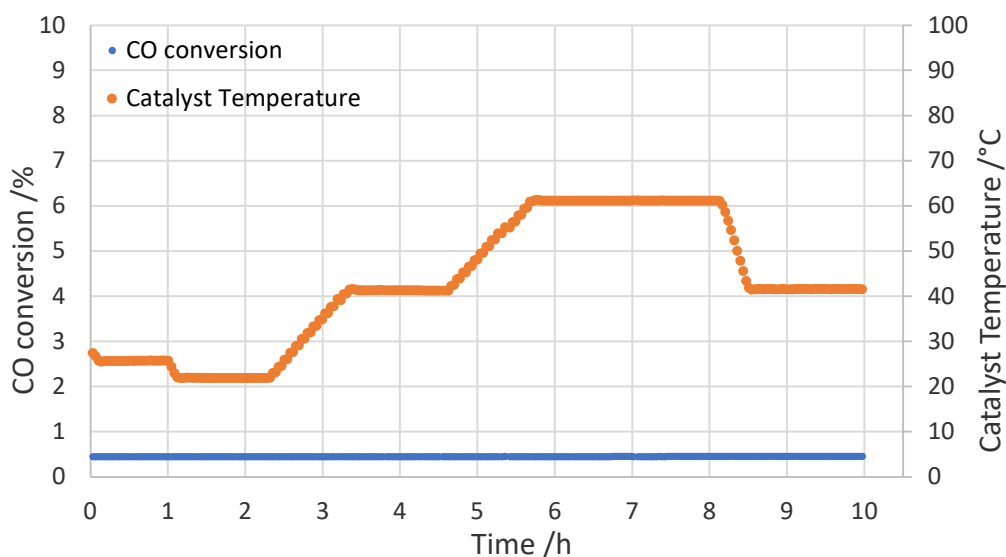


Figure 5.3. CO conversion and temperature of catalytic bed versus time when flowing 25 ml min^{-1} of 2% CO/N_2 and 5 ml min^{-1} of 10% O_2/N_2 (corresponding to $\lambda = 2$) over 25 mg TiO_2 .

Once these supports were found to act as inerts under the set of experimental conditions commonly applied during our studies, three different dilution ratios were tested using those as diluent materials. The natural flow those tests followed is exposed below.

For all cases shown in Figures 5.4-5.14, experimental conditions were kept as similar as possible. This standard set of conditions was chosen based on the feedback previously obtained from the tests ran during the development of the automation software (Chapter 3). In particular, all catalytic samples were left on-stream for 1 hour before starting to test. The temperature range was set to 20 °C – 60 °C with a ramp (up and down) of 10 °C. Each tested temperature was kept constant for 2 hours for most of the cases, only for one of the catalytic samples extra time was needed in order to reach steady state conditions. A stoichiometric ratio of oxygen to carbon monoxide was initially tested, which corresponds to a lambda value of 1 ($\lambda = \frac{2[O_2]}{[CO]}$). However, when too low conversions were found, an excess of oxygen corresponding to $\lambda = 2$ was also monitored.

- $R_{dil} = 1$

As it was defined in Section 5.1.1, the dilution ratio (R_{dil}) refers to the ratio of catalyst mass to the mass of the diluted mixture. Therefore, $R_{dil} = 1$ means the catalytic sample has not been diluted. In this case, 25 mg of catalytic material was packed into the reactor without dilution, so that the catalyst is present in the highest concentration possible at that metal loading. Testing our catalytic materials when undiluted was the first step to know whether or not proceeding with the dilution strategy was needed. Below, the time and temperature dependence of the conversion is plotted and discussed for those catalytic materials tested at this dilution ratio.

From Figure 5.4, corresponding to undiluted Au/TiO₂, it can be seen that conversion values mismatch yield to CO₂ values. This is due to the error carried by the instrument, specifically, the column where the CO is detected. The GC used in this consists of two columns, CO is detected in one of them while CO₂ is in the other. Experimental results presented in this work will evidence that the column

responsible for CO detection carries a bigger error in terms of baseline and also a higher degree of fluctuation. If the baseline is corrected by extracting the error already calculated from data showed in Figures 5.2 and 5.3, both conversion and yield agree with each other as would be expected from the output of CO oxidation alone (see Fig. 5.5). Such baseline correction has already been performed for all forthcoming presented experimental data. Also, the results from the test of undiluted Au/TiO₂ (Figure 5.4) show an occasional 1-2 % peak in CO conversion. However, the origin of these features could not be found.

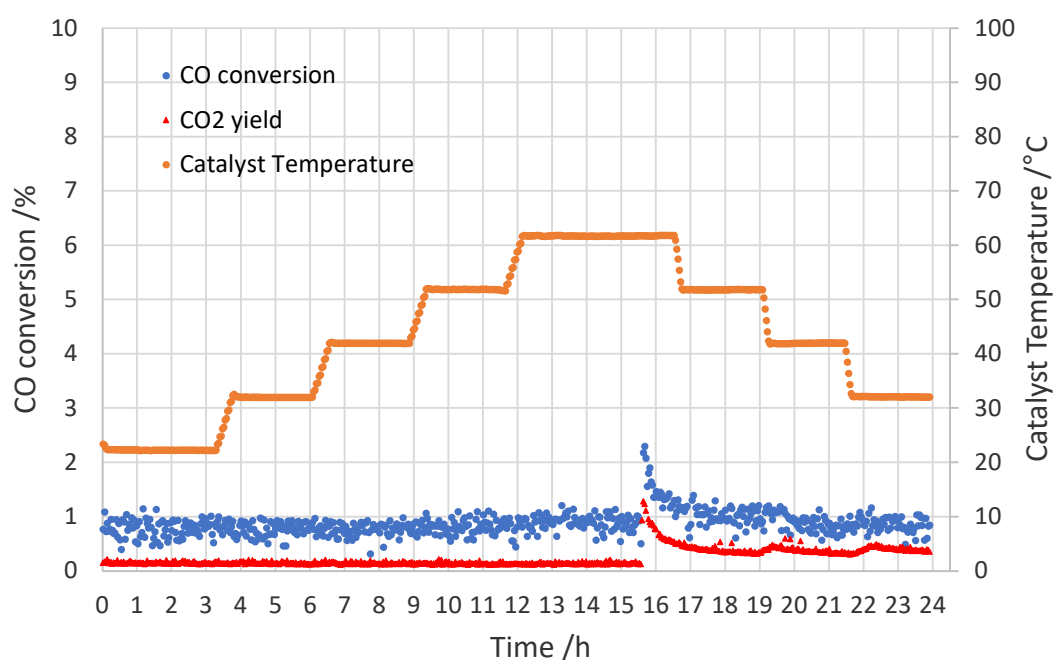


Figure 5.4. CO conversion, yield to CO₂ and temperature of catalytic bed versus time when flowing 27.2 ml min⁻¹ of 2% CO/N₂ and 2.7 ml min⁻¹ of 10% O₂/N₂ (corresponding to $\lambda = 1$) over 25mg 5% Au/TiO₂.

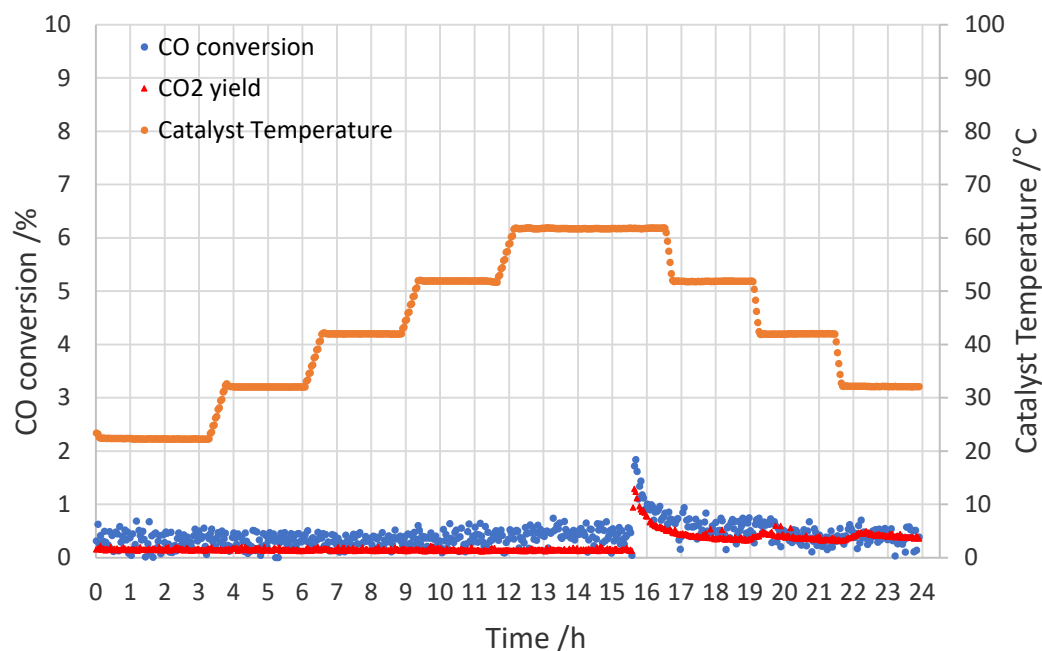


Figure 5.5. Data plotted in Fig. 5.4 after extracting instrumental error.

From the results previously commented when flowing a stoichiometric ratio oxygen to carbon monoxide, an excess of oxygen was also tested. Figure 5.6 shows the experimental results when doubling the ratio O_2/CO , where conversions with maximum values of around 1.3 % at the highest temperature (60 °C) are observed. Taking into consideration that Au/TiO_2 has been repeatedly reported as a highly active catalyst for CO oxidation at low temperature (see Section 1.1 and references therein), these conversions were far below expectations. Additional analyses were performed to give an insight into the possible cause of the poor activity of the Au/TiO_2 catalyst. The outcome of those analyses is presented and discussed at the end of this Section 5.1.1.

Considering the almost zero activity at $\lambda = 1$ obtained with the gold on titania catalyst and as $AuPd/TiO_2$ would be expected to be a material quite similar to Au/TiO_2 , synthesized following the same procedure, an experiment was carried out with a fresh sample at the higher O_2/CO ratio, i.e. $\lambda = 2$. Figure 5.7 shows such results obtained when using $AuPd/TiO_2$ under the same experimental conditions that were applied during the previous test on Au/TiO_2 (Fig. 5.6). As seen in Figure 5.7, higher CO conversion with maximum values of around 2.8 % was obtained in this case. This would be in accordance with literature where an enhanced catalytic

activity has been reported by the addition of gold to supported palladium catalysts for a wide range of reactions¹⁰. With the intention of double-checking this slight higher conversions when having a palladium/gold alloy and, at the same time, investigate the reusability of the material, exactly the same conditions were applied on the same sample after flowing a mix of 10 % O₂ in N₂ at a constant flow rate of 10 ml min⁻¹ for 24 hours. These results are also presented in Figure 5.7 so that they are easily compared to those obtained on the fresh sample. Identical patterns are flowed in both cases, with expected decrease in both conversion and yield. Despite, this decrease in activity is minimal, which features a quite high degree of reusability of this material.

Finally, Au/Al₂O₃ and AuPd/Al₂O₃ were also tested in an undiluted way ($R_{dil} = 1$). Au/Al₂O₃ was initially tested under stoichiometric gaseous conditions ($[O_2] = \frac{1}{2} [CO]$). Low conversions with maximum values of about 1.7 % were obtained. The experiment was repeated keeping all experimental conditions the same but doubling the ratio $\frac{[O_2]}{[CO]}$. Figure 5.8 presents conversions and yields obtained in these experiments on Au/Al₂O₃ and minimal differences can be found when comparing both of them. These results clearly indicate that saturation with oxygen does not increase the amount of CO oxidised, which could be due to a poor concentration of active sites in the material. These findings would be in accordance with Widmann et al.¹¹ study where they studied Au/Al₂O₃ and very low oxygen storage capacity and CO oxidation activity were observed and a 'gold-only mechanism' was proposed as the dominant pathway for this material after they could not identify the direct participation of the support in the reaction. Such reasoning would give an explanation to the almost identical results obtained at both $\lambda = 1$ and $\lambda = 2$ for Au/Al₂O₃.

AuPd/Al₂O₃ was directly tested in an excess of oxygen atmosphere ($\lambda = 2$). Experimental results evidenced near zero catalytic activity, as it is shown in Figure 5.9. Comparing activities of Au/Al₂O₃ and AuPd/Al₂O₃, contrary to what happened on the supported titania materials discussed above, in the case of having alumina as support, alloying gold and palladium results in much lower activities than the gold alone case. This data suggest that the synergetic effect of gold and palladium

is only efficient on materials where the support is directly involved in the mechanism of the reaction. If it is assumed that for the non-reducible catalysts Au/Al₂O₃ and AuPd/Al₂O₃, a 'gold-only mechanism' is in play¹¹, replacing part of the gold content in the catalyst for palladium would consequently decrease the catalytic activity of the material.

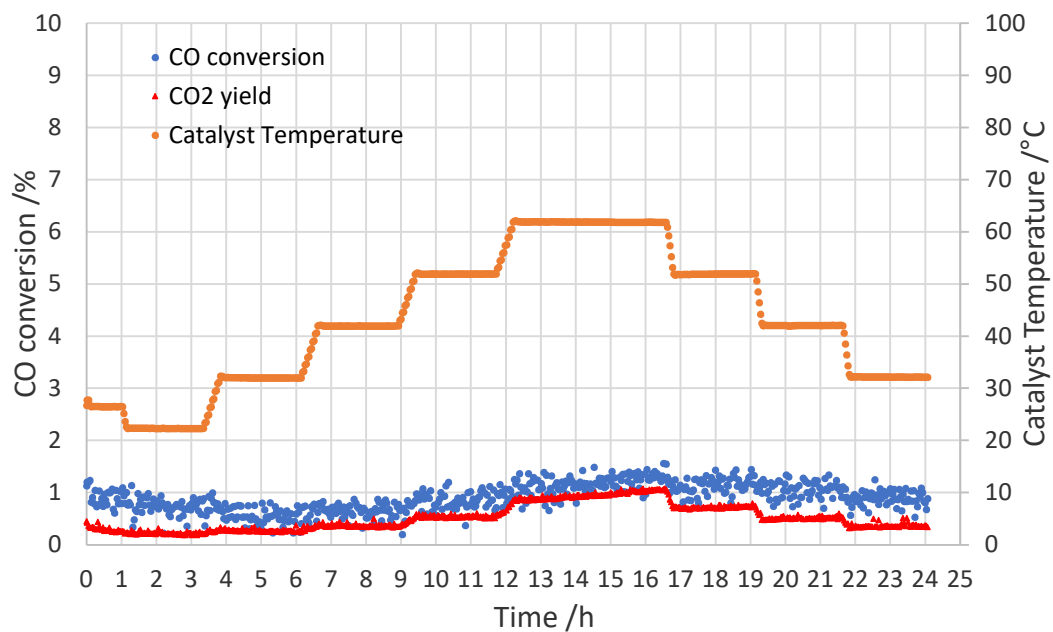


Figure 5.6. CO conversion, yield to CO₂ and temperature of catalytic bed versus time when flowing 25 ml min⁻¹ of 2% CO/N₂ and 5 ml min⁻¹ of 10% O₂/N₂ (corresponding to $\lambda = 2$) over 25mg 5% Au/TiO₂.

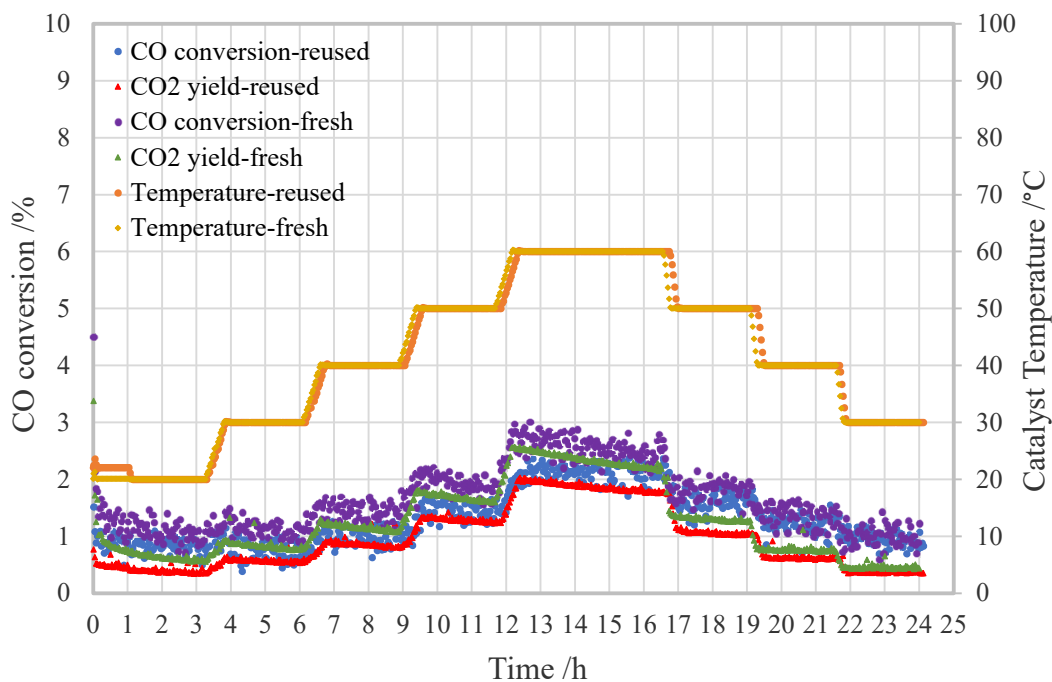


Figure 5.7. CO conversion, yield to CO₂ and temperature of catalytic bed versus time when flowing 25 ml min⁻¹ of 2% CO/N₂ and 5 ml min⁻¹ of 10% O₂/N₂ (corresponding to $\lambda = 2$) over 25 mg of used 5% AuPd/TiO₂ and after 24 hours of flowing 10 ml min⁻¹ of 10% O₂/N₂. This graph also shows results obtained previously on the fresh sample tested under the same conditions for comparison purposes.

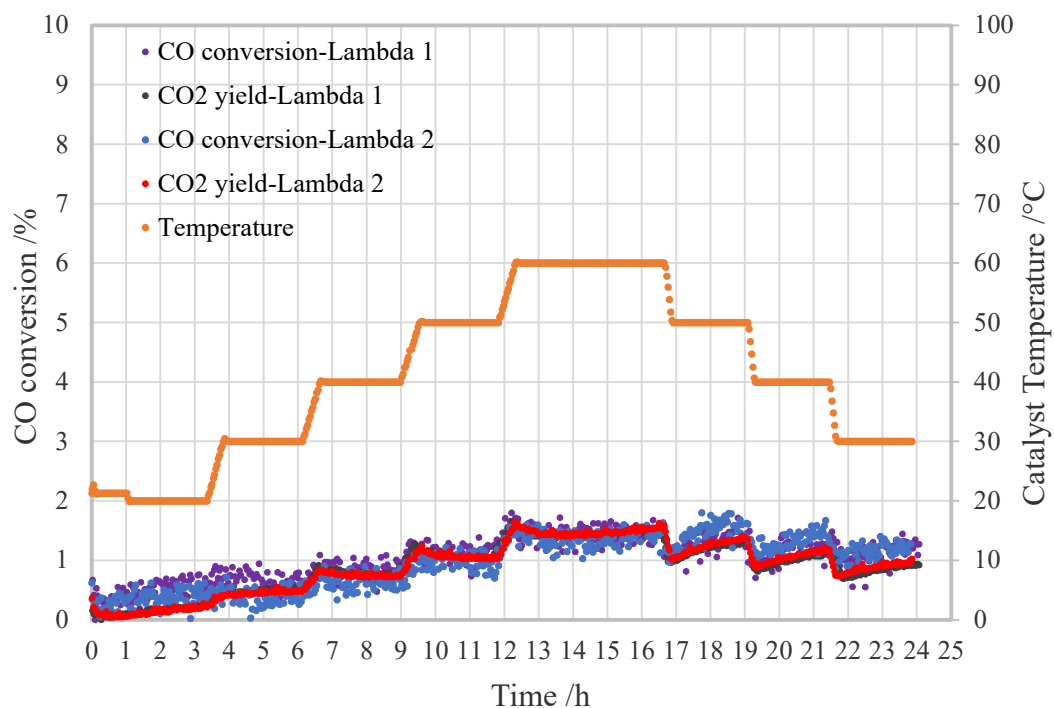


Figure 5.8. CO conversion, yield to CO₂ and temperature of catalytic bed versus time when flowing 27.2 ml min⁻¹ of 2% CO/N₂ and 2.7 ml min⁻¹ of 10% O₂/N₂ (corresponding to $\lambda = 1$) and when flowing 25 ml min⁻¹ of 2% CO/N₂ and 5 ml min⁻¹ of 10% O₂/N₂ (corresponding to $\lambda = 2$) over the same sample (25 mg 5% Au/Al₂O₃).

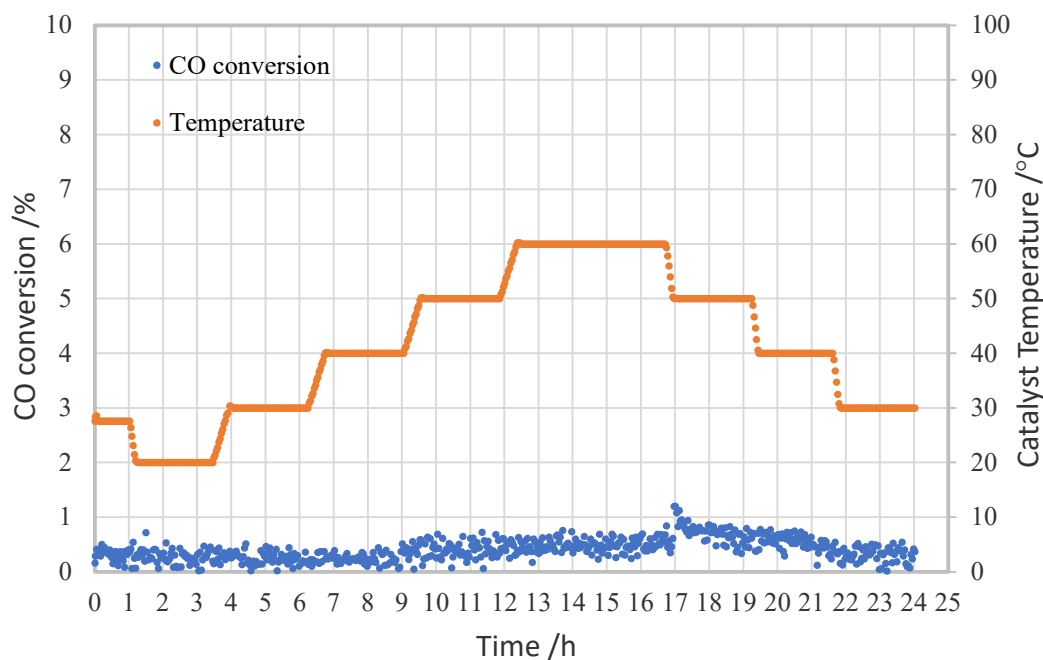


Figure 5.9. CO conversion and temperature of catalytic bed versus time when flowing 25 ml min^{-1} of 2% CO/N₂ and 5 ml min^{-1} of 10% O₂/N₂ (corresponding to $\lambda = 2$) over 25mg 5% AuPd/Al₂O₃.

$$-R_{dil} = 1/5$$

The next step was the dilution of some of the catalytic samples in a ratio 1/5. Specifically, 5 mg of catalytic material was diluted in 20 mg of the chosen diluent. This was the first dilution ratio tried on the gold supported on ceria sample, Au/CeO₂, since very high activity was already expected based not only on literature but on results obtained during the testing of the automation software (Chapter 3). Those samples had a lower content of gold than the ones we focus on in this study and they already presented 100% CO conversion when they were tested undiluted. Figure 5.10 shows conversions up to 90% when using 5% Au/CeO₂ at a dilution ratio of 1/5 and at the commonly applied experimental conditions previously detailed. Nonetheless, the steady state is obviously not reached after 2 hours at a constant temperature of 40 °C during the ramping up in temperature. During this period of time at such a temperature, the conversion steeply increases without any sign of stabilization before the temperature of the system is increased again. A new experiment was performed using a fresh sample of the same catalyst under the same experimental conditions with exception of the period of time each

temperature was kept constant. In this case, 2.5 hours were set instead. As shown in Figure 5.11, again steady state was not reached at 40 °C. In both figures 5.10 and 5.11, it is observed that conversions at 40 °C and 30 °C in the temperature ramp down stage are higher than their respective counterparts during the previous ramping up stage, while conversions at 50 °C are essentially the same at both stages in both experiments (Fig. 5.10 and 5.11). The fact that the catalytic activity experiences such a drastic increase only once the temperature is substantially above room temperature suggests that there are some changes in the state of the catalytic material that could only happen once a certain energy threshold is reached. It seems that such an energy barrier is overcome at 40 °C. A change in the oxidation state of the supported gold particles would offer a plausible explanation. In that case, only characterization of the sample before and after being used would give a certain answer to whether or not the state of the Au particles has changed and in which manner, i.e. from Au^{δ+} to Au⁰ or vice versa. Nonetheless, regardless the specific nature of the predominant oxidation state of the gold particles at the end of this transition process, it is clear that such state is playing the role of active site in our reactive system. From both figures 5.10 and 5.11, one could see that the system stabilizes once the temperature is increased above 40 °C, which indicates that no further changes in the population of active sites are made. Therefore, the system reaches the steady state from this critical temperature point onwards. Such hypothesis on the change of the Au oxidation state just after the necessary threshold is reached and that such threshold corresponds to a temperature of 40 °C would explain why conversions on both temperature ramp up and down stages only differ from each other at 40 °C and lower temperatures, given that comparing conversions from those temperatures would involve the comparison of two materials essentially different.

NAP-XPS analysis was carried out with the intention of finding evidences that could support that above suggested. These results are presented and compared with those obtained for the Au/TiO₂ catalyst at the end of this Section 5.1.1.

The poor catalytic activity of Au/TiO₂, AuPd/TiO₂, Au/Al₂O₃ and AuPd/Al₂O₃ was already evidenced when these materials were tested in an undiluted way, therefore

testing them using a dilution ratio was thought to be unnecessary. Consequently, the next step was trying to find a dilution ratio that decreased the conversions when using Au/CeO₂ with the intention of reducing the undesired effects that such high values could imply (see beginning of this Section 5.1).

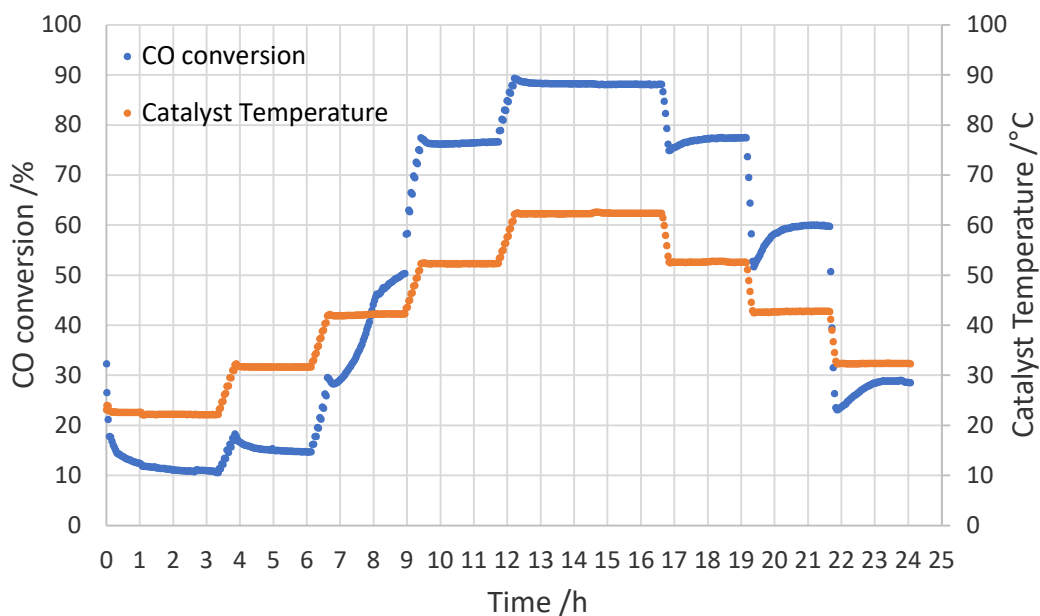


Figure 5.10. CO conversion and temperature of catalytic bed versus time when flowing 27.2 ml min⁻¹ of 2% CO/N₂ and 2.7 ml min⁻¹ of 10% O₂/N₂ over 5mg of 5% Au/CeO₂ diluted in 20 mg of CeO₂ (corresponding to $\lambda = 1$ and $R_{\text{dil}} = 1/5$).

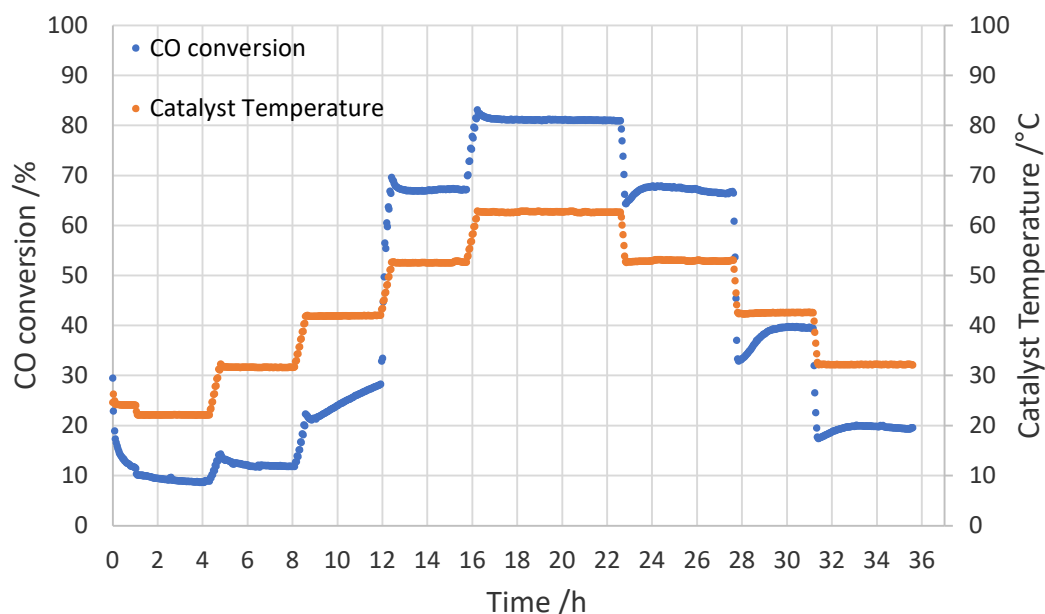


Figure 5.11. CO conversion and temperature of catalytic bed versus time when flowing 27.2 ml min^{-1} of 2% CO/N₂ and 2.7 ml min^{-1} of 10% O₂/N₂ over 5mg of 5% Au/CeO₂ diluted in 20 mg of CeO₂ (corresponding to $\lambda = 1$ and $R_{\text{dil}} = 1/5$). Temperatures were kept constant for 2.5 h instead of the usual value of 2 h.

- $R_{\text{dil}} = 1/9$

A final dilution ratio of 1/9 was tested. In this case, 3 mg of catalytic material was diluted in 24 mg of the chosen diluent and as commented before, decreasing conversions when using the Au/CeO₂ was the main target here. Figure 5.12 shows a clear reduction in the degree of CO oxidation alongside the respective yield to CO₂. Furthermore, the drastic increase in conversion previously observed at 40 °C ($R_{\text{dil}} = 1/5$) are much better controlled. Decreasing the amount of catalytic material in the reactor bed (lower ratio catalyst/diluent), involves less gold particles being present and, in consequence, less Au particles to suffer a transition from its original oxidation state to the one that acts as the active site in the reaction mechanism. From these results, it was considered satisfactory the use of a dilution ratio of 1/9 for the most active catalyst tested till this point, i.e. Au/CeO₂. As such, the test of AuPd/CeO₂ at the same R_{dil} was performed and the output of such experiment is presented in Figure 5.13. Conversions on the supported AuPd catalysts are much lower than in the case of having just gold as supported noble

metal. Nonetheless, conversions respond to changes in temperature and are high enough to be measurable. Thus, $R_{\text{dil}} = 1/9$ was considered the best dilution ratio to be used for the forthcoming experimental studies.

An extra experiment was performed on AuPd/TiO₂ at this dilution ratio since, when undiluted, this was the material which showed the most consistent and reproducible results among the four catalysts tested at $R_{\text{dil}} = 1$. As presented in Figure 5.14, CO oxidation did not happen after dilution of AuPd/TiO₂, with the random higher than zero values sporadically observed (mostly below 0.5 % throughout the experiment) being attributed to the unavoidable instrumental error taking place at its highest values.

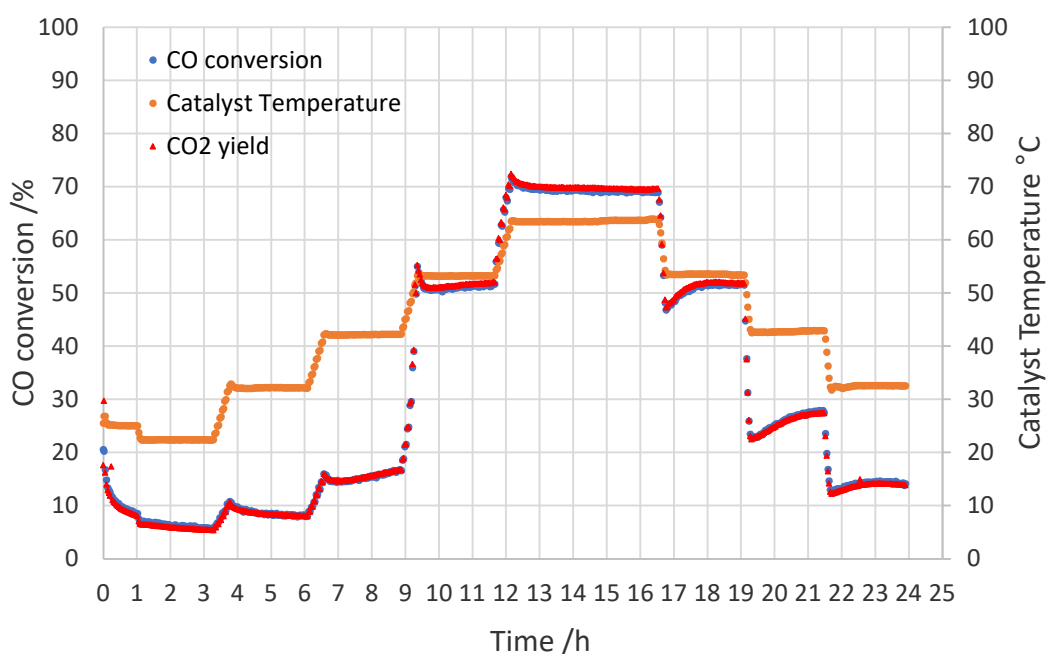


Figure 5.12. CO conversion, yield to CO₂ and temperature of catalytic bed versus time when flowing 27.2 ml min⁻¹ of 2% CO/N₂ and 2.7 ml min⁻¹ of 10% O₂/N₂ over 3mg of 5% Au/CeO₂ diluted in 24 mg of CeO₂ (corresponding to $\lambda = 1$ and $R_{\text{dil}} = 1/9$).

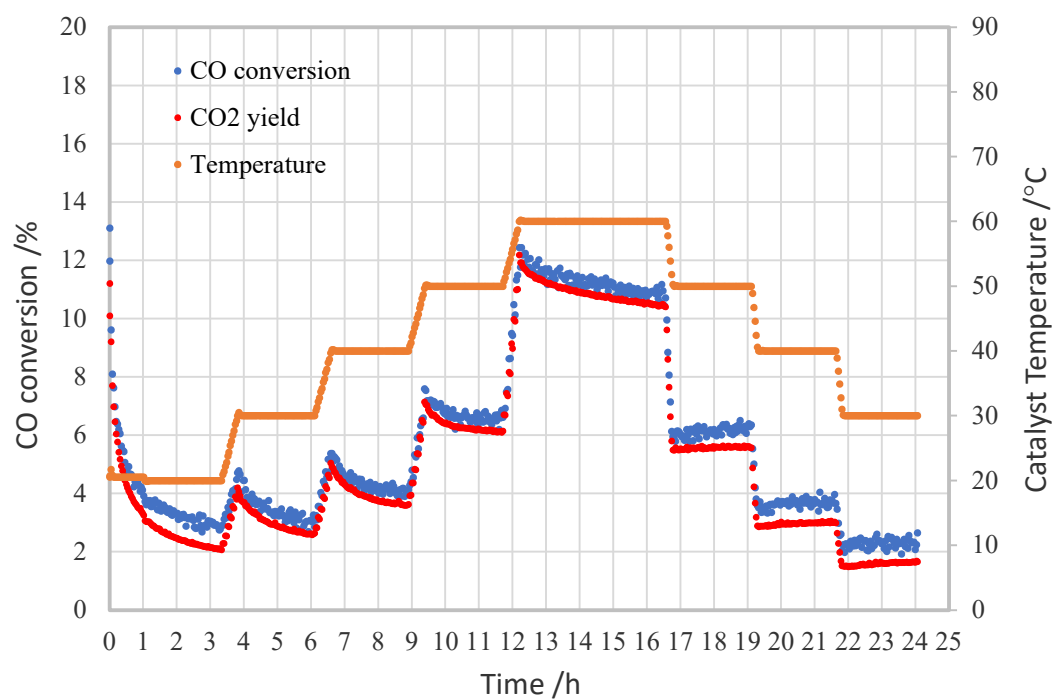


Figure 5.13. CO conversion, yield to CO₂ and temperature of catalytic bed versus time when flowing 27.2 ml min⁻¹ of 2% CO/N₂ and 2.7 ml min⁻¹ of 10% O₂/N₂ over 3mg of 5% AuPd/CeO₂ diluted in 24 mg of CeO₂ (corresponding to $\lambda = 1$ and $R_{dil} = 1/9$).

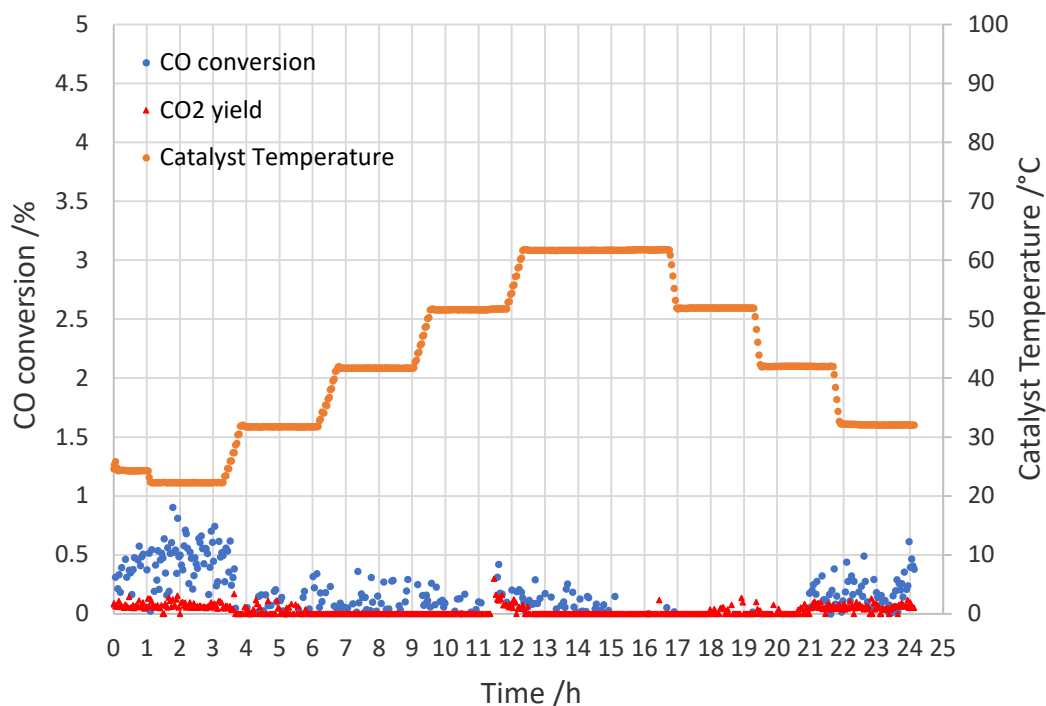


Figure 5.14. CO conversion, yield to CO₂ and temperature of catalytic bed versus time when flowing 27.2 ml min⁻¹ of 2% CO/N₂ and 2.7 ml min⁻¹ of 10% O₂/N₂ over 3mg of 5% AuPd/TiO₂ diluted in 24 mg of TiO₂ (corresponding to $\lambda = 1$ and $R_{dil} = 1/9$).

Table 5.1 below gives a simplified summary of the results previously presented throughout Section 5.1.1.

Table 5.1. Maximum CO conversions measured when various catalysts were tested for the CO oxidation reaction at different dilution ratios (R_{dil}). Values extracted from results presented in Figures 5.5-5.14.

	Au/TiO ₂	AuPd/TiO ₂	Au/Al ₂ O ₃	AuPd/Al ₂ O ₃	Au/CeO ₂	AuPd/CeO ₂
$R_{dil} = 1$	1.8 % ^a 1.6 % ^b	3.0 % ^b	1.8 % ^a 1.8 % ^b	1.2 % ^b	-	-
$R_{dil} = 1/5$	-	-	-	-	89.0 % ^a	-
$R_{dil} = 1/9$	-	0.9 % ^a	-	-	72.5 % ^a	12.3 % ^a

^a Measured when a constant lambda value ($\lambda = \frac{2[O_2]}{[CO]}$) of 1 was maintained in the inlet gas flow to the reactor.

^b Measured when a constant lambda value of 2 was maintained in the inlet gas flow to the reactor.

- Extra analyses to support performances of Au/TiO₂ and Au/CeO₂

Comparing the results presented previously with those reported in literature (see Section 1.1), the lower activity toward CO oxidation of materials such as Au/Al₂O₃ observed in this work was somehow expected. Nonetheless, in the same literature-based discussion (Section 1.1), several studies reported quite good performances of titania supported catalysts, which made the low-activity results obtained from the use of the Au/TiO₂ catalysts in our flow reactor system seem quite controversial. With the intention of finding evidence to explain the unexpected poor catalytic activity shown by the Au/TiO₂ catalyst, two different analysis techniques were applied. Firstly, in order to discard the possibility of having sintered particles of the noble metal as a cause of such an inactivity, transmission electron microscopy (TEM) images were obtained.

Figure 5.15 shows the micrograms of these two materials at different magnifications. From these images, the histograms of particle size distribution were obtained by measuring the diameters of those particles with good perimeter definition (Figures 5.16 and 5.17). As seen in Figure 5.16, although gold particle sizes on the surface of the Au/CeO₂ catalyst are within the range 4-13 nm range, the majority of them have diameters lower than 8 nm. Regarding the Au/TiO₂ catalyst, a particle size distribution over the range 2-11 nm was observed (see Figure 5.17). Nonetheless, like in the case of Au/CeO₂, most the gold particle sizes over the surface of the Au/TiO₂ material are concentrated within the range 2-6 nm. From both histograms, Figures 5.16 and 5.17, mean diameters of 6 nm for Au/CeO₂ and 4 nm for Au/TiO₂ were calculated. These results show that the size of the gold particles present on the surface of both materials are within similar diameter ranges, although within slightly lower values for the case of Au/TiO₂. Consequently, the possibility of sintering as a cause of the inactivity of Au/TiO₂ was rejected.

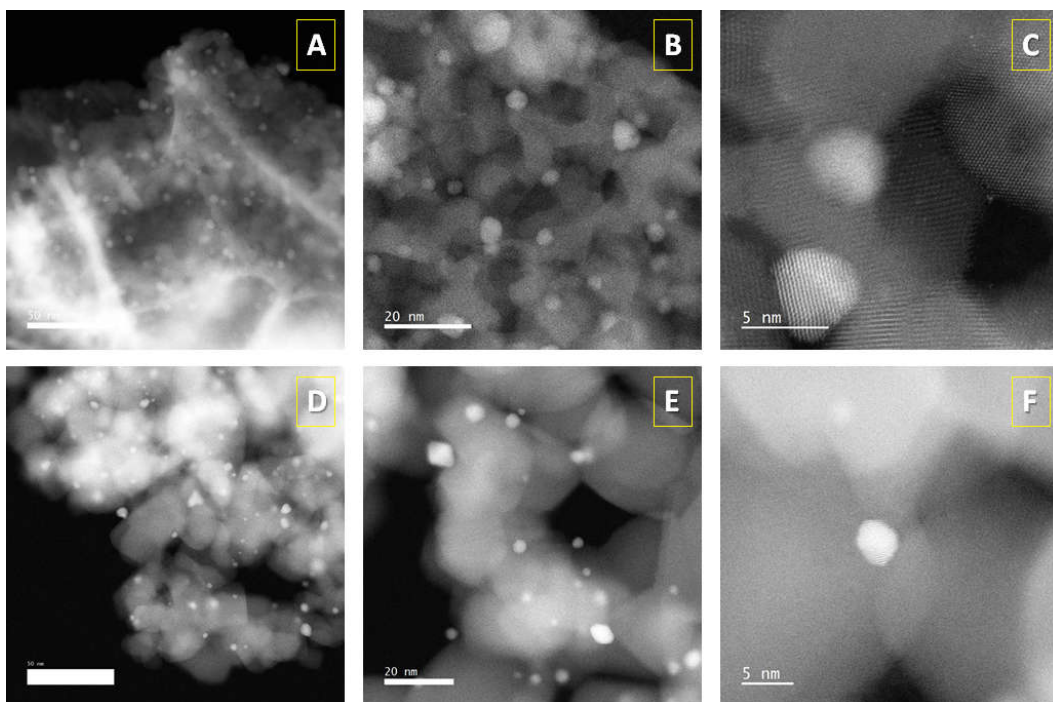


Figure 5.15. Dark field TEM micrograms at different magnifications. Au/CeO₂: A (50 nm), B (20 nm) and C (5 nm). Au/TiO₂: D (50 nm), E (20 nm) and F (5 nm).

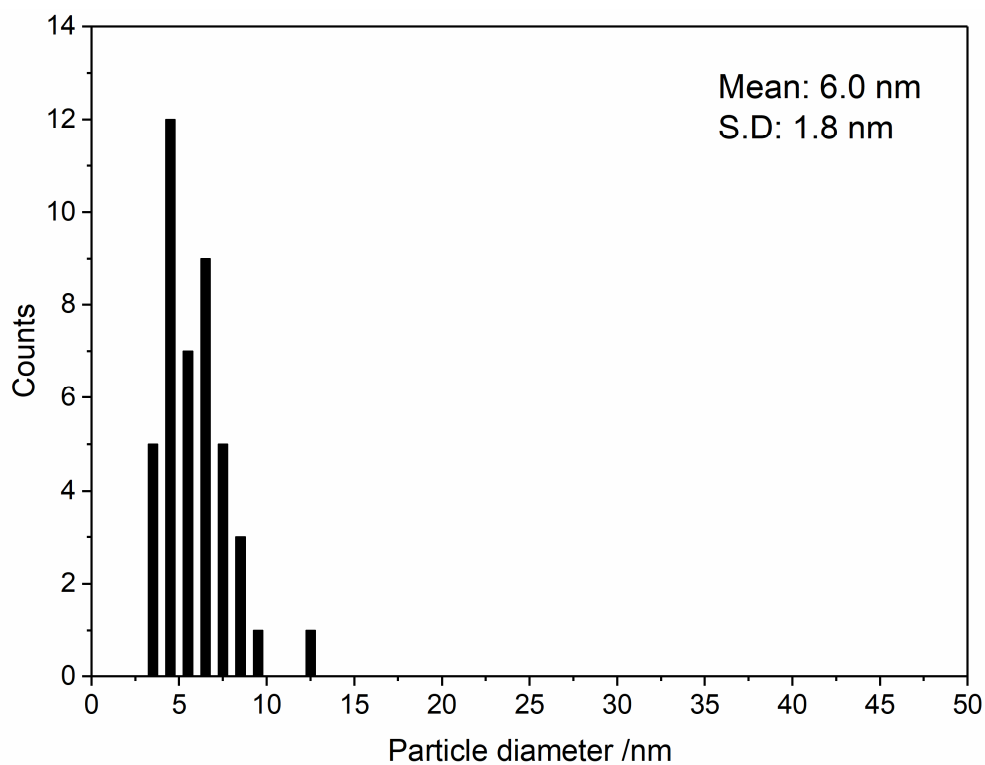


Figure 5.16. Histogram of particle size distribution obtained from Figures 5.15A, 5.15B and 5.15C (Au/CeO₂ catalyst). Mean particle diameter (Mean): 6.0 nm. Standard deviation (S.D): 1.8 nm.

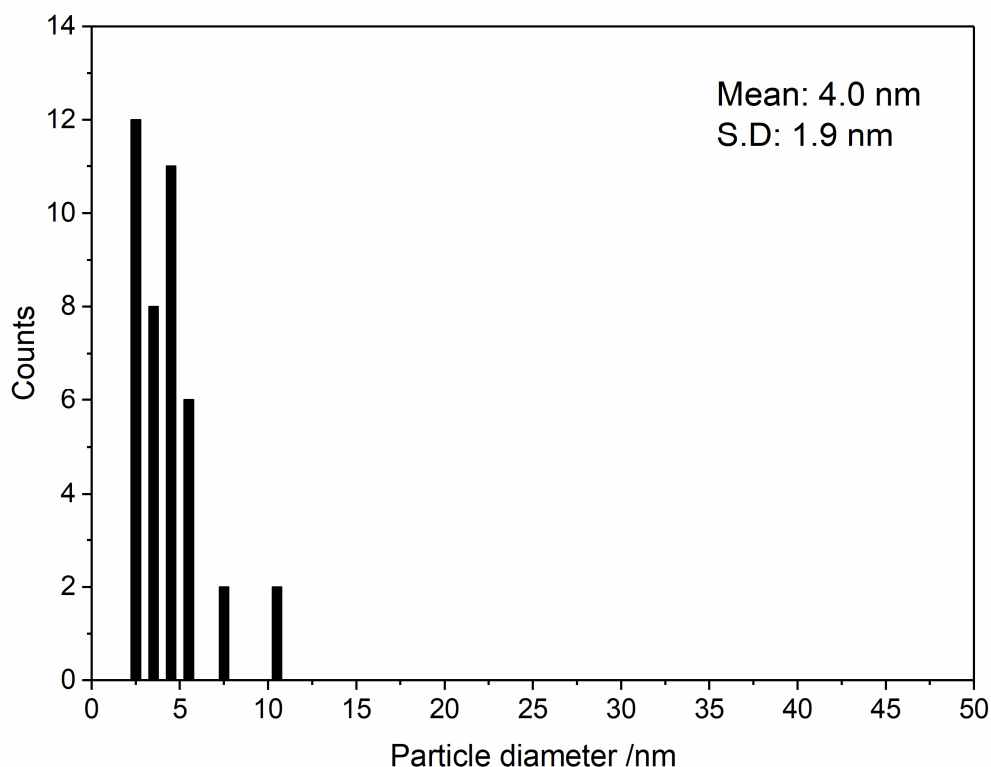


Figure 5.17. Histogram of particle size distribution obtained from Figures 5.15D, 5.15E and 5.15F (Au/TiO₂ catalyst). Mean particle diameter (Mean): 4.0 nm. Standard deviation (S.D): 1.9 nm.

Secondly, the oxidation state of the gold particles on the Au/TiO₂ catalyst and how they compare with those found on Au/CeO₂ were investigated by the application of NAP-XPS techniques. Figure 5.18 shows the curve fitting of the Au 4f spectrum obtained from the analysis of a sample of the Au/TiO₂ catalyst under two different conditions, as received at UHV (Fig. 5.18A) and when flowing both CO and O₂ over it (Fig. 5.18B). Two distinct lines separated by 3.7 eV were observed in both cases, namely the Au 4f_{5/2} and Au 4f_{7/2} lines, which occur because of the spin-orbit splitting of the Au 4f level¹². The position of the Au 4f_{7/2} component was 83.21 eV (Fig. 5.18A) and 83.56 eV (Fig. 5.18B). In comparison to the reference value of bulk metallic gold of 84.04 eV¹², the Au 4f_{7/2} lines was shifted towards lower binding energies by 0.83 eV and 0.48 eV, respectively. Shifts of this type have been reported when studying gold nanoparticles¹³, where those were related to the size and shape of the nanoparticles along with the metal-support interactions. These findings support the assignment of Au⁰ as the oxidation state of the gold particles on the surface of the Au/TiO₂ catalyst and that such oxidation state does not change when

oxygen and carbon monoxide flow into the chamber. For the case of Au/CeO₂ (Figure 5.19), same analysis was carried out. However, in the case of the 'as received' sample under UHV conditions (Fig. 5.19A), broader peaks are observed. The width of those two peaks and the separation between each other do not match with the reference value of bulk metallic gold¹². Nonetheless, if these peaks are fitted to two Au 4f_{7/2} components, one of them at 83.47 eV and the second one shifted by 2 eV from the former, i.e. 84.47 eV, according to reported literature¹⁴ these two components can be attributed to Au⁰ and Au¹⁺, respectively. The observed Au 4f spectrum of the same sample when flowing both O₂ and CO over it (Fig. 5.19B) reveals a single component with the same features as those previously seen for the case of Au/TiO₂ (Figure 5.18). In this particular case (Fig. 5.19B), the Au 4f_{7/2} component is located at 83.58 eV with the respective Au 4f_{5/2} component separated by 3.7 eV from it, i.e. at 87.28 eV. Conclusively, those have been attributed to Au⁰. In agreement with these results, a reduction of the cationic surface gold takes place in a O₂ + CO atmosphere. This also supports the previously suggested idea of a change in the oxidation state of the gold particles when temperature rises as a cause of the drastic increase in conversion observed in the Au/CeO₂ catalyst at temperatures around 40 °C, temperature proposed as the threshold for such a change to take place.

Figure 5.20 shows the O 1s spectrum of the Au/TiO₂ sample as received (Fig. 5.20A) and when flowing CO at room temperature (Fig. 5.20B) and at 60 °C (Fig. 5.20C). The same components were observed in both the 'as received' and the 'CO + heat' cases, Figures 5.20A and 5.20C respectively, attributed to metal oxides and hydroxides. However, a third component appears when the sample is in a CO atmosphere at room temperature, which has been assigned to adsorbed CO species. These results suggest that, although disappeared when heating, CO species get to adsorb on the catalytic surface of Au/TiO₂. This fact along with the difference in the oxidation states of gold found on the surface of the 'as received' samples of both Au/TiO₂ and Au/CeO₂ suggest that the presence of both Au⁰ and Au¹⁺ species is important to kick start the CO oxidation reaction at low temperatures. Thus, the lack of cationic species on the Au/TiO₂ catalyst could explain its poor activity.

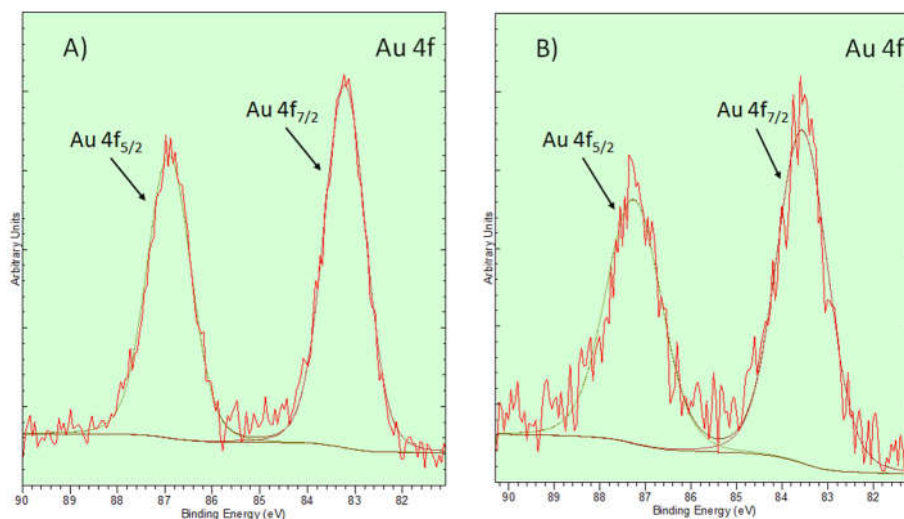


Figure 5.18. XPS spectra of: A) The ‘as received’ sample of Au/TiO₂ under UHV at room temperature. B) Same sample when flowing 3 mbar of O₂ and 6 mbar of CO at 90°C into the chamber. Parameters such as binding energies, width of peaks and separation between each other support the assignment of Au⁰ as the oxidation state of the gold particles in both cases (Fig. 5.18A and 5.18B).

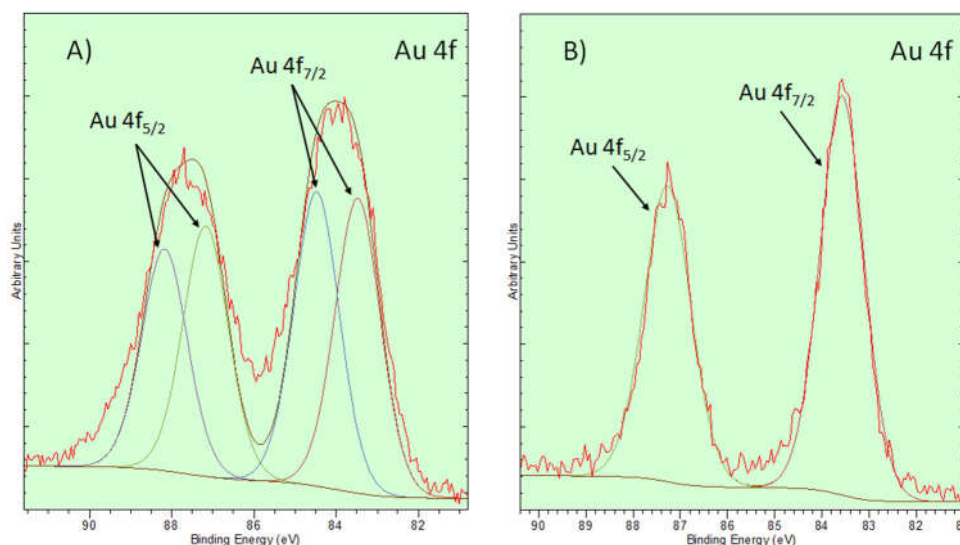


Figure 5.19. XPS spectra of: A) The ‘as received’ sample of Au/CeO₂ under UHV at room temperature. B) Same sample when flowing 3 mbar of O₂ and 6 mbar of CO at 90°C into the chamber. Parameters such as binding energies, width of peaks and separation between each other reveal the presence of both Au⁰ and Au¹⁺ on the surface of the ‘as received’ sample (Fig. 5.19A). Nonetheless, only Au⁰ is observed in Figure 5.19B, which indicates that Au¹⁺ get reduced when both O₂ and CO are flown over the catalytic surface.

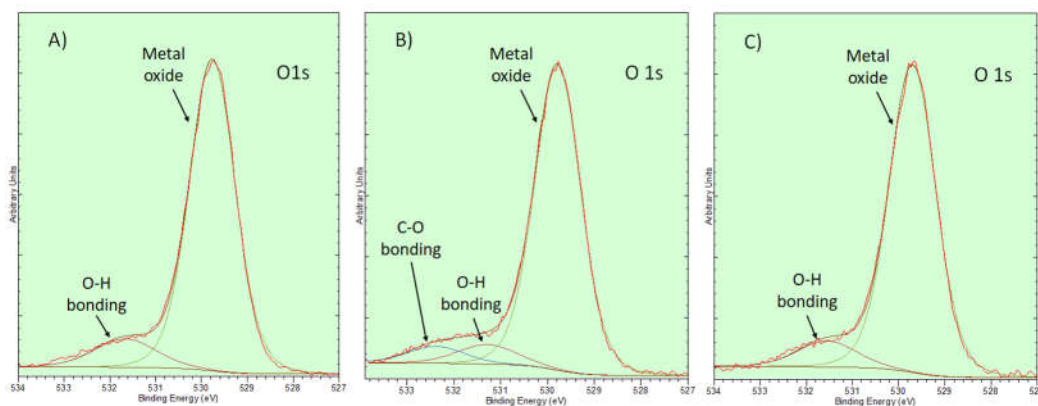


Figure 5.20. XPS spectra of: A) The ‘as received’ sample of Au/TiO₂ under UHV at room temperature. B) and C) Same sample when flowing 6 mbar of CO at room temperature and at 60°C, respectively. While only metal oxides and hydroxides are observed in Figures 5.20A and 5.20C, a third component, assigned to adsorbed CO species, appears when the sample is in a CO atmosphere at room temperature (Fig. 5.20B). These results suggest that, although disappeared when heating, CO species get to adsorb on the catalytic surface of Au/TiO₂.

5.1.2 Effect of contact time and reusability

From all the catalytic samples tested previously on the search for the optimal dilution ratio (Section 5.1.1), only two of them were chosen to be used for the rest of experimental tests. This decision was based on two major arguments. Firstly, comparison of the performances of the different catalytic materials tested under the most similar conditions was one of the main dogmas in our study and the selection of the optimal dilution ratio was not an exception to it. Not too high conversions but appreciable ones were required when a single value of the R_{dil} was applied to different catalytic samples. The dilution ratio that gave best results according to those requirements was $R_{dil} = 1/9$, although only for two catalysts, Au/CeO₂ and AuPd/CeO₂. Secondly, our highly precise and accurate reaction monitored method entails a greatly time consuming process. During the actual experiment, once the desired conditions are set, the software is responsible for the sampling, its frequency, temperature control and syncing of different devices within the reactor rig. Once the experiment is finished, data is also collected easily

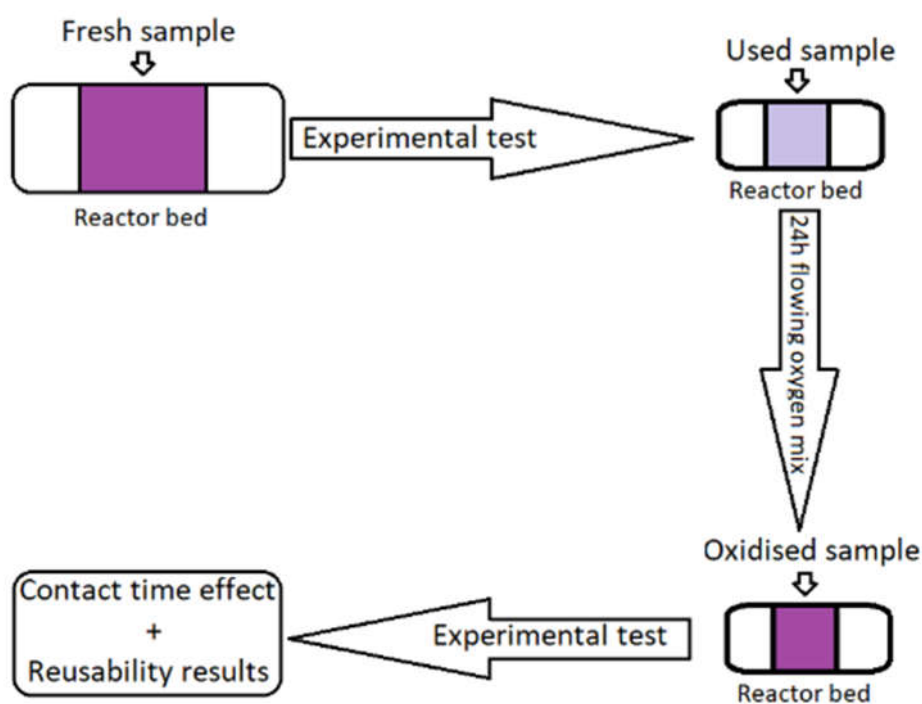
with the use of such software. Nonetheless, considering the common features of our experiments, this process takes an average of 24 hours plus the time to analyse the collected data. Consequently, these two catalysts were the ones selected for the forthcoming experiments.

This section focuses on the presentation and discussion of the effect that different contact times had on the catalytic oxidation of CO into CO₂. Equally to that done in the previous section, experimental conditions were kept as similar as possible. In this case, the effect of contact time on the catalytic performances was monitored by increasing/decreasing the total mass flow entering the reactor, therefore also changing the individual mass flows corresponding to each reactant, i.e. 2% CO/N₂ and 10% O₂/N₂ in our case. In order to truly isolate the effect of contact time from any other, the rest of conditions were kept exactly the same in all cases. Accordingly, the range of temperature tested was 20°C - 60°C with a ramp up/down of 10°C, the period of time each temperature was kept constant equalled 2 hours, the selected dilution ratio of 1/9 was used and a stoichiometric ratio of the reactants equivalent to a lambda value ($\lambda = \frac{2[O_2]}{[CO]}$) of 1 were strictly maintained through every test during this contact time effect investigation.

This Section 5.1.2 is split in two (5.1.2.a and 5.1.2.b). The only difference between these two procedures is related to the usage of the catalytic bed. While in the first approach (subsection 5.1.2.a) a fresh sample was packed before every experimental test, during the second approach (subsection 5.1.2.b), a fresh sample was packed only before the first experiment that was carried out on the specific catalytic material being studied at that moment. The rest of tests were then performed on the already used catalytic sample. The second approach was indeed a consequence of the results obtained during the first approach. Details and discussion on those results are presented below.

5.1.2.a Effect on contact time and reusability – Fresh sample approach

During this set of experiments a fresh sample was loaded in the reactor before the experimental study on the effect of each different contact time. Additionally, the reusability of the catalytic samples was also studied. This was done by repeating the experiment under the same conditions than the previous experimental test on the fresh sample and just after flowing a gas mix consisting of 10% O₂/N₂ over the sample for 24 hours. Scheme 5.1 exemplify such procedure.



Scheme 5.1. Procedure followed in the ‘Fresh sample approach’.

In total, six different mass flows were tested during this process, in particular, 10, 20, 25, 30, 35 and 40 ml min⁻¹, corresponding to six different contact times, i.e. 0.162, 0.081, 0.065, 0.054, 0.046 and 0.0405 g s min⁻¹ respectively. Figures 5.21-5.26 show conversions and yields to CO₂ on fresh samples along with their respective reusability results when using 5% Au/CeO₂ as catalytic material. Comparing conversions/yields from fresh and reused samples, there is an interesting feature. In those figures it can be observed that catalytic activities on the respective reused samples seem to be higher than those presented by the fresh

sample during the ramp up in temperature. Even after flowing oxygen, or an oxygen mix as in our case, with the intention of re-oxidising the catalytic surface, it would not be realistic to think of that as a 100 % efficient process which would get the catalyst to its initial state. Thus, it would be expected a poorer performance of such material when reusing it on the same oxidative process. Despite, the contrary happens during the major part of the temperature ramp up stage for most of the cases showed below (Figures 5.21 - 5.26). In addition to this, looking at the same figures, a higher amount of CO seems to be oxidised during the temperature ramp down stage than that observed in the ramp up stage, both in fresh and used samples.

The results from the NAP-XPS analysis presented in the previous section can be used to understand the above mentioned differences in conversions between temperature ramp up and ramp down stages and between fresh and used samples. Firstly, we have a freshly packed catalytic bed, and after the usual time left on stream to ensure an 'in-equilibrium CO coverage', the temperature monitored test starts. As the temperature rises, some gold particles reduce from their initial oxidation state Au^{1+} to a metal state (Au^0) and this process continues happening until all gold cations are reduced or until no more cations can be reduced at the temperatures tested during our experiments. From our results, the end of this gold oxidation state change process normally happens at 40 °C – 50 °C. According to many authors (see Section 1.1 and references therein), Au^0 is the most active site for CO oxidation. Keeping in mind that the catalytic material inside the reactor would have a different and more active nature at the end of such a process, this could explain why conversions/yields during the ramp down process are higher than the ones observed previously during the temperature increase stage (when there was a higher ratio $\text{Au}^{1+}/\text{Au}^0$). Once the reaction stops, the sample is kept inside the reactor, the inlet flow containing the CO gas mixture is switched off and the oxygen containing flow is set to 10 ml min⁻¹. Water bath heater is also turned off and it is left to cool down to room temperature. After 24 hours, CO and O₂ inlet flows are set to the desired value, which would be the same as those set for the reaction on the fresh sample, and the reaction is started again following exactly the

same procedure. Therefore, everything is essentially placed in an identical way during both the fresh and the used sample experimental tests. Nonetheless, according to the argument exposed above, catalyst would contain a higher population of metallic gold (Au^0) and thus, remaining within our literature based hypothesis, a higher activity would be expected in the CO oxidation reaction being performed. Looking at Figures 5.21-5.26 again, that is exactly what happens. Higher activity of the reused sample during the ramp up stage. Then, during the previous experiment on the fresh sample, the maximum number of gold cations possibly getting reduced at the temperatures run in our test was already obtained, thus an increase in the metallic gold population would not be expected during the test on the used sample, and, consequently, conversions/yields during both temperature ramp up and down should match with each other during such a reusability experiment. Indeed, this is what the results tell. Nonetheless, one could argue now what about the 24 hours when 10% O_2/N_2 was flowed over the already used sample. As commented before, this was a process carried out at room temperature and although the initial intention was trying to re-oxidise the sample in order to get it as close as possible to its initial state, it was quickly realised that initial purpose was not fulfilled. As already pointed out, it was a room temperature process and this could easily serve as a plausible reason for the re-oxidation of the catalytic sample not taking place. Higher energies supply, or temperatures, would very likely be necessary for such an oxidation to occur. Nevertheless, flowing oxygen over the catalytic surface could remove those carbonates species weakly bound to it during the CO oxidation experiment just performed, therefore preparing the catalytic sample for the next test by providing a cleaner surface. Despite, after a reactive process have taken place over such a catalytic surface, this would not be as clean as it was in its fresh state (before any reaction), which would simultaneously explain why during the temperature ramp down stage, during which for both fresh and used samples the transition from cationic to metallic gold already happened previously, the activity in the used case is slightly lower than the former, presumably due to the presence of species that still remained bound to some of the active sites, impeding the contribution of those on the CO oxidation mechanism.

Focusing now in some specific cases, figures 5.23 and 5.25 show a more scattered conversion data than that obtained in the rest of experiments (Fig. 5.21, 5.22, 5.24, 5.26). If we pay attention to the y-axis, maximum values are far smaller in these two cases. As discussed in the previous Section 5.1.1, the GC column responsible for CO detection carries a bigger error than the one for CO₂, hence yields do not show these fluctuations. The lower the conversions, the more obvious this instrumental error is and, as a consequence, the more visual the scatter in the data.

Finally, there is one more thing to point out on the data collected during the contact time study using the Au/CeO₂ catalyst. Figure 5.27 shows a more visual perspective of such data, where a sudden increase in conversions/yields can be observed when testing contact times 0.054 and 0.0405 g s ml⁻¹, corresponding to total mass flows of 30 and 40 ml min⁻¹ respectively. This sudden increase in activities is a trend followed by both fresh and used samples during both temperature ramp up and ramp down stages. Conclusively, it was thought that a non-homogeneous distribution of gold particles across the synthesized catalytic material could be the root of this unexpected data. Figures 5.28-5.29 and Table 5.2 present a sample of the results obtained from the SEM/EDX analysis performed on the Au/CeO₂ catalyst. In Figure 5.28, which shows a range of particle sizes on the 3 μm scale, a larger particle with a different topography than the rest of the analysed area can be distinguished. The elemental mapping on the same area (Figure 5.29), reveals that the same particle is essentially lacking cerium and oxygen (identified as a black area), while its gold loading is relatively low. These results evidence the presence of particles with a composition that does not agree with the Au/CeO₂ catalytic material. In other words, the presence of impurities in the synthesized catalytic batch, which supports the previously commented non-homogeneity as a reason for the results seen in Figure 5.27.

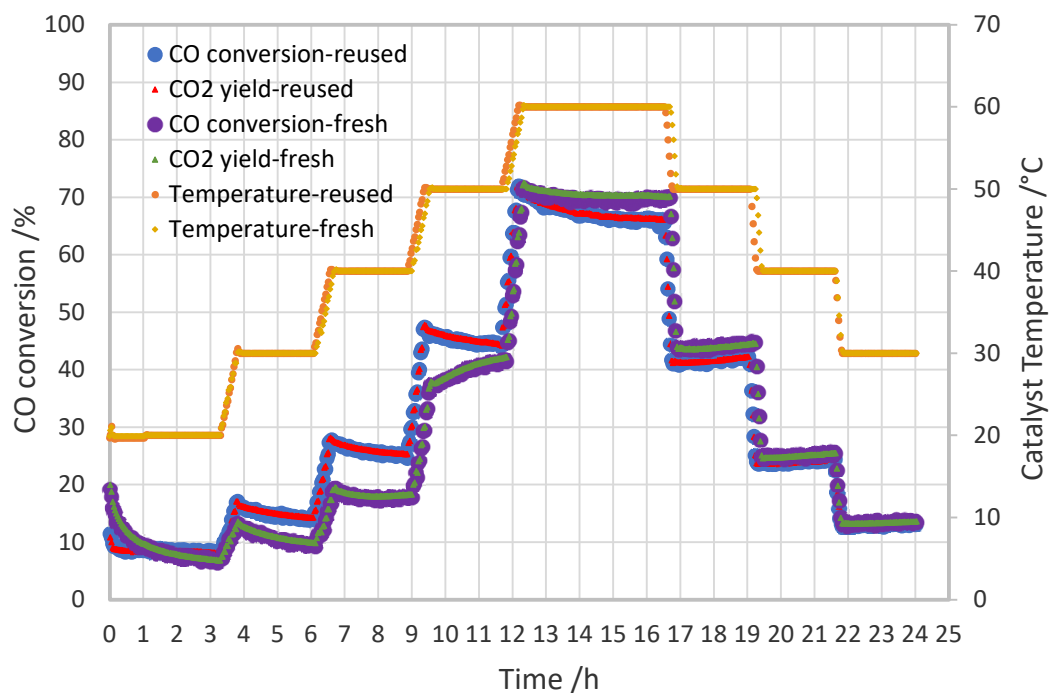


Figure 5.21. CO conversion, yield to CO₂ and temperature of catalytic bed versus time when flowing 9.1 ml min⁻¹ of 2% CO/N₂ and 0.9 ml min⁻¹ of 10% O₂/N₂ over a fresh and used catalytic bed consisting of 3mg of 5% Au/CeO₂ diluted in 24 mg of CeO₂ (corresponding to $\lambda = 1$, $R_{\text{dil}} = 1/9$ and $W/F = 0.162 \text{ g s ml}^{-1}$). The experiment over the already used sample was carried out after 24 hours of flowing 10 ml min⁻¹ of 10% O₂/N₂.

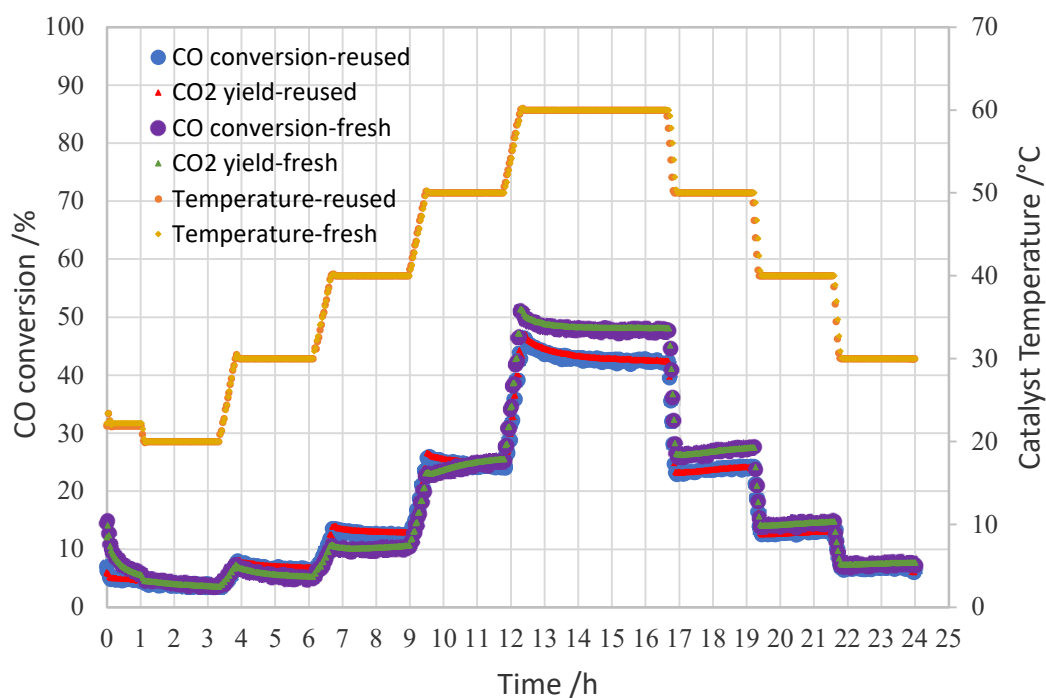


Figure 5.22. CO conversion, yield to CO₂ and temperature of catalytic bed versus time when flowing 18.2 ml min⁻¹ of 2% CO/N₂ and 1.8 ml min⁻¹ of 10% O₂/N₂ over a fresh and used catalytic bed consisting of 3mg of 5% Au/CeO₂ diluted in 24 mg of CeO₂ (corresponding to $\lambda = 1$, $R_{\text{dil}} = 1/9$ and $W/F = 0.081 \text{ g s ml}^{-1}$). The experiment over the already used sample was carried out after 24 hours of flowing 10 ml min⁻¹ of 10% O₂/N₂.

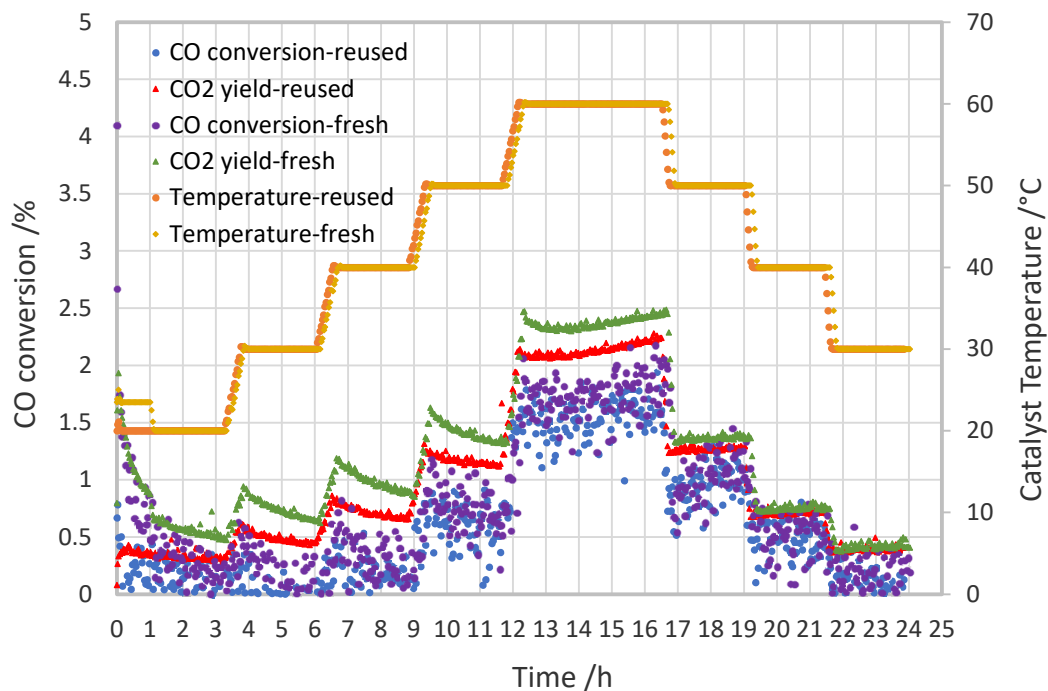


Figure 5.23. CO conversion, yield to CO₂ and temperature of catalytic bed versus time when flowing 22.7 ml min⁻¹ of 2% CO/N₂ and 2.3 ml min⁻¹ of 10% O₂/N₂ over a fresh and used catalytic bed consisting of 3mg of 5% Au/CeO₂ diluted in 24 mg of CeO₂ (corresponding to $\lambda = 1$, $R_{\text{dil}} = 1/9$ and $W/F = 0.065 \text{ g s ml}^{-1}$). The experiment over the already used sample was carried out after 24 hours of flowing 10 ml min⁻¹ of 10% O₂/N₂.

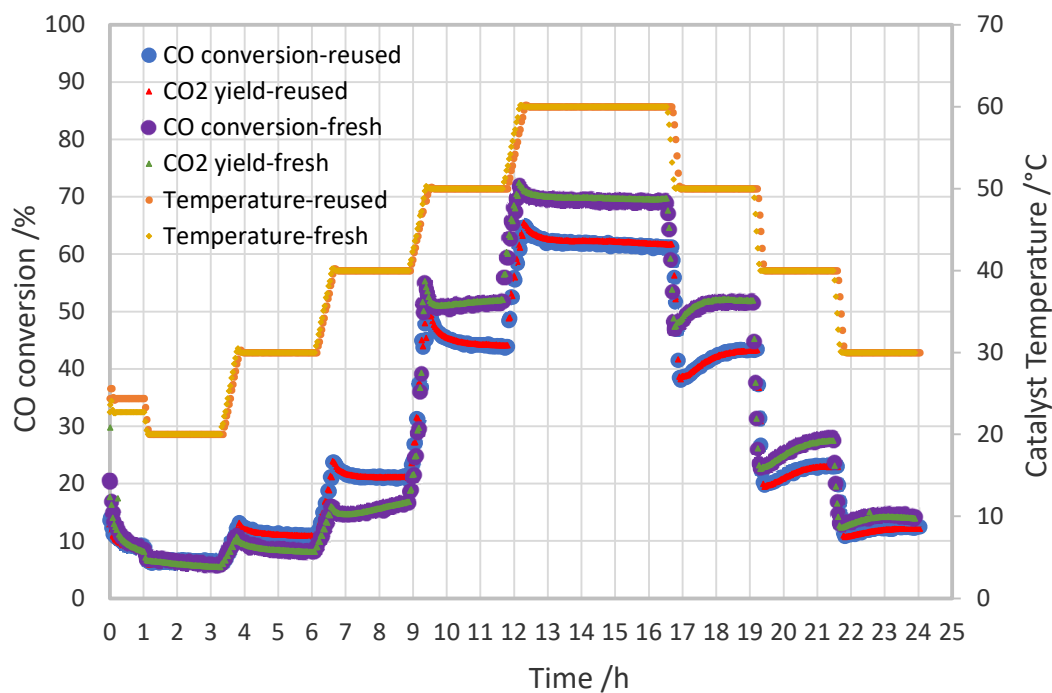


Figure 5.24. CO conversion, yield to CO₂ and temperature of catalytic bed versus time when flowing 27.2 ml min⁻¹ of 2% CO/N₂ and 2.7 ml min⁻¹ of 10% O₂/N₂ over a fresh and used catalytic bed consisting of 3mg of 5% Au/CeO₂ diluted in 24 mg of CeO₂ (corresponding to $\lambda = 1$, $R_{\text{dil}} = 1/9$ and $W/F = 0.054 \text{ g s ml}^{-1}$). The experiment over the already used sample was carried out after 24 hours of flowing 10 ml min⁻¹ of 10% O₂/N₂.

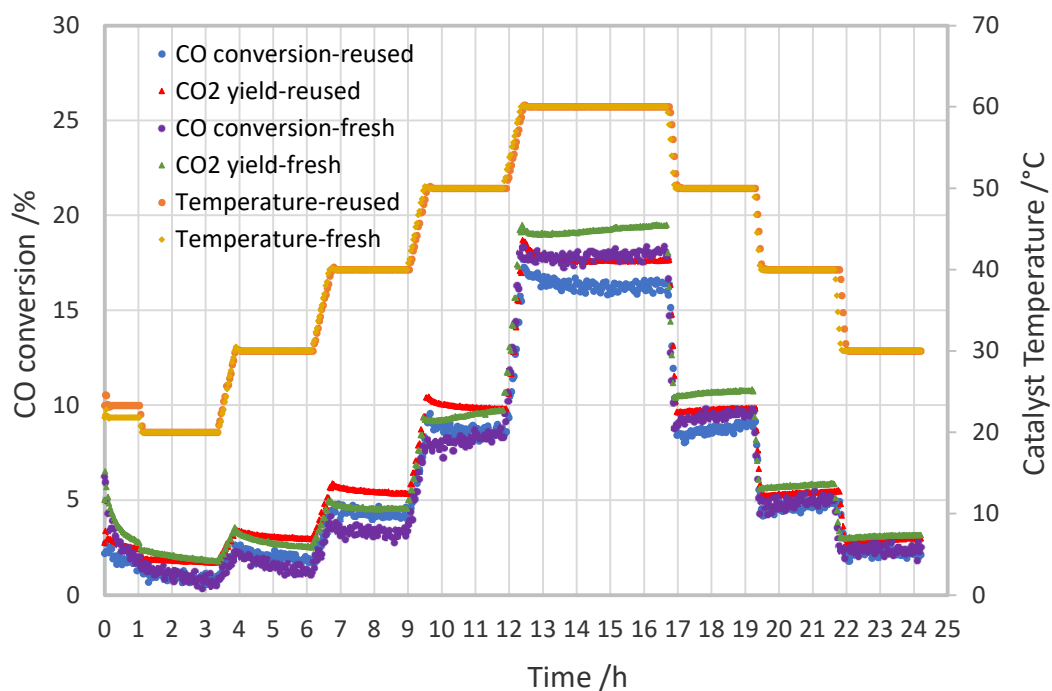


Figure 5.25. CO conversion, yield to CO₂ and temperature of catalytic bed versus time when flowing 31.8 ml min⁻¹ of 2% CO/N₂ and 3.2 ml min⁻¹ of 10% O₂/N₂ over a fresh and used catalytic bed consisting of 3mg of 5% Au/CeO₂ diluted in 24 mg of CeO₂ (corresponding to $\lambda = 1$, $R_{\text{dil}} = 1/9$ and $W/F = 0.046 \text{ g s ml}^{-1}$). The experiment over the already used sample was carried out after 24 hours of flowing 10 ml min⁻¹ of 10% O₂/N₂.

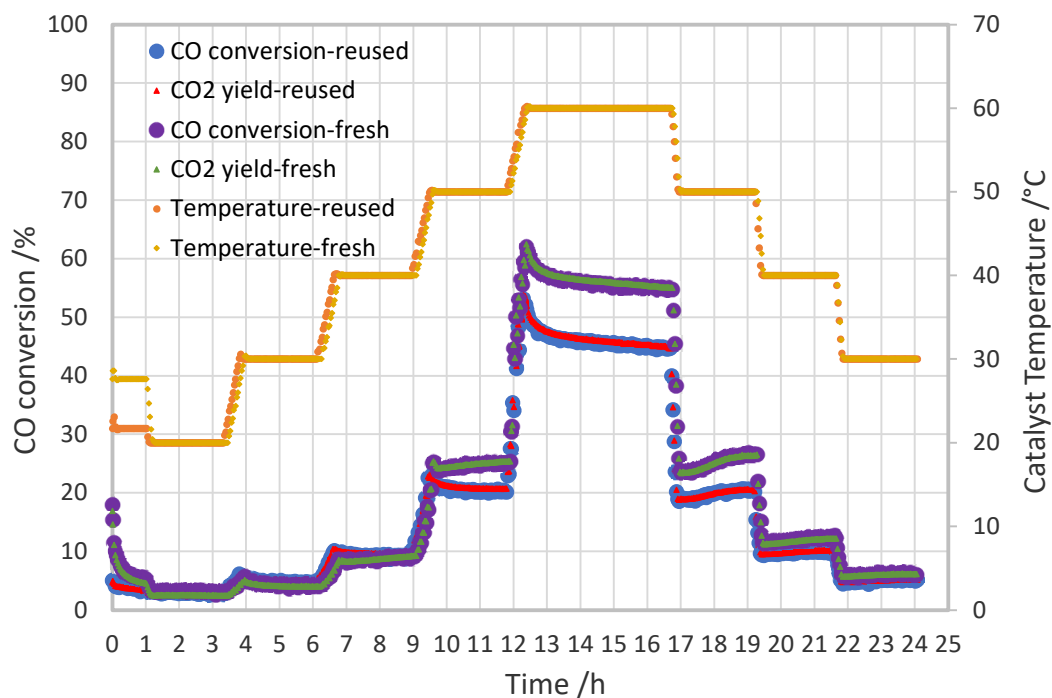


Figure 5.26. CO conversion, yield to CO₂ and temperature of catalytic bed versus time when flowing 36.4 ml min⁻¹ of 2% CO/N₂ and 3.6 ml min⁻¹ of 10% O₂/N₂ over a fresh and used catalytic bed consisting of 3mg of 5% Au/CeO₂ diluted in 24 mg of CeO₂ (corresponding to $\lambda = 1$, $R_{\text{dil}} = 1/9$ and $W/F = 0.0405 \text{ g s ml}^{-1}$). The experiment over the already used sample was carried out after 24 hours of flowing 10 ml min⁻¹ of 10% O₂/N₂.

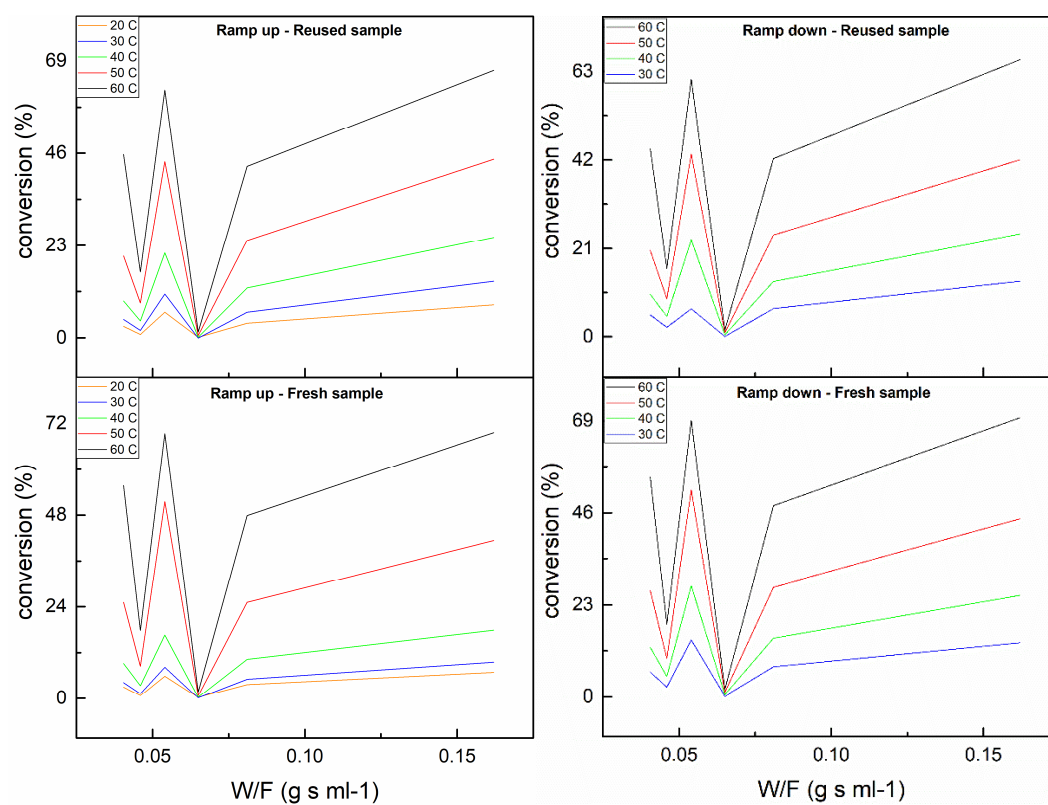


Figure 5.27. CO conversion versus contact time when using fresh and reused 5% Au/CeO₂ diluted on CeO₂ at a dilution ratio $R_{dil} = 1/9$ and at a stoichiometric ratio O₂/CO ($\lambda = 1$) in the gaseous inlet flow. Temperature ramp up and ramp down stages for both fresh and reused samples correspond to plots on the left and on the right respectively.

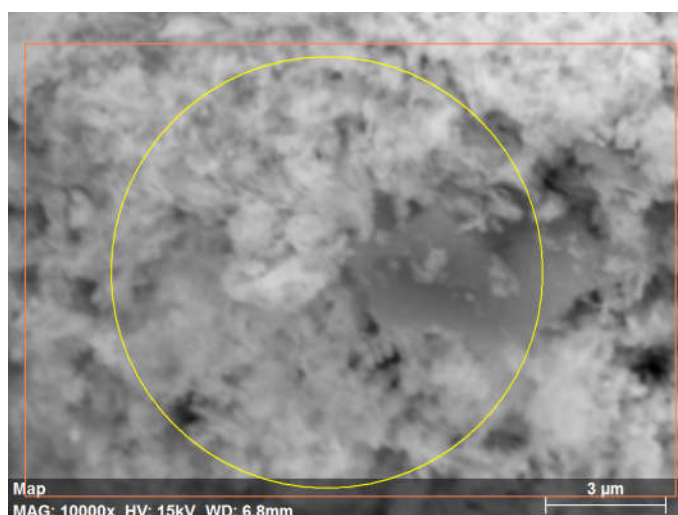


Figure 5.28. SEM imaging showing one of the samples of the Au/CeO₂ catalytic surface where EDX was performed.

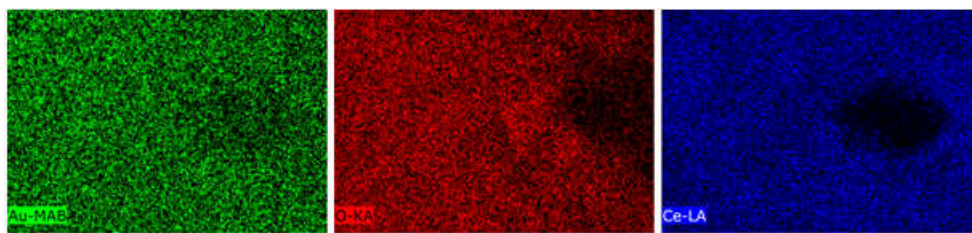


Figure 5.29. Mapping showing the elemental dispersion over the catalytic surface showed in Figure 5.28. Elements mapped are gold, oxygen and cerium (green, red and blue images, respectively).

Element	AN	Series	unn. C [wt.%]	norm. C [wt.%]	Atom. C [at.%]	Error [%]
Oxygen	8	K-series	20.62	21.88	71.39	2.2
Cerium	58	L-series	69.31	73.56	27.40	2.0
Gold	79	M-series	4.30	4.56	1.21	0.2
Total:			94.22	100.00	100.00	

Table 5.2. EDX elemental analysis obtained from the catalytic surface showed in Figure 5.28.

Experimental procedure detailed above when testing the Au/CeO₂ catalyst was also followed for the case of the AuPd/CeO₂ catalyst. As expected from that observed in Section 5.1.1, lower conversions were obtained when using AuPd/CeO₂ (see Figure 5.30). Also, as seen in Figure 5.30, the features associated to the non-homogeneous distribution of the noble metals across the catalytic material, discussed previously for the case of Au/CeO₂, are repeated in this data on the alloy catalyst too. Such features are characterised for not following any reasonable pattern, with lowest conversions/yields at the highest contact time and with sudden increases in catalytic activity at lower contact times (0.081 and 0.054 ml min⁻¹).

These results on the supported AuPd catalyst, along with those previously obtained on the Au/CeO₂ catalyst, led to experiments using an approach in which the same catalyst was used for a whole set of experiments so that sample-to-sample variations could be avoided. This approach has been called 'Reused sample approach' and experiments carried out according to such are detailed in the next section.

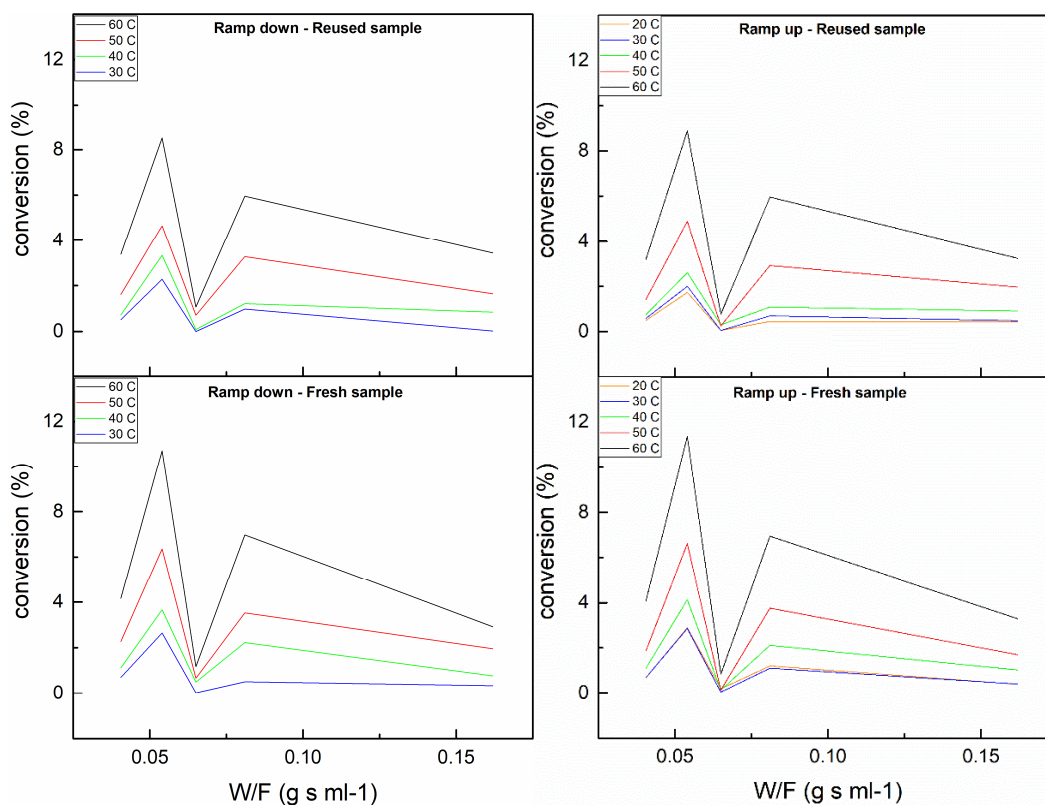
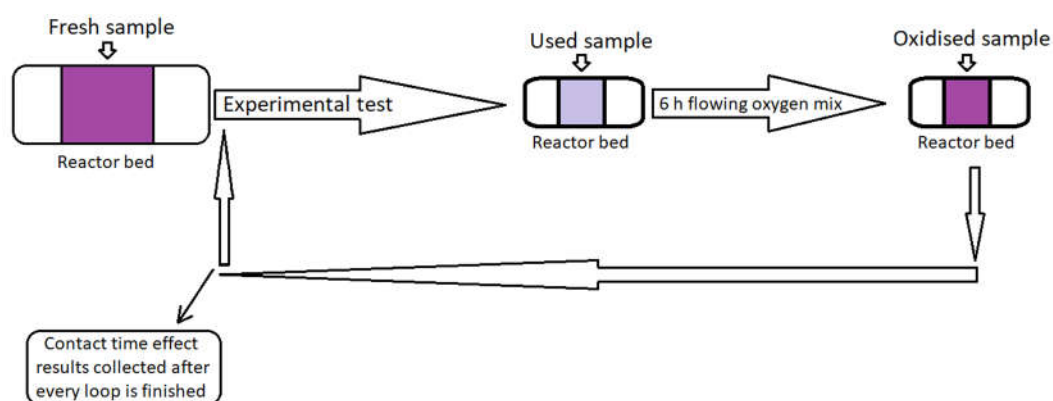


Figure 5.30. CO conversion versus contact time when using fresh and reused 5% AuPd/CeO₂ diluted on CeO₂ at a dilution ratio $R_{\text{dil}} = 1/9$ and at a stoichiometric ratio O₂/CO ($\lambda = 1$) in the gaseous inlet flow. Temperature ramp up and ramp down stages for both fresh and reused samples correspond to plots on the right and on the left respectively.

5.1.2.b Effect on contact time – Reused sample approach

As pointed out in subsection 5.1.2.a, this 'Reused sample approach' was developed as a consequence of the lack of correlation found on the catalytic results obtained from the application of the 'Fresh sample approach'. From those results, two main features were noted. Firstly, both Au/CeO₂ and AuPd/CeO₂ showed an extraordinary degree of reusability. Secondly, the behaviour of these two catalysts did not follow any pattern when studying the effect of contact time (see Figures 5.27 and 5.30), which appeared to be due to significant sample-sample variation in catalytic performance. Thus, it was thought that taking a single catalytic sample, packing it in the reactor and using it as many times as needed to complete each

series of tests would offer a good alternative to deal with that issue. However, for such procedure to yield good results, the catalytic material must have high reusability properties. This was already confirmed in the previous section (see Fig. 5.21-5.26). Additionally, with the intention of making the whole experimental process less time consuming, our oxygen containing gas mixture (10% O₂/N₂) was flowed over the sample for 6 instead of 24 hours after every test was finished and just before starting the next one. As such, the 'Reused sample approach' procedure was set. Scheme 5.2 below exemplify such procedure from a more visual perspective.



Scheme 5.2. Procedure followed in the 'Reused sample approach'

The rest of the experimental conditions followed the approach used in Section 5.1.2.a, i.e. same range of temperatures, same periods of time, same catalytic mass, diluent and dilution ratio. Finally, same mass flows (or contact times) were studied as well, with a constant lambda value ($\lambda = \frac{2[O_2]}{[CO]}$) in the inlet gas flow to the reactor. For the sake of keeping the length of this chapter within the reasonable, only the most representative and most relevant results will be shown from now on.

As noted in subsection 5.1.2.a, figures 5.33 and 5.36 collect all data from the tests on each individual contact time and present it in a visual way that summarizes the pattern both Au/CeO₂ and AuPd/CeO₂ catalytic behaviours follow, respectively.

For the supported gold catalyst, a clear direct relation contact time-CO oxidation can be seen (Figure 5.33), i.e. the higher the contact time the higher the conversion

of CO to CO₂. There is, though, an exception to such a linear trend, occurring at contact time equal 0.046 g s ml⁻¹. This is explained with fact that the catalyst was only in its fresh state (not used previously) at the beginning of this precise contact time test. As discussed previously, the oxidation state on the gold particles present in the catalytic surface are potentially changing once the temperature reaches the threshold needed for such a change in oxidation state to start. Then, it is thought the process continues, providing the temperature is still equal or above that energy threshold, until all available gold particles have changed to the new oxidation state. Notice here that 'available gold particles' must be understood as those gold particles which require an energy equal or below the energy being supplied to the system (heating temperature in our case) to undergo such transition in their oxidation state. Keeping in mind this is a chemical process that changes the nature of the material being tested, it becomes obvious that this 'outside the rule' case is not a real deviation in the catalytic behaviour but rather the behaviour that correspond to a material with that specific chemical nature. Plotting these results along with those obtained on the reused sample (rest of contact times in Figure 5.33) serves as a proof of such a different state of fresh and reused catalytic samples. According to the experimental procedure that this 'Reused sample approach' implies, the catalytic sample is packed and then reused for as many times as it is needed until the series of tests is finished. Nonetheless, and despite these catalytic materials had shown exceptional reusability properties (see subsection 5.1.2.a), it would be unrealistic to think of those materials to remain unperturbed along its cycled reuse. Moreover, it would be plausible to consider that the greater the catalytic involvement in the reaction mechanism the higher the perturbation on the catalytic surface would be. The higher the contact time, the longer the time the reactants have to interact with the catalytic surface, the higher the probabilities of chemical reactions among them to take place and, consequently, the more significantly the catalyst would get involved. In conclusion, the higher the contact time, the more chances to make changes in the nature of the catalytic surface and the chemical species bound to it. Minimizing those chances is essential when it comes to reusability processes and, hence, a lower to higher contact time order of tests was followed. The only exception to such an order comes with the data

obtained at the lowest contact time ($0.0405 \text{ g s ml}^{-1}$), which was tested at the end of the series. Yet, results obtained at this lowest contact time nicely follow the expected trend, i.e. they also show the lowest CO conversions (see Figure 5.33), evidencing the noticeably reusability properties of the 5% Au/CeO₂ catalyst.

The trend seen previously (Figures 5.21-5.26), related to the different catalytic activities during ramp up and ramp down in temperature, is also reproduced in the data obtained from the application of this 'Reused sample approach'. While for the fresh sample (Fig. 5.31), higher conversions/yields are obtained during the ramp down, for the reused cases the opposite behaviour is observed, i.e. higher conversions/yields during the temperature ramp up (Fig. 5.32 gives example of this). The reproducibility of such behaviour along with the NAP-XPS results presented in previous section reinforces the explanation given there. This is, reduction from Au¹⁺ to Au⁰ during the temperature increase stage in the fresh packed sample, resulting in a more active catalytic surface which is evidenced during the ramp down in temperature. For the reused cases, the accumulation of carbonate species bound to the surface as the proposed cause for the slightly lower conversions during the ramp down in temperature compared to the ramp up. Such accumulation of chemical species on the catalytic surface is thought to be likely happening in the fresh packed sample as well. However, the improvement in the catalytic activity gained by the acquired higher ratio Au⁰/ Au¹⁺ would surpass the negative effects due to those chemical species impeding some of the active sites from taking part in the desired reaction.

Finally, there is a quite characteristic feature which is common to the data obtained in all the cases for Au/CeO₂ presented. Such feature has also been typically observed in most of the tests performed not only on this specific material but on all of the catalysts studied previously (see Section 5.1.1). This is related to the decay curve drawn by the CO conversion data during the temperature ramp up and that is missing in their respective counterpart during the temperature ramp down. Repeatedly, conversions/yields reach a maxima just at the end of each temperature ramp up stage, once the water bath heater is set to maintain the current temperature for a period of time. During such period of time (typically 2 hours),

conversions/yields gradually decrease until they reach an almost constant value, which is considered as the system getting into the steady state. As already pointed out, this phenomena is not happening when the temperature of the system is decreased. An explanation to it could be found at the beginning of Section 5.1, where the potential shift from kinetic control to external diffusion control during strongly exothermic reactions was discussed. As commented then, in such external diffusion regime, the activity of the catalyst is determined by conversions rather than heater temperature. The higher the conversion the bigger the amount of heat released, leading to an increase in the temperature of the catalytic bed. When heat is provided to the system in order to increase its temperature, there is a potential risk of having an exothermic heat flux from the reaction that exceeds the heat loss flux, which is the crucial starting point for the shift in regimes to occur. Therefore, it is believed that during the ramping up in temperature, the system enters external diffusion control, which is then returned to its original kinetic regime by stopping the energy supply to the system, i.e. external heater stops heating or decreases its power in order to maintain a constant temperature of the system. During temperature ramp down stages, when heat is extracted from the system, the risk of entering external diffusion control is practically non-existent at our experimental conditions, which would explain that the decay curve drawn by conversions is not observed during cooling down stages.

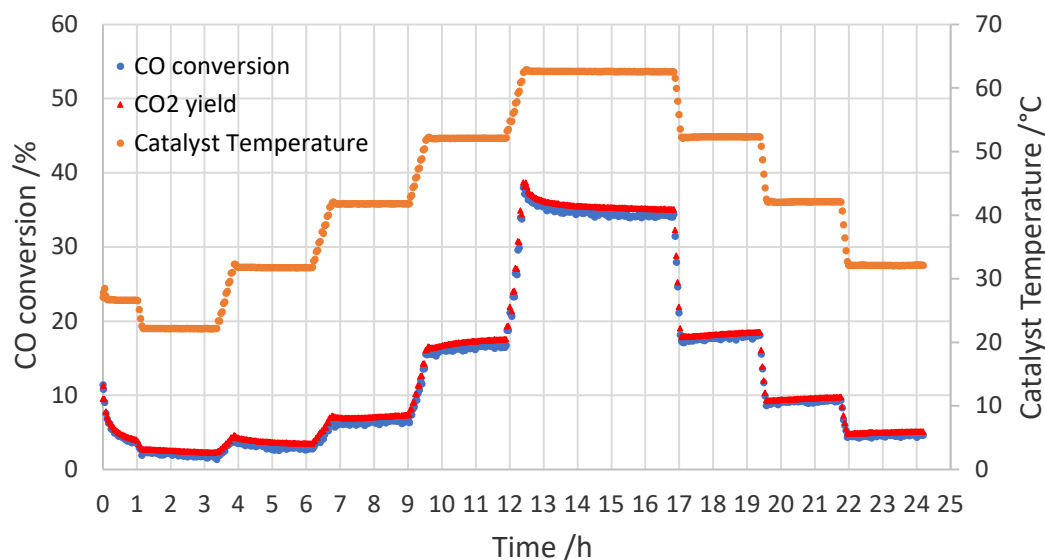


Figure 5.31. CO conversion, yield to CO₂ and temperature of catalytic bed versus time when flowing 31.8 ml min⁻¹ of 2% CO/N₂ and 3.2 ml min⁻¹ of 10% O₂/N₂ over a fresh catalytic bed consisting of 3 mg of 5% Au/CeO₂ diluted in 24 mg of CeO₂ (corresponding to $\lambda = 1$, $R_{dil} = 1/9$ and $W/F = 0.046$ g s ml⁻¹).

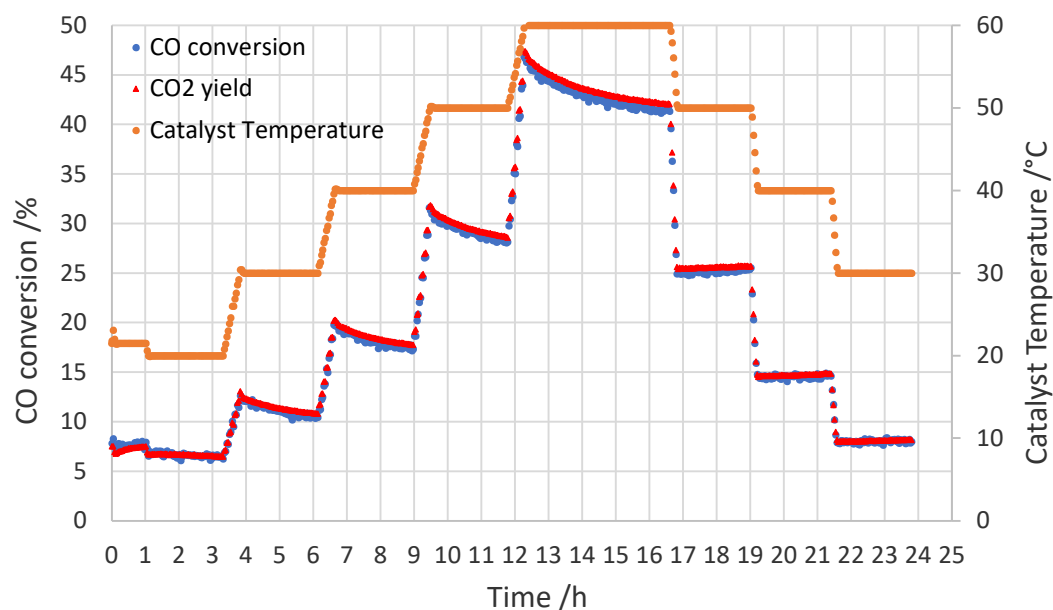


Figure 5.32. CO conversion, yield to CO₂ and temperature of catalytic bed versus time when flowing 9.1 ml min⁻¹ of 2% CO/N₂ and 0.9 ml min⁻¹ of 10% O₂/N₂ over an used catalytic bed consisting of 3 mg of 5% Au/CeO₂ diluted in 24 mg of CeO₂ (corresponding to $\lambda = 1$, $R_{dil} = 1/9$ and $W/F = 0.162$ g s ml⁻¹). The experiment over the already used sample was carried out after 6 hours of flowing 10 ml min⁻¹ of 10% O₂/N₂.

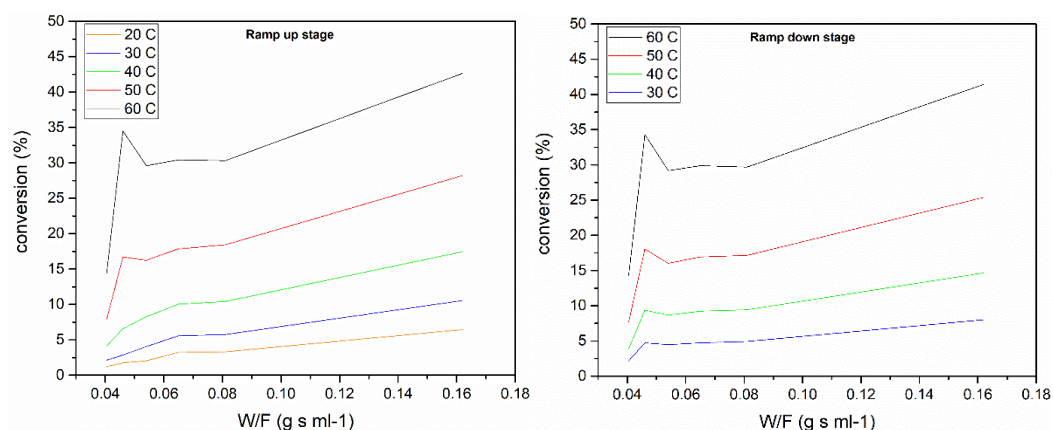


Figure 5.33. CO conversion versus contact time when using 5% Au/CeO₂ diluted on CeO₂ at a dilution ratio $R_{dil} = 1/9$ and at a stoichiometric ratio O_2/CO ($\lambda = 1$) in the gaseous inlet flow. Temperature ramp up and ramp down stages correspond to plots on the left and on the right respectively. Catalytic sample was only fresh at $W/F = 0.046 \text{ g s ml}^{-1}$, for the rest of contact times the same sample was reused.

When it comes to the analysis of those results on AuPd/CeO₂ (Figures 5.34-5.36), mostly everything discussed above for Au/CeO₂ is repeated in the alloy case. However, since a lower catalytic activity is shown here, this material also presents less pronounced reactive features. Thus, less product (CO₂) is yielded and in consequence, less heat is released. With less heat being released, less chances of facing a situation where the exothermic heat flux from the reaction exceeds the heat loss and lower the risk of shifting from kinetic to external diffusion control. Nonetheless, if the system does enter into such external diffusion regime, it would involve a milder process, with the temperature of the system increasing at a lower rate. Accordingly, the decay curve drawn by the CO conversion data during the temperature ramp up observed in the case of Au/CeO₂ should also be observed in the AuPd/CeO₂ catalyst, although with a lesser visual decay in the latter. Having a look back to figures 5.31-5.32 and comparing them with figures 5.34-5.35, such behaviour can be confirmed. Additionally, considering that the supported AuPd catalyst has a lower catalytic activity than the supported Au case, the less reactive surface would not only mean a lower CO₂ yield and also fewer intermediate reactions taking place over such a surface, thus fewer intermediate carbonate species being bound to it. If the surface remains cleaner, conversions/yields during

the temperature ramp down should minimally differ from those obtained during the ramp up stage. Again, having a look at figures 5.34-5.35, effectively there is none or minimal differences in the amount of CO converted during ramp up and ramp down stages in the case of AuPd/CeO₂. It is essential to remember here that those values in conversion need to be compared after the system has reached a mostly stabilized value, i.e. after the 2 hours period of keeping each temperature constant. Finally, the linear relationship conversion-contact time observed in figure 5.36 is broken down at contact time 0.0405 g s ml⁻¹. Similar to what happened with the Au/CeO₂ catalyst at contact time 0.046 g s ml⁻¹ (Figure 5.33), this is due to the fact that the catalysts was only freshly packed at the beginning of this test (Figure 5.34). The implications of having a different oxidation state of the Au in fresh and reused samples exposed previously for Au/CeO₂ can be directly extrapolated to this case, when both gold and palladium undergo a transition in their respective state of oxidation.

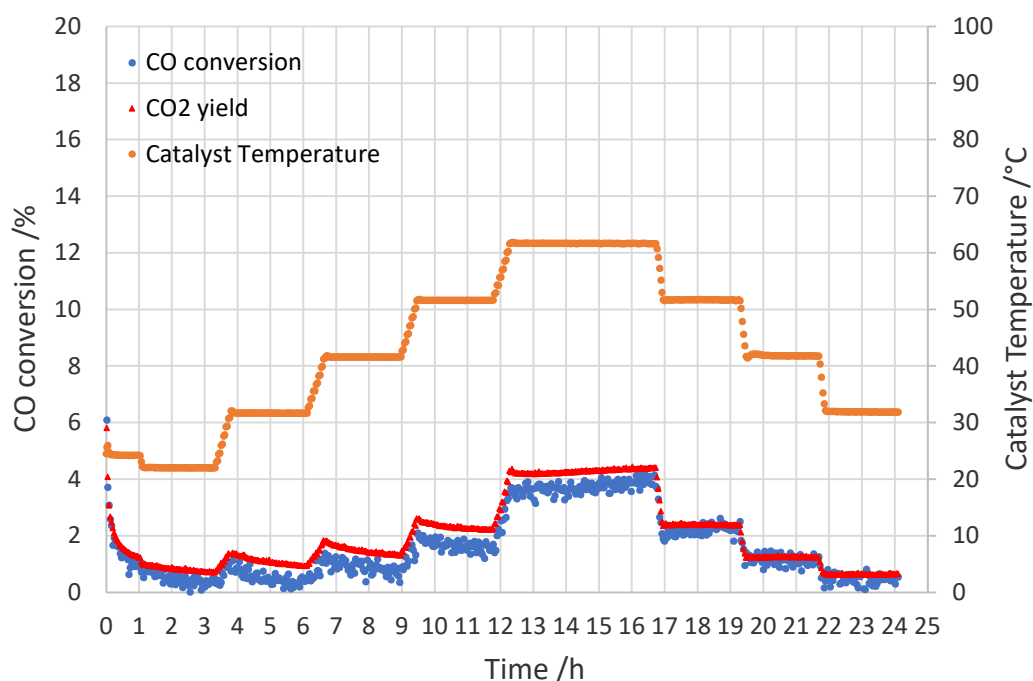


Figure 5.34. CO conversion, yield to CO₂ and temperature of catalytic bed versus time when flowing 36.4 ml min⁻¹ of 2% CO/N₂ and 3.6 ml min⁻¹ of 10% O₂/N₂ over a fresh catalytic bed consisting of 3 mg of 5% AuPd/CeO₂ diluted in 24 mg of CeO₂ (corresponding to $\lambda = 1$, $R_{dil} = 1/9$ and $W/F = 0.0405$ g s ml⁻¹).

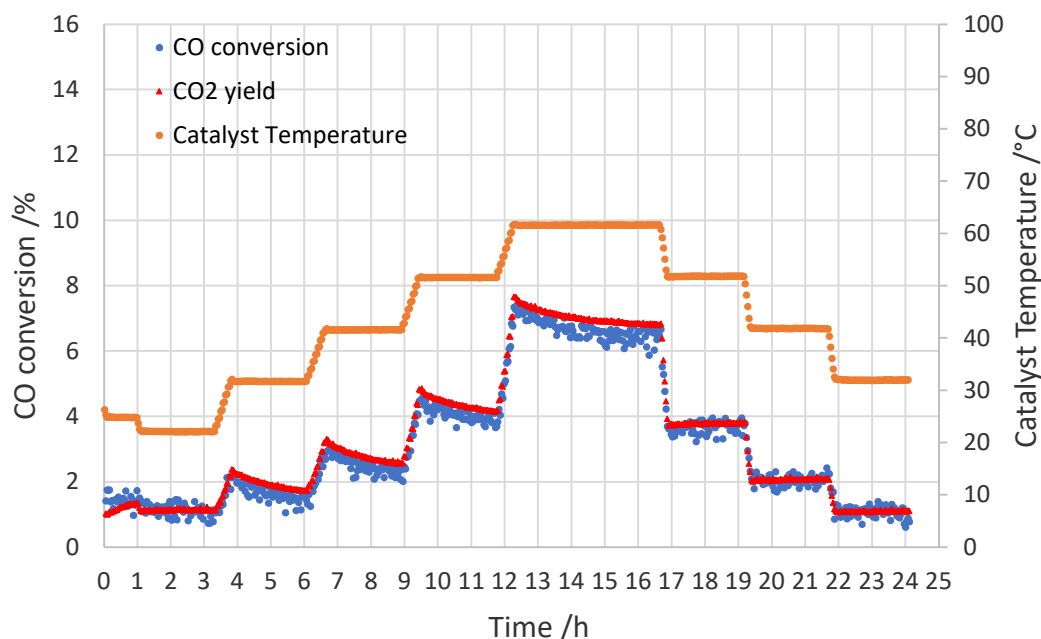


Figure 5.35. CO conversion, yield to CO₂ and temperature of catalytic bed versus time when flowing 9.1 ml min⁻¹ of 2% CO/N₂ and 0.9 ml min⁻¹ of 10% O₂/N₂ over an used catalytic bed consisting of 3 mg of 5% AuPd/CeO₂ diluted in 24 mg of CeO₂ (corresponding to $\lambda = 1$, $R_{\text{dil}} = 1/9$ and $W/F = 0.162 \text{ g s ml}^{-1}$). The experiment over the already used sample was carried out after 6 hours of flowing 10 ml min⁻¹ of 10% O₂/N₂.

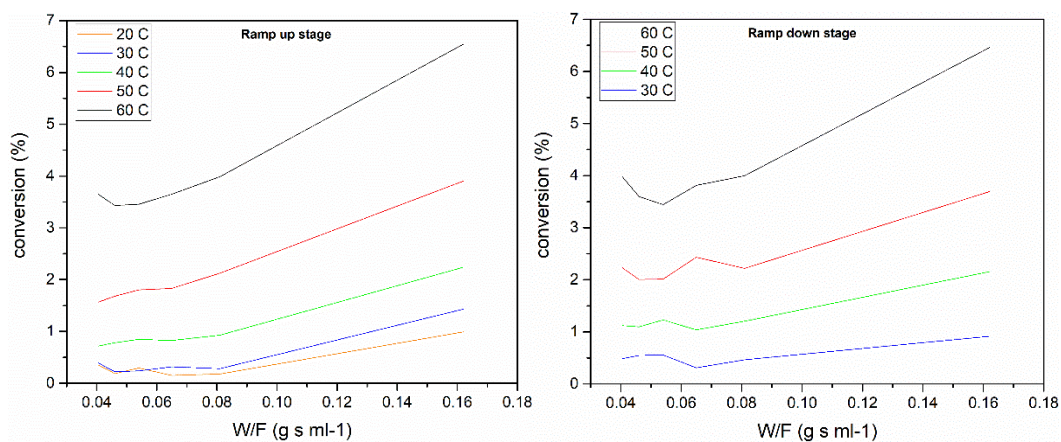


Figure 5.36. CO conversion versus contact time when using 5% AuPd/CeO₂ diluted on CeO₂ at a dilution ratio $R_{\text{dil}} = 1/9$ and at a stoichiometric ratio O₂/CO ($\lambda = 1$) in the gaseous inlet flow. Temperature ramp up and ramp down stages correspond to plots on the left and on the right respectively. Catalytic sample was only fresh at $W/F = 0.0405 \text{ g s ml}^{-1}$, for the rest of contact times the same sample was reused.

In order to make it easier for the reader the direct comparison between the two catalysts (Au/CeO₂ and AuPd/CeO₂) that were tested during the study of the effect of contact time on their activity, a simplified summary of the results previously discussed throughout Section 5.1.2.b is presented in Table 5.3.

Table 5.3. CO conversions obtained when Au/CeO₂ and AuPd/CeO₂ were tested for the CO oxidation reaction at different contact times (W/F). Values extracted from results presented in Figures 5.33 and 5.36. Standard deviations (σ) are given in brackets.

W/F g s ml ⁻¹	20 °C		40 °C		60 °C	
	Au/CeO ₂	AuPd/CeO ₂	Au/CeO ₂	AuPd/CeO ₂	Au/CeO ₂	AuPd/CeO ₂
0.162	6.5 % ($\sigma = 0.13$)	0.99 % ($\sigma = 0.18$)	14.7 % ($\sigma = 0.17$)	2.2 % ($\sigma = 0.15$)	41.4 % ($\sigma = 0.16$)	6.5 % ($\sigma = 0.29$)
0.081	3.3 % ($\sigma = 0.15$)	0.18 % ($\sigma = 0.15$)	9.4 % ($\sigma = 0.17$)	1.2 % ($\sigma = 0.13$)	29.7 % ($\sigma = 0.13$)	4.0 % ($\sigma = 0.15$)
0.065	3.2 % ($\sigma = 0.16$)	0.15 % ($\sigma = 0.07$)	9.2 % ($\sigma = 0.25$)	1.0 % ($\sigma = 0.13$)	29.9 % ($\sigma = 0.11$)	3.8 % ($\sigma = 0.12$)
0.054	2.0 % ($\sigma = 0.11$)	0.29 % ($\sigma = 0.16$)	8.7 % ($\sigma = 0.12$)	1.2 % ($\sigma = 0.18$)	29.2 % ($\sigma = 0.20$)	3.4 % ($\sigma = 0.17$)
0.046	1.8 % * ($\sigma = 0.19$)	0.19 % ($\sigma = 0.11$)	9.4 % * ($\sigma = 0.14$)	1.1 % ($\sigma = 0.09$)	34.3 % * ($\sigma = 0.14$)	3.6 % ($\sigma = 0.26$)
0.0405	1.2 % ($\sigma = 0.14$)	0.35 % * ($\sigma = 0.10$)	3.9 % ($\sigma = 0.28$)	1.1 % * ($\sigma = 0.13$)	14.3 % ($\sigma = 0.27$)	4.0 % * ($\sigma = 0.15$)

* Catalytic sample was freshly packed, i.e. it was not used previously, for the experimental test at this contact time. (Note that, for the rest of contact times, the catalytic sample was re-used according to the procedure detailed at the beginning of Section 5.1.2.b).

5.1.3 Lambda

From results presented in Section 5.1.1, a dilution ratio (R_{dil}) of 1/9 was selected. Then, such a dilution ratio was applied in our study on the effect of contact time discussed previously in Section 5.1.2. The purpose of such study was not only to analyse the catalytic behaviour of the different materials when the reactive gases were flowed at different rates over their surfaces but, also, to select an optimal contact time for the future experiments. For this, same criteria as that followed when choosing a R_{dil} was applied (see beginning Section 5.1.1). Accordingly, not too high conversions but appreciable ones need to be obtained for both Au/CeO₂ and AuPd/CeO₂ at the selected contact time. Going back to Figures 5.33 and 5.36,

it seemed that such criteria was better fulfilled at a total inlet flow of 20 ml min^{-1} , corresponding to a contact time (W/F) of $0.081 \text{ g s ml}^{-1}$.

Once both dilution ratio and contact time were investigated in detail and respective optimal values selected, a broad study on the effect of different lambdas (λ) was carried out. It is important to notice that, although already applied to our catalytic tests, a value of $\lambda = 1$ has been almost exclusively used. Only in very specific cases presented and discussed in Section 5.1.1, a more oxidising gas mixture ($\lambda = 2$) was also applied.

As it was defined in Chapter 2, Section 2.4.2, lambda (λ) is the process parameter that characterizes the oxygen excess with respect to the amount of oxygen required for the oxidation of CO to CO₂. According to Equation 2.14 (Section 2.4.2), when $\lambda = 1$, sufficient oxygen is provided for the complete oxidation of CO to CO₂ in the absence of an oxygen-consuming side reaction. In case of having competitive reactions, such in the case of CO and H₂ oxidations, the lower the selectivity of the process, the higher will be the required lambda value to completely oxidize CO to CO₂. For example, process conditions which yield a selectivity of 50% will afford a complete conversion of CO to CO₂ if the value of λ at the reactor entrance is ≥ 2 . Since 'CO only' oxidation is the focus of the present study, the interrelation between selectivity and λ is not a matter of concern. Nonetheless, the effect that lambda might have on the reaction kinetics is something that certainly need to be considered. With this respect, Engel and Ertl^{15,16} carried out UHV (ultra high vacuum) studies which led them to distinguish between two reaction regimes: (a) a high rate branch where the CO surface concentration is very small, occurring at high temperatures and/or λ -values (oxidizing conditions); (b) a low rate branch in which the surface is predominantly covered with adsorbed CO, occurring at low temperatures and/or λ -values (reducing conditions). Thus, on a surface predominantly covered with adsorbed CO, it would be expected that the reaction occurs in the low rate branch. Later studies dealing with high-pressure CO oxidation^{17,18} came to similar conclusions, indicating that the reaction mechanism of CO oxidation under UHV and high pressure conditions are essentially identical in the absence of mass transport effects. The λ -value at which the transition between

the two reaction branches occurs has been reported to be a function of temperature¹⁹. Since an increase in reaction temperature is concomitant with an increase in the CO desorption rate, the very low temperature profile maintained throughout the present study (20°C - 60°C) should guarantee that a minimal desorption of such surface adsorbed CO occurs due to the temperature effect. The above considerations were key in the implementation of the procedure followed during our differential flow measurements for the determination of reaction orders, which Section 5.3 focuses on.

5.2 Activation energies

The finding of apparent activation energies is an essential of any study where the kinetics of a reaction are considered. In Section 5.1.2.b, the effect of contact time was investigated by application of the so-called 'Reused sample approach' and satisfactory results were obtained. Such results offered reliable data where the catalytic activity dependence on the temperature, or activation energy, could be extracted. Moreover, since six different total mass flows, equivalent to six different contact times, were studied, six values could be obtained for the apparent activation energy of each catalytic material (Au/CeO₂ and AuPd/CeO₂). Hence, assuming that the mechanism is not influenced by contact time, accuracy would be increased by averaging those six values into a single one with its respective error. Furthermore, also with the goal of keeping the accuracy of the calculated value at the highest, only data corresponding to temperature ramp down stages have been used in the present section. This is because, as seen in previous sections, changes in the oxidation state of gold particles on the surface of fresh samples and/or the transient switch to external diffusion control, both happening during temperature ramp up stages, could impede the system from reaching the steady state during the 2 hours period usually left for that to happen.

The first step for the activation energies calculation comes with the application of the Arrhenius equation (Equation 5.2):

$$k = A \cdot e^{-E_a/RT} \quad (5.2)$$

where k is the rate constant, A is the pre-exponential factor, E_a the activation energy, R the ideal gas constant and T the absolute temperature in kelvin.

Applying natural logarithms to both sides of the above equality, Equation 5.3 is obtained:

$$\ln k = \frac{-E_a}{R} \cdot \left(\frac{1}{T}\right) + \ln A \quad (5.3)$$

As described in Section 3.2.2.1, the absolute reaction rate ($r_{CO_{mass}}$) was calculated from data presented in Section 5.1.2.b by application of Equation 3.4. Although different to k , the $r_{CO_{mass}}$ is directly related to it. Therefore, plotting the logarithm of the $r_{CO_{mass}}$ versus the inverse of the temperature (T^{-1}) and applying a linear regression to such data will yield the same slope than that if logarithm of k was used. Consequently, this method allows the experimental approximation of the activation energy with no assumption about the detailed kinetic model. In accordance to this method, results are presented in Figures 5.37 and 5.38 for the case of Au/CeO₂ and AuPd/CeO₂, respectively. In each of those figures, six different regression lines, for each of the six total mass flows studied in 5.1.2.b, are obtained. The slopes values for each of those lines presented in both Figures 5.37 and 5.38 are summarised in Tables 5.4 and 5.5, respectively. Deducted from Equation 5.3, the relationship between the activation energy and the slopes obtained from Figures 5.37 and 5.38 can be defined (Equation 5.4):

$$E_a = -R \cdot slope \quad (5.4)$$

Consequently, by application of such equality, the activation energies can be estimated. Thus, they are also included in Tables 5.4 and 5.5.

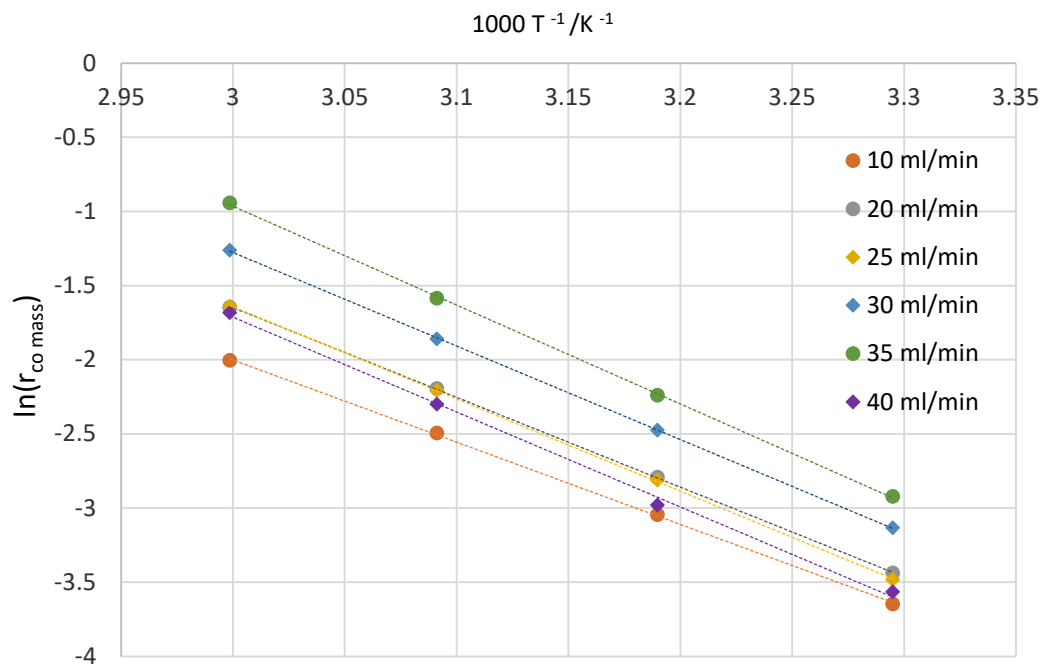


Figure 5.37. Absolute reaction rate ($r_{CO_{mass}}$) in the form of Arrhenius plots obtained from data presented in Figure 5.33 for 5 % Au/CeO₂.

Mass flows	Slope/ K	E_a /kJ·mol ⁻¹
10 ml min ⁻¹	-5.5455	46.1
20 ml min ⁻¹	-6.0565	33.6
25 ml min ⁻¹	-6.2193	37.7
30 ml min ⁻¹	-6.3108	39.2
35 ml min ⁻¹	-6.6688	39.2
40 ml min ⁻¹	-6.4012	42.7

Table 5.4. Slopes obtained from the linear regressions showed in Figure 5.37 and estimated activation energies from the application of Equation 5.4.

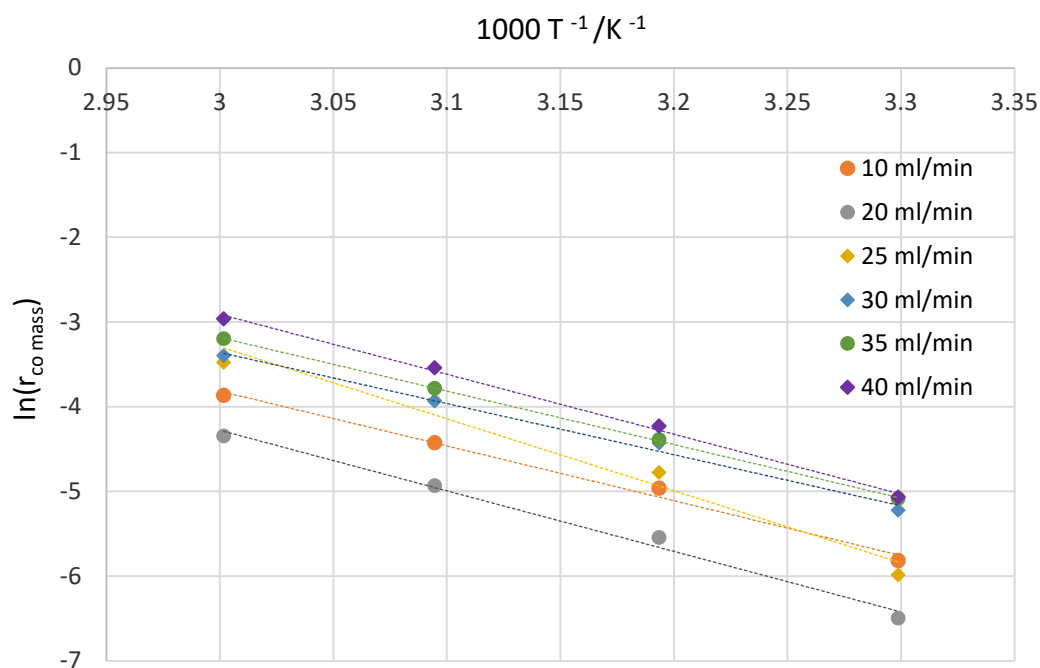


Figure 5.38. Absolute reaction rate ($r_{CO_{mass}}$) in the form of Arrhenius plots obtained from data presented in Figure 5.36 for 5 % AuPd/CeO₂.

Mass flows	Slope/ K	E_a /kJ·mol ⁻¹
10 ml min ⁻¹	-6.4713	53.8
20 ml min ⁻¹	-7.1475	39.6
25 ml min ⁻¹	-8.499	51.5
30 ml min ⁻¹	-6.0394	37.6
35 ml min ⁻¹	-6.3186	39.9
40 ml min ⁻¹	-7.0776	47.2

Table 5.5. Slopes obtained from the linear regressions showed in Figure 5.38 and estimated activation energies from the application of Equation 5.4.

Averaging the values presented in Table 5.4, an activation energy (E_a) of 39.8 kJ mol⁻¹ with a standard deviation of 4.3 kJ mol⁻¹ was obtained for the case of Au/CeO₂. Doing the same for data showed in Table 5.5, an E_a of 44.9 kJ mol⁻¹ with a standard deviation of 6.8 kJ mol⁻¹ was calculated for the case of AuPd/CeO₂.

5.3 Order of reaction with respect to CO at constant λ

The standard method for the determination of reaction orders is to vary the partial pressure of one of the reactants, while keeping all other reactants constant. In the present study, however, this approach was not followed, since it would entail measurements over a large range of λ -values which, in our case, would be undesirable. The main reason for this is that, as previously discussed in Section 5.1.3, a large variation of λ , in particular to high values, would increase the chances of reaching the onset of surface CO desorption. This would imply a transition between different reaction regimes (low to high rate branch), hence invalidating the experimental approach because of a change in mechanism. Furthermore, as already pointed out, a λ -value of 1 was maintained throughout Sections 5.1.1-5.1.3, this way limiting the number of variables coming into equation. Thus, for the investigation of the order of reaction with respect to CO (α_{CO}), both oxygen and CO partial pressures (p_{O_2} and p_{CO} respectively) were changed while keeping not only a constant λ -value but also a constant inlet flow into the reactor. This way to proceed responds to the result of a series of mathematical transformations on the power-law functionality most commonly applied to the expression of the CO oxidation reaction rate, Equation 5.5:

$$r_{CO} = k_{CO} \cdot e^{(-E_a/RT)} \cdot (p_{CO})^{\alpha_{CO}} \cdot (p_{O_2})^{\alpha_{O_2}} \quad (5.5)$$

If both left and right sides of Equation 5.5 are multiplied by $2^{(\alpha_{O_2})}$ and divided by $(p_{CO})^{\alpha_{O_2}}$ the mathematical equality transforms into Equation 5.6:

$$\frac{2^{(\alpha_{O_2})} \cdot r_{CO}}{(p_{CO})^{\alpha_{O_2}}} = k_{CO} \cdot e^{(-E_a/RT)} \cdot (p_{CO})^{\alpha_{CO}} \cdot \left(\frac{2 \cdot p_{O_2}}{p_{CO}}\right)^{\alpha_{O_2}} \quad (5.6)$$

Rearranging terms and considering the definition of λ (Equation 2.14), expression showed in Equation 5.7 is obtained:

$$r_{CO} = \left(k_{CO} / 2^{(\alpha_{O_2})}\right) \cdot e^{(-E_a/RT)} \cdot (p_{CO})^{(\alpha_{CO} + \alpha_{O_2})} \cdot \lambda^{(\alpha_{O_2})} \quad (5.7)$$

Applying logarithms to Equation 5.7 and considering that λ is maintained constant, the slope $\ln(r_{CO})$ versus $\ln(p_{CO})$ is given by Equation 5.8:

$$\left(\frac{\partial \ln(r_{CO})}{\partial \ln(p_{CO})}\right)_{\lambda=const} = \alpha_{CO} + \alpha_{O_2} = \alpha_{CO}^{\lambda} \quad (5.8)$$

Therefore, according to Equation 5.8, varying the CO partial pressure while maintaining λ constant would allow the determination of α_{CO}^{λ} . Then, if α_{O_2} is also estimated, α_{CO} would be given by a straight forward subtraction operation.

Now that λ has been properly defined and the basis for the method followed in the determination of the orders of reaction has been described, the experiments carried out to estimate α_{CO}^{λ} can be covered. Both Au/CeO₂ and AuPd/CeO₂ catalysts were tested under exactly the same experimental conditions. As reported in Section 5.1.3, a total inlet gaseous flow of 20 ml min⁻¹, corresponding to a contact time (W/F) of 0.081 g s ml⁻¹, and a dilution ratio of 1/9 was used for each series of tests presented in this section. Three different λ -values were initially intended to be studied, namely $\lambda = 1, 2$ and 3. Nevertheless, due to the results obtained and discussed further below, an extra λ -value of 1.5 was also investigated. The study of conversions and rate versus λ for the case of each λ -value constituted a series of six tests. From these six tests, two of them are presented to give example of the type of data obtained in each series (Figures 5.39-5.46 for Au/CeO₂ and Figures 5.59-5.66 for AuPd/CeO₂). In order to keep lambda constant while still changing p_{CO} and maintaining the inlet flow at a constant value of 20 ml min⁻¹, a third flow was introduced. Therefore, while only two gaseous mixes were fed into the reactor previously, i.e. 2% CO/N₂ and 10% O₂/N₂, at this point an extra flow of 100% N₂ was also used. Since nitrogen is an inert for the CO oxidation reaction, its only purpose was ensuring the commented above condition of constant inlet flow and λ at a varying p_{CO} . Six different N₂ flows were introduced during each series of tests, i.e. for the study at each λ -value, those being 13.3, 10, 8, 6.7, 5.3 and 3.3 ml min⁻¹. Related to tested temperatures, for the $\lambda = 1$ case, 20°C - 60°C with a ramp of 10°C was studied (Figures 5.39-5.40 for Au/CeO₂ and Figures 5.59-5.60 for AuPd/CeO₂). Nonetheless, due to the time restrictions being faced at this point of the research, the ramp was increased to 20°C for the rest of λ -values, i.e. 2, 3 and 1.5.

Consequently, comparison between ramps up and down for these cases was only possible at a temperature of 40°C (Figures 5.41-5.46 for Au/CeO₂ and Figures 5.61-5.66 for AuPd/CeO₂). For all cases, each temperature was kept constant for a period of 2 hours. Finally, the 'Reused sample approach' discussed in 5.1.2.b was used in this study of the order of reactions as well, since it proved a good solution for the non-homogeneity across the catalytic material observed during the 'Fresh sample approach' (Section 5.1.2.a). Therefore, a fresh sample was loaded into the reactor only at the beginning of each series of tests, then the same sample kept being reused for the rest of tests during that particular series. Also, before starting a new test and just after finishing the previous one, a mix consisting of 10% O₂/N₂ was flowed over the reactor bed for a period of 6 hours.

Starting our focus on the case of Au/CeO₂, each series of tests corresponding to each λ -value will be discussed first. Thus, for $\lambda = 1$ (Figures 5.39 and 5.40), the pattern already observed in the previous section is reproduced once again. For the fresh loaded sample case (Figure 5.39) higher conversions/yields are obtained during ramp down when comparing with their counterparts during the ramp up. Thus, the same explanation given before, based on a change of the oxidation state of the gold particles, would suit this case too. Furthermore, conversions experiment a noticeable increase during the 2 hours period where temperature is kept at 50°C and the steady state is not reached by the end of that period. This behaviour matches that seen previously and can be attributed to the increasing Au⁰ surface population at such temperature. The fact that, once the sample is reused, that pattern is no longer apparent and, instead, essentially the same activity is observed during both ramps up and down (Figure 5.40), reinforces our hypothesis, i.e. the change in the oxidation state of the Au particles.

Due to time limitations, the number of temperature steps were reduced for $\lambda = 2$, 3 and 1.5. Consequently, comparison between ramps up and down is only possible at a temperature of 40°C for those cases. Despite, the above discussed pattern followed by the temperature dependency of conversion/yield at $\lambda = 1$ is persistently observed at the rest of λ -values studied in this work (see Figures 5.41-5.46). Apart from the reduction on the temperatures being monitored, the rest of experimental

conditions were kept exactly the same. Nonetheless, it is worth to signalize Figure 5.43, which shows how the steady state was not reached after 4 hours at 60°C. This led to experiment repetition keeping each temperature constant for 3 instead of 2 hours (Figure 5.44).

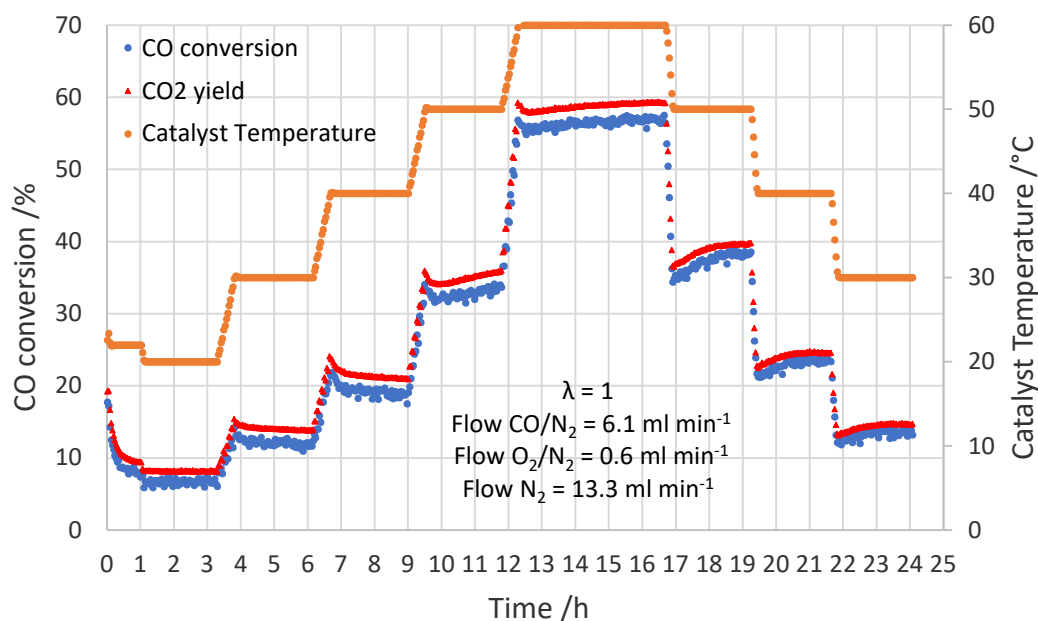


Figure 5.39. CO conversion, yield to CO₂ and temperature of catalytic bed versus time when flowing 6.1 ml min⁻¹ of 2% CO/N₂, 0.6 ml min⁻¹ of 10% O₂/N₂ and 13.3 ml min⁻¹ of pure N₂ over a fresh catalytic bed consisting of 3 mg of 5% Au/CeO₂ diluted in 24 mg of CeO₂ (corresponding to $\lambda = 1$, $R_{dil} = 1/9$ and $W/F = 0.081$ g s ml⁻¹).

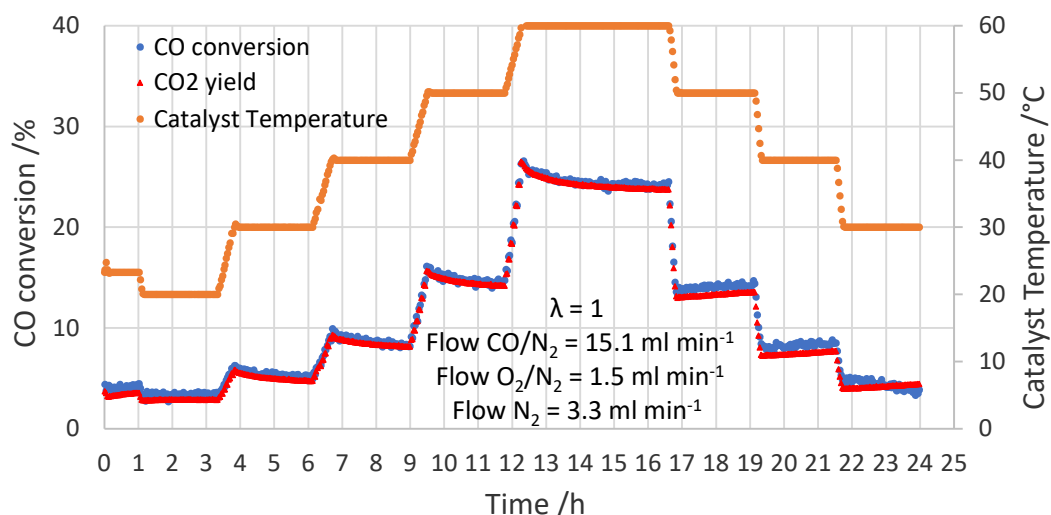


Figure 5.40. CO conversion, yield to CO₂ and temperature of catalytic bed versus time when flowing 15.1 ml min⁻¹ of 2% CO/N₂, 1.5 ml min⁻¹ of 10% O₂/N₂ and 3.3 ml min⁻¹ of pure N₂ over an used catalytic bed consisting of 3 mg of 5% Au/CeO₂ diluted in 24 mg of CeO₂ (corresponding to $\lambda = 1$, $R_{\text{dil}} = 1/9$ and $W/F = 0.081 \text{ g s ml}^{-1}$). The experiment over the already used sample was carried out after 6 hours of flowing 10 ml min⁻¹ of 10% O₂/N₂.

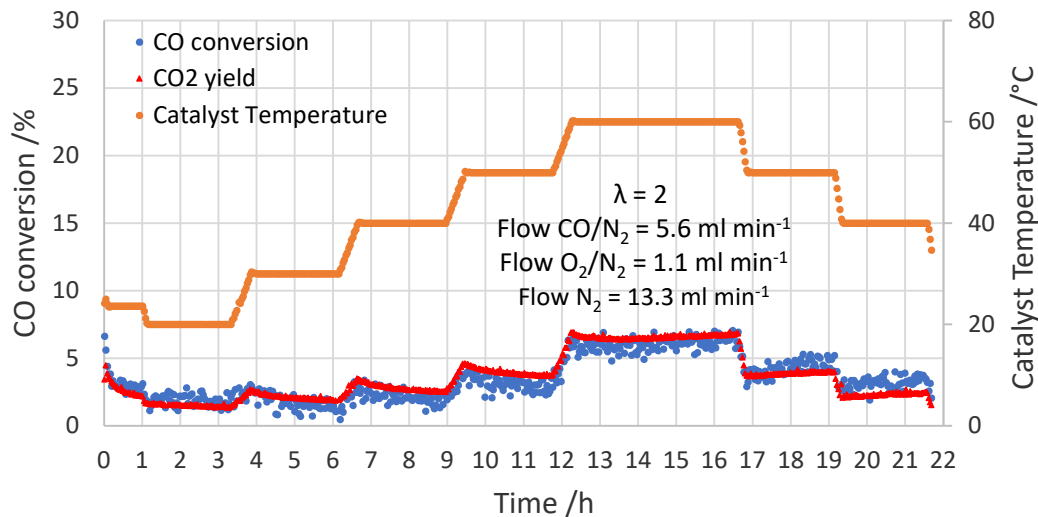


Figure 5.41. CO conversion, yield to CO₂ and temperature of catalytic bed versus time when flowing 5.6 ml min⁻¹ of 2% CO/N₂, 1.1 ml min⁻¹ of 10% O₂/N₂ and 13.3 ml min⁻¹ of pure N₂ over a fresh catalytic bed consisting of 3 mg of 5% Au/CeO₂ diluted in 24 mg of CeO₂ (corresponding to $\lambda = 2$, $R_{\text{dil}} = 1/9$ and $W/F = 0.081 \text{ g s ml}^{-1}$). In order to maintain homogeneity in the tested temperatures from this experiment on, the test was intentionally stopped at the end of the 40°C stage.

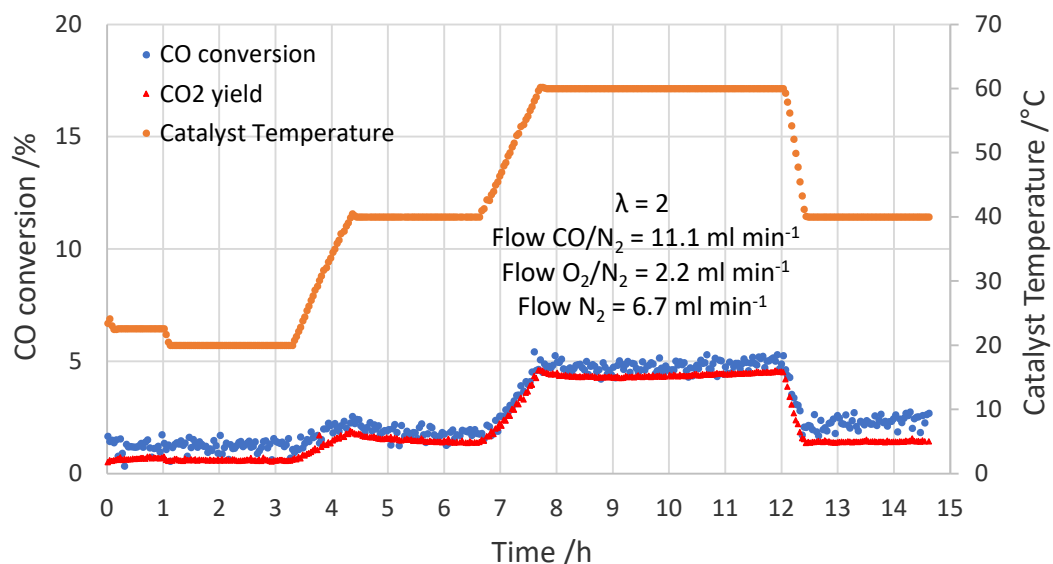


Figure 5.42. CO conversion, yield to CO₂ and temperature of catalytic bed versus time when flowing 11.1 ml min⁻¹ of 2% CO/N₂, 2.2 ml min⁻¹ of 10% O₂/N₂ and 6.7 ml min⁻¹ of pure N₂ over an used catalytic bed consisting of 3 mg of 5% Au/CeO₂ diluted in 24 mg of CeO₂ (corresponding to $\lambda = 2$, $R_{\text{dil}} = 1/9$ and $W/F = 0.081 \text{ g s ml}^{-1}$). The experiment over the already used sample was carried out after 6 hours of flowing 10 ml min⁻¹ of 10% O₂/N₂.

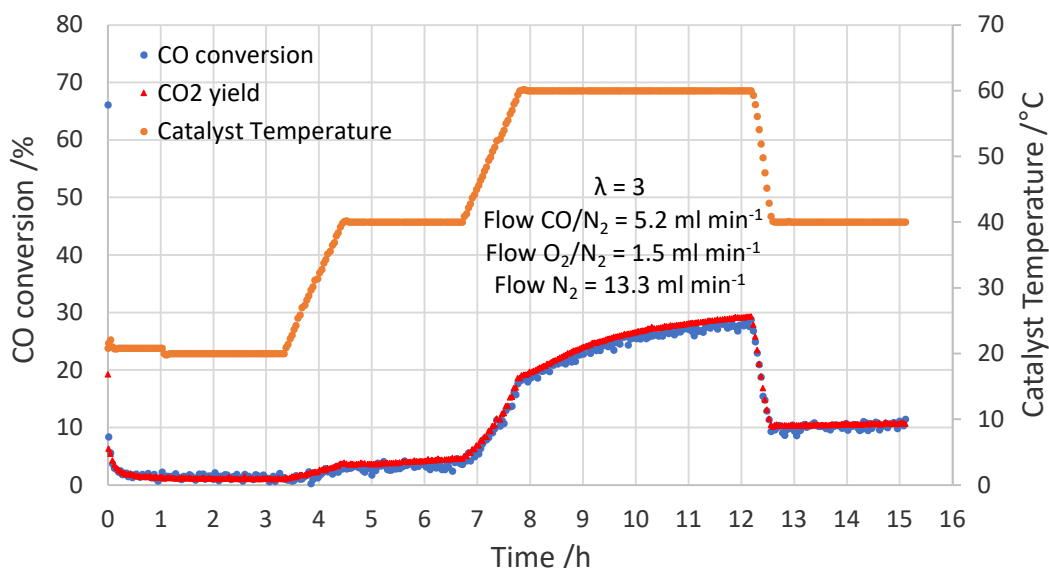


Figure 5.43. CO conversion, yield to CO₂ and temperature of catalytic bed versus time when flowing 5.2 ml min⁻¹ of 2% CO/N₂, 1.5 ml min⁻¹ of 10% O₂/N₂ and 13.3 ml min⁻¹ of pure N₂ over a fresh catalytic bed consisting of 3 mg of 5% Au/CeO₂ diluted in 24 mg of CeO₂ (corresponding to $\lambda = 3$, $R_{\text{dil}} = 1/9$ and $W/F = 0.081 \text{ g s ml}^{-1}$). Steady state is not reached after 4 hours at 60°C.

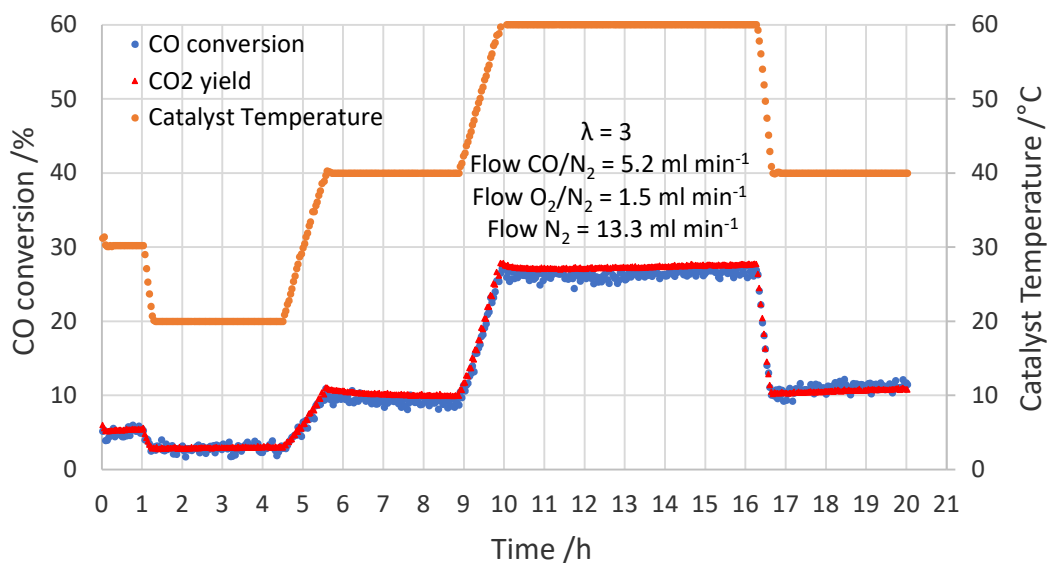


Figure 5.44. CO conversion, yield to CO₂ and temperature of catalytic bed versus time when flowing 5.2 ml min⁻¹ of 2% CO/N₂, 1.5 ml min⁻¹ of 10% O₂/N₂ and 13.3 ml min⁻¹ of pure N₂ over an used catalytic bed consisting of 3 mg of 5% Au/CeO₂ diluted in 24 mg of CeO₂ (corresponding to $\lambda = 3$, $R_{\text{dil}} = 1/9$ and $W/F = 0.081 \text{ g s ml}^{-1}$). The experiment over the already used sample was carried out after 6 hours of flowing 10 ml min⁻¹ of 10% O₂/N₂. Each temperature was kept constant for 3 h instead of the usual value of 2 h.

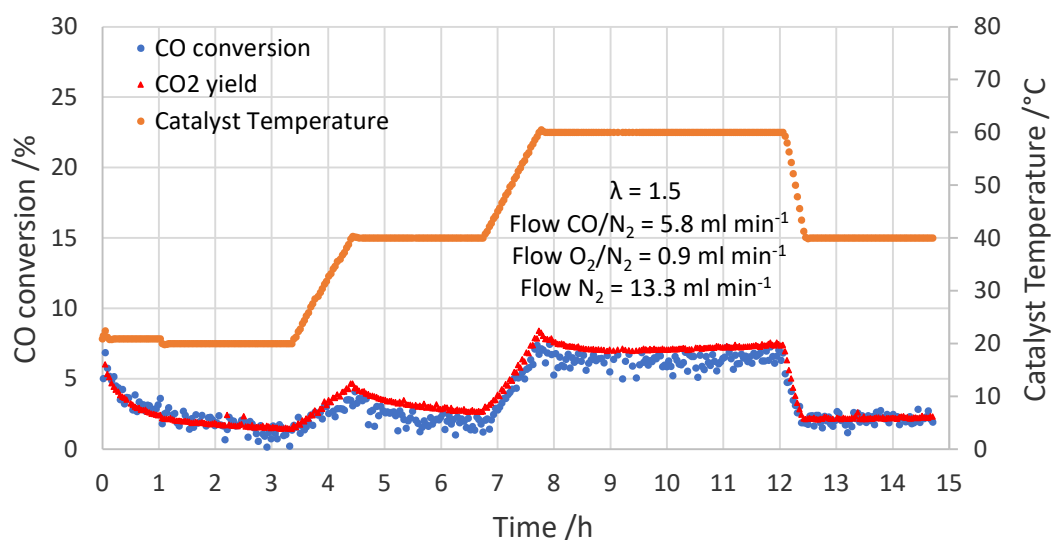


Figure 5.45. CO conversion, yield to CO₂ and temperature of catalytic bed versus time when flowing 5.8 ml min⁻¹ of 2% CO/N₂, 0.9 ml min⁻¹ of 10% O₂/N₂ and 13.3 ml min⁻¹ of pure N₂ over a fresh catalytic bed consisting of 3 mg of 5% Au/CeO₂ diluted in 24 mg of CeO₂ (corresponding to $\lambda = 1.5$, $R_{dil} = 1/9$ and $W/F = 0.081$ g s ml⁻¹).

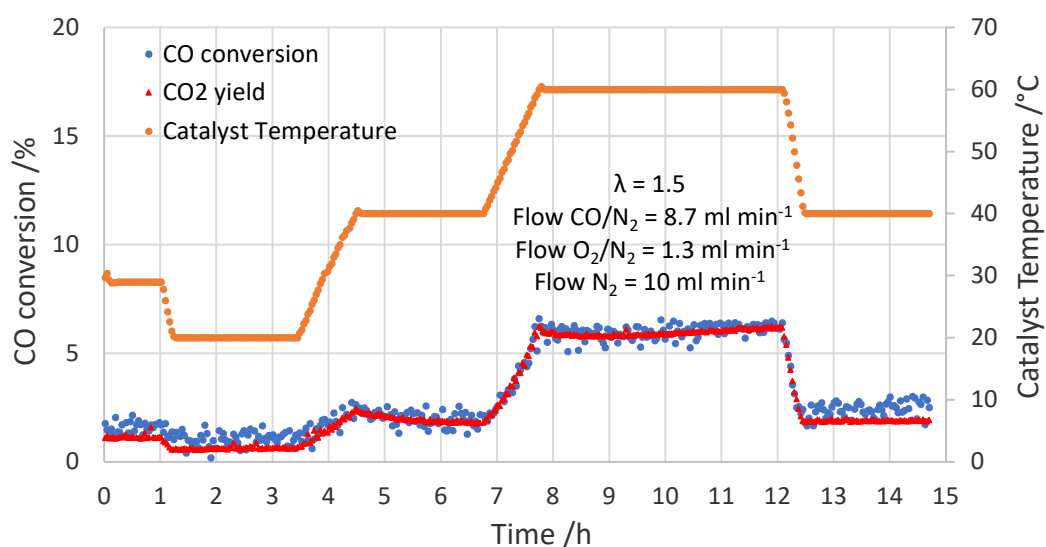


Figure 5.46. CO conversion, yield to CO₂ and temperature of catalytic bed versus time when flowing 8.7 ml min⁻¹ of 2% CO/N₂, 1.3 ml min⁻¹ of 10% O₂/N₂ and 10 ml min⁻¹ of pure N₂ over an used catalytic bed consisting of 3 mg of 5% Au/CeO₂ diluted in 24 mg of CeO₂ (corresponding to $\lambda = 1.5$, $R_{dil} = 1/9$ and $W/F = 0.081$ g s ml⁻¹). The experiment over the already used sample was carried out after 6 hours of flowing 10 ml min⁻¹ of 10% O₂/N₂.

From the above discussed experimental procedure, CO conversion results obtained for each individual λ -value have been separately collected for both tested temperatures, 40°C and 60°C, during both ramps up and down. For each individual case, the value resulting from the average of the last ten CO conversion points has been then plotted against its respective CO partial pressure as shown in Figures 5.47-5.50 presented down below.

As it can be appreciated in Figure 5.47, quite similar conversion dependence on CO partial pressure is shown at lambda 1.5 and lambda 2 with a clear direct relationship, i.e. the higher the p_{CO} the higher the conversion. In contrast, a very pronounced inverse dependence is observed at lambda 1, with the conversion steeply decreasing with higher CO concentrations in the reactor gaseous feed. A negative slope is also obtained when plotting conversion versus p_{CO} at lambda 3. In this case, the scatter in the data is noticeably higher, thus the greater error carried by those values should be taken into consideration.

Figure 5.48 shows the same data presented in Figure 5.47 with the difference that, in this case, the data corresponds to the temperature ramp down stage, i.e. when temperature is decreased from the previous tested temperature instead of increased. Results from both ramp up and down stages at 40°C agree with each other in all cases with exception of $\lambda = 2$. In this case, as shown in Figure 5.48, the highly scattered data resulted in a really poor linear regression, which makes such data not suitable for comparison purposes.

The indirect CO partial pressure dependence of the conversion obtained at 40°C for $\lambda = 1$ and 3 is reproduced at 60°C (Figures 5.49 and 5.50), although a drastically steeper slope is observed in this latter case. Looking at the same figures, CO conversions at lambda 1.5 consistently follows the same trend observed at 40°C (Figures 5.47 and 5.48), although its dependence on the CO concentration is highly attenuated. Finally, at $\lambda = 2$, once again the scatter in data make it unfeasible to make any conclusion in relation to the CO concentration tendency towards the CO partial pressure.

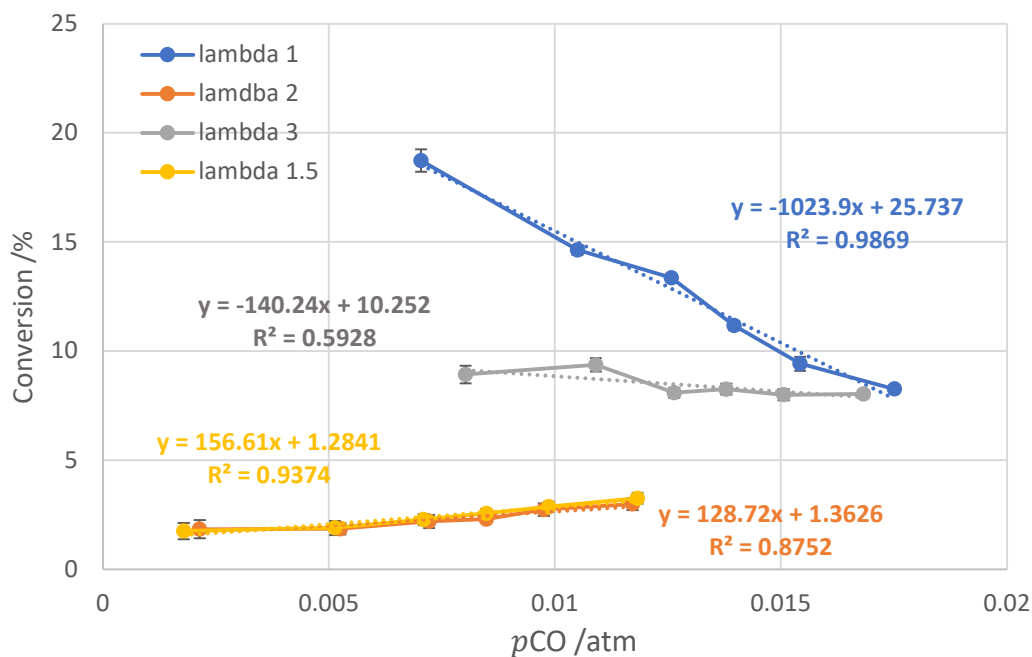


Figure 5.47. CO concentration dependence of conversion at $\lambda = 1, 1.5, 2$ and 3 and at 40°C during the temperature ramp up stage when using Au/CeO_2 . R_{dil} was $1/9$, total mass flow rate of 20 ml min^{-1} . Catalyst mass weight 27 mg .

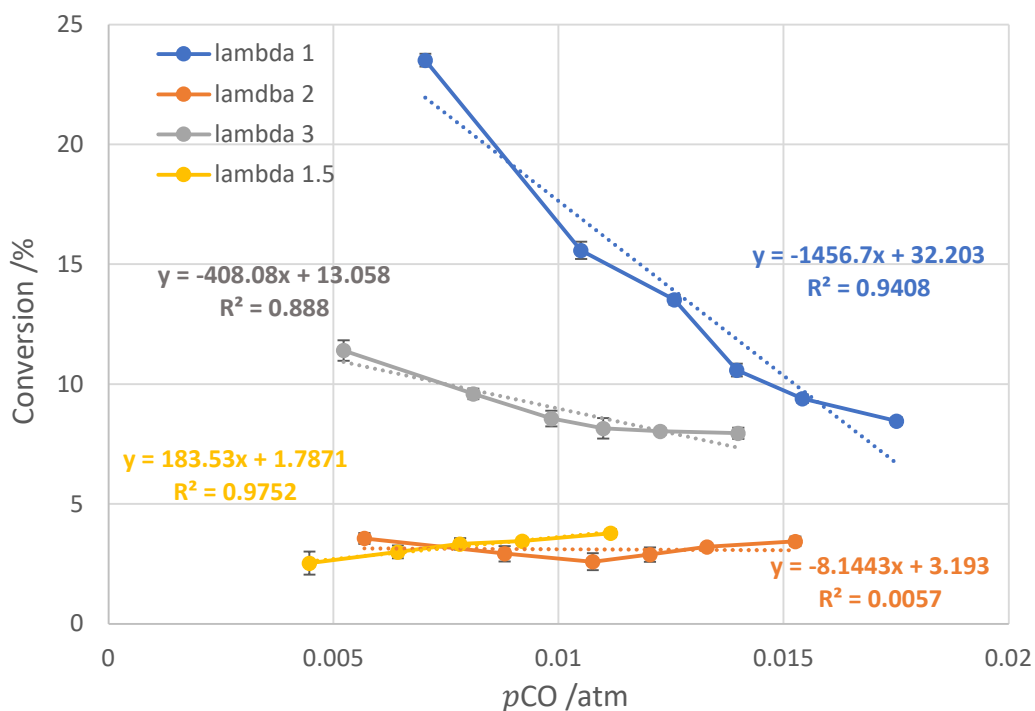


Figure 5.48. CO concentration dependence of conversion at $\lambda = 1, 1.5, 2$ and 3 and at 40°C during the temperature ramp down stage when using Au/CeO_2 . R_{dil} was $1/9$, total mass flow rate of 20 ml min^{-1} . Catalyst mass weight 27 mg .

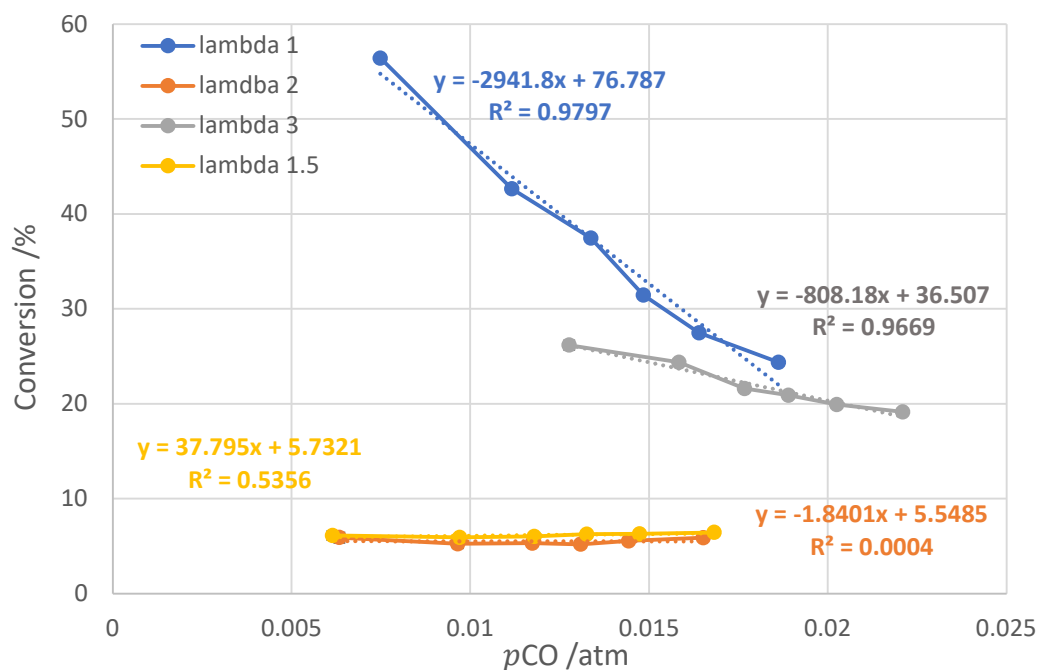


Figure 5.49. CO concentration dependence of conversion at $\lambda = 1, 1.5, 2$ and 3 and at 60°C during the temperature ramp up stage when using Au/CeO₂. Rdil was 1/9, total mass flow rate of 20 ml min⁻¹. Catalyst mass weight 27 mg.

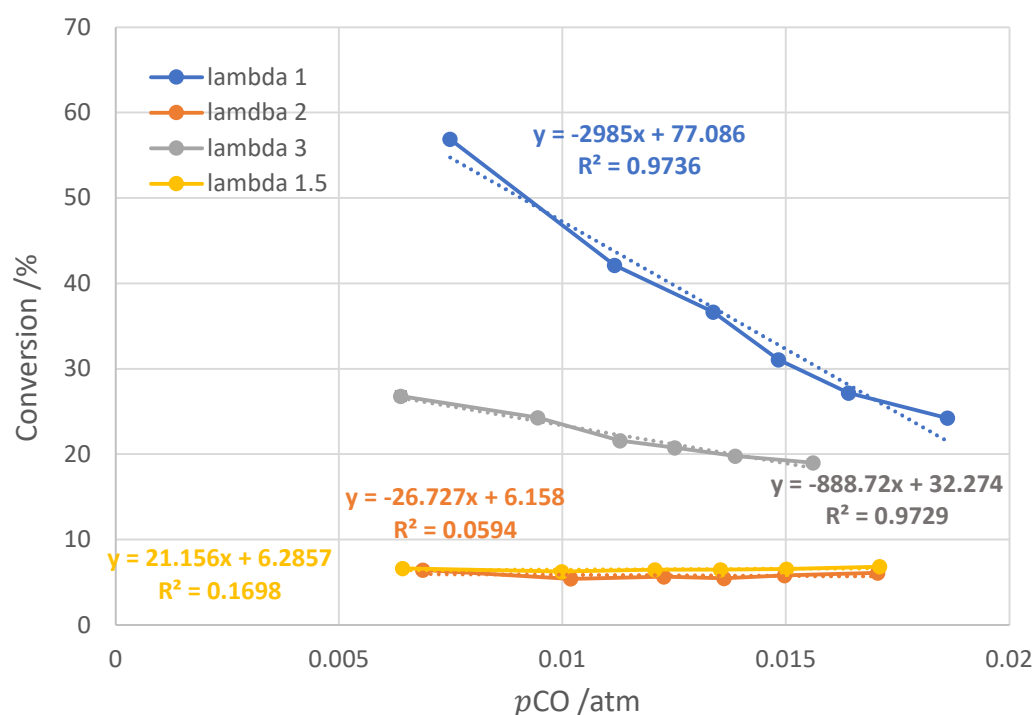


Figure 5.50. CO concentration dependence of conversion at $\lambda = 1, 1.5, 2$ and 3 and at 60°C during the temperature ramp down stage when using Au/CeO₂. Rdil was 1/9, total mass flow rate of 20 ml min⁻¹. Catalyst mass weight 27 mg.

Once the CO conversion dependence on the CO partial pressure has been reviewed, it is time to clear up an essential concept which could be misunderstood. This is related to the fact that an indirect relationship between the percentage of CO conversion and the CO concentration in the feed line does not mean an indirect relationship between the total amount of CO oxidized and such CO concentration. For example, going back to Figure 5.50, it was observed that at $\lambda = 3$, the percentage of CO converted decreased with increasing the CO partial pressure. Even so, it can be safely stated that the total amount of CO oxidized experiences an increase instead. If we focus on two particular data points, at a p_{CO} of 0.0064 atm, a CO conversion of 26.8% was obtained while, at 0.0156 atm, the conversion was around 19%. Nonetheless, the total CO oxidized at 0.0064 atm was, indeed, lower than that at 0.0156 atm. Specifically, the total CO oxidized was 1.7 times higher at the higher CO partial pressure than that obtained at the lowest, i.e. $[(0.0156 \text{ atm} \times 19\%) / (0.0064 \text{ atm} \times 26.8\%)]$. This is why, to objectively study the influence that the CO partial pressure has on the amount of CO being converted, the concept of absolute reaction rate ($r_{CO_{mass}}$) gains importance. As described in Section 3.2.2.1, the $r_{CO_{mass}}$ for data presented in Figures 5.47-5.50 was calculated and the results are plotted in Figures 5.51-5.58 below.

Raw data is presented in Figures 5.51, 5.53, 5.55 and 5.57, which correspond to 40°C and 60°C during both temperature ramp up and down stages, respectively. In all cases, results obtained for the case of $\lambda=1$ not only greatly differ from those at the rest of λ -values but, also, their response to the changes in p_{CO} does not seem to follow any rational trend. A possible reason for this could be related to the very low oxygen flows (F_{O_2}) used when α_{CO}^λ at $\lambda=1$ was investigated. According to the experimental procedure followed (detailed at the beginning of Section 5.3), in order to keep a constant λ -value while still changing p_{CO} and maintaining the inlet flow at a constant value of 20 ml min⁻¹, a third flow was introduced. This consisted of a 100 % N₂ gaseous flow. Six different N₂ flows were introduced during each series of tests, i.e. for the study at each λ -value, those being 13.3, 10, 8, 6.7, 5.3 and 3.3 ml min⁻¹. However, this implied that when a ratio between reactants corresponding to $\lambda=1$ was maintained, F_{O_2} was very small throughout the entire series (see Table 5.6).

According to data presented in Table 5.6, higher oxygen flows were allowed when λ was increased, i.e. $\lambda = 1.5, 2$ and 3 . Therefore, it is thought that the very low oxygen flows (F_{O_2}) at $\lambda=1$ could imply a slow diffusion of the reactant from the bulk to the catalyst surface, which would involve the presence of mass transfer limitations. Thus, if relevant mass transfer effects are playing an important role in this case ($\lambda=1$), that would explain the different profile observed when comparing with the results at the rest of λ -values ($\lambda = 1.5, 2$ and 3).

Table 5.6. N_2 , CO and O_2 flows (F_{N_2} , F_{CO} , F_{O_2} , respectively) used during the study of α_{CO}^λ at different λ -values.

	$\lambda = 1$		$\lambda = 1.5$		$\lambda = 2$		$\lambda = 3$	
F_{N_2}	F_{CO}	F_{O_2}	F_{CO}	F_{O_2}	F_{CO}	F_{O_2}	F_{CO}	F_{O_2}
13.3	6.1	0.6	5.8	0.9	5.6	1.1	5.2	1.5
10	9.1	0.9	8.7	1.3	8.3	1.7	7.7	2.3
8	10.9	1.1	10.4	1.6	10	2	9.2	2.8
6.7	12.1	1.2	11.6	1.7	11.1	2.2	10.2	3.1
5.3	13.3	1.3	12.8	1.9	12.2	2.5	11.3	3.4
3.3	15.1	1.5	14.5	2.2	13.9	2.8	12.8	3.9

According to that above discussed, data obtained at $\lambda=1$ was excluded from the present study on the α_{CO}^λ . This is also the reason why $\lambda=1.5$ was tested at the latest stage of the study. Since $\lambda=1$ data was excluded, a new λ -value needed to be tested in order to confirm those results obtained at the other two λ -values ($\lambda = 2$ and 3).

A double-logarithmic plot of the $r_{CO_{mass}}$ versus p_{CO} data previously shown (Figures 5.51, 5.53, 5.55 and 5.57) is presented in Figures 5.52, 5.54, 5.56 and 5.58. As it can be seen in the $r_{CO_{mass}}$ versus CO partial pressure plots, the regression lines are not defined by a $y = mx$ equation type, but rather by $y = mx+n$. In other words, their intercept does not happen at $y = 0$, as they should. These non-zero values of the $r_{CO_{mass}}$ at $p_{CO} = 0$ (when no CO is entering the reactor) are due to residual errors (n) occurring when real experiments are carried out. Nonetheless, they should be subtracted before continuing treating such data. Therefore, the correction on the y-axis was carried out by performing such subtraction, i.e. $y_{corrected} = y-n$. Then, logarithms have been applied. The linear regression obtained is quite good in all

cases (see Figures 5.52, 5.54, 5.56 and 5.58) and the value of the pursued α_{CO}^λ could be extracted from the slopes of those lines. A practical summary of the slopes values obtained for each λ -value at each temperature is presented in Table 5.7. From those results, averaging all slopes obtained at 40°C (ramp up and down), a value of $\alpha_{CO}^\lambda = 0.86$ with standard deviation of 0.24 is obtained. Doing the same for the case of 60°C, $\alpha_{CO}^\lambda = 0.97$ with standard deviation of 0.22 is given. The values are similar and, taking into account the errors associated to them, they could be considered essentially the same. Therefore, it is concluded that the increase in temperature from 40°C to 60°C does not affect the order of reaction with respect of CO at constant lambda.

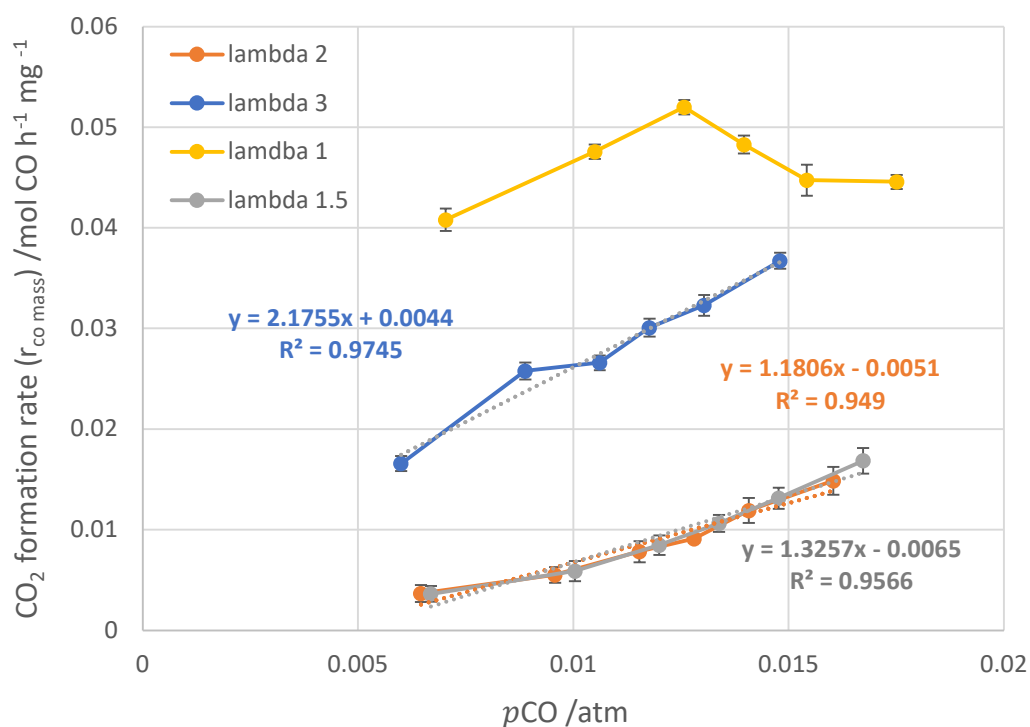


Figure 5.51. $r_{CO_{mass}}$ versus CO partial pressure at constant λ ($\lambda = 1, 1.5, 2$ and 3) and at 40°C during the temperature ramp up stage when using Au/CeO₂. Rdil was 1/9, total mass flow rate of 20 ml min⁻¹. Catalyst mass weight 27 mg.

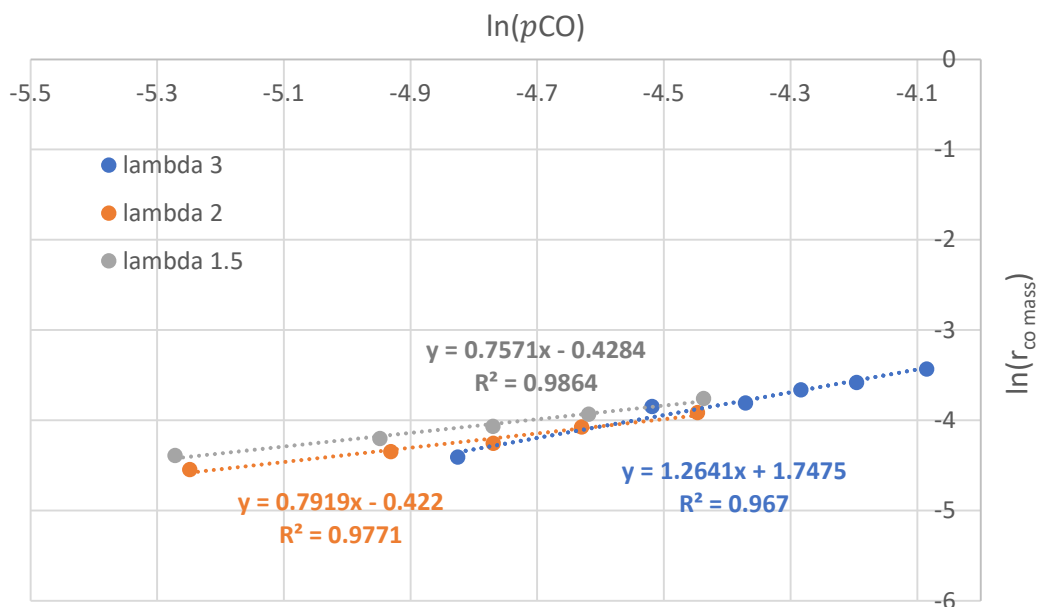


Figure 5.52. Double-logarithmic plot of $r_{CO_{mass}}$ versus CO partial pressure based on the data shown in Figure 5.51 after its correction with respect to the y-axis ($r_{CO_{mass}}$).

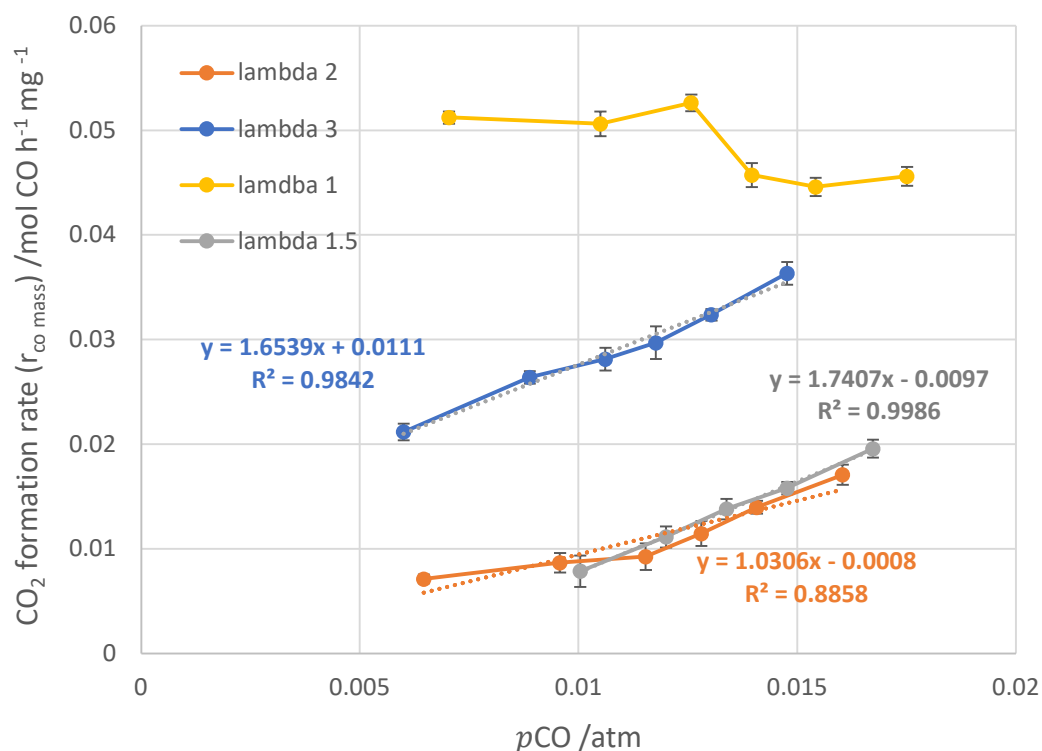


Figure 5.53. $r_{CO_{mass}}$ versus CO partial pressure at constant λ ($\lambda = 1, 1.5, 2$ and 3) and at 40°C during the temperature ramp down stage when using Au/CeO₂. Rdil was $1/9$, total mass flow rate of 20 ml min^{-1} . Catalyst mass weight 27 mg .

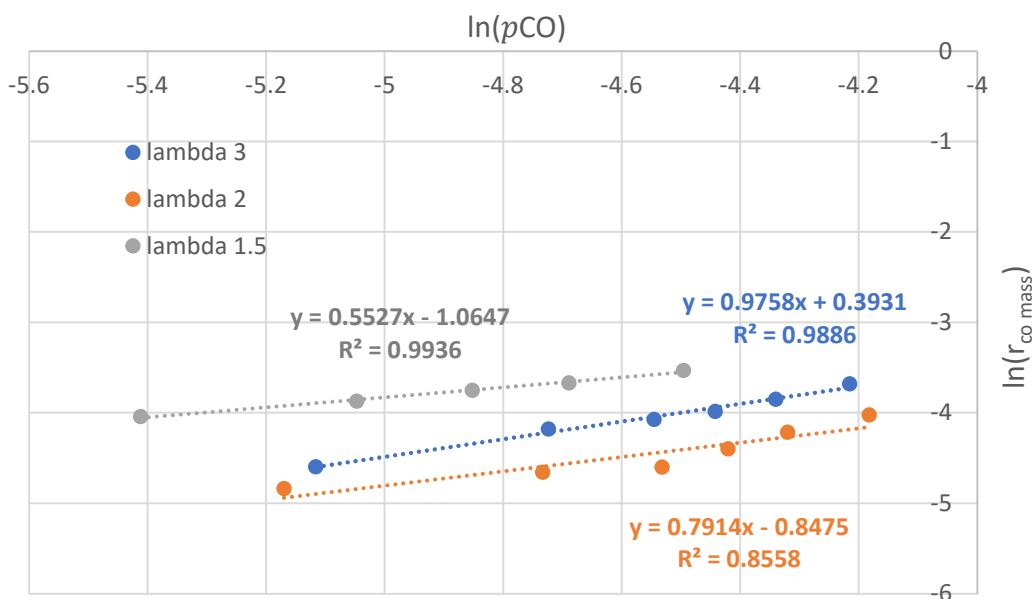


Figure 5.54. Double-logarithmic plot of $r_{CO_{mass}}$ versus CO partial pressure based on the data shown in Figure 5.53 after its correction with respect to the y-axis ($r_{CO_{mass}}$).

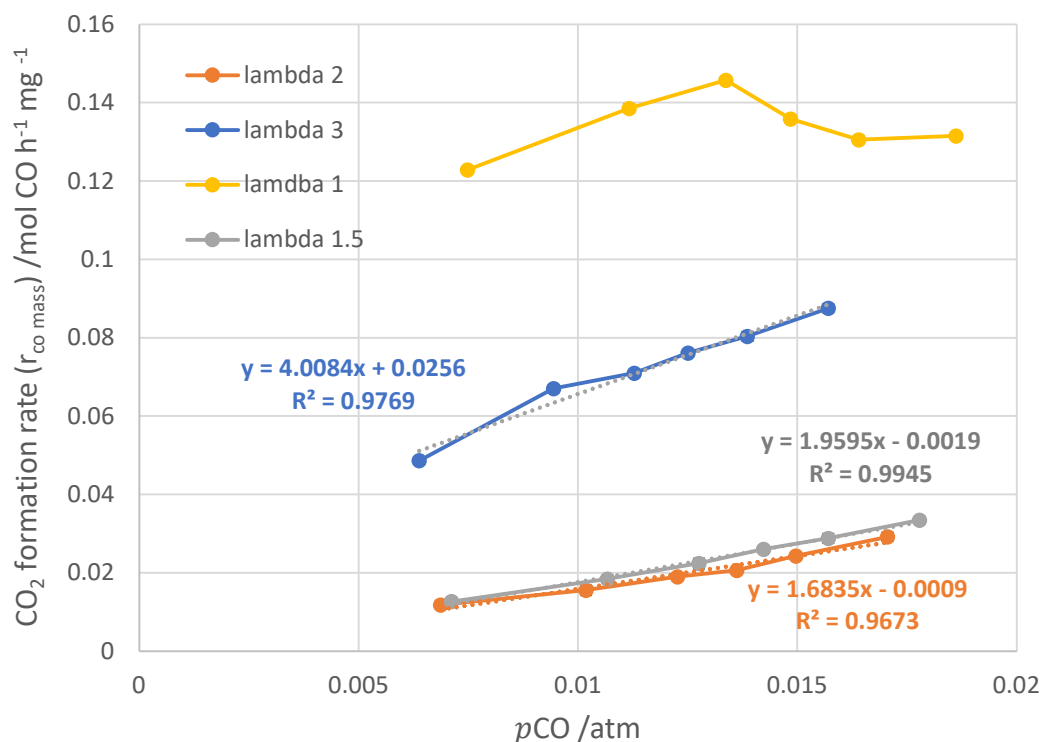


Figure 5.55. $r_{CO_{mass}}$ versus CO partial pressure at constant λ ($\lambda = 1, 1.5, 2$ and 3) and at 60°C during the temperature ramp up stage when using Au/CeO₂. R_{dil} was 1/9, total mass flow rate of 20 ml min⁻¹. Catalyst mass weight 27 mg.

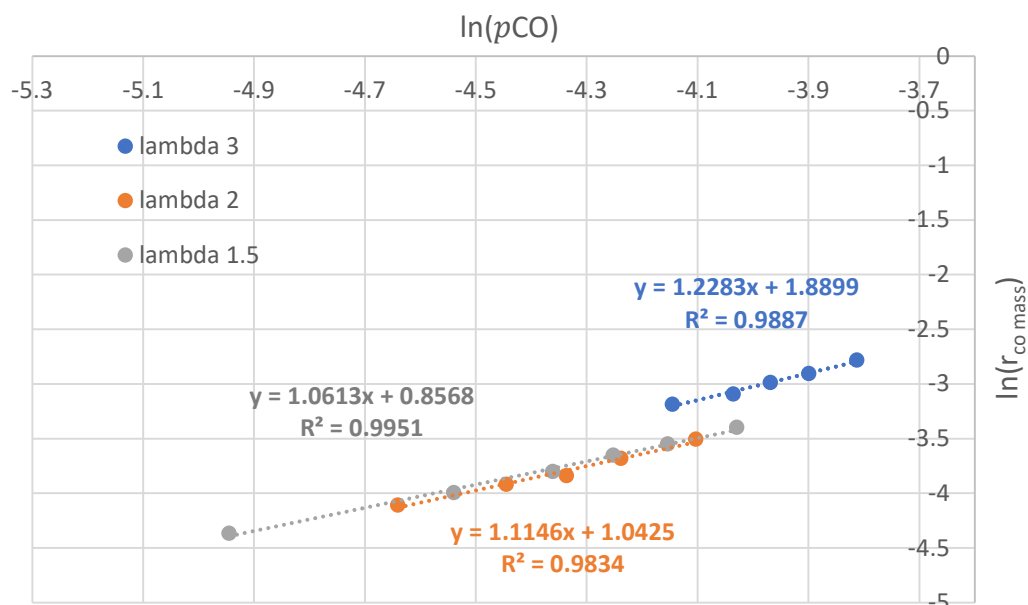


Figure 5.56. Double-logarithmic plot of $r_{CO_{mass}}$ versus CO partial pressure based on the data shown in Figure 5.55 after its correction with respect to the y-axis ($r_{CO_{mass}}$).

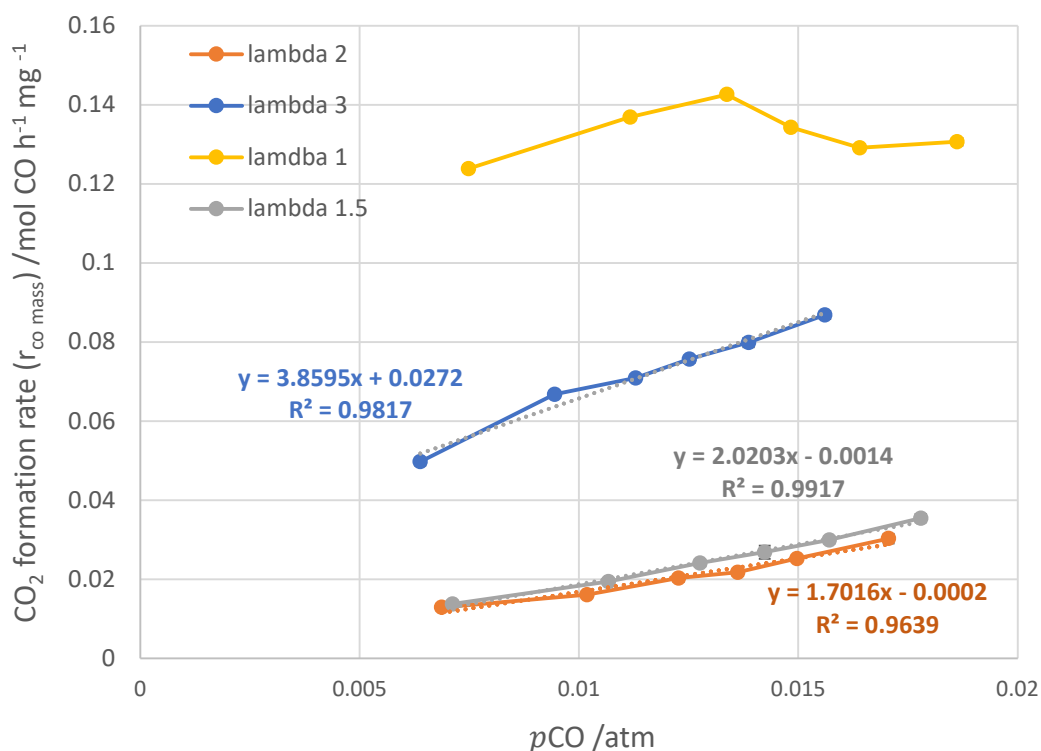


Figure 5.57. $r_{CO_{mass}}$ versus CO partial pressure at constant λ ($\lambda = 1, 1.5, 2$ and 3) and at 60°C during the temperature ramp down stage when using Au/CeO₂. Rdil was 1/9, total mass flow rate of 20 ml min^{-1} . Catalyst mass weight 27 mg.

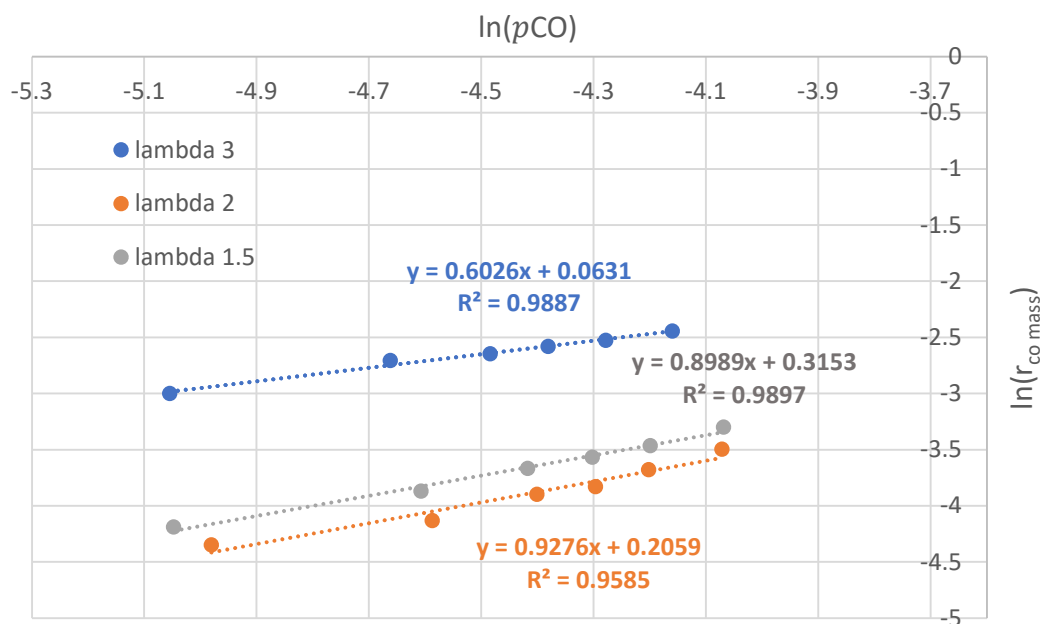


Figure 5.58. Double-logarithmic plot of $r_{CO_{mass}}$ versus CO partial pressure based on the data shown in Figure 5.57 after its correction with respect to the y-axis ($r_{CO_{mass}}$).

Table 5.7. Slopes obtained from the linear regression showed in Figures 5.52 (1st column), 5.54 (2nd column), 5.56 (3rd column) and 5.58 (4nd column).

	40°C		60°C	
	Ramp up	Ramp down	Ramp up	Ramp down
$\lambda = 1.5$	0.7571	0.5527	1.0613	0.8989
$\lambda = 2$	0.7919	0.7914	1.1146	0.9276
$\lambda = 3$	1.2641	0.9758	1.2283	0.6026

At the beginning of this Section 5.3, the method followed and experimental conditions applied were discussed in detail and it was already pointed out that both Au/CeO₂ and AuPd/CeO₂ catalysts were tested using the same procedure. Accordingly, CO conversion, yield to CO₂ and temperature of catalytic bed versus time for the cases of $\lambda = 1$ (Figures 5.59-5.60), $\lambda = 2$ (Figures 5.61-5.62), $\lambda = 3$ (Figures 5.63-5.64) and $\lambda = 1.5$ (Figures 5.65-5.66) are shown below. Exactly same features than those previously pointed out for the Au/CeO₂ case are also

reproduced in the metal supported gold-palladium catalyst. Nonetheless, it is worth to mention one specific case. As it was described at the start of this section, to ensure the constant total inlet flow at 20 ml min^{-1} and a constant λ during each series of experiments, pure nitrogen was included to the gaseous mix entering the reactor. In particular, six different N_2 flows were introduced during each series of tests, i.e. for the study at each λ -value, those being 13.3, 10, 8, 6.7, 5.3 and 3.3 ml min^{-1} . However, for the case of $\lambda = 1.5$, when using the AuPd/CeO₂ catalyst, the 3.3 ml min^{-1} N_2 test is left out. Last experiment carried out corresponds to the results showed in Figure 5.66, where 12.8 ml min^{-1} of 2% CO/ N_2 , 1.9 ml min^{-1} of 10% O₂/ N_2 and 5.3 ml min^{-1} of pure N_2 were flowed over the catalytic bed. Looking at that figure, it can be appreciated that, at around 7 hours from the start of the experiment, the CO conversion initiates an almost linear drop until, around one and a half hour later, it reaches a zero value and continues that way until the end of the test. As it can be read in the caption of such a figure, the gradual decrease in the CO conversion corresponds to the gradual decrease in the amount of CO entering the reactor. The gas cylinder containing the 2% CO/ N_2 mix getting empty during the course of the experiment is the cause for the CO flow entering the reactor being shut down. Nevertheless, despite this could be found as an unfortunate event, it actually lights up the mechanism by which CO₂ is produced. Since the yield continues responding to the increase in temperature even after all gaseous CO has been consumed, this certainly serves as a proof which confirms that surface absorbed rather than gaseous CO is involved in such mechanism toward the production of CO₂.

Similar to that done in Figures 5.47-5.50 for the case of Au/CeO₂, Figures 5.67-5.70 presents the CO conversion dependence on the CO concentration (p_{CO}) for each individual λ -value. Again, disparate results with direct and indirect dependences along with some apparent random relationships can be observed. Nonetheless, these results do not allow conclusive analysis since they do not reflect the total amount of CO being oxidized. As such, $r_{\text{CO}_{\text{mass}}}$ instead of conversions should be used. Figures 5.71-5.78 present the $r_{\text{CO}_{\text{mass}}}$ dependence on p_{CO} based on the data showed in Figures 5.67-5.70.

In the same way as in Table 5.7, in Table 5.8 the slopes obtained from the linear regressions showed in Figures 5.72, 5.74, 5.76, 5.78 are summarized. From those results, averaging all slopes obtained at 40°C (ramp up and down), a value of $\alpha_{CO}^\lambda = 1.13$ with standard deviation of 0.34 is obtained. Doing the same for the case of 60°C, $\alpha_{CO}^\lambda = 1.04$ with standard deviation of 0.17 is given. Bearing in mind the errors both values carry out, they could be considered essentially the same. Consequently, the same way as it happened in the case of Au/CeO₂, the increase of temperature from 40°C to 60°C does not seem to affect the order of reaction with respect to CO at constant lambda.

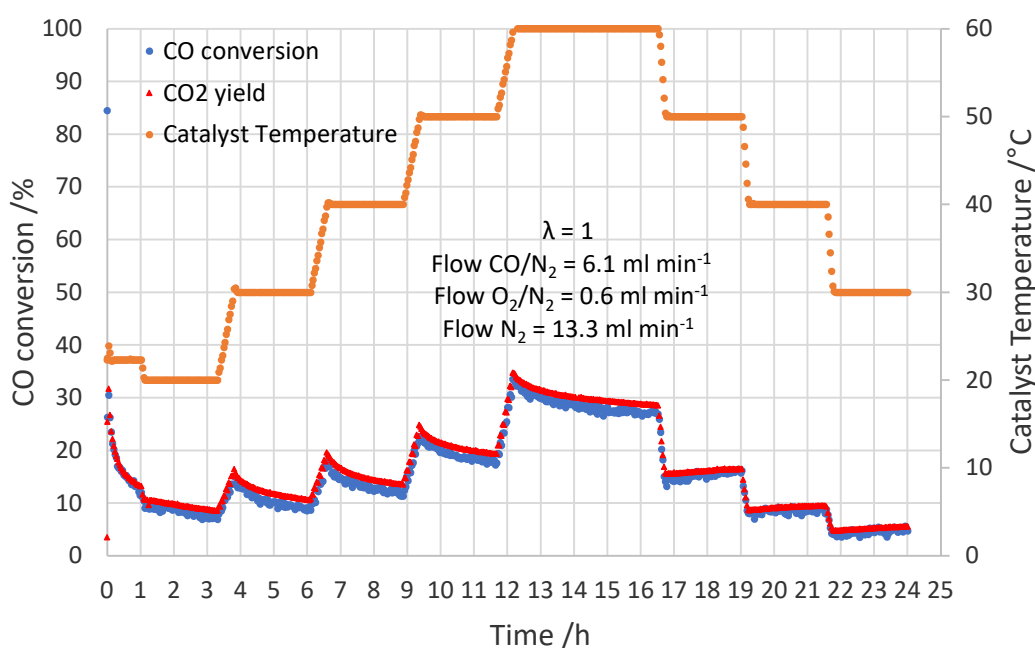


Figure 5.59. CO conversion, yield to CO₂ and temperature of catalytic bed versus time when flowing 6.1 ml min⁻¹ of 2% CO/N₂, 0.6 ml min⁻¹ of 10% O₂/N₂ and 13.3 ml min⁻¹ of pure N₂ over a fresh catalytic bed consisting of 3 mg of 5% AuPd/CeO₂ diluted in 24 mg of CeO₂ (corresponding to $\lambda = 1$, $R_{dil} = 1/9$ and $W/F = 0.081$ g s ml⁻¹).

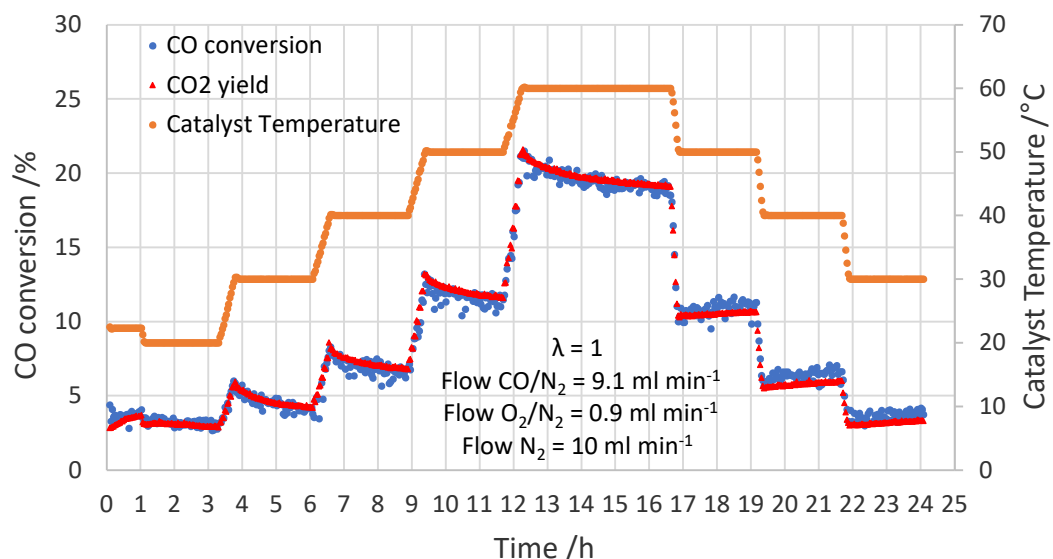


Figure 5.60. CO conversion, yield to CO₂ and temperature of catalytic bed versus time when flowing 9.1 ml min⁻¹ of 2% CO/N₂, 0.9 ml min⁻¹ of 10% O₂/N₂ and 10 ml min⁻¹ of pure N₂ over an used catalytic bed consisting of 3 mg of 5% AuPd/CeO₂ diluted in 24 mg of CeO₂ (corresponding to $\lambda = 1$, $R_{\text{dil}} = 1/9$ and $W/F = 0.081 \text{ g s ml}^{-1}$). The experiment over the already used sample was carried out after 6 hours of flowing 10 ml min⁻¹ of 10% O₂/N₂.

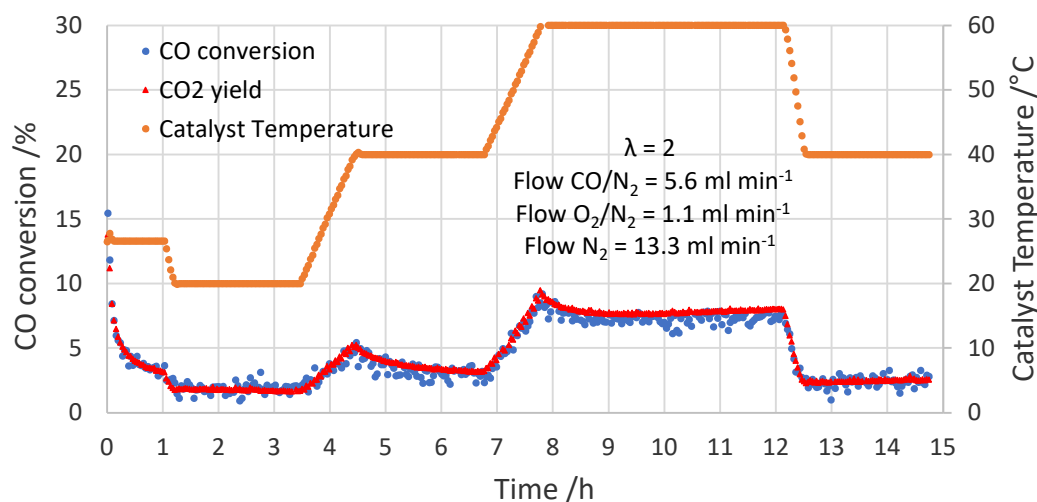


Figure 5.61. CO conversion, yield to CO₂ and temperature of catalytic bed versus time when flowing 5.6 ml min⁻¹ of 2% CO/N₂, 1.1 ml min⁻¹ of 10% O₂/N₂ and 13.3 ml min⁻¹ of pure N₂ over a fresh catalytic bed consisting of 3 mg of 5% AuPd/CeO₂ diluted in 24 mg of CeO₂ (corresponding to $\lambda = 2$, $R_{\text{dil}} = 1/9$ and $W/F = 0.081 \text{ g s ml}^{-1}$). In order to maintain homogeneity in the tested temperatures from this experiment on, the test was intentionally stopped at the end of the 40°C stage.

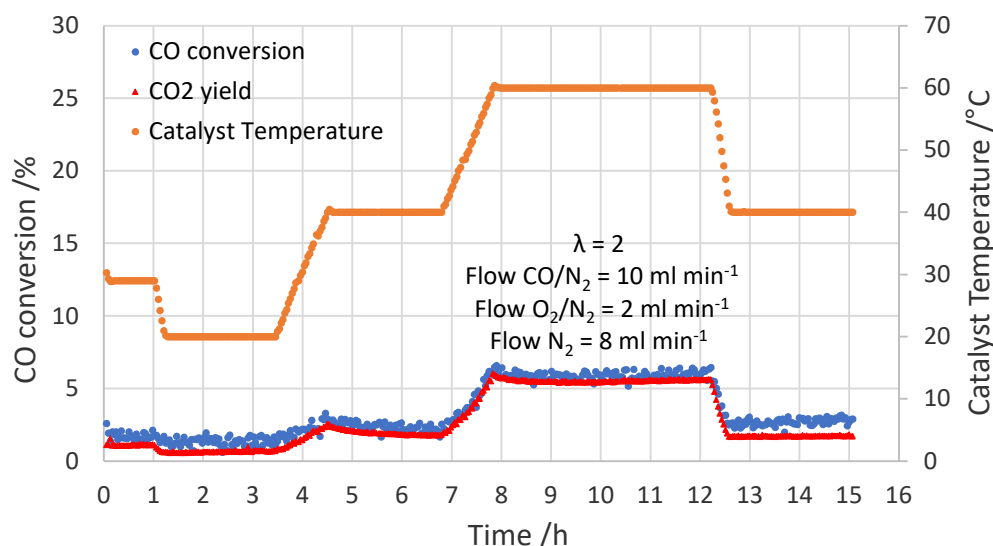


Figure 5.62. CO conversion, yield to CO₂ and temperature of catalytic bed versus time when flowing 10 ml min⁻¹ of 2% CO/N₂, 2 ml min⁻¹ of 10% O₂/N₂ and 8 ml min⁻¹ of pure N₂ over an used catalytic bed consisting of 3 mg of 5% AuPd/CeO₂ diluted in 24 mg of CeO₂ (corresponding to $\lambda = 2$, $R_{\text{dil}} = 1/9$ and $W/F = 0.081 \text{ g s ml}^{-1}$). The experiment over the already used sample was carried out after 6 hours of flowing 10 ml min⁻¹ of 10% O₂/N₂.

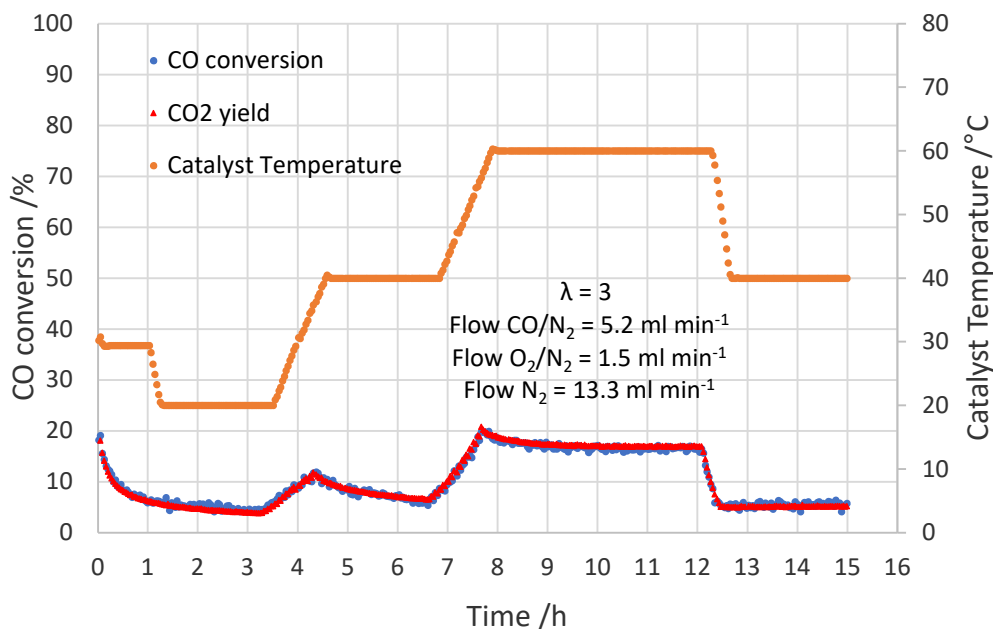


Figure 5.63. CO conversion, yield to CO₂ and temperature of catalytic bed versus time when flowing 5.2 ml min⁻¹ of 2% CO/N₂, 1.5 ml min⁻¹ of 10% O₂/N₂ and 13.3 ml min⁻¹ of pure N₂ over a fresh catalytic bed consisting of 3 mg of 5% AuPd/CeO₂ diluted in 24 mg of CeO₂ (corresponding to $\lambda = 3$, $R_{\text{dil}} = 1/9$ and $W/F = 0.081 \text{ g s ml}^{-1}$).

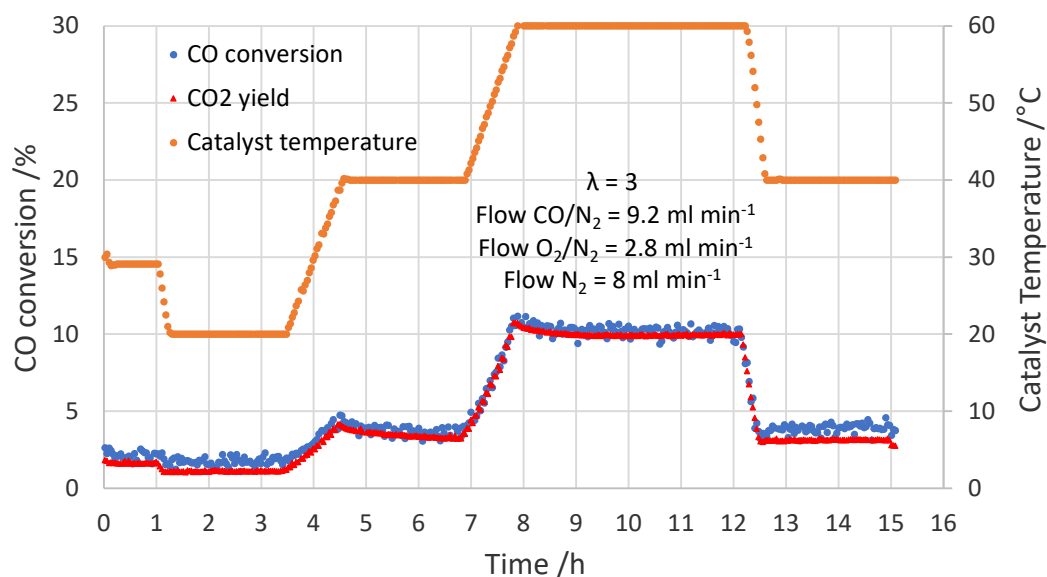


Figure 5.64. CO conversion, yield to CO₂ and temperature of catalytic bed versus time when flowing 9.2 ml min⁻¹ of 2% CO/N₂, 2.8 ml min⁻¹ of 10 % O₂/N₂ and 8 ml min⁻¹ of pure N₂ over an used catalytic bed consisting of 3 mg of 5% AuPd/CeO₂ diluted in 24 mg of CeO₂ (corresponding to $\lambda = 3$, $R_{\text{dil}} = 1/9$ and $W/F = 0.081 \text{ g s ml}^{-1}$). The experiment over the already used sample was carried out after 6 hours of flowing 10 ml min⁻¹ of 10 % O₂/N₂.

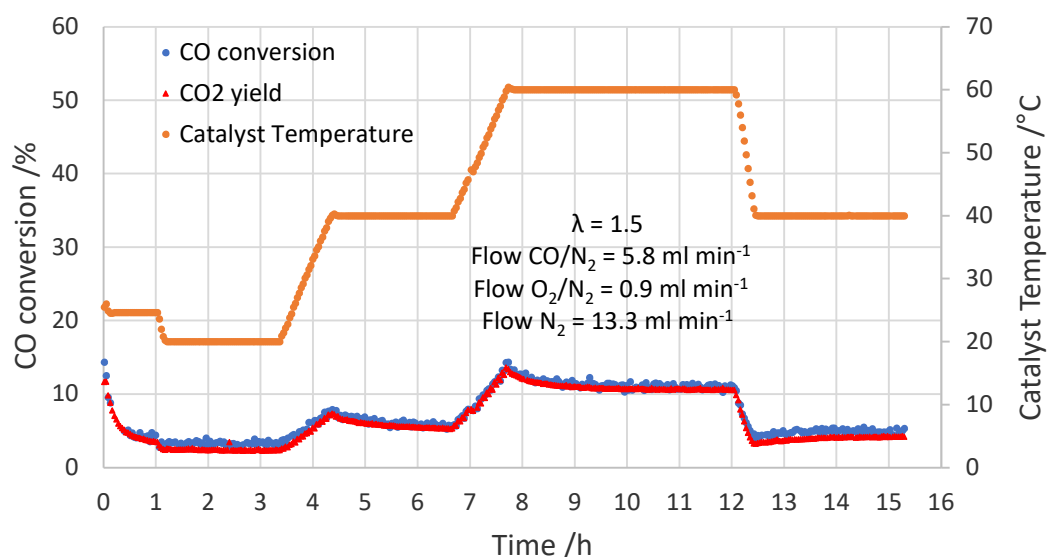


Figure 5.65. CO conversion, yield to CO₂ and temperature of catalytic bed versus time when flowing 5.8 ml min⁻¹ of 2% CO/N₂, 0.9 ml min⁻¹ of 10% O₂/N₂ and 13.3 ml min⁻¹ of pure N₂ over a fresh catalytic bed consisting of 3 mg of 5% AuPd/CeO₂ diluted in 24 mg of CeO₂ (corresponding to $\lambda = 1.5$, $R_{\text{dil}} = 1/9$ and $W/F = 0.081 \text{ g s ml}^{-1}$).

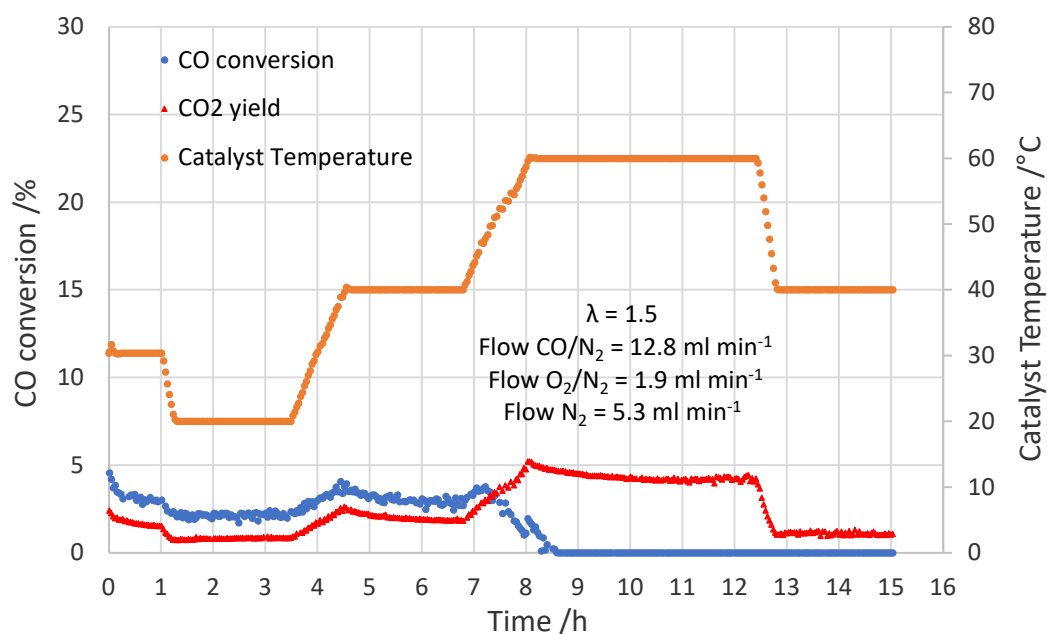


Figure 5.66. CO conversion, yield to CO₂ and temperature of catalytic bed versus time when flowing 12.8 ml min⁻¹ of 2% CO/N₂, 1.9 ml min⁻¹ of 10% O₂/N₂ and 5.3 ml min⁻¹ of pure N₂ over an used catalytic bed consisting of 3 mg of 5% AuPd/CeO₂ diluted in 24 mg of CeO₂ (corresponding to $\lambda = 1.5$, $R_{dil} = 1/9$ and $W/F = 0.081$ g s ml⁻¹). The experiment over the already used sample was carried out after 6 hours of flowing 10 ml min⁻¹ of 10% O₂/N₂. The gradual decrease the CO conversion corresponds to the gradual decrease in amount of CO entering the reactor due to the gas cylinder containing the 2% CO/N₂ mix getting empty during the course of the experiment.

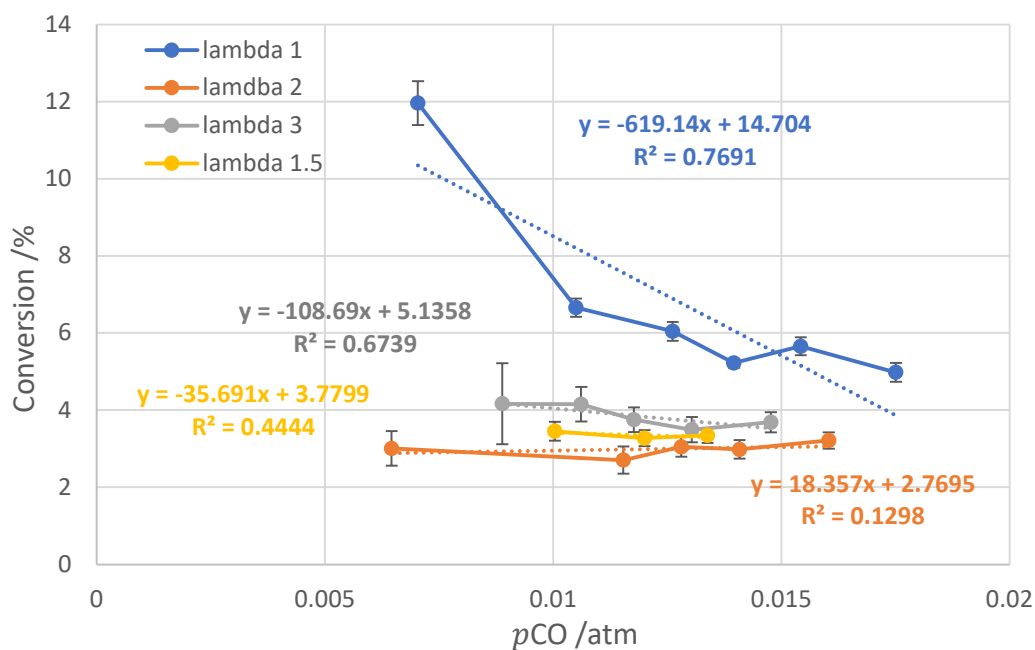


Figure 5.67. CO concentration dependence of conversion at $\lambda = 1, 1.5, 2$ and 3 and at 40°C during the temperature ramp up stage when using AuPd/CeO₂. Rdil was 1/9, total mass flow rate of 20 ml min^{-1} . Catalyst mass weight 27 mg.

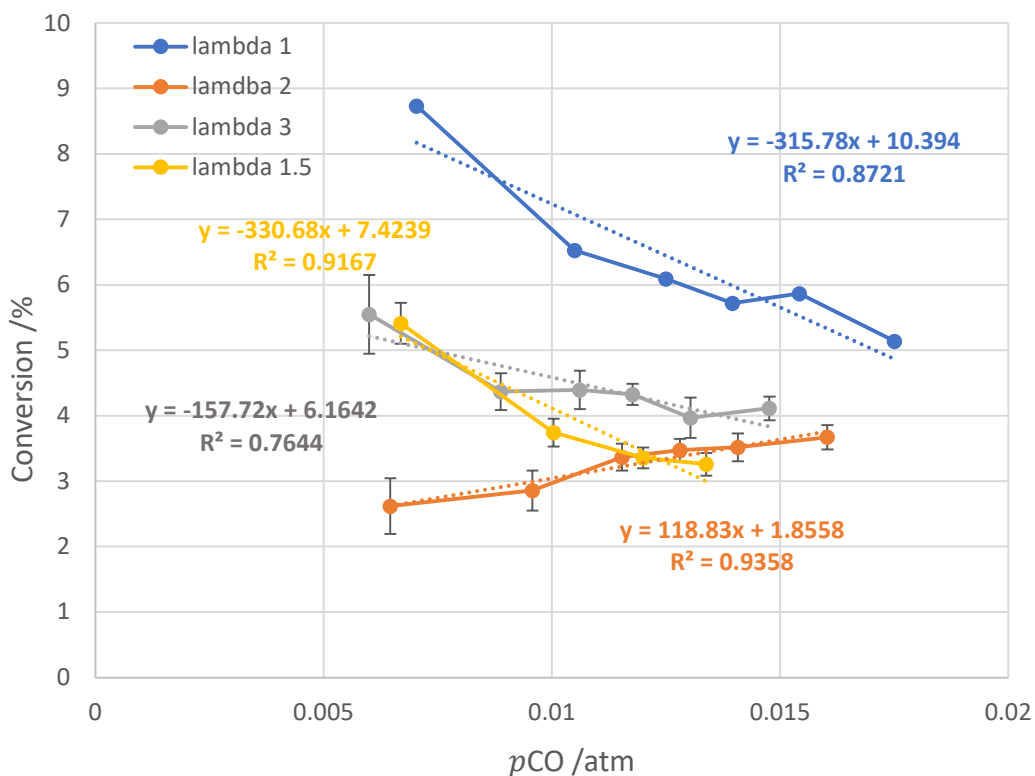


Figure 5.68. CO concentration dependence of conversion at $\lambda = 1, 1.5, 2$ and 3 and at 40°C during the temperature ramp down stage when using AuPd/CeO₂. Rdil was 1/9, total mass flow rate of 20 ml min^{-1} . Catalyst mass weight 27 mg.

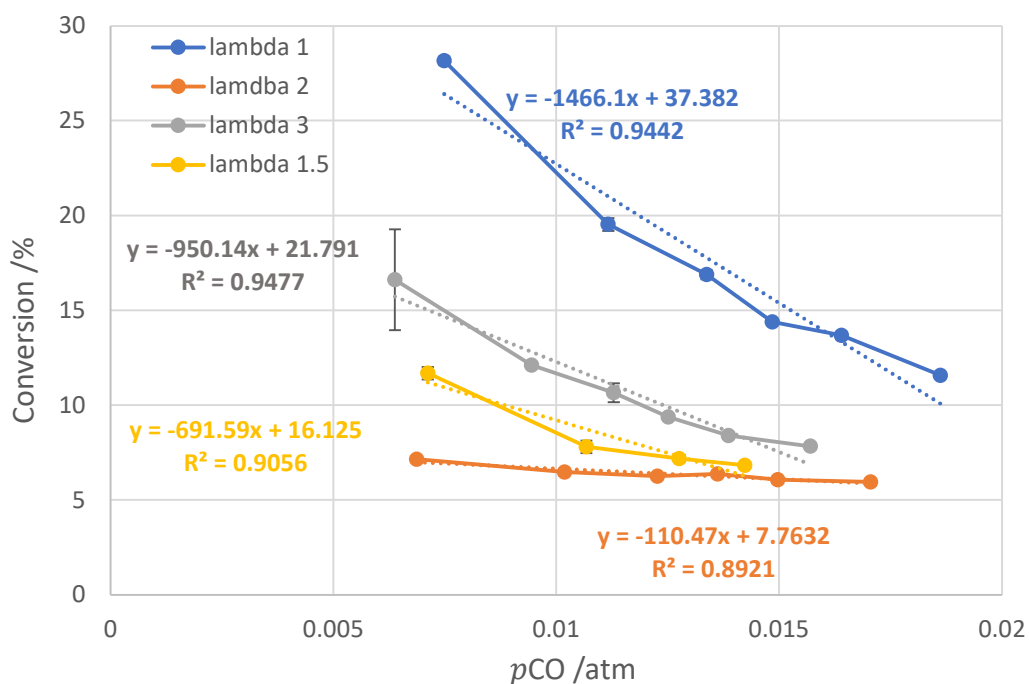


Figure 5.69. CO concentration dependence of conversion at $\lambda = 1, 1.5, 2$ and 3 and at 60°C during the temperature ramp up stage when using AuPd/CeO₂. Rdil was $1/9$, total mass flow rate of 20 ml min^{-1} . Catalyst mass weight 27 mg .

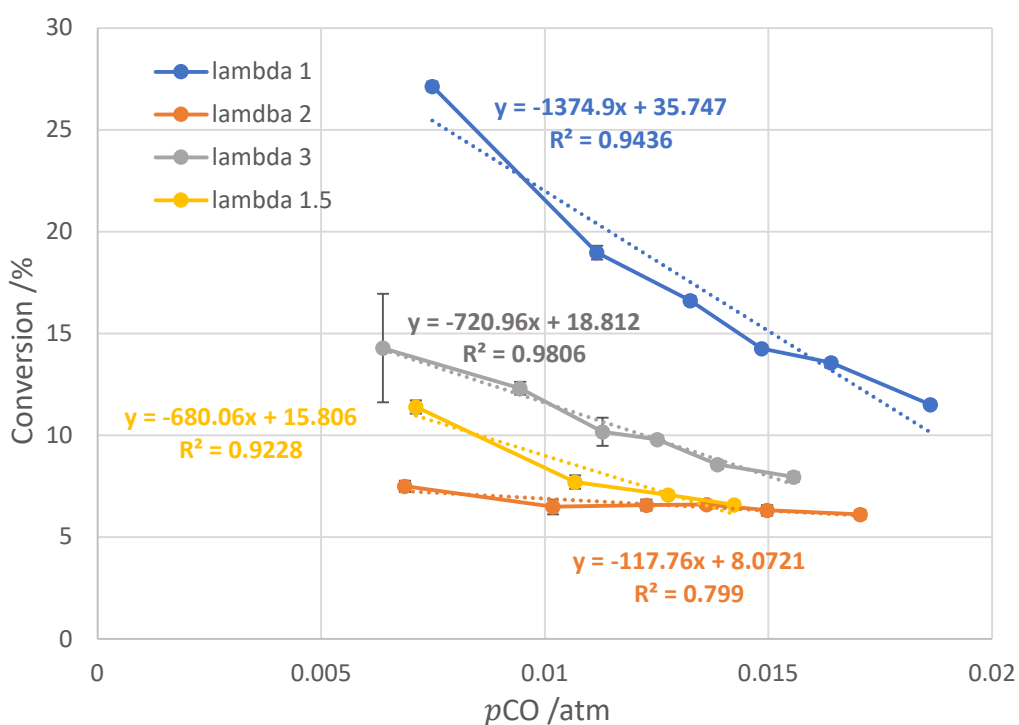


Figure 5.70. CO concentration dependence of conversion at $\lambda = 1, 1.5, 2$ and 3 and at 60°C during the temperature ramp down stage when using AuPd/CeO₂. Rdil was $1/9$, total mass flow rate of 20 ml min^{-1} . Catalyst mass weight 27 mg .

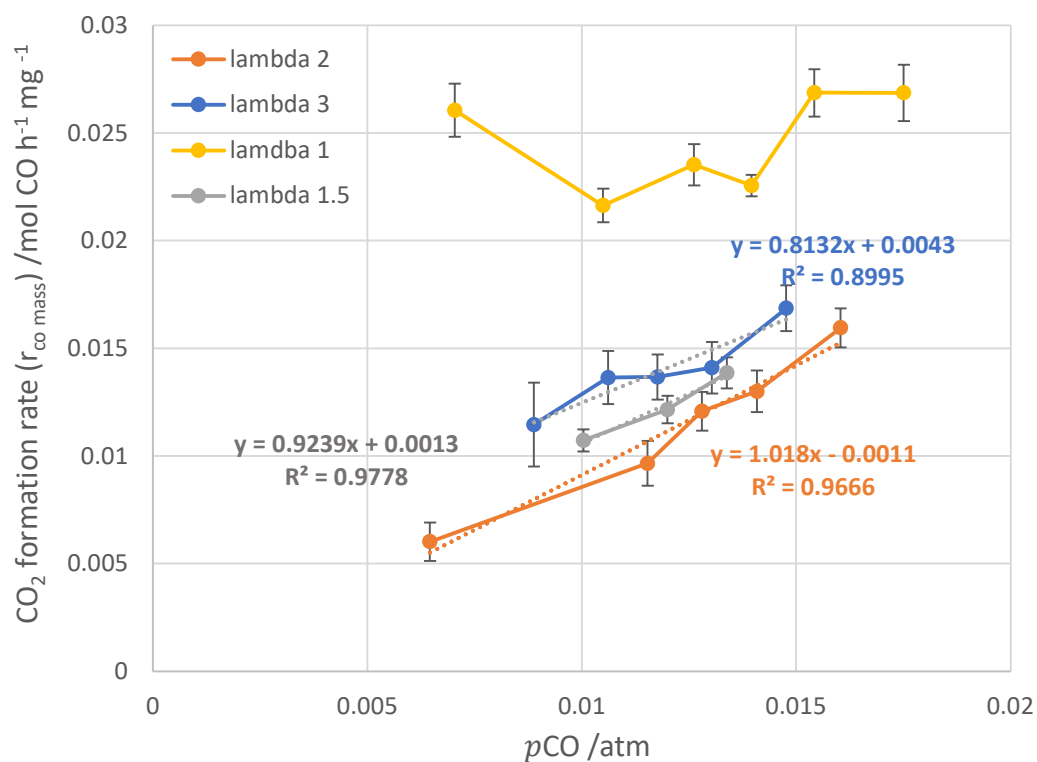


Figure 5.71. $r_{CO_{mass}}$ versus CO partial pressure at constant λ ($\lambda = 1, 1.5, 2$ and 3) and at 40°C during the temperature ramp up stage when using AuPd/CeO₂. Rdil was 1/9, total mass flow rate of 20 ml min⁻¹. Catalyst mass weight 27 mg.

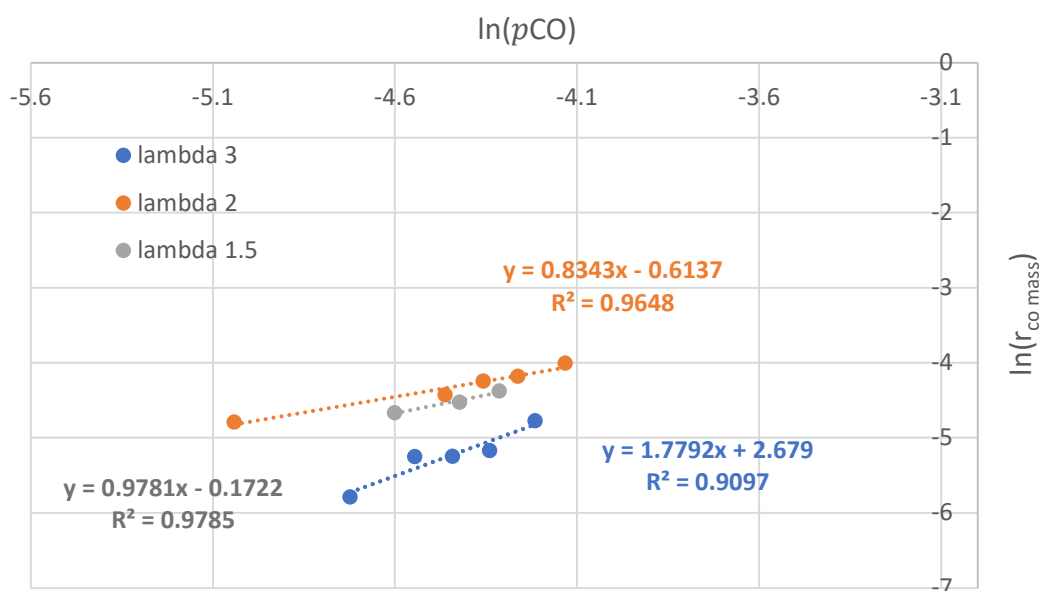


Figure 5.72. Double-logarithmic plot of $r_{CO_{mass}}$ versus CO partial pressure based on the data shown in Figure 5.71 after its correction with respect to the y-axis ($r_{CO_{mass}}$).

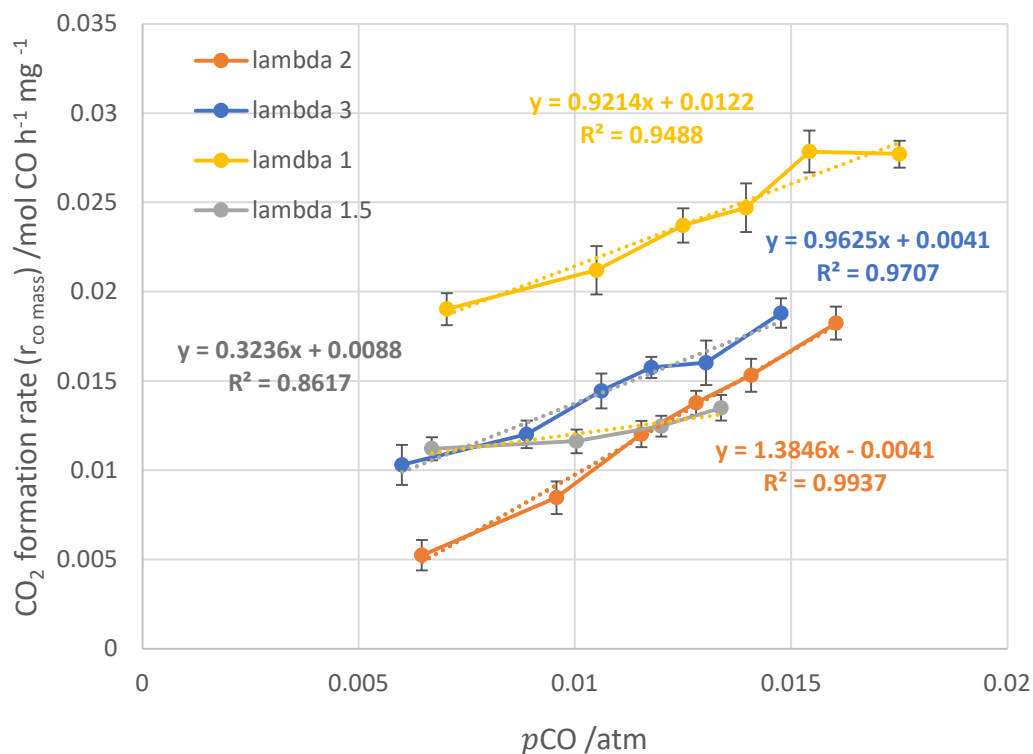


Figure 5.73. $r_{CO_{mass}}$ versus CO partial pressure at constant λ ($\lambda = 1, 1.5, 2$ and 3) and at 40°C during the temperature ramp down stage when using AuPd/CeO₂. R_{dil} was 1/9, total mass flow rate of 20 ml min⁻¹. Catalyst mass weight 27 mg.

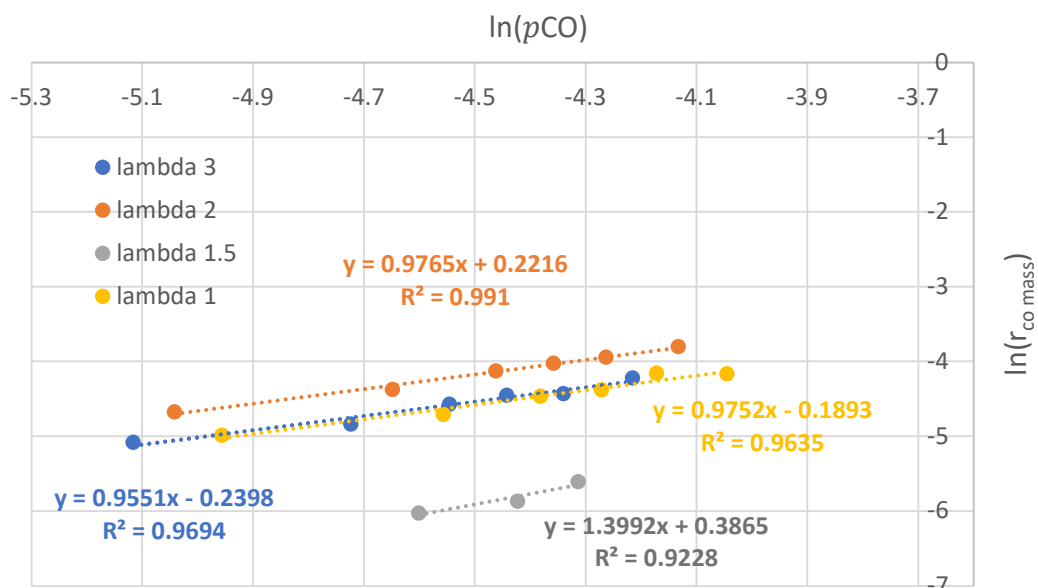


Figure 5.74. Double-logarithmic plot of $r_{CO_{mass}}$ versus CO partial pressure based on the data shown in Figure 5.73 after its correction with respect to the y-axis ($r_{CO_{mass}}$).

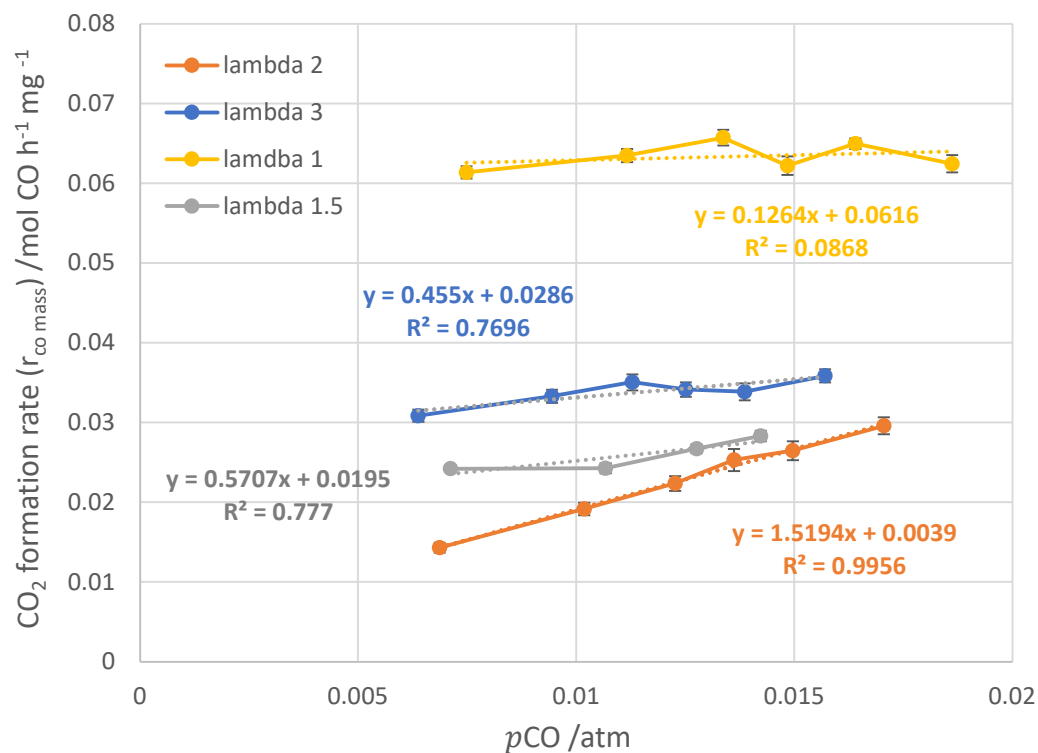


Figure 5.75. $r_{CO_{mass}}$ versus CO partial pressure at constant λ ($\lambda = 1, 1.5, 2$ and 3) and at 60°C during the temperature ramp up stage when using AuPd/CeO₂. Rdil was 1/9, total mass flow rate of 20 ml min^{-1} . Catalyst mass weight 27 mg.

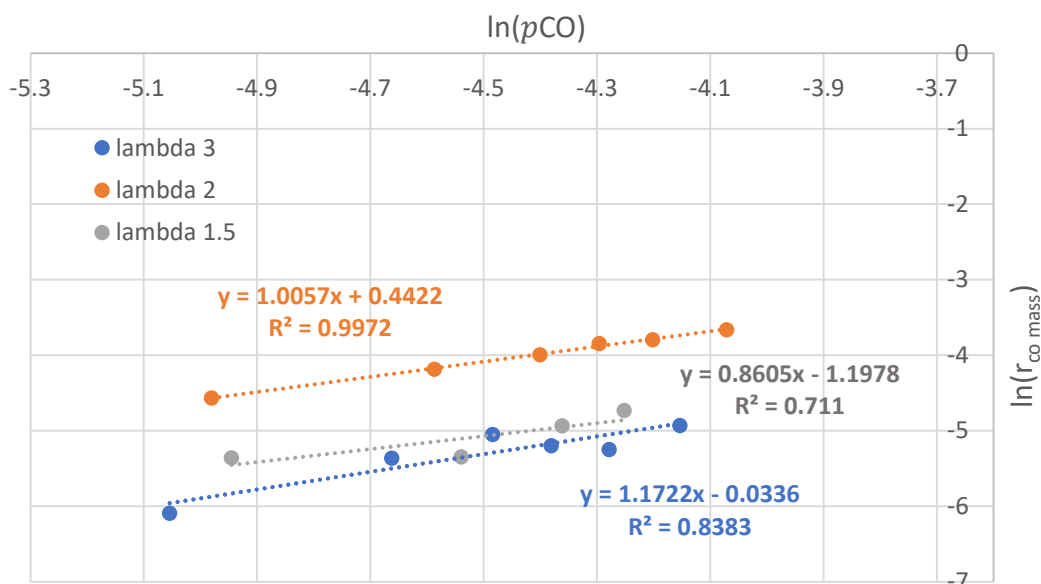


Figure 5.76. Double-logarithmic plot of $r_{CO_{mass}}$ versus CO partial pressure based on the data shown in Figure 5.75 after its correction with respect to the y-axis ($r_{CO_{mass}}$).

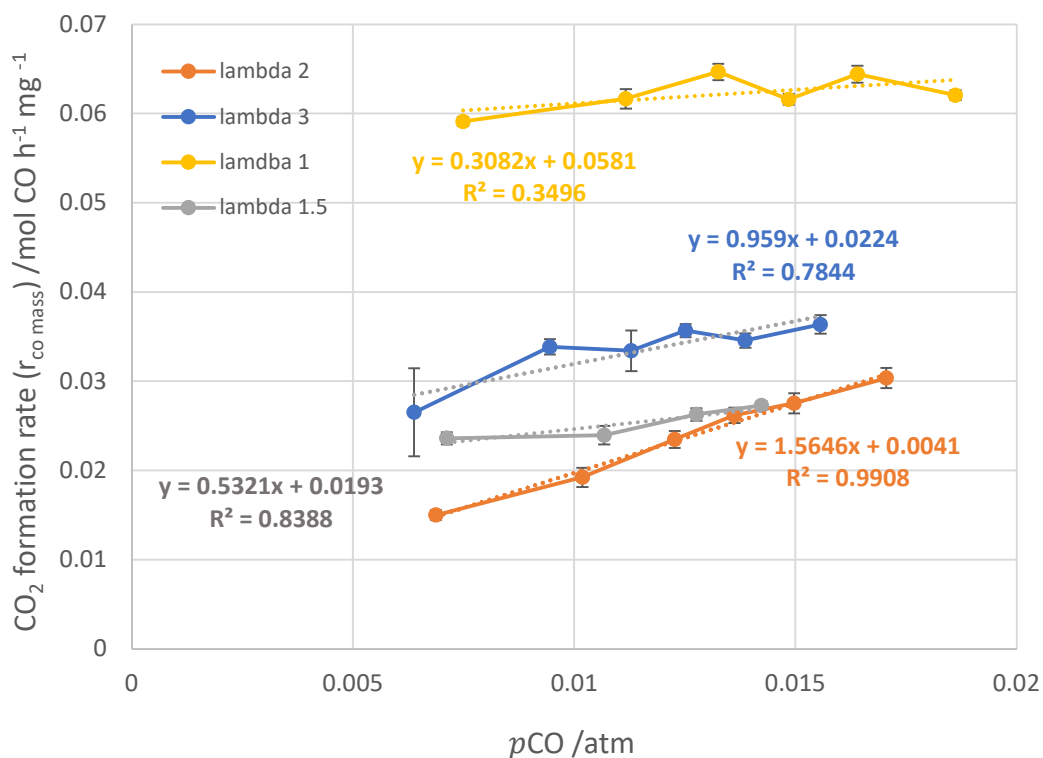


Figure 5.77. $r_{CO_{mass}}$ versus CO partial pressure at constant λ ($\lambda = 1, 1.5, 2$ and 3) and at 60°C during the temperature ramp down stage when using AuPd/CeO₂. Rdil was 1/9, total mass flow rate of 20 ml min⁻¹. Catalyst mass weight 27 mg.

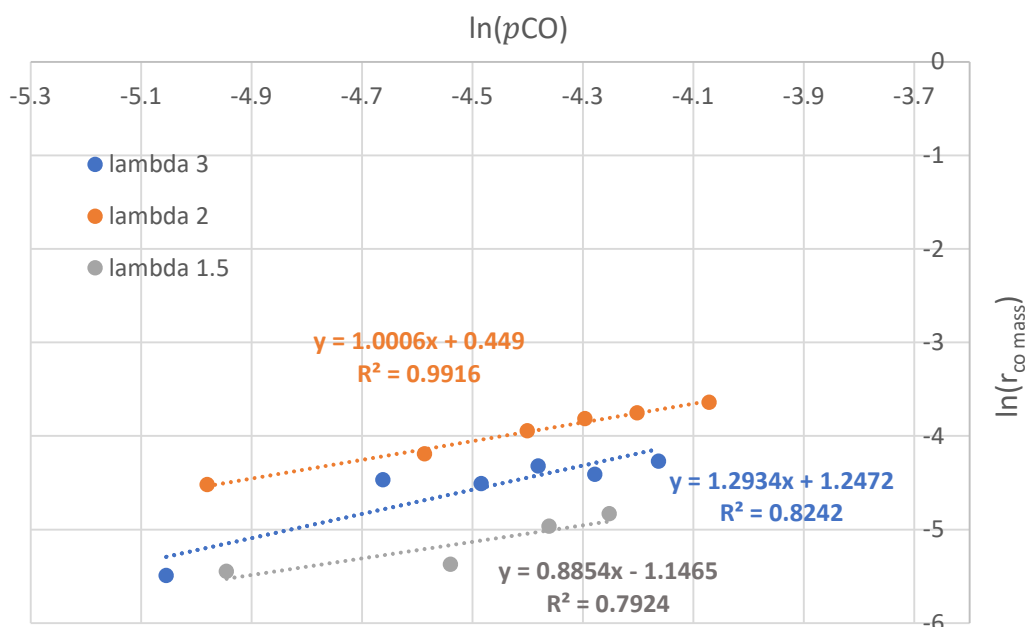


Figure 5.78. Double-logarithmic plot of $r_{CO_{mass}}$ versus CO partial pressure based on the data shown in Figure 5.77 after its correction with respect to the y-axis ($r_{CO_{mass}}$).

Table 5.8. Slopes obtained from the linear regression showed in Figures 5.72 (1st column), 5.74 (2nd column), 5.76 (3rd column) and 5.78 (4nd column).

	40°C		60°C	
	Ramp up	Ramp down	Ramp up	Ramp down
$\lambda = 1$	-	0.9752	-	-
$\lambda = 1.5$	0.9781	1.3992	0.8605	0.8854
$\lambda = 2$	0.8343	0.9765	1.0057	1.0006
$\lambda = 3$	1.7792	0.9551	1.1722	1.2934

5.4 Summary

The catalytic results obtained by the use of a mostly automated flow reactor system have been presented and discussed in this chapter. With the intention of getting our catalytic materials sparsely distributed across the reactor bed and avoiding the exotherm of the reaction controlling the temperature of the system, the catalyst dilution strategy at different ratios (R_{dil}) was investigated in Section 5.1.1. From those results, $R_{dil} = 1/9$ was selected as the optimal value to work with. Furthermore, due to poor activity shown by the rest of catalytic samples and also due to time constrains, only Au/CeO₂ and AuPd/CeO₂ were chosen as the best materials to be used during the rest of the investigation.

The effect of contact time was focus of Section 5.1.2, which was split in two subsections (5.1.2.a and 5.1.2.b) where two different approaches were discussed. The latter, the 'Reused sample approach', aimed to sort out the non-homogeneous distribution of the gold and palladium particles across the synthesized catalytic materials evidenced from the application of the initial approach, the 'Fresh sample approach'. Satisfactory results were obtained by such a strategy change. Repetitive features in the catalytic behaviour of both Au/CeO₂ and AuPd/CeO₂ have been observed throughout the entire chapter. These features were related to the different catalytic activities during ramp up and ramp down in temperature. While for the fresh sample, higher conversions/yields were obtained during the ramp down, for the reused cases, the opposite behaviour was observed, i.e. higher

conversions/yields during the temperature ramp up. This reproducibility in such behaviour reinforced the idea of the reduction of the surface noble metal particles from their cationic form to their metal oxidation state during the temperature increase stage in the fresh packed sample. As a consequence, a more active catalytic surface during the next stage, the ramp down in temperature, was noticed. This idea was supported by the NAP-XPS analysis on the Au/CeO₂ catalyst (Section 5.1.1). On the other hand, for the reused cases, the accumulation of carbonate species bound to the surface during the course of the experiment could explain the slightly lower conversions during the decrease in temperature stage than those obtained during the ramp up. Although such accumulation of chemical species on the catalytic surface was thought to be happening in the fresh packed sample as well, in this case the improvement in the catalytic activity gained by the acquired higher ratio Au⁰/Au^{δ+} (or Pd⁰/Pd^{δ+}) would likely blind the negative effects due to those chemical species adsorbing to the catalytic surface.

Another characteristic feature was also discussed in subsection 5.1.2.b, which was commonly appreciated along all the experimental tests presented in this chapter. In particular, conversions/yields typically reaching a maxima just at the end of each temperature ramp up stage, once the water bath heater had been set to maintain the current temperature for a period of time. During such period of time (typically 2 hours), conversions/yields gradually decreased until they reached an almost constant value, which was considered as the system getting into the steady state. Such phenomenon was not happening when the temperature of the system was decreased, i.e. water bath was cooling down. The cause of such behaviour has been attributed to the shift from kinetic control to external diffusion control discussed in Section 5.1. Accordingly, the given explanation was based on the hypothesis of the system entering external diffusion control during the ramping up in temperature and then being returned to its original kinetic regime due to the energy supply to the system being shut down in order to maintain a constant temperature. The extraction of heat from the system during temperature ramp down stages would prevent such a shift in regimes, explaining the absence of the same phenomenon during temperature ramp down stages.

Activation energies for both Au/CeO₂ and AuPd/CeO₂ were calculated in Section 5.2, which resulted in very similar values although slightly higher for the case of the metal supported AuPd case. Finally, the study of the orders of reaction by firstly finding the order of reaction with respect to CO at constant λ (α_{CO}^λ) was developed in Section 5.3. The subsequent calculation of the order of reaction with respect to oxygen (α_{O_2}) and application of Equation 5.8 was the approach proposed for the final calculation of α_{CO} . For both Au/CeO₂ and AuPd/CeO₂ catalysts, α_{CO}^λ at 40°C and 60°C were calculated. Quite similar results with values around 1 were obtained at both temperatures for both catalytic materials. Despite most of the pursued catalytic properties were already studied at this point of the research, the lack of any more time left to continue with the experimental investigation implied the impossibility to obtain an experimental estimation for α_{O_2} and the final calculation of α_{CO} .

References

- 1 O. Knacke, O. Kubaschewski, and K. Hesselmann: Thermochemical properties of inorganic substances I & II; 2nd edition, Springer-Verlag, Berlin, 1991.
- 2 M. S. Chen, Y. Cai, Z. Yan, K. K. Gath, S. Axnanda and D. W. Goodman, *Surf. Sci.*, 2007, **601**, 5326–5331.
- 3 P. A. Carlsson and M. Skoglundh, *Appl. Catal. B Environ.*, 2011, **101**, 669–675.
- 4 A. Abedi, R. Hayes, M. Votsmeier and W. S. Epling, *Catal. Letters*, 2012, **142**, 930–935.
- 5 D.A. Frank-Kamenetskii, Diffusion and Heat Transfer in Chemical Kinetics, Plenum press, New York, 1969, p. 487.
- 6 M. Kipnis, *Appl. Catal. B Environ.*, 2014, **152–153**, 38–45.
- 7 M. J. Kahlich, H. A. Gasteiger and R. J. Behm, *J. Catal.*, , DOI:10.1006/jcat.1997.1781.
- 8 F. Mariño, B. Schönbrod, M. Moreno, M. Jobbágy, G. Baronetti and M. Laborde, *Catal. Today*, 2008, **133–135**, 735–742.
- 9 S. D. Lin, M. Bollinger and M. A. Vannice, 1993, **17**, 245–262.
- 10 G. J. Hutchings, *Chem. Commun.*, 2008, **7345**, 1148–1164.
- 11 D. Widmann, Y. Liu, F. Schüth and R. J. Behm, *J. Catal.*, 2010, **276**, 292–305.
- 12 T. D. Thomas and Peter Weightman, *Phys. Rev. B*, 1986, **33**, 5406-5413.
- 13 J. Radnik, C. Mohr and P. Claus, *Phys. Chem. Chem. Phys.*, 2003, **5**, 172–177.
- 14 A. M. Venezia, G. Pantaleo, A. Longo, G. Di Carlo, M. P. Casaletto, F. L. Liotta and G. Deganello, *J. Phys. Chem. B*, 2005, **109**, 2821–2827.
- 15 T. Engel and G. Ertl, *Adv. Catal.*, 1979, **28**, 1–78.
- 16 Engel, T., and Ertl, G., in “The Chemical Physics of Solid Surfaces and Heterogeneous Catalysis” (D. A. King and D. P. Woodruff, Eds.), Vol. 4, p. 73,

Elsevier Scientific, Amsterdam, 1982.

- 17 J. A. Rodriguez and D. Wayne Goodman, *Surf. Sci. Rep.*, 1991, **14**, 1–107.
- 18 S. Fuchs and T. Hahn, *Stud. Surf. Sci. Catal.*, 1995, **96**, 275–284.
- 19 D. HAALAND, *J. Catal.*, 1982, **76**, 450–465.

6 | TAP Reactor

The TAP reactor system, previously described in Section 2.5, has constituted the essential tool that allowed the experimental results presented and discussed in this chapter. As already mentioned back in Chapter 2, TAP reactor systems have an extended literature serving as a proof of their potential when it comes to kinetics studies. However, operational issues related to malfunctions of different parts of our TAP system made it unfeasible to carry out detailed analysis of TAP pulse features. Despite, different experimental approaches were implemented in order to perform a series of calculations commonly needed within any TAP reactor study that is carried out. In the following sections, such procedures are discussed in detail.

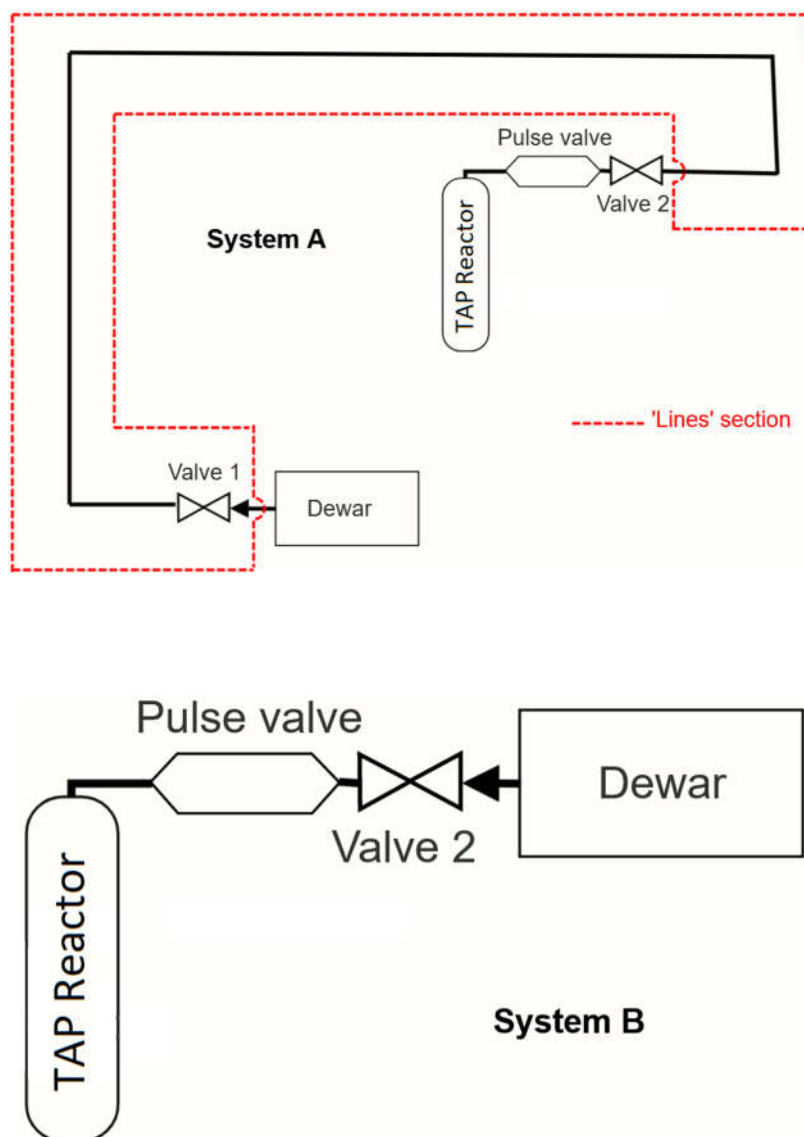
6.1 Number of molecules per pulse calculation procedure

One of the most essential needs when it comes to TAP reactor kinetic studies with quantitative purposes is the calculation of the average pulse size, which is normally given by the number of molecules per average pulse. It is also useful to calculate the number of molecules per unit area. This relates to the total area underneath the curve obtained as a response for each molecular species and that is subsequently detected by the mass spectrometer. This section is dedicated to explain how this measurement were performed and the results obtained.

In order to get an experimental estimation of the pulse size, two different approaches were performed before carrying out any pulse experiment, i.e. without pulsing any gas into the reactor.

Both 'non pulse' experiments were aimed to get an average of the volume being injected in each pulse. Such a volume is equivalent to the one contained in the pulse valve, where the gas is collected before its ejection into the reactor. Two different parameters were obtained from those two approaches, namely the total volume

contained in both lines and pulse valve, $(V_L + V_I)$, and the volume inside the lines alone, V_L . Thus, from both values, the average volume being injected in a typical pulse, V_I , was obtained. Pure argon was the gas used during all experimental procedures this section is dedicated to. Such a gaseous chemical was initially contained in a Dewar, which volume was known and equal to 1 litre. Schemes 6.1 gives a simplify view of the two different systems this section is focused on.



Scheme 6.1. Simplify scheme of the two systems being studied in Section 6.1, System A (above) and System B (below).

Sections 6.1.1 and 6.1.2 are dedicated to explain the whole process carried out in this investigation of the pulse size.

6.1.1 Non pulse experiments, calculation of V_I .

In order to make it easier to understand the flow of experiments carried out, this part has been dissected in the following two subsections, 6.1.1.a and 6.1.1.b.

6.1.1.a Calculation of $(V_L + V_I)$

Taking System A in Scheme 6.1 presented above as a starting point, the procedure followed for the collection of the parameters presented in Table 6.1 is detailed below:

After system was depressurised to UHV conditions, Valve 2 was closed and the lines were detached from it. Subsequently, the Dewar containing pure argon was disconnected from Valve 1 and reconnected to Valve 2, thus switching from System A to System B (see Scheme 6.1). Once System B was established, Valve 2 was opened and argon inside the Dewar released into the Pulse valve. Once pressure in the system was stabilized, Valve 2 was closed and values for both pressure and temperature of the system were noted, P_{read}^1 and T_{ini} respectively.

Returning to System A was the next step, which implied disconnecting Dewar from Valve 2, attaching lines back to such a valve and reconnecting Dewar to Valve 1. After System A was once again established, and after it was vacuumed, Valve 1 was opened and argon inside Dewar released. Then, after pressure stabilization, both pressure and temperature of the system were read, P_{read}^2 and T_{end} respectively. Procedures to obtain P_{read}^1 , T_{ini} , P_{read}^2 and T_{end} were repeated three times each. Temperatures obtained this way are the ones presented in Table 6.1. However, for the case of the pressure readings, these needed to be treated in order to get their equivalents in SI units, i.e. Pascals (Pa). The values read in the pressure monitor at the TAP reactor rig have no units, although their equivalents in atmospheres can be easily found. Disconnecting the lines from Valve 1 or Valve 2 would result in a reading at the pressure monitor (P_{atm}) which equals 1 atm. It is also important to note the value this pressure monitor reads when the system is at vacuum (P_{vac}). Then, by applying Equation 6.1, P_{ini} and P_{end} , as presented in Table 6.1, were calculated.

$$P_x = \frac{P_{read}^\delta - P_{vac}}{P_{atm} - P_{vac}} \cdot \frac{1.013 \cdot 10^5 \text{ Pa}}{1 \text{ atm}} \quad (\text{in Pa}) \quad (6.1)$$

where P_{read}^δ is the pressure monitor reading, where $\delta = 1$ or 2 , P_{atm} is the pressure reading under atmosphere pressure (equal to 1001) and P_{vac} is the pressure reading under vacuum conditions (equal to -14). $x = ini$ or end , depending on whether δ equals 1 or 2, respectively.

Table 6.1. Experimental values collected for the calculation of $(V_L + V_I)$ and by application of Equation 6.1.

	Measurement 1	Measurement 2	Measurement 3
T_{ini}/K	299	299	299
T_{end}/K	299	299	299
P_{ini}/Pa	1.412×10^5	1.843×10^5	1.519×10^5
P_{end}/Pa	1.383×10^5	1.807×10^5	1.487×10^5

As already mentioned, the volume of the Dewar was known and equal to 0.001 m^3 . Bearing in mind that the pressure sensor that allowed the reading of P_{read}^1 in System B is located just after Valve 2 and before the Pulse valve and considering the volume in between such a sensor and the outlet of the Dewar small enough to be ignored, the number of moles contained in the Dewar (N_{total}) during each measurement can be calculated by applying the ideal gas law, as it is shown in Equation 6.2:

$$N_{total} = \frac{P_{ini} \cdot V_{Dewar}}{R \cdot T_{ini}} \quad (6.2)$$

where R is the ideal gas constant, $8.3145 \text{ J mol}^{-1} \text{ K}^{-1}$.

Since these measurements did not imply pulse experiments, N_{total} should be the same after swapping back to System A for the reading of P_{end} . As such, the total volume contained in both lines and pulse valve, $V_L + V_I$ was calculated according to Equation 6.3:

$$V_L + V_I = \frac{N_{total} \cdot R \cdot T_{end}}{P_{end}} - V_{Dewar} \quad (6.3)$$

Applying Equations 6.2 and 6.3 to those values obtained during each of the three measurements carried out (see Table 6.1), results presented in Table 6.2 were calculated. Therefore, by averaging the three volumes, a final $(V_L + V_I)$ of $(2.087 \times 10^{-5} \pm 9.708 \times 10^{-7}) \text{ m}^3$ was obtained.

Table 6.2. Calculated values from application of Equations 6.2 and 6.3.

	Measurement 1	Measurement 2	Measurement 3
N_{total}/mol	5.685×10^{-2}	7.416×10^{-2}	6.109×10^{-2}
$(V_L + V_I)/\text{m}^3$	2.092×10^{-5}	1.988×10^{-5}	2.182×10^{-5}

6.1.1.b Calculation of V_I

In this case, taking System A in Scheme 6.1 as a starting point, the procedure followed for the collection of the parameters presented in Table 6.3 is detailed below:

After system was depressurised to UHV conditions, Valve 2 was closed and argon was released from the Dewar to the lines through Valve 1. Once pressure was stabilized, Valve 1 was closed again. Pressure and temperature readings were taken, P_{read}^1 and T_{ini} respectively. Subsequently, Valve 2 was opened, allowing the gas to enter inside the Pulse valve. Once again, after pressure stabilization, P_{read}^2 and T_{end} were noted. This procedure was repeated three times. As in subsection 6.1.1.a, P_{ini} and P_{end} presented in Table 6.3 below were calculated by application of Equation 6.1.

Table 6.3. Experimental values collected for the calculation of V_I and by application of Equation 6.1.

	Measurement 1	Measurement 2	Measurement 3
T_{ini}/K	300	300	300
T_{end}/K	300	300	300
P_{ini}/Pa	2.978×10^4	1.502×10^5	1.041×10^5
P_{end}/Pa	2.543×10^4	1.283×10^5	8.894×10^4

The first step towards the estimation of V_I is the calculation of the volume consisting of the lines without the Pulse valve (V_L). Since $(V_L + V_I)$ was previously obtained, such a calculation is easily performed by applying Equation 6.4:

$$\frac{P_{end} \cdot (V_L + V_I)}{P_{ini}} = \frac{n \cdot R \cdot T_{end}}{n \cdot R \cdot T_{ini} / V_L} \quad (6.4)$$

Finally, a simple subtraction would give V_I (Equation 6.5).

$$V_I = (V_L + V_I) - V_L \quad (6.5)$$

Values obtained for each of the three measurements are collected in Table 6.4. Then, averaging those resulted in a V_I of $(3.046 \times 10^{-6} \pm 6.362 \times 10^{-9}) \text{ m}^3$.

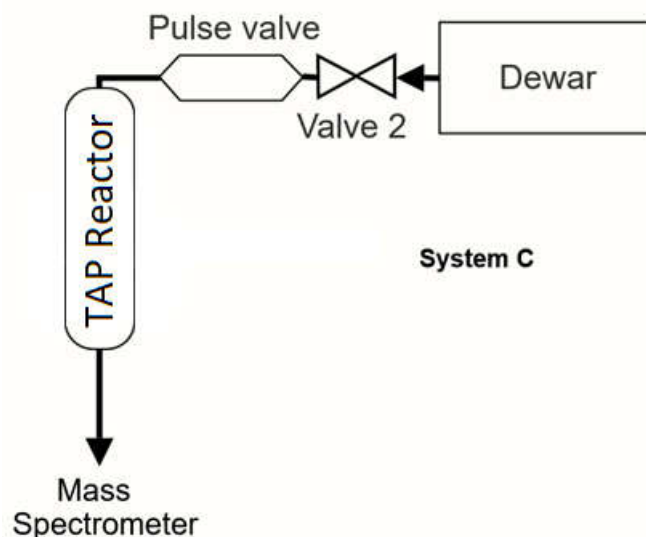
Table 6.4. Calculated values from application of Equations 6.4 and 6.5 to data presented in Table 6.3 and $(V_L + V_I)$ calculated in subsection 6.1.1.a.

	Measurement 1	Measurement 2	Measurement 3
V_I / m^3	3.053×10^{-6}	3.040×10^{-6}	3.046×10^{-6}

6.1.2 Pulse experiments, calculation of the pulse size.

As mentioned at the beginning of Section 6.1, the average pulse size is commonly given by the number of molecules per average pulse. Nonetheless, since every experiment and calculation performed in this Chapter 6 was intended to provide the most basic TAP reactor database for future quantitative kinetic studies, the calculation of the number of molecules per unit area of mass spec would definitively constitute another useful addition to it. Therefore, this subsection is dedicated to describe the procedure followed to obtain such data.

In this case, pulse experiments were involved. Thus, argon gas was repeatedly pulsed into the TAP reactor, flowing through it and across its outlet to finally be detected by the mass spectrometer. Furthermore, for these experiments, System B (Scheme 6.1) was set as an all-time system with the only difference that in this case there was a gaseous flow through the reactor. Such a reactor setup has been called System C and it is shown in Scheme 6.2.



Scheme 6.2. Simplified scheme of the system studied in subsection 6.1.2.

With the reactor setup showed in Scheme 6.2, two series of experiments consisting of 999 argon pulses each were performed. The number of pulses (Np) was set to 999 as this is the maximum number of pulses the software installed in the Cardiff TAP reactor unit allows to be performed in a single run. Temperature and pressure readings were taken before (T_{ini}, P_{ini}) and after (T_{end}, P_{end}) each series of experiments with values presented in Table 6.5 below.

Table 6.5. Experimental values collected for the calculation of the pulse size.

	Measurement 1	Measurement 2
Np	999	999
T_{ini}/K	299	300
T_{end}/K	300	300
P_{ini}/Pa	1.532×10^5	1.513×10^5
P_{end}/Pa	1.513×10^5	1.501×10^5

Since V_I was already calculated, the number of moles before starting to pulse (n_{ini}) and at the end of the experiment (n_{end}) are easily obtained by using the values collected in Table 6.5 and the ideal gas law (Equation 6.6).

$$n_{ini} = \frac{P_{ini} \cdot V_I}{T_{ini} \cdot R}; \quad n_{end} = \frac{P_{end} \cdot V_I}{T_{end} \cdot R} \quad (6.6)$$

From this, a straightforward subtraction would yield the total number of moles pulsed by the end of the pulse experiment (Δn), Equation 6.7:

$$\Delta n = n_{ini} - n_{end} \quad (6.7)$$

The total number of molecules pulsed by the end of the experiment (M_{total}) is given by Equation 6.8.

$$M_{total} = \Delta n \cdot N_A \quad (6.8)$$

where N_A is the Avogadro number.

Finally, dividing M_{total} by Np (999 pulses) resulted in the aimed calculation of the number of molecules per average pulse, M_p , as shown in Equation 6.9 below:

$$M_p = \frac{M_{total}}{Np} \quad (6.9)$$

Regarding the number of molecules per unit area of mass spectrometer response, calculation of the zeroth moment (M_0) is a necessary prior step. For this, our TAP software described and discussed in Chapter 4 was used. Since we were looking for an average value rather than a specific one, the total zeroth moment, i.e. the sum of the zeroth moments for each of the 999 pulse responses, was calculated. This has been called M_{0total} and it is essential to obtain the number of moles per unit area of mass spectrometer response (n_{MS}) by application of Equation 6.10:

$$n_{MS} = \frac{\Delta n}{M_{0total}} \quad (6.10)$$

Thus, once n_{MS} was calculated, the number of molecules per unit area of mass spectrometer response (M_{MS}) was simply obtained accordingly to Equation 6.11.

$$M_{MS} = n_{MS} \cdot N_A \quad (6.11)$$

The implementation of calculations described in Equations 6.6-6.11 yielded the results presented in Table 6.6. According to such results, an average of 1.382×10^{15} molecules per pulse and 7.958×10^{11} molecules per unit area of mass spectrometer response were obtained.

Table 6.6. Calculated values from application of Equations 6.6-6.11 and data presented in Table 6.5.

	Measurement 1	Measurement 2
n_{ini} /mol	1.877×10^{-4}	1.850×10^{-4}
n_{end} /mol	1.850×10^{-4}	1.831×10^{-4}
Δn /mol	2.7566×10^{-6}	1.830×10^{-6}
M_{total} /molecules	1.660×10^{18}	1.102×10^{18}
M_p /molecules	1.661×10^{15}	1.103×10^{15}
M_{0total}	1870450.861	1565352.329
n_{MS} /mol	1.473×10^{-12}	1.170×10^{-12}
M_{MS} /molecules	8.874×10^{11}	7.042×10^{11}

6.2 Harvard Data - Qualitative reactive features based on experimental TAP responses

The main purpose of this is the analysis of the experimental TAP data obtained during a brief visit at Harvard University. The short time spent in the facilities along with the occurrence of an important damage of some parts of the TAP reactor there significantly reduced the number of experiments carried out. Consequently, testing the most prolific catalyst among all our samples, i.e. Au/CeO₂, became the main focus of those experiments. The outcome from such tests is presented and qualitatively discussed below.

25 milligrams of Au/CeO₂ were weighted and packed into the reactor in the usual sandwiched way, i.e. between two layers of inert SiC material. The system was then pumped down until UHV conditions were reached and experiments were started.

The sample was firstly oxidised by performing 500 pulses of a gaseous mix consisting of 10% O₂ in argon at 150°C. Right after this, 40 pulses of 10% CO/Ar were pulsed over the catalytic sample at the same temperature. Figure 6.1 shows the results from such reduction series. It can be observed that the argon response follows an essentially constant pattern, while the CO exit flow intensities fluctuate

along the experiment, thus not following the same trend as the inert gas did. This is in accordance with the fact that CO_2 is being produced, hence some of the CO is reacting with the surface adsorbed oxygen species. As showed in Figure 6.1, CO_2 production is higher at the beginning of the experiments and it is decreasing with the number of pulses. One explanation for such a behaviour could be the reduction of the amount of surface oxygen species available to be bound to the CO entering the reactor. However, in that case, the CO pulse response should show the opposite trend, this is, lower to higher pulse response intensities. Since this is not the case, the pattern observed in the case of the CO_2 could be due to an adjustment in the gain at which it is obtained from the TAP software installed in the computer connected to the mass spectrometer, within the TAP rig. Nonetheless, since the experimental conditions a catalytic sample undergoes in a flow reactor are much different from those in a TAP reactor, the only production of carbon dioxide in this system is already a relevant achievement.

After the experimental test commented above, another oxidation-reduction series was carried out. In this case, 70 pulses of 10% CO/Ar were performed after re-oxidizing the sample. The outcome is presented in Figure 6.2. CO_2 is once again produced, this time with a mostly constant pulse response intensity. This fact reinforces the idea of the random adjustment of the gain as a cause for the trend previously observed in Figure 6.1. Also, since a mostly constant intensity was observed in this case, the average of the pulse responses to get a representative curve for each inert, reactant and product would be possible. From such an average, a CO conversion of approximately 1.7% was calculated. Figure 6.3 shows the obtained average curves for argon, CO and CO_2 after their height normalisation. This was done by dividing each pulse response by its respective maxima. Such procedure makes every peak having the same normalised height, this being equal to 1. By doing so, the qualitative analysis of such responses is much easier. This followed the reasoning given by Gleaves et al.¹, who reviewed the broad spectrum of physicochemical mathematics that support TAP reactor studies and that gives the necessary means for both quantitative and qualitative data analysis. Although our measurement at Harvard University were not sufficient for a quantitative study,

they did carry enough information for a qualitative assessment. As such, considering their review¹ and focusing now in Figure 6.3 down below, the CO pulse response clearly shows the fingerprints of a diffusion+irreversible adsorption/reaction process, which are featured by curves smaller than, and that do not cross the curve for diffusion-only (argon curve). This agrees with that expected for our reactant CO. The order of the peaks, i.e. CO₂ curve peaks after the CO one, indicates that CO₂ is formed from CO, which would not be surprising at all. On the other hand, the CO curve is the broadest of the three cases and it crosses the Ar curve. Those matches the typical characteristics of diffusion+reversible adsorption processes. Furthermore, since the width of the curves gives information about the residence time for each molecule, the fact that the CO₂ curve is not much broader than the diffusion-only curve indicates that CO₂ adsorbs very weakly to the surface and it rapidly desorbs and exits the reactor.

After the reduction series discussed above, a multi-pulse TAP experiment was carried out. This was performed at the same temperature (150°C) and consisted of 22 pulses of 10% CO/Ar and 22 pulses of 10% O₂/Ar, alternatively fired over the same sample of Au/CeO₂. Results from such experiment are presented in Figure 6.4, which shows the pulse responses for every component involved in the CO oxidation reaction, along with the inert response for reference. From this data and following the same procedure reported above for the previous reduction series, a mean CO conversion of 1.1% and an O₂ conversion 0.7% were obtained and the height normalised exit flows were plotted as shown in Figure 6.5. As observed, the O₂ curve falls inside the diffusion-only curve without crossing it, in agreement with a diffusion+irreversible adsorption/reaction mechanism. CO₂, on the other hand, shows a curve which peaks after the O₂ and the Ar ones, crossing the latter just after its peak time. This behaviour, in conjunction with the fact that the residence time for CO is higher than that for O₂ (wider peak), suggests that CO is previously surface adsorbed in a weak manner before it reacts with O₂. The very narrow peak observed for the case of the dioxygen molecule, along with the already pointed out absence of a crossing point with the Ar curve, advocate for O₂ molecules directly reacting in their gaseous form with the previously adsorbed CO. This would indicate

an Eley-Rideal reaction type mechanism. However, bearing in mind the CO and O₂ conversions obtained, with higher O₂ conversions than those expected from a stoichiometric reaction, it is thought that dioxygen molecules were consumed by both reacting and by replenishing oxygen vacancies in the lattice surface, thus a combination of Eley-Rideal and Langmuir-Hinshelwood mechanisms are proposed. Regarding the CO₂ curve response, comparing Figure 6.3 with figure 6.5, they both share the same features, although much more noticeable for the case of the multi-pulse experiment (Figure 6.5). Thus, when both O₂ and CO enter the reactor, the CO₂ peak is much broader than that observed when only CO was fired. This long residence time could be the result of its formation from multiple paths of varying rates, which in turn will be in accordance with the suggested hypothesis of two different mechanisms taking place.

In order to reaffirm the results discussed above, another CO oxidation experiment at an increased temperature (300°C) was performed. The same features that were observed previously in Figures 6.4 and 6.5 are repeated in this case (Figures 6.6 and 6.7), although with narrower CO and CO₂ peaks. This is in fact an expected effect of increasing the reaction temperature, which would make easier the desorption of the adsorbed species or even impeding their adsorption in the first place, thus decreasing their residence time.

In regard to these residence times, as it can be checked in Figures 6.3, 6.5 and 6.7, such residence times are around 0.5 seconds. Going back to Chapter 5 where flow reactor studies were discussed, the range of residence times investigated for the case of Au/CeO₂ could be estimated. Considering that the average length of the catalytic bed was around the 5 mm and the internal diameter of the U-tube reactor is 5 mm, an average volume of 0.098 ml is approximated. Also, a total catalytic mass of 27 mg was packed into the reactor (dilution ratio equal to 1:9) and contact times studied back then were within the 0.04-0.16 g s ml⁻¹ range. This is equivalent to residence times within 0.15-0.59 seconds. Therefore, values studied in the TAP reactor lay within the range of those studied in our flow reactor experiments (see Chapter 5). Consequently, although bearing in mind that experimental conditions were not the same, both flow and TAP reactor results could be considered for reactions occurring on a similar timescale.

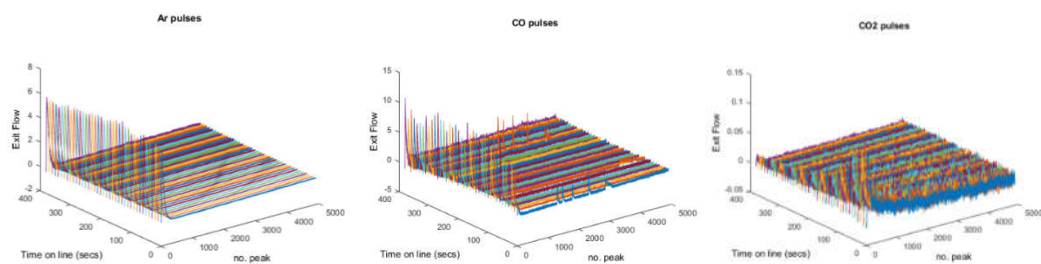


Figure 6.1. Reduction series: 40 pulses of a gaseous mix consisting of 10% CO in argon over 25 mg of Au/CeO₂ at a temperature of 150°C. Pulse experiment was carried out after the sample was previously titrated with 500 pulses of a 10% O₂/Ar gaseous mix.

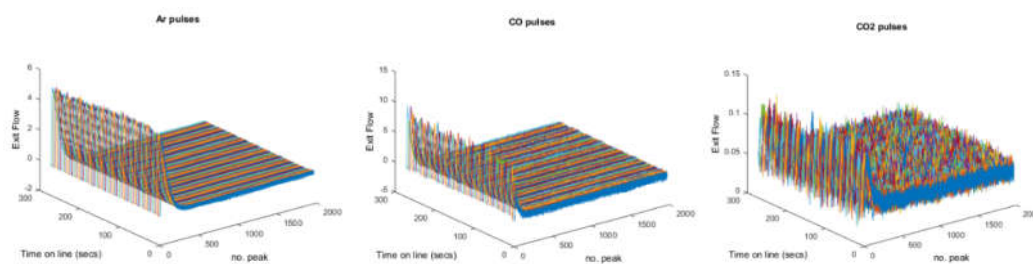


Figure 6.2. Reduction series: 70 pulses of a gaseous mix consisting of 10% CO in argon over 25 mg of Au/CeO₂ at a temperature of 150°C. Pulse experiment was carried out after an oxidation series (500 pulses of a 10% O₂/Ar gaseous mix) was performed over the reduced sample resulting from experiment presented in Figure 6.1.

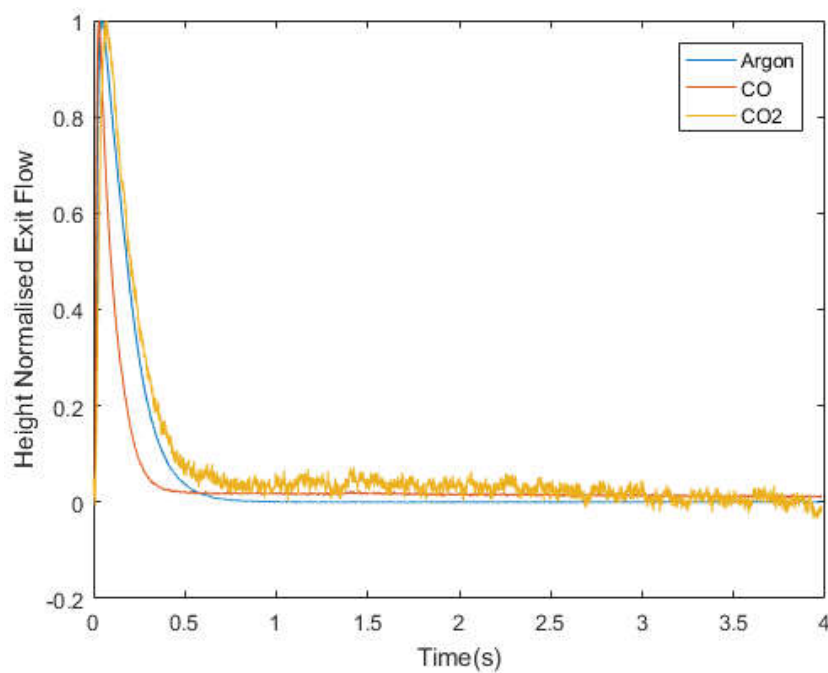


Figure 6.3. Height normalised exit flows versus time calculated from averaging data represented in Figure 6.2.

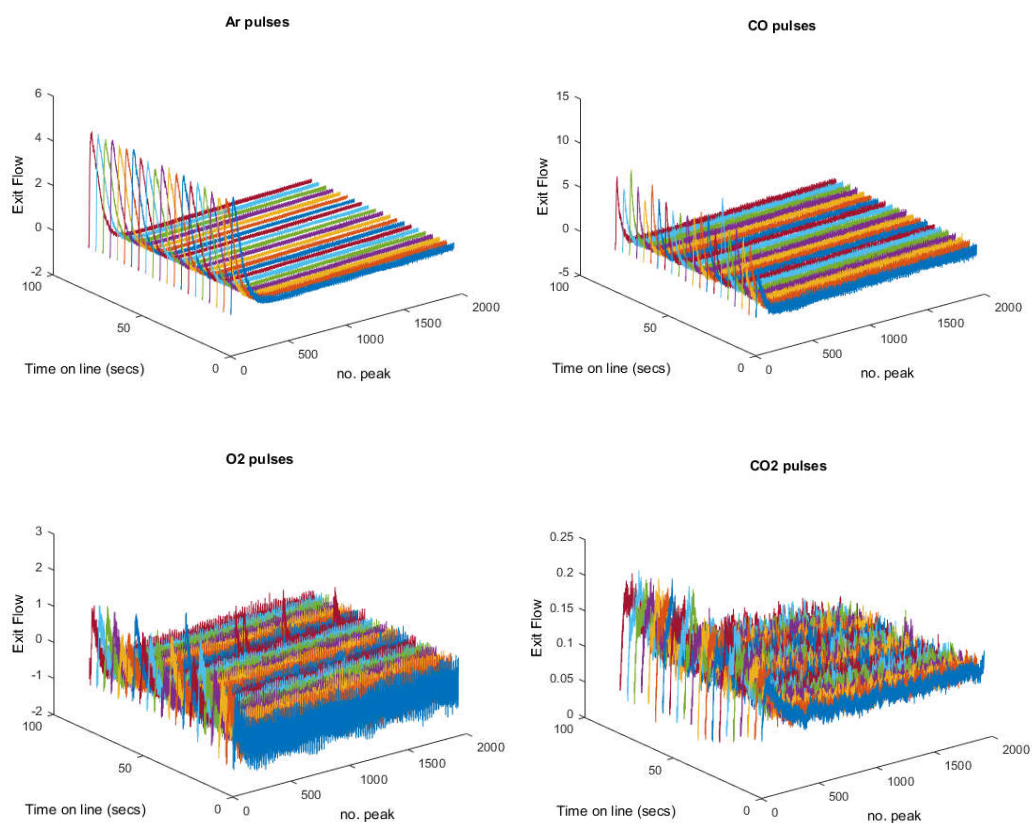


Figure 6.4. Multi-pulse TAP experiment: CO oxidation experiment consisting of 22 pulses of 10% CO/Ar and 22 pulses of 10% O₂/Ar, alternatively performed, over 25 mg of Au/CeO₂ at a temperature of 150°C. Pulse experiment was carried out after straight after reduction series presented in Figure 6.2.

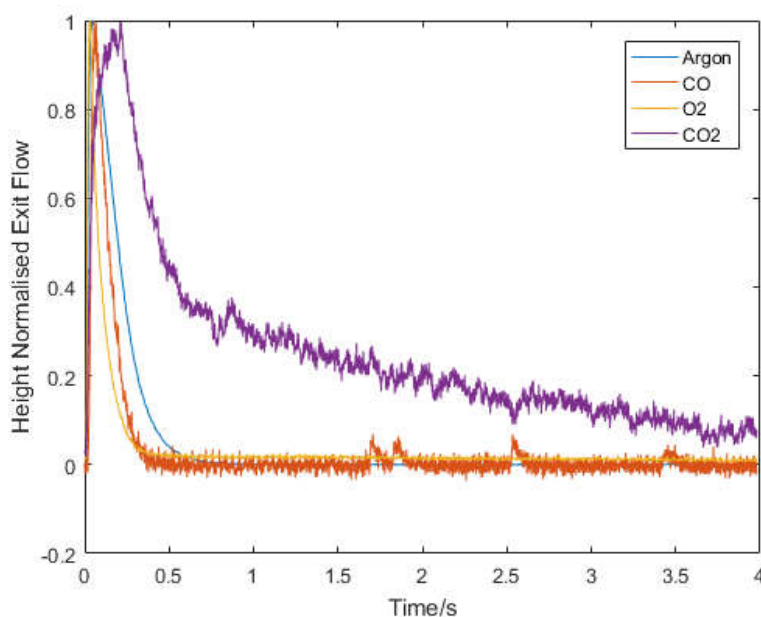


Figure 6.5. Height normalised exit flows versus time calculated from averaging data represented in Figure 6.4.

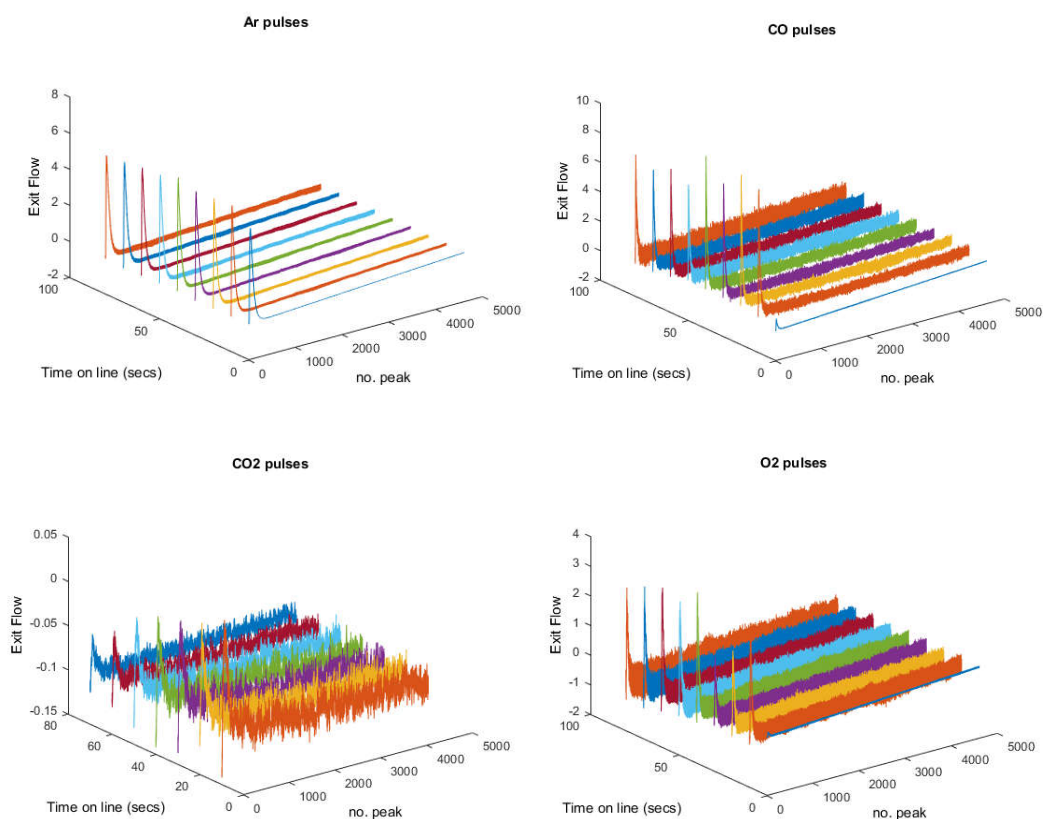


Figure 6.6. Multi-pulse TAP experiment: CO oxidation experiment consisting of 9 pulses of 10% CO/Ar and 9 pulses of 10% O₂/Ar, alternatively performed, over 25 mg of Au/CeO₂ at a temperature of 300°C. Pulse experiment was carried out after straight after reduction series presented in Figure 6.4.

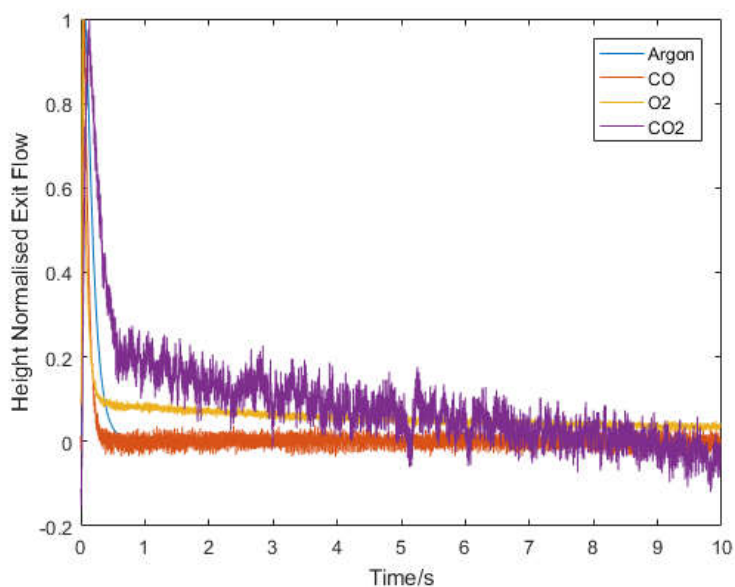


Figure 6.7. Height normalised exit flows versus time calculated from averaging data represented in Figure 6.6.

6.3 Cardiff Data

After the estimation of the pulse size was already made, it was time to carry out TAP pulse experiments in an attempt to produce CO₂ from the O₂ and CO titration of our catalytic samples. This section is dedicated to the results obtained when performing such experiments in the TAP reactor located at Cardiff University. Although almost the totality of the experimental approaches developed in this work have been implemented by making use of such a reactor rig, some of them were carried out in the TAP reactor at Harvard University, hence the relevance on the differentiation made between 'Harvard Data' and 'Cardiff Data', Sections 6.2 and 6.3 respectively. Regarding this present section, it has been split in two parts, corresponding to below subsections 6.3.1-6.3.2.

6.3.1 Troubleshooting

At the beginning of this chapter, the impossibility of conducting quantitative kinetic studies with reliable results was mentioned. As it was pointed out then, a series of issues related to different parts of our TAP reactor rig (Cardiff unit) made it unfeasible to perform the necessary experiments that lead to trustworthy data. This subsection is focused on detailing the procedure followed over the course of our Cardiff based TAP reactor catalytic tests. Nonetheless, the fact that the majority of these tests yielded flawed data, due to such physical issues, is the reason for this to be closer to a troubleshooting series rather than anything else, hence the title for this subchapter. The way it has been schematized below follows the order the different catalytic samples were tested. Accordingly, four different parts corresponding to the four samples loaded into the reactor bed have resulted. For all four cases, the same catalytic material was used. This was a consequence of two factors. Firstly, the time restrictions faced during this work led us to choose the most active of all our catalytic materials from the flow reactor studies as the best catalyst to begin with. Secondly, the flawed response data continually obtained over the course of the experiments pushed away the possibility of testing any other

catalytic material, therefore limiting the number of variables playing a role in those faulty results. Although the initial intention was to study both Au/CeO₂ and AuPd/CeO₂ in order to establish correlations with the results previously obtained in our flow reactor studies, the already commented difficulties ended up leaving no more time for carrying on with the experiments. Consequently, Au/CeO₂ was the only catalyst used during the experimental series presented in this Section 6.3. As already mentioned, four samples were loaded and tested. For all of them, the chosen mass of Au/CeO₂ was sandwiched between two layers of inert material, in particular, silica carbide (SiC). Thus, since same catalyst and same inert material were used in every case, the only difference among them was the mass of catalyst and the moment, within our TAP study process, they were tested at.

Pulse responses showed down below are the result of applying the TAP analysis software developed during this work (see Chapter 4) to the raw data obtained in each experiment. In order to objectively see if there is any change due to chemical processes in the response of both reactants and products, every pulse response have been area normalized with respect to its respective raw argon response, which is done by default when our TAP analysis software is run.

- Sample 1

30 mg Au/CeO₂ was packed into the reactor (Sample 1) and, once the system was under UHV conditions, consecutive TAP pulse experiments were carried out. Those consisted of a series of O₂ pulses followed by a series of CO, usually referred as oxidation and reduction series, respectively. Both oxygen and CO were pulsed along with argon, which is the inert gas used as our internal standard. For the reduction series, a pre-made gas mixture consisting of 20% CO in argon was used. On the other hand, for the oxidation series, an in-situ mixture needed to be made from pure argon and pure Oxygen. Although, in most of the experimental tests, the same percentage as that used for the CO was aimed, i.e. 20% O₂, the nature of the manual gas mixing made it difficult to get such an exact percentage value. This is the reason for the variable gas compositions, all of them near the 20% set point, that were used over the course of the entire TAP reactor experimental procedure at our

Cardiff University unit. Five complete oxidation-reduction sequences were performed over Sample 1. Reaction temperatures were varied from room temperature to a maximum of 200°C. Nonetheless, yielded results from those five sequences were essentially the same, these being no CO₂ production and pulse response detection at mass 28 over the course of the oxidation series. Figures 6.8 and 6.9, which correspond to the 3rd oxidation-reduction sequence, exemplify such results. The absence of carbon dioxide in the reactor outlet simply means that the conditions tested in the TAP reactor were not conducive for the CO oxidation reaction to occur. The detection of pulse response at mass 28, when only oxygen and argon were entering the reactor, did have a more relevant significance. Now, it is important to point out that CO has a molecular mass of 28. However, since the entire system was under vacuum after each oxidation and each reduction series and only a mix O₂/Ar was pulsed into the reactor, the possibility of CO being the responsible for such a signal was vanished. The next candidate would be N₂, which has indeed the same molecular mass as CO. The presence of nitrogen in the system could only mean that it is leaking in from the atmospheric air and thus the existence of one or more leaks along the lines (see Scheme 6.1, System A) was thought to be the root of this issue. As mentioned before, results obtained from the five oxidation-reduction sequences were all showing the same features. However, there was one exception. This was related to the oxygen pulse response observed during the 3rd oxidation series, reason why this is the one showed in Figure 6.8 below. It is clearly evident that the O₂ signal is null for more than half the series of pulses. Then, all of a sudden, O₂ peaks appear and increase in size with time, till they get to stabilize. This behavior could be translated as the oxygen being adsorbed on the catalyst surface until this get fully oxidized. Reaching such an oxygen saturation of the surface would mark the point from which the O₂ starts to exit the reactor and thus being detected by the mass spectrometer. Nevertheless, bearing in mind that these results were obtained in the potential presence of one or multiple leaks along the system lines, they cannot be considered reliable enough to make any kind of conclusions, nor any kind of calculation from them. Figure 6.9 shows the counterpart of Figure 6.8, i.e. the 3rd reduction series carried out over

Sample 1. The main purpose of this figure is to make it clear that the absence of CO_2 is common for both oxidation and reduction pulse experiments.

After the series of experiments commented above, two main actions were to be made. Firstly, fixing the leak issue. This was initially attempted by tying every section and junction along the system lines, which turned out to be ineffective. Eventually, by replacing some of the line sections the issue was finally sorted out. Secondly, the hypothesis of the reactants being adsorbed on the surface and not reacting with each other led to the decision of trying a lower mass of catalyst. This follows to the next part, where experimental procedures on Sample 2 are discussed.

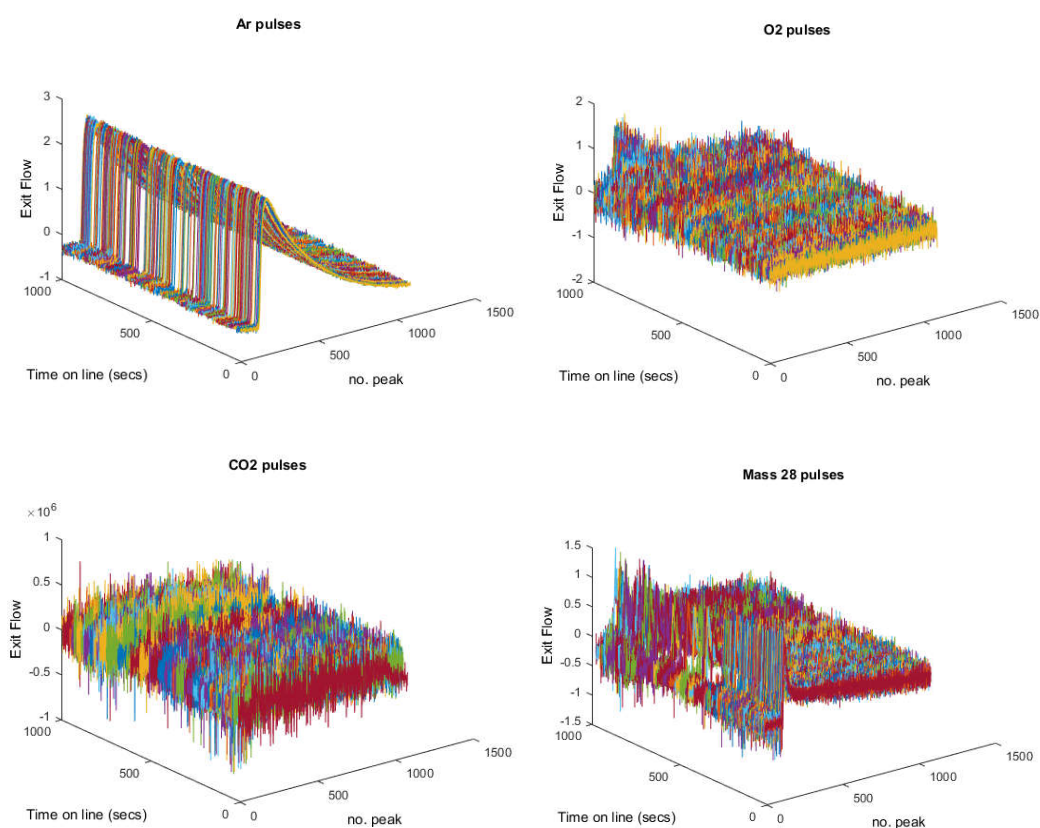


Figure 6.8. Oxidation series: 500 pulses of a gaseous mix consisting of 20% O_2 in Ar over 30 mg of Au/CeO_2 at a temperature of 170°C and 5.4 V. All pulse responses have been area normalized with respect to the raw argon response.

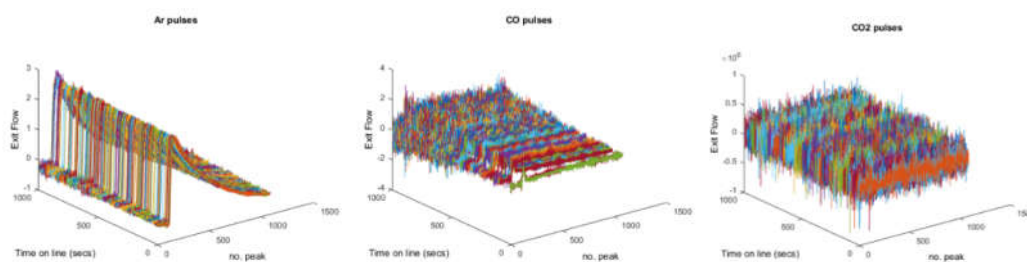


Figure 6.9. Reduction series: 500 pulses of a gaseous mix consisting of 20% CO in Ar over 30 mg of Au/CeO₂ at a temperature of 170°C and 5.4 V.

- Sample 2

As referred above, after the leak issue was solved, the next step was to test a smaller quantity of catalyst. In this case, 9 mg of Au/CeO₂ were packed into the reactor (Sample 2). Similar to that done with Sample 1, Sample 2 was alternatively titrated with O₂ and CO through a series of oxidation and reduction pulse experiments. Again, those series were performed at different temperatures, these within a range going from room temperature to a maximum of 200°C. Figures 6.10-6.12 shows the different responses after the first oxidation-reduction sequence was carried out over Sample 2. As observed in those figures, nothing different from that previously seen with Sample 1 was obtained. Both oxygen and CO responses present the same pattern as argon, Figures 6.10 and 6.11 respectively. No CO₂ is produced in this case either (Figure 6.12). The only thing to remark is the sudden increase of noise in the signals over the course of the oxidation series (Figure 6.10). This increment of the noisiness during the last 100 pulses was an unexpected phenomenon which does not correspond to any change on the external variables of the system, thus no explanation could be found. Unfortunately, such a phenomenon was not unusually observed and rather, as it could be checked in the results presented across this section, constituted a quite familiar behaviour of the Cardiff TAP reactor unit.

After the first oxidation-reduction sequence, a second sequence at 115°C was performed, this yielding essentially the same unproductive results. As a consequence of the poor outcome, another strategy was implemented, which consisted of leaving the entire system on vacuum for two days without any experiment carried out during that period. The purpose of such approach was to get rid of any species adsorbed on the

catalytic surface. This was based on the theory that, by de-adsorbing the chemical species over the surface, the active sites they were bonded to would then get free to re-adsorb the new oxygen molecules entering the reactor in the next oxidation series. If this so happens, the cleaned catalytic surface, i.e. with no species adsorbed to it, could be considered as being fully reduced. Figures 6.13-6.15 shows the pulse responses obtained after two consecutive oxidation series were performed over Sample 2 (after it was left under UHV conditions for two days). The reason why the usual one to one oxidation-reduction sequence was not carried out comes with the O₂ pulse response observed after the first 500 O₂/Ar pulses (Figure 6.13). In that figure, it is easily distinguished that, while the argon pulses maintain a practically constant area, the oxygen response is null for the vast majority of the entire oxidation series, suddenly being detected with increasing peak areas towards the end of the experiment. This is similar to the behaviour seen back in Figure 6.8, although with the main difference that, in this present case, the leak issue previously commented was now fixed. Thus, results presented in Figure 6.13 could be considered as a reliable source of information, which suggested that our purpose of removing any species bonded to the catalytic active sites got fulfilled. Accordingly, the absence of any oxygen peak would correspond to this being adsorbed to such active sites, therefore not getting to exit the reactor. The sudden appearance of O₂ response could then be explained with the catalytic surface starting to get saturated with oxygen, hence some of the oxygen molecules that enter the reactor have not available site to adsorb to and, thus, they go through the exit towards the mass spectrometer, where they are detected. The increase in the O₂ peak areas with time belong to the fact that the surface is getting more and more saturated. Since no stabilization on such peak areas is reached by the end of the 500 O₂/Ar pulses, instead of performing a reduction series, another oxidation series consisting of 999 O₂/Ar pulses was carried out. The oxygen pulse response obtained during this second oxidation series is presented in Figure 6.14. In this case, the O₂ peak areas stabilization is reached. Such a stabilization point happens at around the pulse number 660, considering the previous 500 pulses already performed. Consequently, it could be estimated that 660 pulses of a gas mixture consisting of 20% O₂ in argon were needed to fully oxidize the fully reduced surface of 9 mg of our Au/CeO₂ catalyst. This information

has been used for the calculations performed in the next subsection 6.3.2. Relating to CO₂ production, none was produced during both consecutive oxidation series (Figure 6.15). This, in turn, was completely expected since the system was under vacuum for two days and only oxygen and argon had been pulsed over the sample after such a period, hence there was not available carbonate species either in a gaseous state or adsorbed on the surface for the formation of any CO₂ to take place. Unfortunately, the CO titration performed afterwards over that completely oxidised version of Sample 2 did not yield any CO₂ either. Such titration was carried out at 160°C and consisted of 999 pulses of the commonly used 20% CO/Ar mix. Since the CO oxidation did not get to happen by alternative oxidation and reduction series, the simultaneous titration of the catalytic sample with O₂ and CO was subsequently attempted. This approach was carried out by combining the pre-made 20% CO/Ar mix with pure O₂ in a way that the final gas mixture had a composition with a λ -value within the range previously studied under flow reactor conditions (see Chapter 5). As such, a CO oxidation series, i.e. simultaneous O₂ and CO titration, with λ -value equal 2.2 in the gas feed was performed at 135°C. Figure 6.16 presents the pulse responses obtained then, which once again resulted in the absence of CO₂ being produced. There is another relevant feature to point out about those results, which is related to signal obtained for CO. As observed in Figure 6.16, such signal is null with only noise been detected and a random peak during the second half of the pulse series. This peak should not be considered as the CO response at that specific pulse but rather the result of another faulty performance of our TAP reactor system (Cardiff Unit). The fact that pulses are set to be fired during the very first milliseconds of every 2 seconds, which is the total time each pulse (pulse and tail) takes, make it easy to discard such a peak as any kind of chemical response. Although the absence of CO being exiting the reactor was initially thought to be due to it getting adsorbed on the surface, the repetition of the experiment with the same concerning outcome led to the decision of turning off the system and unloading the already several time heated Sample 2. In order to double check if this behaviour continued happening under the same conditions already tested, the experimental process followed with Sample 2 was repeated over the so-called Sample 3. More details are given in the next part.

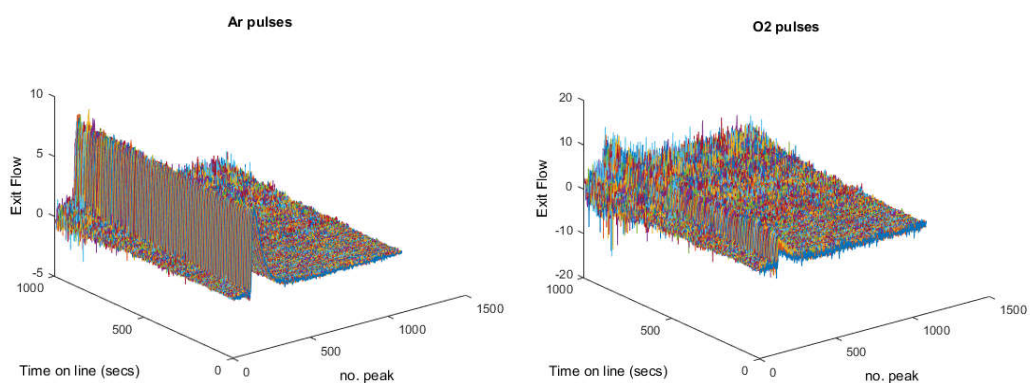


Figure 6.10. Oxidation series: 500 pulses of a gaseous mix consisting of 20.1% O₂ in Ar over 9 mg of Au/CeO₂ at room temperature and 5.4 V.

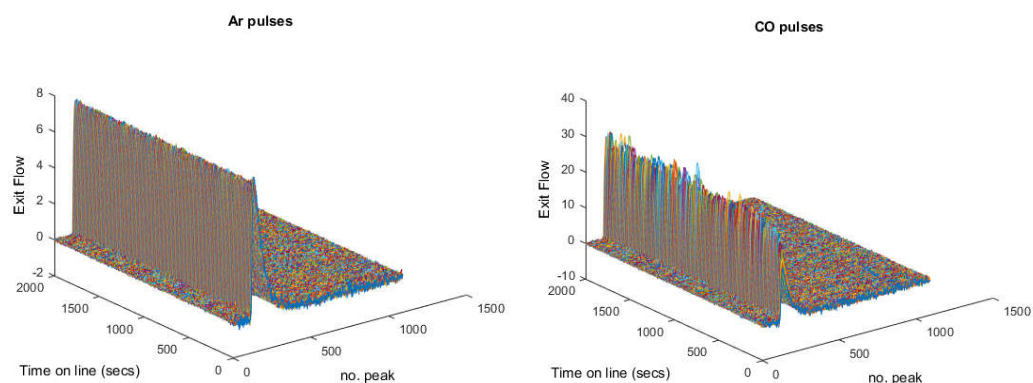


Figure 6.11. Reduction series: 999 pulses of a gaseous mix consisting of 20% CO in Ar over 9 mg of Au/CeO₂ at room temperature and 5.4 V.

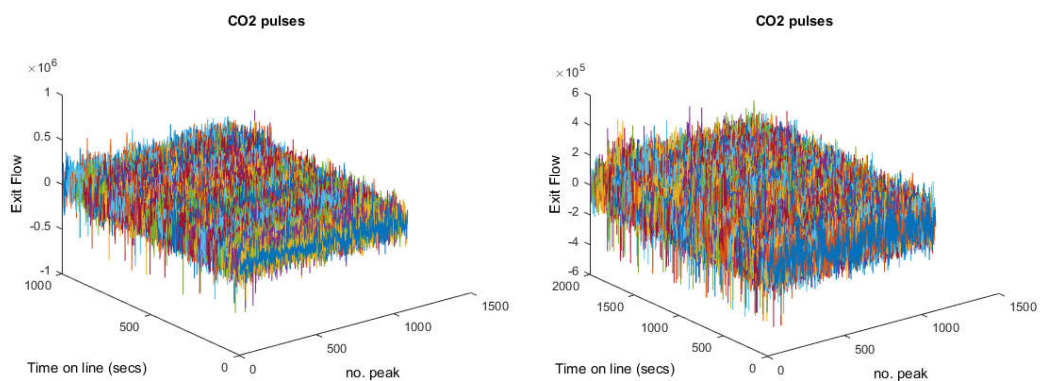


Figure 6.12. CO₂ output signal from oxidation and reduction series shown in Figures 6.10 and 6.11, figures on the left and on the right, respectively.

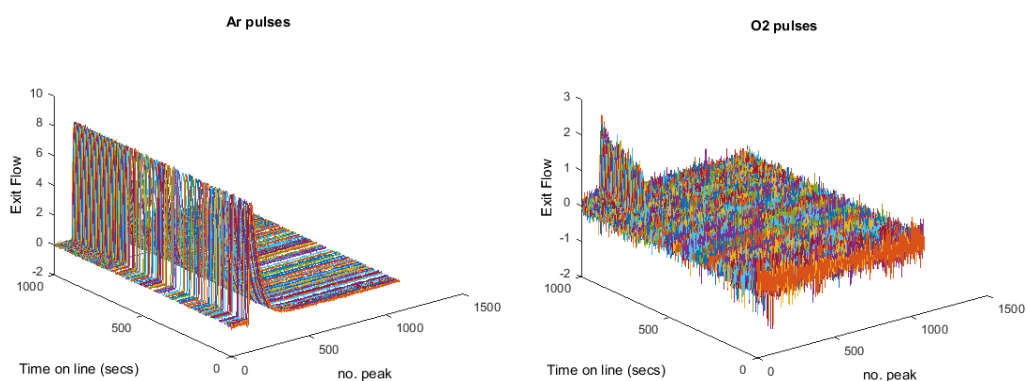


Figure 6.13. Oxidation series: 500 pulses of a gaseous mix consisting of 20% O₂ in Ar over 9 mg of Au/CeO₂ at room temperature and 5.4 V. Pulse experiment was carried out after the system was kept under vacuum conditions for 2 days.

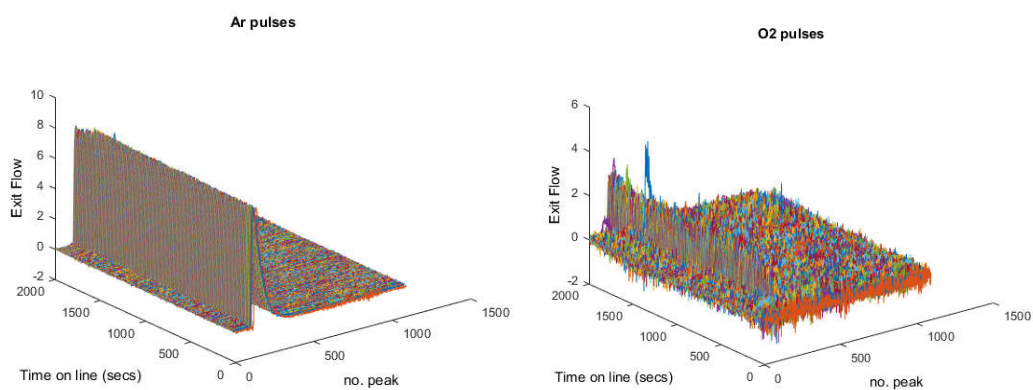


Figure 6.14. Oxidation series: 999 pulses of a gaseous mix consisting of 20% O₂ in Ar over 9 mg of Au/CeO₂ at room temperature and 5.4 V. Pulse experiment was carried out right after 500 pulse oxidation series shown in Figure 6.13.

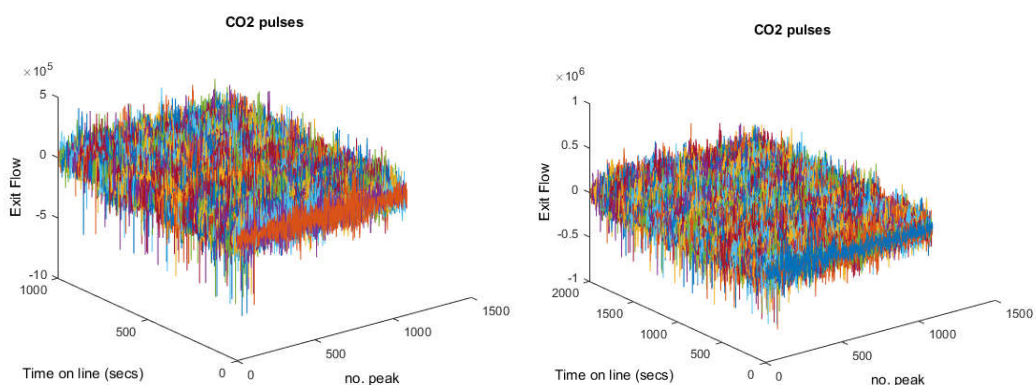


Figure 6.15. CO₂ output signal from oxidation series shown in Figures 6.13 and 6.14, figures on the left and on the right respectively.

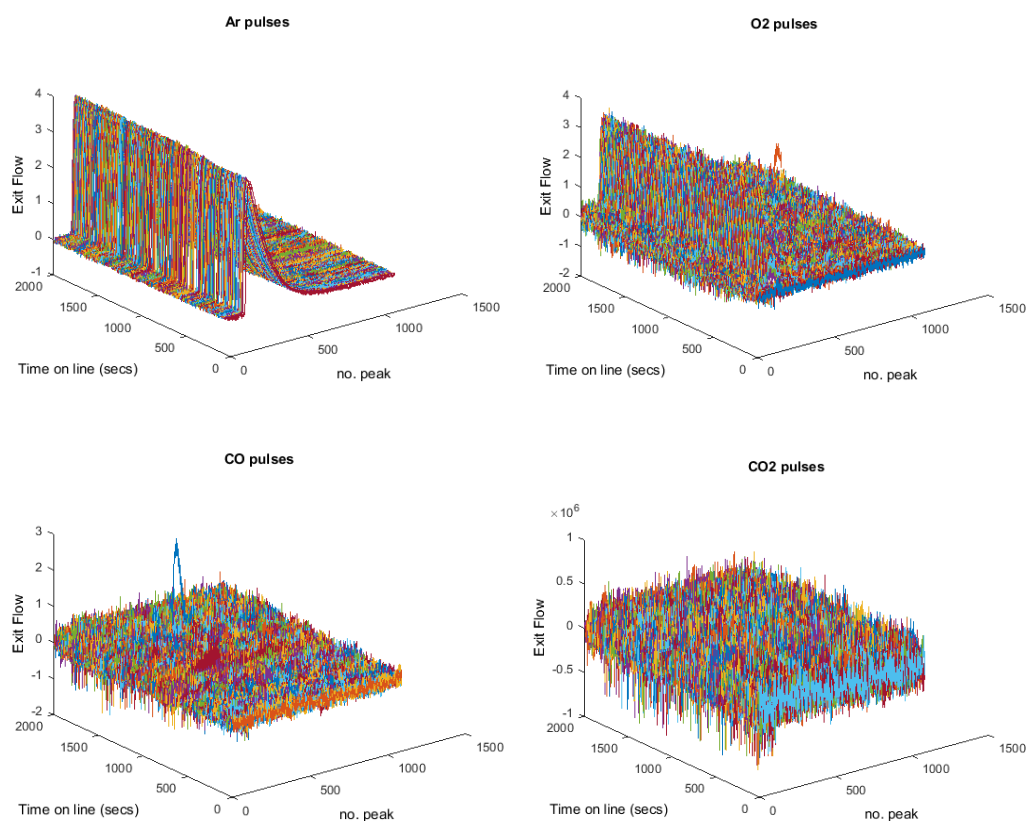


Figure 6.16. CO Oxidation series: 999 pulses of a gaseous mix consisting of 18.2% O₂ and 16.4% CO ($\lambda = 2.2$) in argon over 9 mg of Au/CeO₂ at a temperature of 135°C and 5.4 V. All pulse responses have been area normalized with respect to the raw argon response.

- Sample 3

As mentioned before, procedure followed with Sample 2 was repeated once again. Accordingly, 9 mg of Au/CeO₂ were packed into the reactor bed. After UHV conditions were established, an oxidation-reduction sequence was carried out. No CO₂ was obtained in this case either. Nonetheless, in order to continue with the showcase series of technical issues this subsection 6.3.1 is focused on, oxygen and carbon monoxide responses along with their respective argon responses are presented in Figures 6.17 and 6.18. The sudden increase in the noise of the signal during the second half of the pulse series already seen in Figure 6.10 is mimicked in Figure 6.17, although in this case the effect is even more visual. As already discussed above for Sample 1, no change on any external variable was made, considering these as any variable that could be controlled over, measured or

perceived. Hence, explanation to such noisy phenomenon could not be found. Then, as shown in Figure 6.18, CO seemed to be detected again. However, intensity of the fired gases was far from stable. As evidenced, there are two major peaks which greatly surpass the average intensity of the rest of the pulses. Differently to that seen in Figure 6.16, these peaks in the CO pulse response correlates with those observed for the case of the internal standard argon (Figure 6.18). Furthermore, they happen at the same time frame than the rest of peaks. Thus, these high intensity peaks indeed belong to the respective chemical being detected. Both phenomena observed in Figure 6.16 and 6.18, where the pulse system gave sporadic high intensity peaks, constituted quite familiar events during our TAP reactor experiments rather than isolated episodes.

Since no CO₂ was produced at room temperature, this was raised up to 184°C and a new oxidation-reduction sequence performed. Such an increase in the reaction temperature did not make any difference toward the CO oxidation taking place as it can be seen in both Figures 6.19 and 6.20. Unfortunately, the previously observed issue related to CO being undetected happened again (see Figure 6.20). In order to discard the possibility of our reactant getting surface adsorbed as a reason for such an outcome, reiterate reductions series were carried out one after another without any oxidation series in between (Figures 6.21-6.24). After five reduction series were performed in a row and no CO was detected in any of them, the adsorption hypothesis was certainly out of place. Despite, and since getting some catalytic activity in our TAP reactor experiment was our greatest intention, a very last attempt was put in practice. Results are shown in next part dedicated to Sample 4.

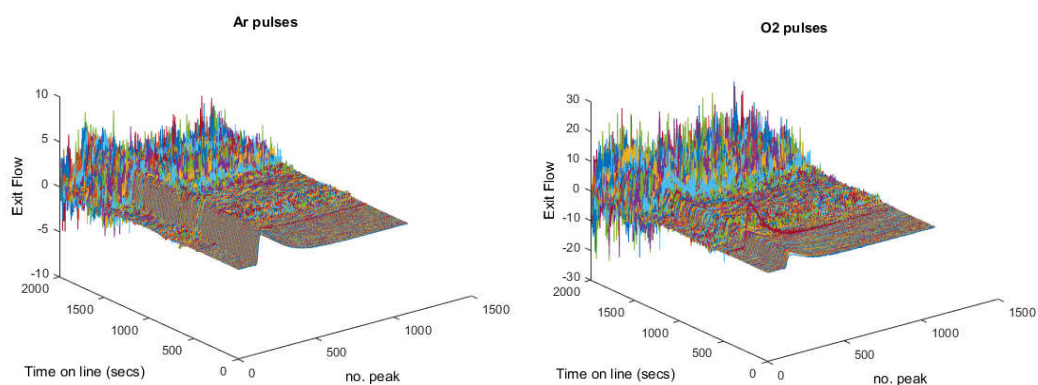


Figure 6.17. Oxidation series: 999 pulses of a gaseous mix consisting of 23.7% O₂ in Ar over 9 mg of Au/CeO₂ at room temperature and 5.4 V.

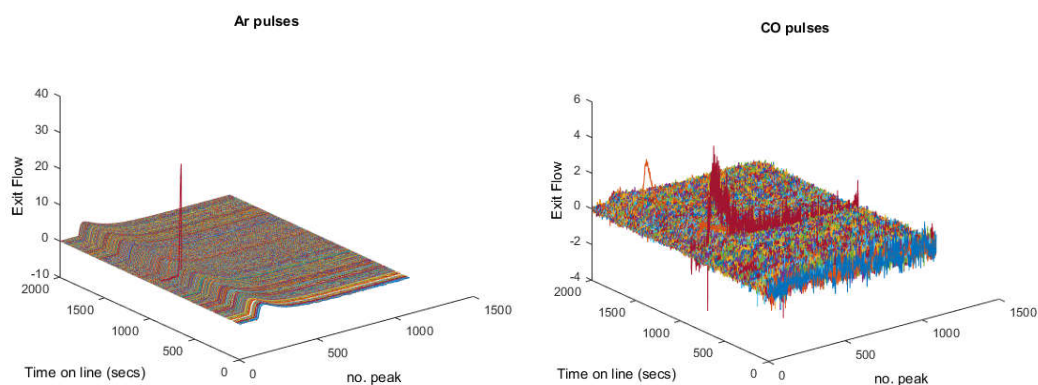


Figure 6.18. Reduction series: 999 pulses of a gaseous mix consisting of 20% CO in Ar over 9 mg of Au/CeO₂ freshly packed at room temperature and 5.4 V.

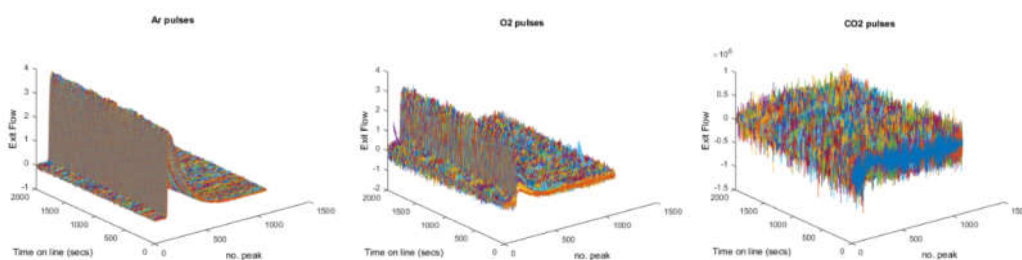


Figure 6.19. Oxidation series: 999 pulses of a gaseous mix consisting of 19.04% O₂ in Ar over 9 mg of Au/CeO₂, freshly packed, at a temperature of 184°C and 5.4 V.

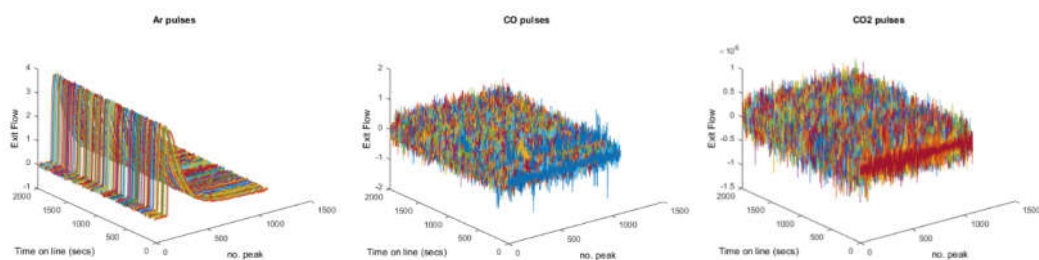


Figure 6.20. Reduction series: 999 pulses of a gaseous mix consisting of 20% CO in Ar over 9 mg of Au/CeO₂ at a temperature of 184°C and 5.4 V. Pulse experiment was carried out straight after the oxidation series shown in Figure 6.19.

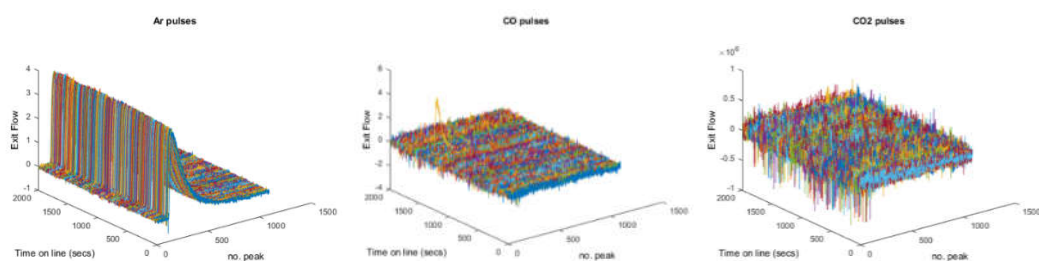


Figure 6.21. Reduction series: 999 pulses of a gaseous mix consisting of 20% CO in Ar over 9 mg of Au/CeO₂ at a temperature of 170°C and 5.4 V. Pulse experiment was carried out after the reduction series shown in Figure 6.20.

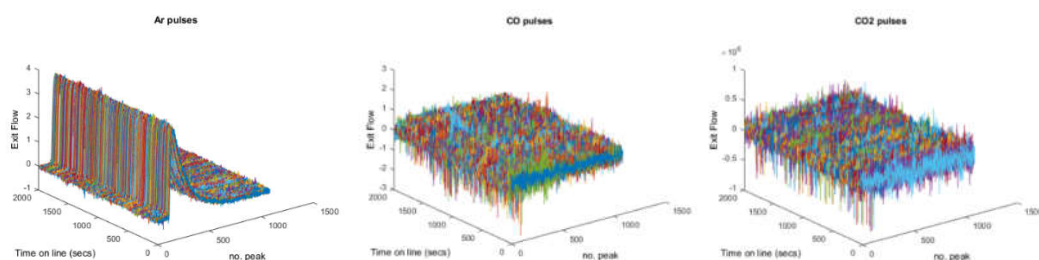


Figure 6.22. Reduction series: 999 pulses of a gaseous mix consisting of 20% CO in Ar over 9 mg of Au/CeO₂ at room temperature and 5.4 V. Pulse experiment was carried out after the reduction series shown in Figure 6.21.

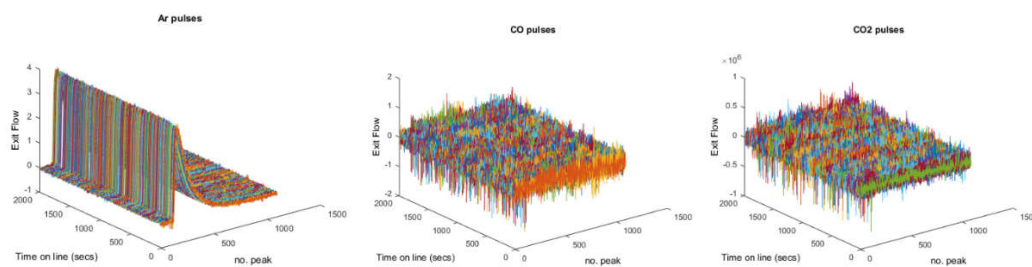


Figure 6.23. Reduction series: 999 pulses of a gaseous mix consisting of 20% CO in Ar over 9 mg of Au/CeO₂ at a temperature of 165°C and 5.4 V. Pulse experiment was carried out after the reduction series shown in Figure 6.22.

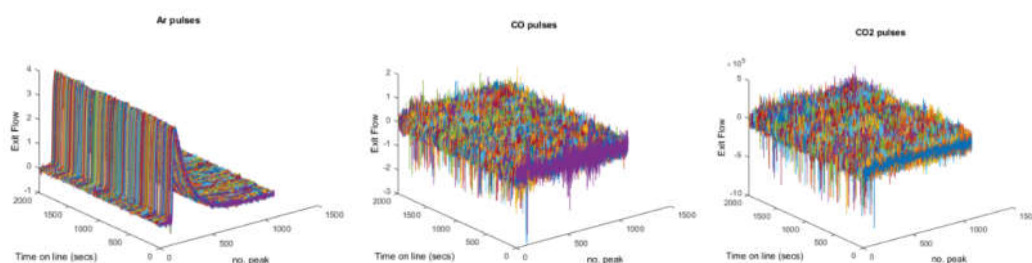


Figure 6.24. Reduction series: 999 pulses of a gaseous mix consisting of 20% CO in Ar over 9 mg of Au/CeO₂ at a temperature of 160°C and 5.4 V. Pulse experiment was carried out after the reduction series shown in Figure 6.23.

- Sample 4

Sample 4 consisted of 18 mg of Au/CeO₂. After the usual procedure getting the system under UHV conditions, an oxidation-reduction sequence at room temperature was carried out. Results from such a sequence are presented in Figures 6.25 and 6.26. Since CO was not detected, a similar approach to that followed previously with Sample 3 was implemented, i.e. consecutive reduction series in a row. In this case the temperature was not raised and all of them were performed at room temperature, therefore essentially the same conditions were replicated every time (see Figures 6.27-6.30). 4 reduction series were performed in total with no CO detection in any of them. This data clearly evidenced the issue was not related to any interaction among our reactants and surface but rather a

technical problem related to the mass spectrometer detection system. These last experiments were carried out at the very end of the given time for the completion of this research work, fact that made it unfeasible to further study any feasible way of fixing the issue and getting any more valuable data. As a consequence, the only practical information gathered during the entire pulse experiment study carried out in our TAP reactor at Cardiff University is resumed in the next subsection 6.3.2.

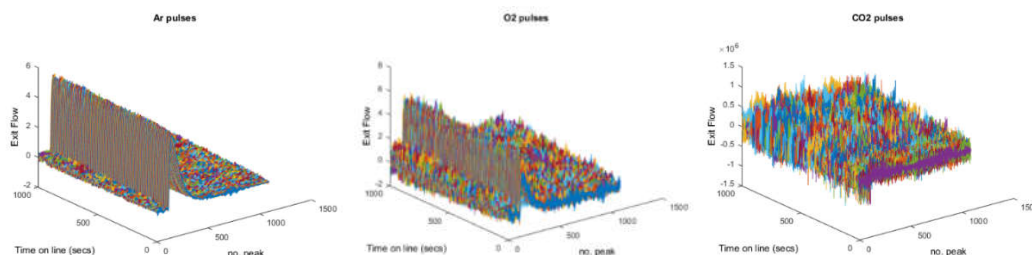


Figure 6.25. Oxidation series: 500 pulses of a gaseous mix consisting of 20.13% O₂ in Ar over 18 mg of Au/CeO₂, freshly packed, at room temperature and 5.2 V.

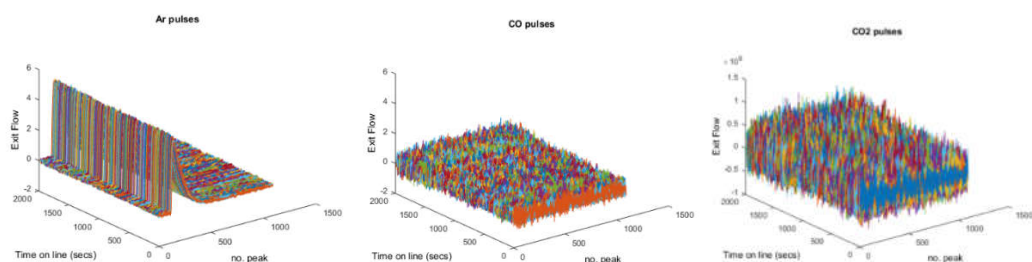


Figure 6.26. Reduction series: 999 pulses of a gaseous mix consisting of 20% CO in Ar over 18 mg of Au/CeO₂ at room temperature and 5.2 V. Pulse experiment was carried out straight after the oxidation series shown in Figure 6.25.

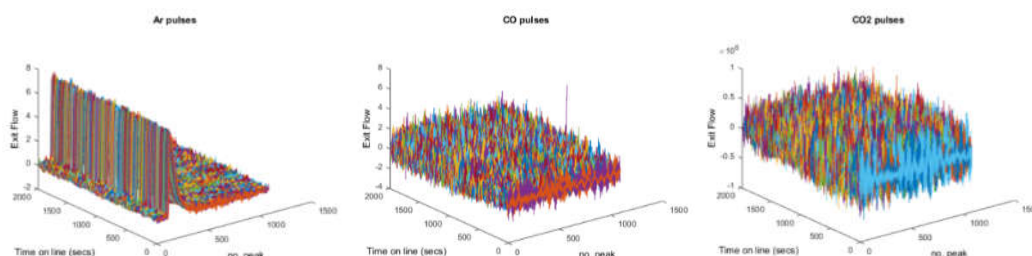


Figure 6.27. Reduction series: 999 pulses of a gaseous mix consisting of 20% CO in Ar over 18 mg of Au/CeO₂ at room temperature and 5.2 V. Pulse experiment was carried out after the reduction series shown in Figure 6.26.

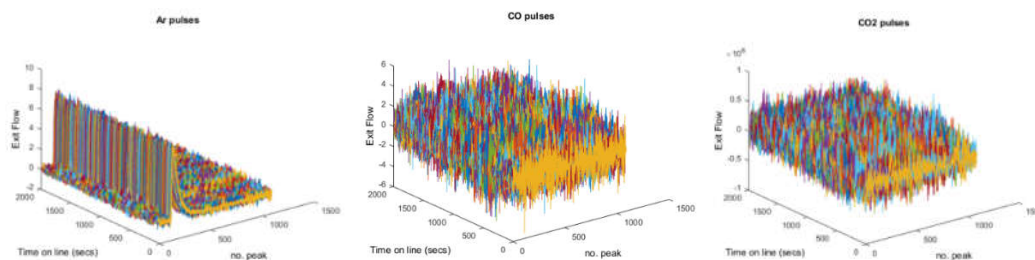


Figure 6.28. Reduction series: 999 pulses of a gaseous mix consisting of 20% CO in Ar over 18 mg of Au/CeO₂ at room temperature and 5.2 V. Pulse experiment was carried out after the reduction series shown in Figure 6.27.

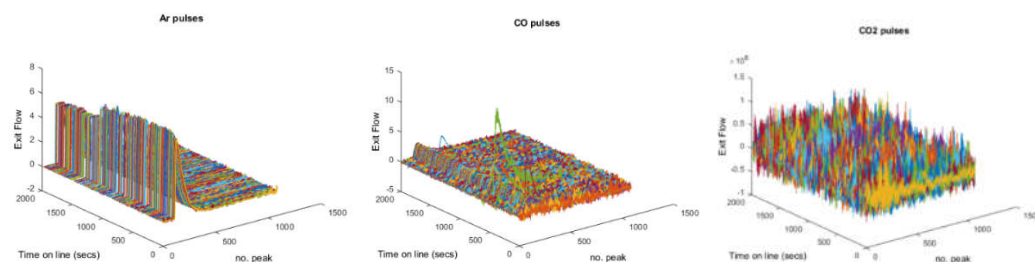


Figure 6.29. Reduction series: 999 pulses of a gaseous mix consisting of 20% CO in Ar over 18 mg of Au/CeO₂ at room temperature and 5.0 V. Pulse experiment was carried out after system was de-vacuumed and vacuumed again for 2 days after the reduction series shown in Figure 6.28.

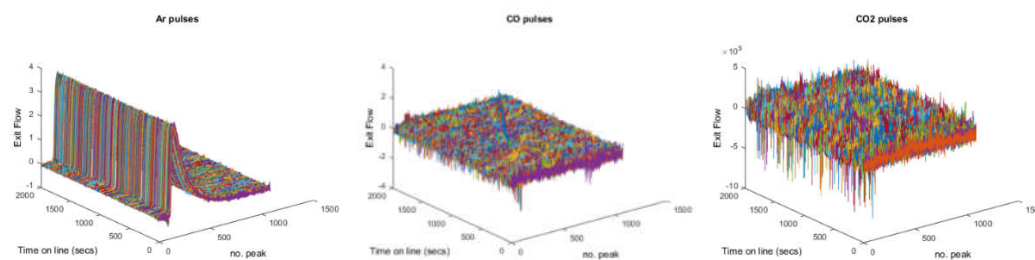


Figure 6.30. Reduction series: 999 pulses of a gaseous mix consisting of 20% CO in Ar over 18 mg of Au/CeO₂ at room temperature and 5.4 V. Pulse experiment was carried out straight after the oxidation series shown in Figure 6.29.

6.3.2 Empirical estimation to the number of active surface oxygen

The purpose of the present subsection is to extract any catalytic information about the material studied during the TAP pulse experiment detailed previously, i.e. 5% Au/CeO₂. Due to that exposed and discussed in subsection 6.3.1, such information is reduced to just one specific feature, the empirical estimation of the number of active surface oxygen. This has been sourced from the experimental data presented in Figures 6.13 and 6.14 and the procedure followed for its calculation is based on the reasoning already given when discussing those figures. In order to approximate the pulse number from which the area of the oxygen peaks get to stabilise, a comparison with the internal standard peak areas should be done. This comparison is easily performed by dividing each argon peak area by the respective oxygen one. From the definition of moments given back in Chapter 2, which was implemented in the calculations performed by our TAP analysis software (Chapter 4), it can be noticed that those peak areas, properly defined as the area underneath the peak curves, correspond to the definition of the zeroth moment (M_0). Accordingly, the zeroth moment of each argon and oxygen peak, M_{0_Ar} and $M_{0_O_2}$ respectively, were calculated and so was the ratio $M_{0_O_2}/M_{0_Ar}$. How such a ratio changes with the number of pulses was then represented as is shown in Figure 6.31. From such figure, 660 pulses have been estimated as the necessary number of pulses to fully oxidize the fully reduced surface of 9 mg of our Au/CeO₂ catalyst (when using a gaseous mix of 20% O₂ in argon to titrate the catalytic sample).

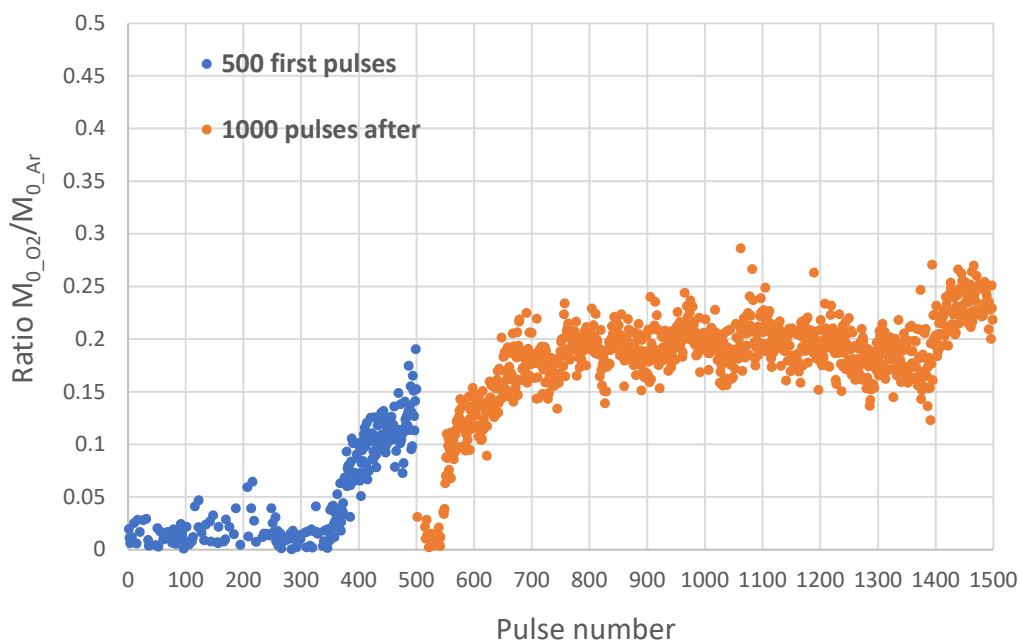


Figure 6.31. Ratio $M_{0_{O_2}}/M_{0_{Ar}}$ versus pulse number, calculated from data presented in Figures 6.13 and 6.14. The first 500 pulses (blue points) correspond to oxidation series showed in Figure 6.13. 1000 pulses after (orange points) belong to oxidation series in Figure 6.14.

From the BET and EDX characterization procedures carried out on our Au/CeO₂ catalyst (see Chapter 2), a surface area of 58.376 m² g⁻¹ (A_s) and a mean value of 4.072 % of surface gold ($\%Au_s$) were obtained respectively. In previous Section 6.1.2, the pulse size was calculated to an average of 1.382×10^{15} molecules per pulse (M_p). Furthermore, from data presented in Figure 6.31, an estimation of the number of pulses needed to fully oxidize a fully reduced catalytic surface (Np_{ox}) was accomplished. This data provides sufficient information to approximate the percentage of active surface oxygen in our catalytic sample. The mathematic procedure followed to get such an estimation along with the rest of data presented in Table 6.7 is detailed below.

From A_s and $\%Au_s$, the total area occupied by surface gold (A_s^{Au}) is given by Equation 6.12:

$$A_s^{Au} = A_s \cdot \left(\frac{\%Au_s}{100} \right) \quad (6.12)$$

Considering that a gas mix consisting of 20% O₂ in argon was used during the oxidation series that yielded the data for the calculation of Np_{ox} , the number of O₂ molecules per pulse ($M_p^{O_2}$) is obtained when Equation 6.13 is applied:

$$M_p^{O_2} = M_p \cdot \left(\frac{20 \text{ O}_2 \text{ molecules}}{100 \text{ molecules}} \right) \quad (6.13)$$

Since each O₂ molecules counts for two oxygen atoms, application Equation 6.14 results in the number of oxygen atoms per pulse (O_{atom_p}):

$$O_{atom_p} = 2 \cdot M_p^{O_2} \quad (6.14)$$

Considering as active oxygen sites those which were replenished after the fully oxidation of the previously fully reduced catalytic surface of the Au/CeO₂ catalytic sample, the number of those active sites (O_s^{Act}) can be estimated using Equation 6.15:

$$O_s^{Act} = O_{atom_p} \cdot Np_{ox} \quad (6.15)$$

As it was pointed out previously, the catalytic mass packed into the TAP reactor (SP_m) during the oxidation series discussed in this section was 9 mg. Therefore, this sample surface area (SPA_s) can be calculated according to Equation 6.16:

$$SPA_s = (SP_m) \cdot (A_s) \quad (6.16)$$

Since the atomic oxygen radius (O_r) has been approximated in literature to be around 0.7665 Å (7.665×10⁻¹¹ m), and assuming hemispherical surface oxygen particles, the total area covered by active surface oxygen (AO_s^{Act}) is given by Equation 6.17:

$$AO_s^{Act} = \pi \cdot (O_r)^2 \cdot (O_s^{Act}) \quad (6.17)$$

Finally, the percentage of active surface oxygen ($\%O_s^{Act}$) is estimated according to Equation 6.18:

$$\%O_s^{Act} = \left(\frac{AO_s^{Act}}{SPA_s} \right) \cdot 100 \quad (6.18)$$

The implementation of calculations described in Equations 6.12-6.18 gave the results presented in Table 6.7 below.

Table 6.7. Calculated values from application of Equations 6.12-6.18.

A_s^{Au}	2.377 m ² g ⁻¹
Np_{ox}	660 pulses
$M_p^{O_2}$	2.765 × 10 ¹⁴ O ₂ molecules
O_{atom_p}	5.530 × 10 ¹⁴ oxygen atoms
O_s^{Act}	3.650 × 10 ¹⁷ oxygen atoms
SPA_s	0.525 m ²
AO_s^{Act}	7 × 10 ⁻³ m ²
$\%O_s^{Act}$	1.28 %

6.4 Summary

TAP reactor experimental studies have constituted the focus of the present chapter. The estimation of the number of molecules per pulse and per unit area have been carried out through the implementation of the different approaches discussed in Section 6.1. Values obtained and presented in Table 6.6 agreed with those expected for TAP reactor studies under Knudsen diffusion conditions².

In Section 6.2, qualitative TAP assessments were made based on the experimental data obtained at Harvard University. Comparative review of both residence and peak times constituted the source for the suggestion of the different mechanism taking place. Finally, in Section 6.3, the different attempts made to obtain useful data from the TAP reactor at Cardiff University were discussed, from which an approximation to the oxygen storage capacity (OSC), in the form of percentage of active surface oxygen ($\%O_s^{Act}$), was calculated. The obtained low percentage of active oxygen present on the Au/CeO₂ surface (1.28%) correlates with reported studies^{3,4,5}, which assign the sites present at the gold particles perimeter as the precursors for CO oxidation.

References

- 1 J. T. Gleaves, G. S. Yablonskii, P. Phanawadee and Y. Schuurman, *Appl. Catal. A Gen.*, 1997, **160**, 55–88.
- 2 J. T. Gleaves, G. Yablonsky, X. Zheng, R. Fushimi and P. L. Mills, *J. Mol. Catal. A Chem.*, 2010, **315**, 108–134.
- 3 M. Kotobuki, R. Leppelt, D. A. Hansgen, D. Widmann and R. J. Behm, *J. Catal.*, 2009, **264**, 67–76.
- 4 D. Widmann, Y. Liu, F. Schüth and R. J. Behm, *J. Catal.*, 2010, **276**, 292–305.
- 5 D. Widmann, R. Leppelt and R. J. Behm, *J. Catal.*, 2007, **251**, 437–442.

7 | General Conclusions

The study of chemical kinetics of various catalytic systems has been the focus of the work encompassing this thesis, with a flow and a TAP reactor constituting the major tools such work relied on. Regarding the particular flow reactor rig used for this study, its design was the very first stage of the research. Thus, the traditional laboratory rig consisting of microreactor, bath, thermometer, gas chromatographer (GC) and chronometer was replaced with a more accurate and reliable piece of apparatus. The substitution of most of those components with newer instruments that offer the possibility to establish remote communications and the implementation of a software system to control and coordinate everything meant a significant boost over the traditional flow reactor experimental approaches. Although getting to the final version of that software system took a substantial time, the fact that this code performs as the brain of the system, communicating with each component within the rig and synchronising ones with others so that automatic reactions can take place really made up for that time. Within the software system, a series of scripts containing different codes responsible for the various actions involved in the automated process. A very detailed description of the code and the way it works was discussed in Chapter 3, while the extensive experimental results achieved upon its use were presented in Chapter 5. In such experimental phase, where the CO oxidation reaction at low temperatures (mainly below 60 °C) was investigated, the implementation of different approaches has been explained in detail in both Chapter 5 and 6, where a series of outcomes are to be highlighted.

In Section 5.1.1, a clear superior catalytic activity of the ceria supported catalysts, Au/CeO₂ and AuPd/CeO₂, over those materials where alumina or titania were used as the support instead, was evidenced. Comparing these results with those reported in literature (see Section 1.1), the lower activity toward CO oxidation of materials such as Au/Al₂O₃ observed in this work was somehow expected. Nonetheless, in the same literature-based discussion (Section 1.1), several studies reported quite good performances of titania supported catalysts, which made the

non-activity results obtained from the use of the Au/TiO₂ catalyst in our flow reactor system seem quite controversial. This led to the application of characterisation techniques such as TEM and NAP-XPS on both Au/TiO₂ and Au/CeO₂, so additional information could support the flow reactor findings. TEM images revealed that gold particles sizes within very similar ranges were present on both Au/TiO₂ and Au/CeO₂ materials, thus the possibility of sintering as a cause of the inactivity of the titania supported catalyst was discarded. Secondly, the oxidation state of the gold particles on the Au/TiO₂ catalyst and how they compared with those found on Au/CeO₂ were investigated by the application of NAP-XPS techniques. The main difference between the catalysts was found on the 'as received' samples. Thus, while both Au⁰ and Au¹⁺ species were present on the Au/CeO₂ sample, only Au⁰ was detected on Au/TiO₂. These results suggested that the presence of both cationic and metallic gold species is important to kick start the CO oxidation reaction at low temperatures. Hence, the lack of Au¹⁺ on the Au/TiO₂ catalyst could explain its poor activity.

The conversion dependence on contact time was the main focus of the experiments discussed in Section 5.1.2. Two different approaches were implemented, with the so-called 'Reused sample approach' (subsection 5.1.2.b) aimed to sort out the non-homogeneous distribution suspected from the data obtained after applying the 'Fresh sample approach' (subsection 5.1.1.a). Such non-homogeneity was then confirmed by SEM/EDX analysis of the Au/CeO₂ catalytic surface, which revealed the presence of impurities in the catalytic batch. Nonetheless, satisfactory results were obtained by such change in the followed approach, with data showing a direct correlation conversion-to-contact time. Furthermore, based on the different activities observed when comparing conversions during temperature ramp up and ramp down stages and those from fresh and reused samples, a change in the oxidation state of the surface gold particles was suggested. In particular, the transition from Au⁺¹ to Au⁰ starting at a temperature threshold of around 40-50 °C was proposed. The difference between the oxidation states of the gold particles present on the 'as received' and the 'used' sample of the Au/CeO₂ catalyst,

observed in the NAP-XPS analysis results previously presented in Section 5.1.1, reinforced the proposed oxidation state transition.

The approach adopted in this study for the estimation of apparent activation energies was discussed in Section 5.2, which resulted in E_a of 39.8 kJ mol⁻¹ and 44.9 kJ mol⁻¹ for the Au/CeO₂ and AuPd/CeO₂ catalysts, respectively. The final phase of the continuous flow investigation concluded with the calculation of the order of reaction with respect to CO at constant λ (α_{CO}^λ), developed in Section 5.3. For both Au/CeO₂ and AuPd/CeO₂ catalysts, α_{CO}^λ at 40°C and 60°C were estimated, resulting in quite similar results with values around 1 at both temperatures for both catalytic materials.

To further investigate the mechanism involved in the catalytic CO oxidation reaction, flow reactor studies were complemented with TAP reactor experiments at both Cardiff and Harvard Universities. The piece of software needed to read and analyse such experimental data was also coded as part of this work and the different phases of its design, with full detail on its mode of operation, was described in Chapter 4. Then, in Chapter 6, the different TAP reactor experimental approaches along with resulting data were discussed. Experiments at Cardiff (Section 6.1 and 6.3) were mainly aimed to estimate relevant parameters such as the number of molecules per pulse or the percentage of active surface oxygen ($\%O_s^{Act}$), which resulted in a value of 1.28%. This low percentage of active oxygen on the Au/CeO₂ surface is in agreement with reported literature^{1,2,3} which assign the sites present at the gold particles perimeter as the precursors for CO oxidation.

Finally, qualitative TAP assessments were made based on the experimental data obtained at Harvard University (Section 6.2). Comparative review of both residence and peak times constituted the source of information to propose a combination of Eley-Rideal (E-R) and Langmuir-Hinshelwood (L-H) mechanisms taking place when Au/CeO₂ was used as the catalyst. In particular, the very narrow peak observed for the case of the dioxygen molecule along with the absence of a crossing point with the Ar curve (Figure 6.5) advocated for O₂ molecules directly reacting in their gaseous form with the previously adsorbed CO. This suggested an E-R reaction type

mechanism. However, the fact that higher O₂ conversions than those expected from a stoichiometric reaction were estimated contributed to the idea that dioxygen molecules were consumed by both reacting and by replenishing oxygen vacancies in the lattice surface, leading to propose a combination of the two different mechanisms (E-R + L-H). Moreover, the long residence time observed from the CO₂ curve when both O₂ and CO entered the reactor (Figure 6.5), much broader than the one seen when only CO was fired (Figure 6.3), pointed to the CO₂ formation from multiple paths of varying rates, ultimately contributing to the idea of the double mechanism taking place.

7.1 Future work

As has been mentioned at different points of this thesis, there have been a series of studies which, due to the limited-time nature of the PhD research, could not be finished with all initial goals accomplished. Therefore, the list of things to do as the future work related to the present one would have those ‘uncovered’ studies numbered at the very beginning of such list.

Firstly, continuing the proposed approach for the calculation of the orders of reaction (Chapter 5) would nicely complete the relevant investigation developed in this work. Thus, since α_{CO}^λ was already estimated (Section 5.3), the next step would involve the calculation of the order of reaction with respect to oxygen (α_{O_2}). From then, the estimation of the order of reaction with respect to CO (α_{CO}) would be as straight forward as applying Equation 5.8 using the already calculated values of α_{CO}^λ and α_{O_2} .

Secondly, reproduce the investigation of the CO oxidation reaction carried out in this work on the PROX (preferential CO oxidation) reaction. As it was explained in Chapter 3, the software system developed as part of this study to automate reactions was designed to offer a quite high degree of flexibility. This means that, although it was experimentally used to test CO oxidation reactions, this code is able to manage PROX reactions (among others) in a similar way. Thus, the advantages this thesis has evidenced on the use of this software system could also be

experienced when studying the CO oxidation reaction in a hydrogen rich atmosphere.

In addition to the above studies, the experimental investigation initiated in this work could be expanded in numerous directions. For example, broadening the list of supported metals under study and narrowing the support material being used to a single type of oxide. This could be a series of metals such as gold, platinum, palladium and rhodium supported on ceria (i.e. Au/CeO₂, Pt/CeO₂, Pd/CeO₂ and Rd/CeO₂). In order to mimic the approach followed in this work, narrowing the number of variables coming into play would be important. Therefore, the weight percent of each of those supported metals should be the same and it would also imply those catalytic materials being synthesized following the same preparation method.

From a software development point of view, although quite satisfactory functionality has already been achieved by the current version of the CO oxidation automation and analysis software, there is still room for improvement. Thus, the system could be greatly boosted by further developing the code so that mass flow controllers (MFCs) are also included in the instrument-computer remote communications. This would increase the experimental flexibility related to the investigation of reaction dependence on contact time and ratio among reactants. Finally, although not included in the current version of the TAP analysis software developed in this work, calculation of first and second moments along with theoretical-based fitting strategies would be a great addition to further develop such piece of software.

References

- 1 D. Widmann, R. Leppelt and R. J. Behm, *J. Catal.*, 2007, **251**, 437–442.
- 2 D. Widmann, Y. Liu, F. Schüth and R. J. Behm, *J. Catal.*, 2010, **276**, 292–305.
- 3 M. Kotobuki, R. Leppelt, D. A. Hansgen, D. Widmann and R. J. Behm, *J. Catal.*, 2009, **264**, 67–76.